

Search for a cosmic neutrino flux  
from all neutrino flavours  
with ANTARES

Suche nach einem diffusen kosmischen Neutrinofluss  
von allen Neutrino-Flavours mit ANTARES

Der Naturwissenschaftlichen Fakultät  
der Friedrich-Alexander-Universität Erlangen-Nürnberg  
zur Erlangung des Doktorgrades Dr. rer. nat.

vorgelegt von  
Jutta Schnabel

Als Dissertation genehmigt  
von der Naturwissenschaftlichen Fakultät  
der Friedrich-Alexander-Universität Erlangen-Nürnberg

Tag der mündlichen Prüfung      18. März 2019

Vorsitzender des Promotionsorgans	Prof. Dr. Georg Kreimer
Erstgutachter	Prof. Dr. Uli Katz
Zweitgutachter	PD Dr. Thomas Eberl

---

# Abstract

In this analysis, a search for cosmic neutrinos with the neutrino telescope *ANTARES* from all neutrino flavours is introduced. The Cherenkov telescope *ANTARES*, which is situated off the French coast at 2.5 km depth in the Mediterranean Sea, has been taking data since 2007 with the goal to measure high-energy neutrinos of cosmic origin. To this end, two multivariate classifiers are developed in this work to select the cosmic neutrino signal from the atmospheric muon and neutrino background simultaneously for all neutrino flavours. While former analyses targeted either muons originating from muon neutrinos' charged-current interactions producing a long particle track in the detector, or electronic and hadronic particle cascades from other neutrino interactions, the classifiers incorporate common features from both signature types.

Analysing finally 913 days of data taking due to simulation constraints, a sensitivity to a cosmic neutrino flux with  $\lambda = 2.5$  of  $\Phi_{90\%} = 5.5 \times 10^{-6} \text{ GeV}^{-1} \text{ sr}^{-1} \text{ s}^{-1} \text{ cm}^{-2}$  between 6.74 TeV and 1.12 PeV is reached, with a non-significant excess of events being observed over the number of expected background events. The analysis approach increases the overall sensitivity of *ANTARES* towards the cosmic neutrino flux beyond that reached in former signature-specific cosmic neutrino searches.



---

# Zusammenfassung

In der vorliegenden Arbeit wird eine Analyse zur Suche nach kosmischen Neutrinos mit dem Neutrino-Teleskop *ANTARES* unter Verwendung von multivariaten Selektionsmethoden entwickelt und auf die von dem Neutrino-Teleskop zwischen 2007 und 2013 gesammelten Daten angewendet.

**Neutrinoastronomie** In der Neutrinoastronomie vereinen sich mit der Astrophysik und Teilchenphysik zwei Teilbereiche der Physik, in denen die Grundlagenforschung mit einer Vielzahl von Theorien und Modellen versucht, sowohl kosmologische Gegebenheiten als auch Struktur und Bildung von Materie genauer zu erklären. Auf astronomischer Seite stehen Neutrino-Teleskope neben der klassischen optischen Beobachtung von astronomischen Objekten in einer Reihe von Experimenten, die die Astronomie in anderen Wellenlängenbereichen oder mit anderen Botenteilchen wie kosmischer Strahlung betreiben. Hierbei steht das Verständnis der Beschleunigungsprozesse und Teilcheninteraktionen in galaktischen und kosmischen Beschleunigern im Vordergrund, wie beispielsweise in Supernovae, bei Gammablitzen oder Aktiven Galaxienkernen. Primäres Ziel der Neutrino-Teleskope wie *ANTARES* ist daher die Identifizierung von Quellen kosmischer Neutrinos und die Beschreibung des diffusen kosmischen Neutrino-Flusses, auch wenn keine direkten Quellen für die kosmischen Neutrinos zugeordnet werden können. Darüber hinaus können Hochenergie-Neutrinoexperimente seitens der Teilchenphysik Beiträge leisten, beispielsweise in der Erforschung der physikalischen Natur des Neutrinos durch Messung von Neutrinooszillationen oder bei der Suche nach Neutrinos aus Dunkler Materie.

**ANTARES** Das *ANTARES* Neutrino Teleskop ist ein Cherenkov-Detektor, der hochenergetische Neutrinos  $\nu_l$  und deren Antiteilchen misst, indem die Cherenkov-Strahlung der aus der Interaktion der Neutrinos entstandenen geladenen Sekundärteilchen detektiert wird. Die 12 Detektionslinien von *ANTARES*, die am Meeresboden vor der südfranzösischen Küste in 2,5 km Tiefe verankert sind, sind dafür mit je 75 sogenannten Optischen Modulen versehen, die aus druckresistenten Glaskugeln mit Photomultipliern und Ausleseelektronik bestehen. Durch die Messung von einzelnen Photonen mit einer Genauigkeit innerhalb weniger Nanosekunden und Zentimeter können in *ANTARES* die Richtung von Myonenspuren und Kaskaden von elektromagnetischen und hadronischen Schauern rekonstruiert und die Gesamtenergie der erzeugenden Neutrinos geschätzt werden.

**Analyseansatz** *ANTARES* ist optimiert auf die Messung von Myonenspuren, da diese durch ihre Länge von mehreren Metern bis zu Kilometern besonders gut für eine Richtungsrekonstruk-

tion der erzeugenden Myonneutrinos geeignet sind. Um diese neutrinoerzeugten Myonen von atmosphärischen Myonen zu unterscheiden, die den Detektor von oben kommend durchströmen, konzentriert sich die Spurselektion auf Myonen, deren Trajektorie von unterhalb des Horizontes kommt, wodurch die Erde effektiv als Filter genutzt wird. Allerdings werden in atmosphärischen Kaskaden auch Neutrinos erzeugt, die einen irreduziblen Untergrund für die Messung der kosmischen Neutrinos bilden, da sie sowohl die Erde passieren als auch energetisch im TeV-Bereich der kosmischen Neutrinos liegen. Die Suche nach einem diffusen Fluss kosmischer Neutrinos fokussiert sich daher auf die höchstenergetischsten Neutrinos, um sowohl atmosphärische Myonen als auch atmosphärische Neutrinos in der Teilchenselektion herauszufiltern. In *ANTARES* wurden erste Analysen des diffusen kosmischen Neutrinoflusses unter der Verwendung von Myonenspuren durchgeführt, später kamen mit der Entwicklung von Kaskadenrekonstruktionen Analysen hinzu, die sich nur auf kaskadenerzeugende Neutrinointeraktionen spezialisierten. In dieser Arbeit werden alle Arten von Neutrinoereignissen in *ANTARES* betrachtet.

**Multivariate Klassifizierung** In einer Vorstudie zeigte sich, dass die Sensitivität der Analyse für einen kosmischen Neutrinofluss erhöht werden kann, wenn sich die Analyse nicht allein auf Auswahlkriterien beschränkt, die durch die Ereignisrekonstruktion bei *ANTARES* geliefert werden, da diese jeweils auf die Spezifika der Myonenspuren oder Kaskaden optimiert waren, sondern zusätzliche signaturunabhängige Kriterien eingeführt werden. Diese fokussieren die Ereignisauswahl stärker auf die Eigenschaften, die die kosmischen Neutrinos von Untergrundeignissen unterscheiden, wie Richtung und Energie des erzeugenden Neutrinos. Daher wurden in einer Testreihe unter Verwendung verschiedensten Observablen der Neutrinoereignisse in mehreren multivariaten Verfahren zwei multivariate Klassifikatoren zur Selektion der kosmischen Neutrinoereignisse aus dem kompletten Datensatz entwickelt. Zum einen wird in der Analyse ein geboosteter Entscheidungsbaum (boosted decision tree, BDT) zur Klassifizierung von atmosphärischen Myonen herangezogen, zum anderen wird eine Klassifikation auf Basis der Fisher-Diskriminanzfunktion zur Unterscheidung zwischen atmosphärischen und kosmischen Neutrinoereignissen eingesetzt.

**Ereignisselektion aus 6 Jahren Datennahme** Da die Vorhersage der zu erwartenden Ereigniszahlen und die Entwicklung der gesamten Analyse auf einer Monte Carlo Simulation der bei *ANTARES* gemessenen Daten basiert, die beginnend mit der Neutrinointeraktion mit hoher Detailtreue versucht, die Interaktionsprozesse der Teilchen, Ausbreitung der Photonen im Wasser, Reaktion der Optischen Module und Effekte der Ausleseelektronik nachzubilden, ist eine Übereinstimmung der Simulation mit den tatsächliche gemessenen Daten ein Kernpunkt der Analyse. Da die Datennahme bei *ANTARES* vor allem stark durch die Umweltbedingungen in der Tiefsee und die Aktivität biolumineszenter Lebewesen beeinflusst wird, werden Simulationen auf Basis mehrstündiger Datennahmeeinheiten für die gesamte Messdauer erzeugt. Zum Zeitpunkt der Analyse lag jedoch kein homogener Satz von Simulationen für die gesamte Datensatz vor, denn es fehlten vor allem Simulationen für das Jahr 2013 und für kaskadenartige Neutrinoereignisse. Da der Versuch, die Simulationen für die fehlenden Datennahmeeinheiten aus dem übrigen Satz zu rekonstruieren, fehlschlug, wurde schließlich die Analyse auf Basis eines Datensatzes von 913 Tagen mit entsprechenden Simulationen durchgeführt.

---

**Ergebnis** Als Grundlage der Schätzung des kosmischen Neutrinoflusses diente zum einen die theoretische Vorhersage von Waxman und Bahcal, dass der Fluss einem Spektrum mit dem Spektralindex  $\lambda = 2.0$  folge, zum anderen die Messungen durch das *IceCube* Neutrinoobservatorium, welches eine erste signifikante Messung des Neutrinoflusses bereits durchführen konnte und sowohl die Stärke des kosmischen Neutrinoflusses als auch einen Spektralindex des Flusses bis zu  $\lambda = 2.5$  bestimmte. In dem Datensatz wurden 12 Neutrinoereignisse gefunden, wobei die Simulation 9,5 Ereignisse atmosphärischen Ursprungs und 4,6 – 4,9 Ereignisse kosmischen Ursprungs vorhersagt. Somit wurden zwar mehr Neutrinos gemessen als für eine reine Untergrundmessung erwartet wird, allerdings ist der Überschuss nicht groß genug, um von einer signifikanten Entdeckung sprechen zu können. Die Qualitätsgröße der Analyse, ihre Sensitivität, liegt bei  $\Phi_{90\%IC2.0} = 1.4\Phi_{IC2.0}$  zwischen 16,4 TeV to 7.1 PeV für eine theoretischen Fluss  $\Phi_{IC2.0}$  mit  $\lambda = 2.0$  und der Stärke des *IceCube*-Flusses, oder  $\Phi_{90\%IC2.5} = 1.35\Phi_{IC2.5}$  zwischen 6.74 TeV and 1.12 PeV für einen entsprechenden Fluss mit  $\lambda = 2.5$ . Damit ist die Analyse sensitiver als vorangegangene Analysen und als Analysen, deren Ereignis Selektion allein auf Selektionskriterien aus Kaskaden- und Myonenspurrekonstruktion beruht.



# Contents

<b>I</b>	<b>Aim and Instrument</b>	<b>5</b>
<b>1</b>	<b>Cosmic neutrinos</b>	<b>7</b>
1.1	Charged cosmic rays . . . . .	7
1.2	Neutrinos . . . . .	13
1.3	High-energy neutrino astrophysics . . . . .	15
<b>2</b>	<b>The ANTARES detector</b>	<b>21</b>
2.1	Measuring neutrinos . . . . .	21
2.2	Building a high-energy neutrino detector . . . . .	25
2.3	Detector operation in the deep sea . . . . .	28
<b>II</b>	<b>Toolbox</b>	<b>35</b>
<b>3</b>	<b>Monte Carlo Simulation</b>	<b>37</b>
3.1	Particle Generators . . . . .	38
3.2	Particle Propagation and Photon Production . . . . .	40
3.3	Detector Response . . . . .	41
<b>4</b>	<b>Event Reconstruction</b>	<b>45</b>
4.1	Muon track reconstruction . . . . .	45
4.2	Cascade reconstruction . . . . .	48
4.3	Energy reconstruction . . . . .	49
4.4	Further useful parameters . . . . .	51
<b>5</b>	<b>Analysis approach</b>	<b>53</b>
5.1	Analysis goal and optimization parameters . . . . .	53
5.2	Analysis strategy study . . . . .	54
<b>6</b>	<b>Multivariate Tools development</b>	<b>59</b>
6.1	Multivariate classification methods . . . . .	59
6.2	Parameter selection . . . . .	64
6.3	Tools assessment . . . . .	69
6.4	Atmospheric muon classifier . . . . .	73

---

6.5 Atmospheric neutrino classifier . . . . .	78
<b>III Analysis</b>	<b>85</b>
<b>7 Event selection and simulation additions</b>	<b>87</b>
7.1 Data selection . . . . .	87
7.2 Simulation extensions and adaptations . . . . .	92
<b>8 Search for cosmic neutrinos</b>	<b>97</b>
8.1 Classifier selection . . . . .	97
8.2 Application to the full simulation . . . . .	100
8.3 Error estimates . . . . .	101
8.4 Test on a data subsample . . . . .	105
<b>9 Analysis results</b>	<b>109</b>
9.1 Results from the full sample . . . . .	109
9.2 A closer look at the final events . . . . .	111
9.3 Results from selection 1 . . . . .	116
<b>10 Investigation and Outlook</b>	<b>123</b>
10.1 Simulation discrepancies . . . . .	123
10.2 Signature-specific analysis and update . . . . .	125
<b>A Appendix</b>	<b>129</b>
A.1 Monte Carlo Simulation Definition . . . . .	129
A.2 Mathematical methods . . . . .	131
A.3 Fluxes . . . . .	131
A.4 Parameter selection . . . . .	132
A.5 TMVA optimization . . . . .	138
A.6 Summary of simulation sets used during this work . . . . .	140
A.7 Cosmic neutrino candidates . . . . .	143
<b>List of Figures</b>	<b>160</b>
<b>List of Tables</b>	<b>164</b>
<b>Bibliography</b>	<b>166</b>
<b>Danksagung</b>	<b>173</b>

---

# Introduction

Human nature has instilled in us curiosity as the need to explore what we do not understand and make it understood. In modern science, this drive has led us to sophisticated systems of models to satisfy the need for knowing what it is we see when we look into a starry sky, what the substance that we are and walk on is made of and how it is possible that we are intelligible beings. In astrophysics, the simple star gazer has found ways to look far beyond what the eye can see, particle physics is at a crossroads where new theories about the fundamental building blocks and forces seem more abundant than our inventory of the latest star catalogue, and where the fast rise of computing power has come with an unprecedented understanding of data acquisition and processing that is inspired by the search for artificial intelligence.

On this way from simplicity to multitude, human nature has also made sure that we are left with enough pitfalls and short-sightedness that the search for scientific knowledge is not only an intellectual challenge but also one to battle one's own inaptitude. While the blank result of knowledge gathered by deliberation and testing become short lines in the history books, the daily bread of science is that of trial and error and of striking the right balance between detail and simplification.

In this thesis, the limits of human aspiration are as much at display as a multiplicity of scientific concepts is touched upon to answer the main question that grandfather stargazer would not have even been capable of formulating: Can we claim to measure neutrinos of cosmic origin in the deep-sea neutrino telescope *ANTARES*? He would probably ask: What are neutrinos and where should they come from? What is *ANTARES*? And how do you measure with this telescope? Before answering the main question of the thesis itself, a look at these underlying concepts is therefore necessary.

Here, the astrophysical laboratory of high-energy particle accelerators like active galactic nuclei is used to probe for an elusive component of particle physics, the neutrino. Bearing a part of the answer to a better understanding of both astrophysical objects as well as high-energy particle physics, the neutrino is a unique messenger which requires the construction of specified detectors. In these, the secondary products of neutrino interaction can be measured using their Cherenkov radiation in a medium which is naturally abundant like water or ice. To the end of capturing cosmic neutrinos, the *ANTARES* collaboration has therefore constructed a deep-sea neutrino telescope in the Mediterranean Sea and taken data since 2005. After a short view at the scientific framing of neutrinos in the astrophysical laboratory and their particular role in particle physics in Chapter 1, the specific construction of the *ANTARES* detector will be

explained further in Chapter 2.

With the construction of the detector, the necessity to deal with large amounts of data comes hand in hand. Here, the advancements in computing science come to the aid of the physicist, who is generally a lover of analytic formula rather than non-continuous complex correlation. In Chapter 3 and 4, the data simulation and reconstruction in the *ANTARES* detector are introduced, before embarking on the core question of the analysis: How to best achieve a high sensitivity in the analysis of the *ANTARES* data for the cosmic neutrino signal?

Due to the different radiative patterns of secondary particles induced by the different neutrino flavours and types in *ANTARES*, these different event types are generally approached as separate phenomena for which specified and well optimized event reconstruction algorithms have been developed. While former analyses focused either on track-like events from interaction of neutrinos producing a high energy muon  $\nu X \rightarrow \nu_\mu \mu Y$ , or on shower-like events originating from a bundle of secondary particles with a shorter trajectory, this analysis includes both event types. After an initial toy analysis investigation comparing the analysis sensitivity with event-type specific event selection approaches to an analysis with a dedicated event selection including all event types in a common selection procedure, the development of dedicated all-flavour event selection tools was favoured over the sole combination of two signature-specific analysis chains. To this end, two multivariate classification tools for the de-selection of atmospheric muons and neutrino events of atmospheric origin from the cosmic neutrino signal are introduced, yielding the preference for analytic formula to the practicability of machine-learning algorithms on an evolving set of Monte Carlo simulations.

With these dedicated tools, the implementation of the cosmic neutrino event selection and the according analysis chain is described in Chapter 8. In this step, the application of theoretical modelling to the real world conditions pose the main challenge. With simulation for some event types still under development for parts of the data taking between 2007 and 2013, a matching procedure is introduced to allocate simulated data to periods lacking dedicated simulated events. After additional adjustments for non-represented event classes and estimation of the error of the procedure, the analysis is tested on a sub-sample before disclosing the complete set of measurements taken from 2007 to 2013. However, the application of the analysis chain developed to the full data sample in Chapter 9 showed a deficit of measured neutrino events in comparison to expectation. As the effect was especially apparent in the part of the data where simulation had been allocated by the matching procedure, the analysis was finally limited to the comparatively well understood part of the measurements with dedicated simulations. Therefore, the full search for a diffuse cosmic neutrino signal from all flavours in *ANTARES* was finally performed on 913 days of measurements.

While learning the lesson that thorough testing of the accurate representation of all relevant data features in the simulation is a complex undertaking which is a study in itself, and which at the point of the analysis was not sufficiently well developed to allow an interpretation of the full set of measurements, the analysis still succeeds in introducing an all-flavour search for cosmic neutrinos drawing on the common features of cosmic neutrino events in comparatively small-scale telescopes (among high-energy neutrino telescopes) like *ANTARES*. The inclusion of data mining techniques and multivariate tools as computational aids in the modelling of

---

complex systems here leads to the increase of the *ANTARES* sensitivity to a diffuse cosmic neutrino flux with spectral index  $\gamma = -2.0$  towards  $\Phi_{90\%2.0} = 1.57 \times 10^{-8} \text{ GeV}^{-1} \text{ sr}^{-1} \text{ s}^{-1} \text{ cm}^{-2}$  per flavour within 16.4 TeV to 7.1 PeV, at the time of publication [1] the most sensitive diffuse flux analysis in the experiment.



## **Part I**

# **Aim and Instrument**



# 1 | Cosmic neutrinos

## 1.1 Charged cosmic rays

### 1.1.1 The beginning of astroparticle physics

Astronomy in the classic sense is understood as the observation of the solar system, galaxy and entire cosmos by using photons in the optical range that can penetrate Earth's atmosphere. However, with the development of the understanding of the nature of light and matter and development of particle physics, it was only a matter of time until light of different wavelength and ultimately particles arriving at Earth would be used to extend astrophysics by including these new messengers. Therefore, when Viktor Hess first described the observation of an ionizing radiation in the atmosphere that increased with altitude<sup>1</sup> and the radiation was soon found to contain high-energy charged particles of non-terrestrial origin, his discovery marked the birth of astroparticle physics.

The scientific investigation of the continuous bombardment of our atmosphere by cosmic particles would not only turn towards the origin of the cosmic rays to gain new insights into astrophysical processes, but cosmic rays also provide us with a free-of-charge laboratory for high energy particle physics through study of atmospheric particle cascades from cosmic ray interactions. Research of both the processes underlying the production of, inter alia, cosmic rays on the one hand and their interaction at Earth on the other hand have boosted not only the field of astrophysics, but also furthered the understanding of particle physics, especially at energies far beyond what could be produced by Earth-bound particle accelerators.

### 1.1.2 Cosmic rays at Earth

Cosmic rays arriving at the top of Earth's atmosphere have been found to mostly consist of electrons, protons, helium and some heavier nuclei, the energies of which can reach up to the TeV range, see Figure 1.1. As particle energies therefore lie far above those of the constituents of the solar wind, the origin of those particles points outside the solar system to larger objects containing larger acceleration regions required for the highest energies, which will be introduced in more detail below.

Considering the wide range of possible sources for cosmic rays, the bumpy form of the cosmic ray spectrum measured at Earth can be expected and is considered to be indicative of

---

<sup>1</sup>V. F. Hess. *Über Beobachtungen der durchdringenden Strahlung bei sieben Freiballonfahrten*. Physikalische Zeitschrift, 13:1084-1091, November 1912.

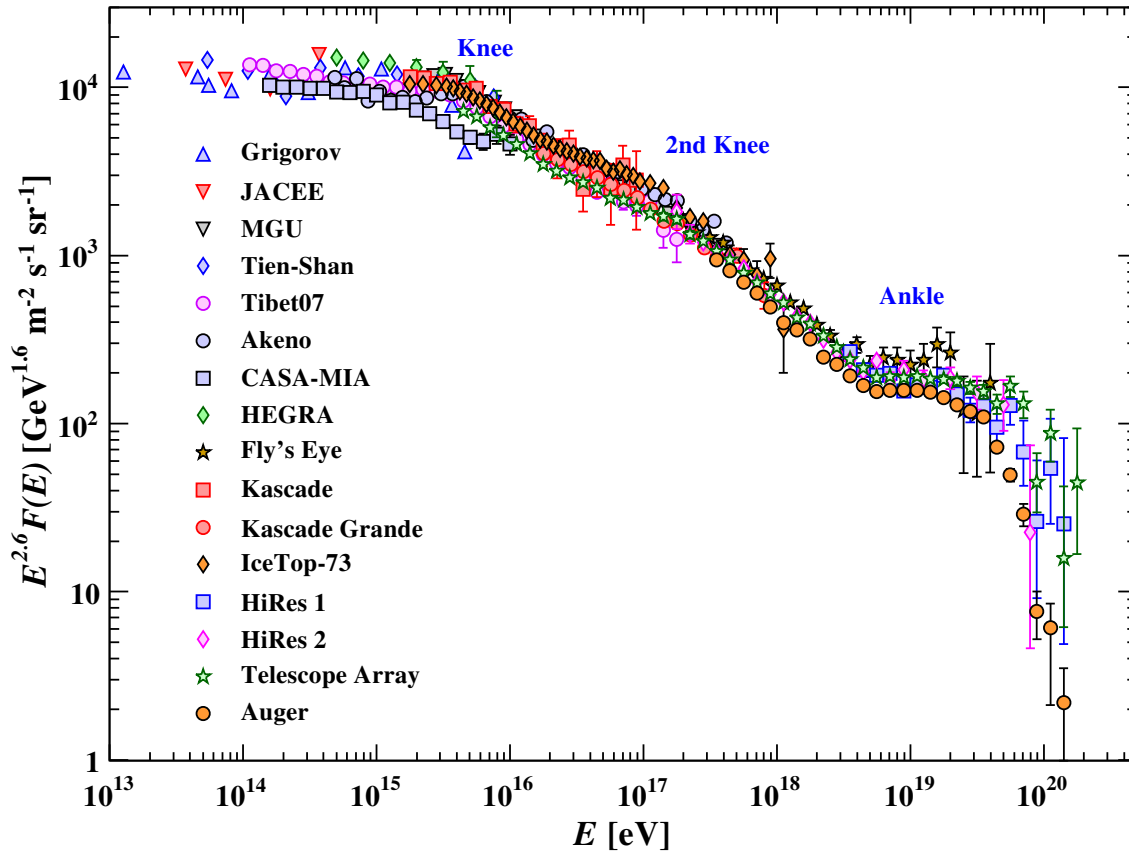


Figure 1.1: All-particle primary cosmic ray spectrum as a function of energy per nucleus from various air shower measurements. From [2]

contributions from different particle accelerators in the different energy ranges. Here, the three mainly discernible features of the spectrum are called the knee, second knee and ankle of the spectrum and can be attributed to contributions from different sources of cosmic rays. Particles from most galactic accelerators, e.g. some types of supernova remnants, are not expected to reach particle energies above the knee. Generally, the available acceleration processes and propagation and the assumption of confinement of particles to the galaxy restricts galactic particles to energies well below the ankle (i.e.  $E < 10^{18}$  eV). Therefore, the ankle shows the onset of an extragalactic component to the spectrum which becomes dominant at energies unreachable for galactic accelerators [2].

The intensity of cosmic rays at Earth's atmosphere for the relevant energy range for high-energy neutrino astronomy between several GeV to beyond 100 GeV can be approximated [2] as

$$I_N(E) \approx 1.8 \times 10^4 (E/1 \text{ GeV})^{-\alpha} \frac{\text{nucleons}}{\text{m}^2 \text{ s sr GeV}} \quad (1.1)$$

with  $E$  being the energy-per-nucleon including rest-mass energy and  $\alpha (= \gamma + 1) = 2.7$  as the differential spectral index of the cosmic ray flux, while  $\gamma$  is the integral spectral index. This spectrum is not only indicative of the astrophysical processes leading to the generation of cosmic rays, but is also the cause for those particles originating from atmospheric cascades.

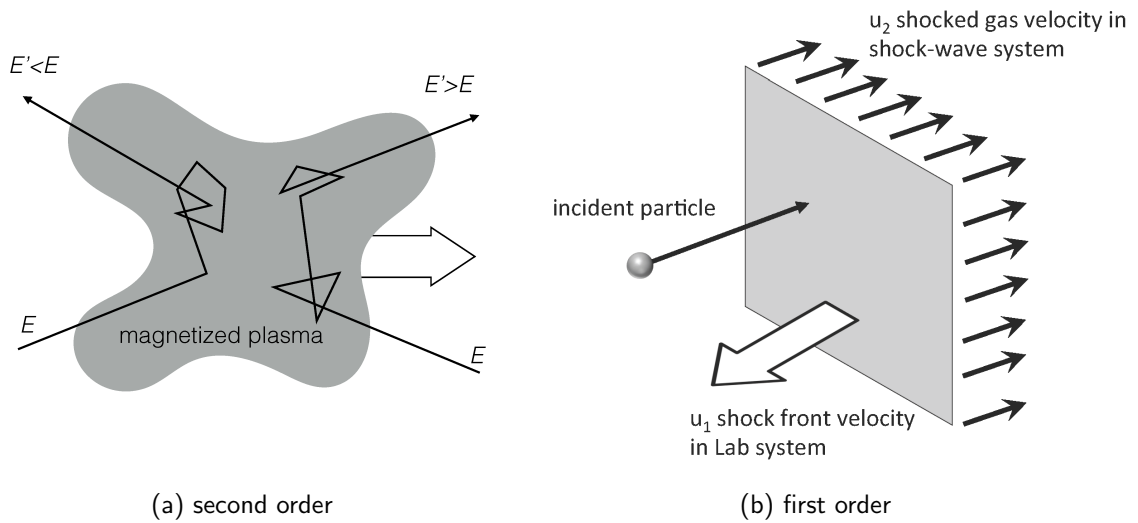


Figure 1.2: Schematic of the second order and first order Fermi mechanisms. From [5]

The distribution of cosmic rays at Earth's atmosphere is isotropic up to a level of  $10^{-3}$  as observed by IceCube, Milagro and the Tibet-III air shower array [3], which also allows for the assumption of an isotropic distribution of particles from atmospheric cascades. It should be noted that the accuracy of cosmic ray spectral modelling translates directly into uncertainties of the flux of secondary atmospheric particles, which in turn constitute also the background of any direct measurement of cosmic rays. Therefore, an accurate understanding of cosmic ray composition and atmospheric cascade formation is a key aspect in many connected fields of astroparticle physics.

### 1.1.3 The origin of high-energy cosmic rays

The processes and dynamics underlying the generation of the cosmic ray spectrum are manifold, as cosmic rays do not only originate from different sources but are also modulated by magnetic fields and accompanied by secondary particles which originate from the interaction of primary cosmic rays with the interstellar medium. In addition to charged cosmic rays, astrophysical research also extends to uncharged high-energy messenger particles, namely  $\gamma$ -rays and high-energy neutrinos, which is the focus of this work. All three constituents, cosmic rays,  $\gamma$ -rays and neutrinos are considered to be produced at cosmic particle accelerators in the presence of a strong magnetic field, and emerge from these acceleration sites at a roughly comparable luminosity [4]. Therefore, research in all three areas is highly interlinked and proves reciprocally helpful to enhance the understanding of these cosmic high-energy particle laboratories.

#### Acceleration mechanisms

Acceleration of cosmic particles occurs through the interplay of charged particles with strong magnetic fields through processes comparable to collisions or scattering between the particle and the magnetic field.

In the so-called Fermi mechanism, the encounter of a charged particle with a slowly-moving

cloud at  $v = \beta$ , in which the reflected particle can enter from a random direction, can transfer energy as  $\langle \Delta E/E \approx 4/3\beta^2 \rangle$  [6], see Figure 1.2. Although the probability of a head-on collision of particles is more probable, leading to a general acceleration of particles in the vicinity of the cloud, the mechanism is not sufficient to explain high-energy cosmic rays. However, in case of first-order Fermi acceleration, a shock front of plasma is considered to move coherently instead of randomly, thus creating a wall with downstream particles moving away from the shock front. Here, the energy gain turns linear, with  $\Delta E/E \approx 4/3\beta$ . As processes in acceleration regions are generally turbulent, the particle can interact with the same shock front repeatedly. After repetitive deposit of  $\Delta E = \zeta E$  through interaction after time interval  $T$ , the particle can thus reach an energy  $E = E_0(1 + \zeta)^n$ . Assuming an escape probability  $P_i$  after each interaction, Fermi acceleration turns out to produce a power-law spectrum with  $\frac{dN}{dE} \approx (E/E_0)^{-\gamma}$  and  $\gamma = -\frac{\ln(1-P_i)}{\ln(1+\zeta)} + 1$ . Fermi acceleration is therefore commonly assumed to accelerate particles at least up to the knee of the cosmic ray spectrum.

### Producing gamma rays and neutrinos

High-energy astrophysics is multi-messenger physics, as cosmic rays only constitute one type of particles emerging from acceleration sites and lose their directional information due to magnetic field interaction. On the other hand, gamma rays are an ever-present signal from these sources. In the production of gamma rays, two scenarios can be considered, the first one involving solely leptonic processes including synchrotron radiation and Compton scattering. In the Synchrotron Self-Compton (SSC) model [6], these mechanisms suffice to generate synchrotron radiation in the infrared, which then in turn interact through (inverse) Compton interaction with the electrons, leading to the production of gamma rays in the GeV to TeV range. While the resulting spectrum has been well observed from the Crab nebula, gamma ray emission from AGN seems to lack the X-ray counterpart of the spectrum.

This lack could be explained by a second production mechanism, this time on a hadronic basis. Here, the interaction of photons from synchrotron radiation with accelerated protons or heavier nuclei leads to a hadronic cascade, which produces gamma rays primarily through  $\pi^0 \rightarrow \gamma\gamma$ , leading to a bump in the spectrum at 70 MeV. In contrast to the leptonic scenario, hadronic cascades would also produce high-energy neutrinos, which can therefore serve as an indicator for the presence of hadronic processes within an accelerator.

### Sources of high-energy cosmic neutrinos

The capability of astrophysical objects to accelerate charged particles and therefore be a source of high-energy cosmic rays, gamma rays and neutrinos, depends on both the size of the object and the magnetic field strength, as the containment of charged particles in the magnetic field of the object and the possibility for repetitive interaction with the magnetic field determines the magnitude of the acceleration. This interdependence can be seen in the Hillas plot Fig. 1.3, where galactic and cosmic accelerators are shown with regard to their size and magnetic field strength. Following the hand-waving argument that containment arises from Lorentz force on charge  $Z$ , the maximum energy reached at the sites of size  $R$  is  $E_{max} \propto ZR\beta B$ , with magnetic field strength  $B$  and particle shock velocities  $\beta$ . The diagonal lines ( $B \times R$ ) in the Hillas plot therefore correspond to  $E_{max}$ . It can be seen that, of the more compact objects in the galaxy,

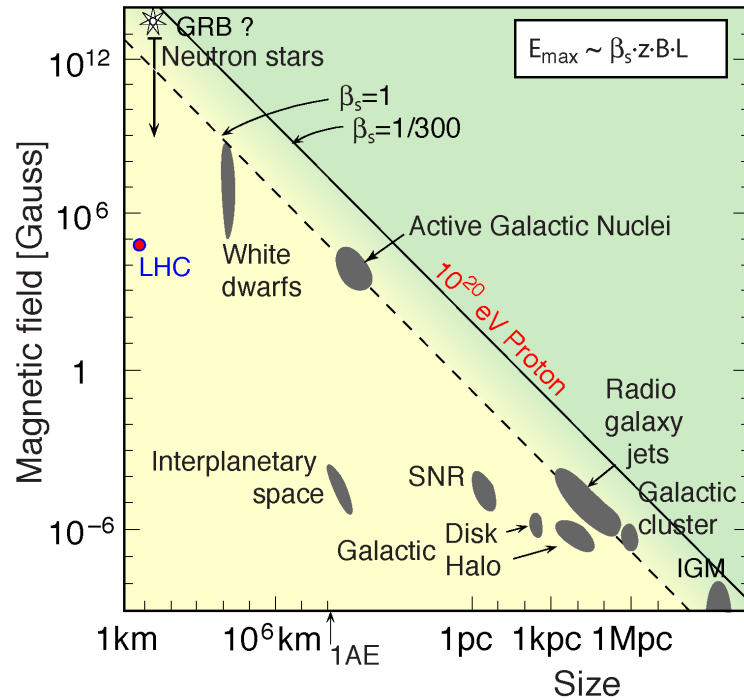


Figure 1.3: The Hillas plot, showing the dependence on particles at an acceleration site on the magnetic field strength correlated to the size of the site. From [5]

Supernova Remnants (SNRs) are a hot candidate for cosmic ray production, while the most highly energized particles stem from extragalactic sources, with Gamma Ray Bursts (GRBs) and Active Galactic Nuclei (AGNs) as two candidates for compact acceleration sites.

**Supernova Remnants** At the end of the life cycle of massive stars, a core collapse and expulsion of the outer plasma layers of the star lead to the formation of a supernova remnant (SNR). They account for up to 90% of the galactic gamma ray emission. Depending on the size and type of the core, SNRs can expand from neutron stars, pulsars or black holes. While the remnant is called a Shell Supernova Remnants in older objects, younger objects with a neutron star at the core are Pulsar Wind Nebulae. In the supernova remnant, the shock fronts in the nebula can accelerate particles up to the TeV range.

**Gamma Ray Bursts** Very luminous outbreaks of gamma ray emission are considered to originate from different sources. They either stem from large mass supernovae in the case of long outbreaks which last longer than a few seconds, while the origin of shorter Gamma Ray Bursts (GRBs) in galaxies of old star populations has recently been further illuminated by the first coincidental observation of a short GRB and gravitational waves, stemming from the merging of two neutron stars [8]. Although no neutrinos were found from the merger, the emission of neutrinos along the outflow jet was not directed towards Earth, providing a possible explanation for the lack of neutrino observations. The well-established fireball model for GRBs allows for

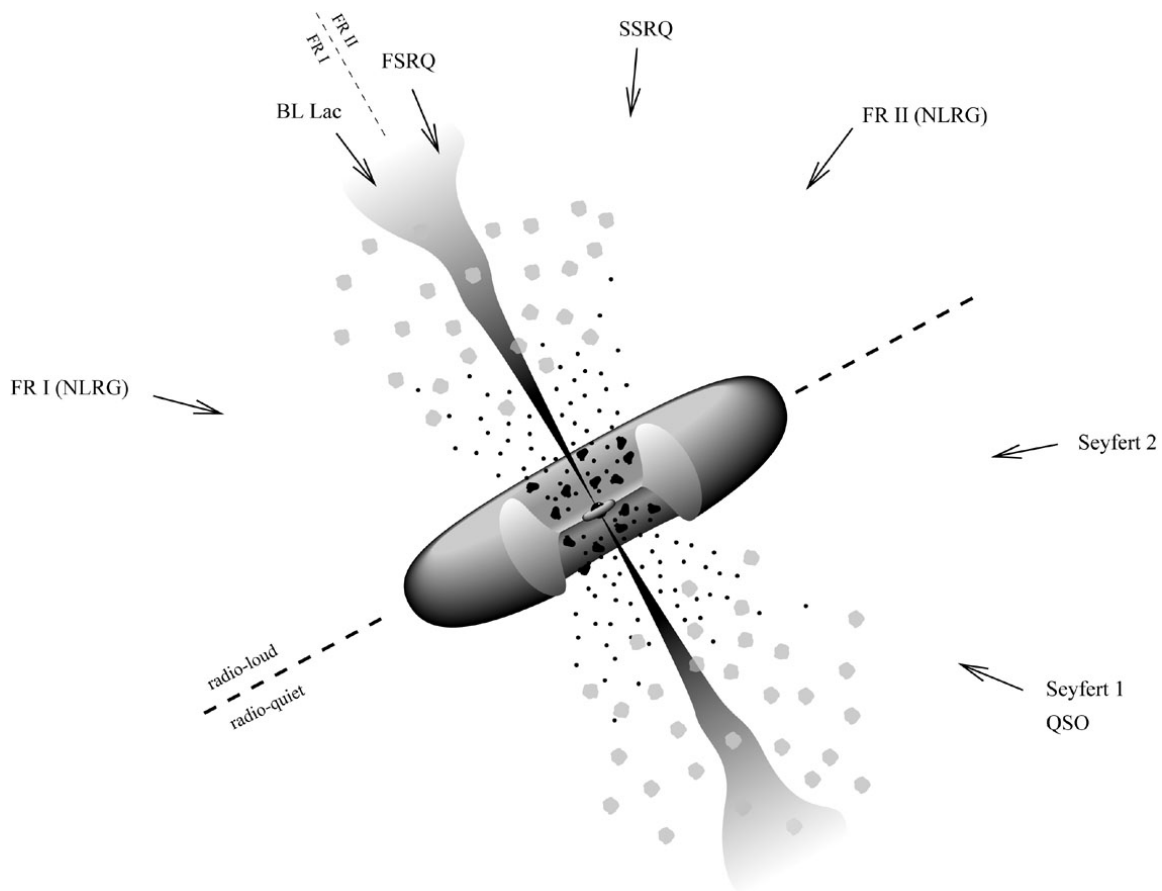


Figure 1.4: Model of an Active Galactic Nucleus, and the respective classification depending on the observation angle. From [7]

neutrino production in shock front and describes the process in three stages, where first the formation of a black hole creates a relativistic accretion disk of charged matter, forming a strong magnetic field as pre-shock. Secondly, matter is released along the axis, forming jets which act like a "fireball", producing gamma rays through collision, but which are only released when the matter has cooled enough to become transparent. These photons, travelling ahead of the shock front, appear through their relativistic shift towards us as gamma-rays. In an afterglow, where the shock front interacts with the local medium, additional photons of lower energy are also created as the shock front cools down.

**Active Galactic Nuclei** A super-massive black hole lying at the center of a galaxy provides an accretion disc of matter. In about 10% of cases, the accretion leads to the formation of relativistic jets, which serve as particle acceleration sites, leading to the formation of an Active Galactic Nucleus (AGN). Depending on the observation angle, their resulting appearance from Earth and additional radio emission from the galaxies, AGN are categorized into different objects, see Figure 1.4.

## 1.2 Neutrinos

As a particle which was first postulated as explanation for the elusive energy loss of electrons from  $\beta$  decay by Wolfgang Pauli in the 1930s, neutrinos have a notorious history of being hard to measure. From the first observation of neutrinos in the 1956 by Cowan and Reines<sup>2</sup> to the establishment of the three-flavour regime and the detection of the  $\nu_\tau$  in 2000, theoretical predictions ran generally ahead of measurements.

### 1.2.1 Neutrino properties

**Interaction and cross-section** The small cross-section of neutrinos, see Figure 1.5, poses the main challenge for their detection, leading to large-scale, long-time and high-statistics experiments for neutrino measurements. As neutrinos only interact through weak force and gravity, the influence of the latter being negligible due to its small mass, this turns them on the other hand into ideal long-distance messengers in astrophysics.

**Neutrino flavours** For the three charged leptons of the standard model,  $e$ ,  $\mu$  and  $\tau$ , the observation of the decay of heavier leptons to a continuous spectrum of lighter leptons without the emission of another detectable particle leads, via the assumption of lepton number conservation, to the introduction of a corresponding (anti-)neutrino for each type of charged leptons, so that e.g.  $\mu^- \rightarrow e^- + \bar{\nu}_e + \nu_\mu$ . Therefore, each charged lepton is in the standard model assigned its corresponding neutrino ( $l^-, \nu_l$ ), with the corresponding antiparticles ( $l^+, \bar{\nu}_l$ ) carrying the the according negative lepton number. The six lepton types are commonly referred to as flavours and grouped into three so-called generations of neutrinos. Neutrinos carry a spin  $\pm 1/2$  which is antiparallel to its direction of momentum, giving it a left-handed helicity (with antineutrinos being right-handed).

**Oscillation and flavour mixing** The first theoretical introduction of the assumption of a non-zero neutrino mass by Pontecorvo in 1957<sup>3</sup> suggesting it to be observable as oscillation of neutrinos between the different flavours again preceded the observation of changed neutrino flavour ratios in solar neutrinos. In both solar experiments as well as long-baseline experiments, the change of the proportion from the expected contributions of neutrinos of a specific flavour are well established and have been used to determine the exact mixing parameters for neutrino oscillation.

In order to allocate mass to neutrinos, three distinct neutrino mass eigenstates are introduced,  $\nu_i$ , which produce the observed neutrino flavour eigenstates through weak interaction as a coherent superposition of these mass eigenstates, i.e.

$$\begin{pmatrix} \nu_e \\ \nu_\mu \\ \nu_\tau \end{pmatrix} = \begin{pmatrix} U_{e1} & U_{e2} & U_{e3} \\ U_{\mu1} & U_{\mu2} & U_{\mu3} \\ U_{\tau1} & U_{\tau2} & U_{\tau3} \end{pmatrix} \begin{pmatrix} \nu_1 \\ \nu_2 \\ \nu_3 \end{pmatrix}. \quad (1.2)$$

<sup>2</sup>Through the reaction  $\bar{\nu}_e + p \rightarrow e^+ + n$ , in C. Cowan, F. Reines et al. *Detection of the Free Neutrino: a Confirmation*. Science, Vol. 124, No. 3212, p. 103-4, July 20 1956.

<sup>3</sup>B. Pontecorvo. *Mesonium and Antimesonium*. Journal of Experimental and Theoretical Physics, Vol. 6, No. 2, p. 429, February 1958.

$U$ , also called the PMNS-matrix, is assumed to be a unitary matrix, leading to its common parametrization with mixing angles  $\theta_{12}$ ,  $\theta_{13}$ ,  $\theta_{23}$  and phases  $\delta$ ,  $\xi$ ,  $\zeta$ . Here,  $\xi$  and  $\zeta$  are only physical if neutrinos are Majorana fermions, i.e. they would be their own antiparticle. The matrix is then parametrized as  $\tan^2 \theta_{12} = |U_{e2}|^2/|U_{e1}|^2$ ,  $\tan^2 \theta_{23} = |U_{\mu 3}|^2/|U_{\tau 3}|^2$  and  $\sin \theta_{13} e^{-i\delta} = U_{e3}$ .

**Neutrino masses and hierarchy** With the investigation of the mixing angles, also the question of the ordering of the mass eigenstates and the actual neutrino masses started<sup>4</sup>. The parametrization of the PMNS-matrix already suggests that access to the measurement of neutrino masses is gained by determination of  $\Delta m_{ij}^2$ . With mass differences between pairs of neutrino eigenstates having been determined from measurements, two possible ordering schemes for the clear identification of the physical states present themselves, called normal ( $m_3^2 > m_2^2 > m_1^2$ ) and inverted ( $m_2^2 > m_1^2 > m_3^2$ ) mass hierarchy. In addition to that, an upper limit can currently be given on neutrino masses as  $m_\beta < 2.0\text{eV}$  with  $m_\beta^2 = \sum_i |U_{ei}|^2 m_i^2$ . Both the determination of the neutrino mass hierarchy and pushing the upper limit for the direct measurement of neutrino masses are currently highly investigated topics.

## 1.2.2 Beyond the standard model

While the discovery of the non-zero mass of neutrinos already provided a first step beyond the standard model, current neutrino research plays a vital role in various fields of physics from a grand unified theory to cosmology and new physics. Some of the open issues regarding neutrinos are the nature of the neutrino as Majorana or Dirac particle, the invariance under CP-transformation or the existence of further types of neutrinos, points of research which relate to crucial questions of central physical models, see [9].

**Chirality and CP-violation** The difference between a neutrino and its antiparticle generally lies in the sign of the lepton number and the chirality, a quantum number denoting the transformation of the particle state by a right- or left-handed representation of the Poincaré group. While chirality is equivalent to helicity for massless particles, the non-zero mass of neutrinos allows for opposing chirality.

Charge transformation, from one particle to its antiparticle, is conserved together with parity, the directional mirroring of the state, in the generally assumed in CP-symmetry. However, CP-symmetry violation has been observed in  $K$ -meson decay, and can be assumed for neutrinos, which opens the door towards additional neutrino types and properties.

**Sterile neutrinos** The formalism allows for various possibilities to further determine the nature of neutrinos. Right-handed neutrinos could exist, which do not interact in weak interactions and are therefore called "sterile". The existence of these neutrinos could offer explanations for the huge discrepancy in mass between charged leptons and their neutrinos, or the observed matter-antimatter asymmetry in the universe. As additional neutrino types would enter neutrino mixing, their existence might be traced in oscillation experiments, some of which already report to have found first hints. Therefore, also the current account of only three generations of neutrinos might not tell the full tale of neutrino types.

<sup>4</sup>For a general overview of neutrino properties and current research, see [9].

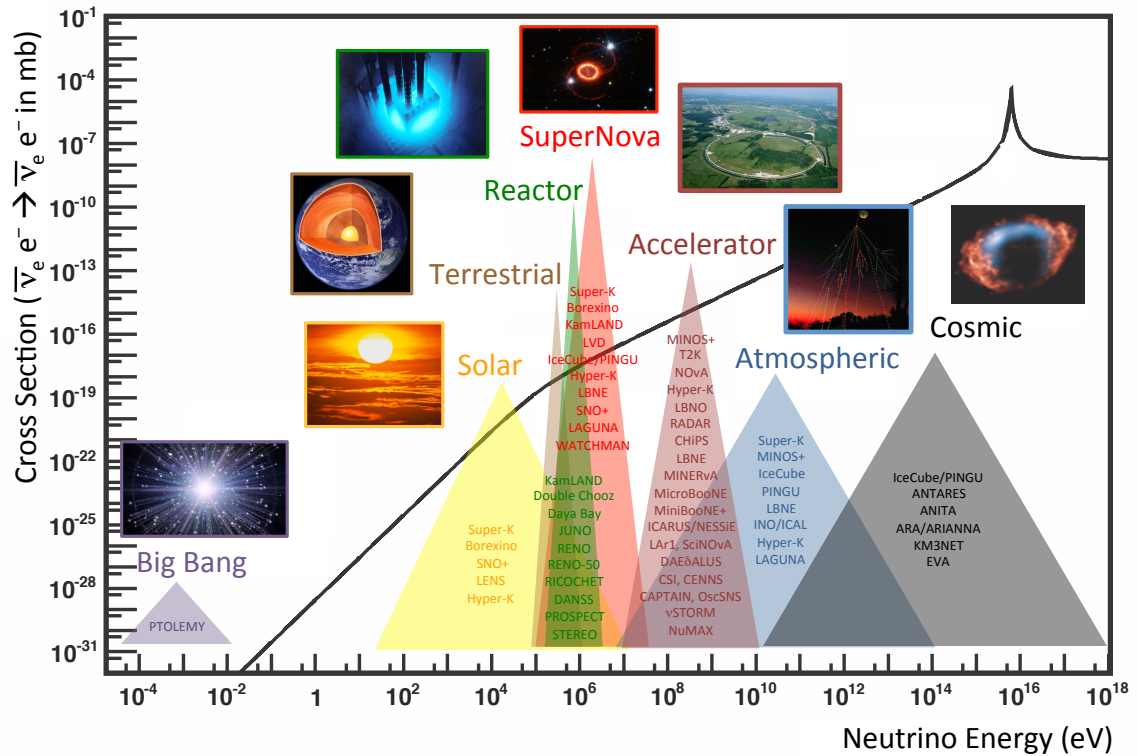


Figure 1.5: Neutrino cross section and overview over neutrino sources and experiments in the various energy regimes. From [9].

**Majorana particle** At the moment, it is not clear whether neutrinos and the corresponding antineutrinos are two different kind of particles, so-called Dirac particles, or if they are actually the same particle only with opposing chirality, i.e. Majorana particles. In this case, the  $\xi$  and  $\zeta$  mixing angle become physical. Evidence for the Majorana nature of the neutrino could come from the observation of a neutrinoless double-beta decay in which the neutrinos from two  $\beta$ -decay annihilate, which would also violate CP and lepton number conservation. However, so far no conclusive evidence for a neutrinoless double-beta decay was discovered.

### 1.3 High-energy neutrino astrophysics

In the wide range of messengers from cosmic objects, neutrinos play a special role. Especially their small cross-section is both as a blessing and a curse for high-energy astrophysics. On the one hand, neutrinos can escape acceleration regions while charged particles and photons are still trapped in the shock, as the first detection of astrophysical neutrinos from the supernova *SN1987A* before the visual detection of the supernova showed. On the other hand, their detection requires large-scale dedicated observatories to gather sufficient data to reach significant results because of the low cross-section. The experiments scale also with the energy of the targeted neutrino population due to the increasing length of the trajectory of secondary particles from neutrino interaction. Some of these experiments together with the according neutrino cross section are listed in Fig. 1.5.

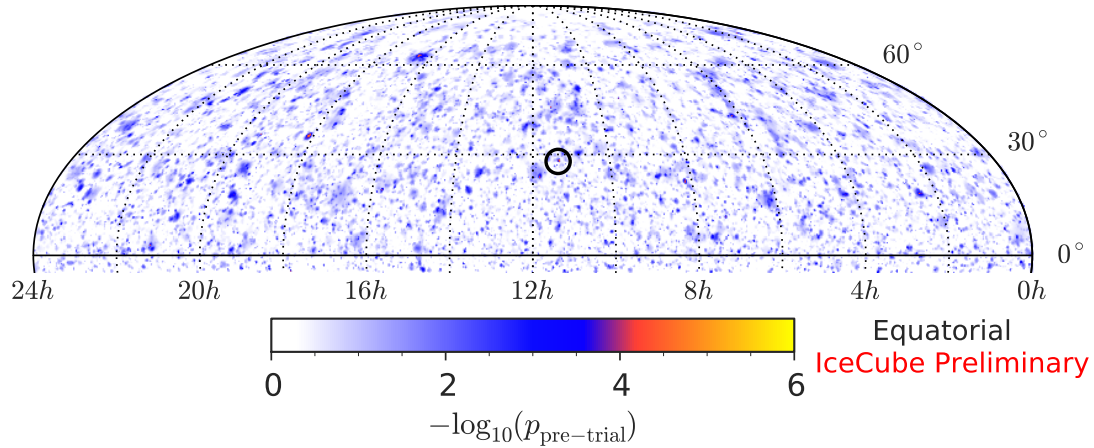


Figure 1.6: Pre-trial p-value sky map of the Northern hemisphere scan in equatorial coordinates. The position of the hottest spot is indicated by a black circle. From [11].

The presence or absence of neutrinos in cosmic accelerators is a decisive factor for the understanding of particle interaction models in the acceleration regions, and unlike charged particles and gamma rays, their interaction probability along the line of sight from extragalactic objects is small, allowing for a directional determination of the source. In addition to that, the measurement of neutrinos from known sources can contribute to some of the key questions of neutrino physics introduced in this chapter. In searches for neutrinos from theoretical sources of e.g. dark matter interactions, high-energy neutrino observatories also extend their physics agenda to new physics. Some research questions of the two largest neutrino observatories, *IceCube* and *ANTARES*, are introduced here before the current status of the search for a diffuse neutrino flux is highlighted.

### 1.3.1 Searches for astrophysical sources of neutrinos

The first evidence for astrophysical neutrinos, apart from supernova neutrinos from 1987A, was discovered by the *IceCube* observatory in 2013 [10]. The South Pole-based Cherenkov detector uses a similar detection strategy to *ANTARES* (see Chapter 2) in ice. The first claim of discovery of astrophysical neutrinos in *IceCube* was triggered by the measurement of extremely high-energy events with an almost negligible probability of being atmospheric neutrinos. These neutrinos are reconstructed with energies in the PeV range and light up a larger part of the *IceCube* detector.

**Cosmic propagation of neutrinos** Charged particles lose the directional information over large distances due to the alteration of their trajectory in magnetic fields, and both gamma rays and cosmic rays suffer a high degree of absorption and attenuation. The GZK process [6], in which photons from the Cosmic Microwave Background (CMB) interact with cosmic rays, leads to a loss of energy for protons at highest energies such that after 50 – 100 Mpc their energy has dropped under the threshold of about  $6 \times 10^{19}$  eV. On the other hand, gamma rays undergo

pair production through the presence of extragalactic background photons, which stem from the extragalactic photons, the CMB or radio background, depending on the energy range.

### **Astrophysical point source searches**

The search for astrophysical sources of neutrinos drives the design of the large-scale neutrino observatories, which aim to enhance the directional resolution of the detected neutrinos first, and secondly the number of detectable neutrinos, as both high count rate and good resolution are vital to statistically select actual cosmic neutrinos. In point source searches, a cumulation of incident neutrinos from a given direction or region is targeted either by a random search, or from prior knowledge of the position of a candidate list of possible neutrino sources. Neither *IceCube* nor *ANTARES* have, to this date, found a significant single source of neutrinos, with the "hottest" spot in Figure 1.6 having a p-value of 90.5%.

### **Galactic neutrino emission**

In addition to single point sources, the search for cosmic neutrino sources is further narrowed down by targeting a specific region of assumed neutrino emission. In *ANTARES*, for which the center of the Galaxy lies in the field of view, additional limits could be set on the maximum flux of neutrinos originating from the center of the Galaxy, for which no significant excess of cosmic neutrino candidates were found. Also, the so called Fermi-bubbles present a region of interest, as these areas of high  $\gamma$  radiation originating from the Galaxy could also be sources of neutrinos. Again, the current research can only put limit on the maximum flux [12].

### **Multi-messenger searches**

The cosmic neutrino search can further be narrowed down if the observation of an astrophysical event which is expected to produce neutrino and seen by cosmic ray, photon-based or other observatories can be used as an external trigger. These include the search for neutrinos from near-by supernovae, Gamma Ray Bursts or even gravitational waves. While a neutron star merger GW170817 producing detectable gravitational waves did not come accompanied by a neutrino [8], *IceCube* was able to allocate the first coincident neutrino event from an identified astrophysical source since supernova 1987A to  $\gamma$ -ray blazar TXS 0506+056 in 2017 [13], which was at the time in a flaring state and emitting very high-energy  $\gamma$  rays. Vice versa, high-energy neutrino incidents are used as trigger for an according follow-up observation, combining efforts in the wider astrophysical research community.

## **1.3.2 Diffuse cosmic neutrino flux analyses**

Lacking the capacity to measure the individual neutrino fluxes from specified sources, one of the most fruitful analysis approaches to cosmic neutrino detection lies in the analysis of the diffuse cosmic neutrino flux, which targets the spectral distribution of the measured neutrinos regardless of neutrino direction. Although the *ANTARES* detector did so far not collect enough data to claim a discovery of astrophysical neutrinos, which is mostly due to its comparatively smaller detection volume, the *ANTARES* collaboration had been able to set a strong upper limit on the astrophysical neutrino flux [15] already during the developmental phase of *IceCube*.

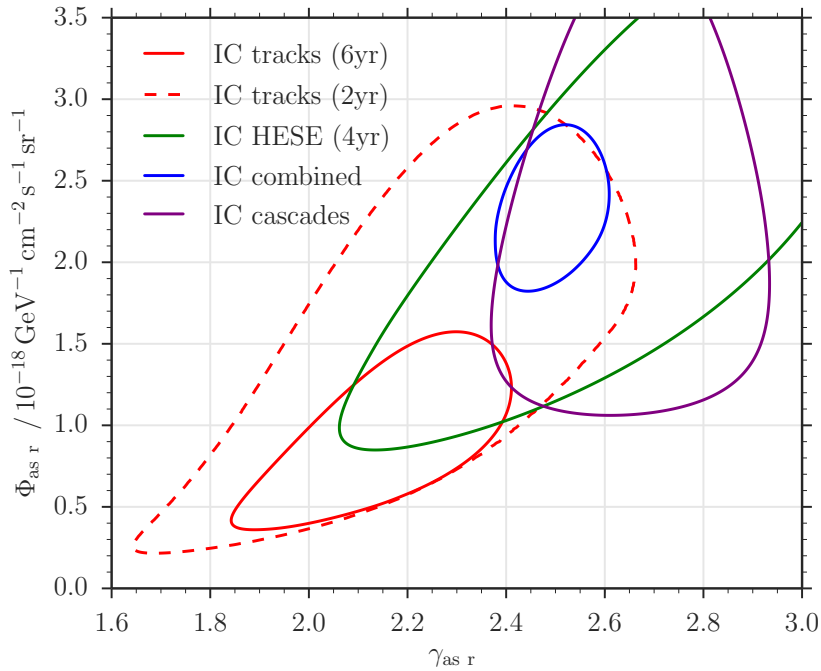


Figure 1.7: Results of different *IceCube* analyses measuring the astrophysical flux parameters  $\Phi_{astro}$  and  $\gamma_{astro}$ , with the contour lines showing the 90% CL. *IC HESE, 4yr* shows the latest muon track analysis, *IC cascades* an analogous cascade analysis, *IC combined* an integrated results of several analyses and *IC tracks (2yr)* and *(6yr)* shows upgoing muon track based analysfs. From [14]

### Neutrino spectrum measurements by IceCube

*IceCube* has provided various analyses on the spectral and spacial distribution of astrophysical neutrinos. Dividing the data samples according to building phases of employed strings in the ice and later detection years of the completed detector, and employing different veto strategies for event filtering, *IceCube* has started to map out the parameter space for the astrophysical neutrino spectrum [14]. Especially the measurement of several events in the PeV range can be regarded as a first detection of astrophysical neutrinos dating back to 2013.

In Figure 1.7, the results of various *IceCube* analyses are shown together with a specialized analysis for upgoing tracks only, i.e. neutrinos from the Northern hemisphere entering the detection volume from below. The diverging best fit results show a harder neutrino flux spectrum for the Northern hemisphere which excludes the galactic plane, indicating towards different neutrino spectra from galactic sources compared to the overall spectrum.

In Figure 1.8, the unfolded neutrino spectrum containing these events can be seen, alongside with the best fit for the conventional atmospheric flux and an upper limit on the prompt atmospheric flux, which will be introduced in more detail in Chapter 2.3.1. A contribution from these prompt atmospheric neutrinos, which could have an impact on the measurement of astrophysical neutrinos due to its harder expected spectrum, was not found in the latest *IceCube* measurements.

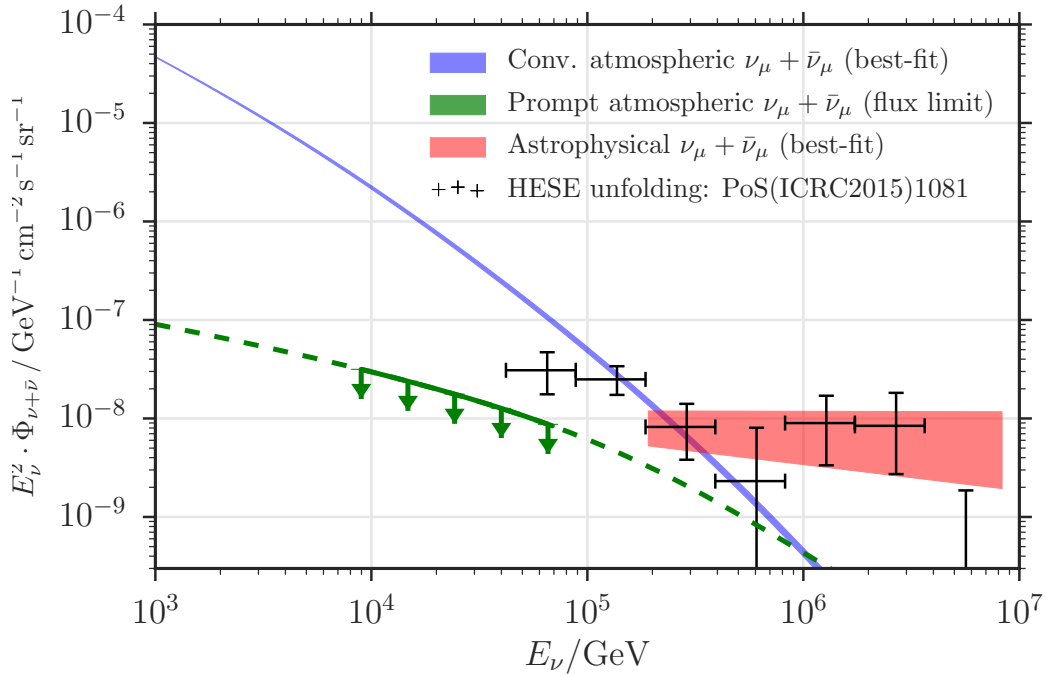


Figure 1.8: Best-fit neutrino spectra for an unbroken power-law model. From [14]

### Diffuse neutrino flux analyses in ANTARES

Concerning the investigation of a diffuse cosmic neutrino flux, the standard analysis of  $\nu_\mu$  muon track events lies, in principle, at the core of most diffuse neutrino flux analyses in *ANTARES*. While the first analysis specifically targeted muon track events, the following development of cascade reconstruction led to a separate analysis of neutrinos producing this event signature [16], which will be discussed in more detail during the following work. In addition to that, an ultra-high energy analysis targeted a  $\nu_\mu$  flux of cosmic origin in [17]. The details of these analyses will be considered in Chapter 5 when developing the approach to a combined track and shower diffuse neutrino flux search.

With the smaller instrumented volume of the *ANTARES* detector in comparison to *IceCube*, the later analyses of *ANTARES* data will certainly not be able to reach a competitive sensitivity to *IceCube*. However, this analysis will investigate the possibility to increase sensitivity in the diffuse cosmic neutrino flux analysis by developing an integrated approach including all neutrino types.

### 1.3.3 Neutrino physics and dark matter

The neutrino telescopes can also contribute to some of the research questions of neutrino physics by using e.g. the constant background of atmospheric neutrinos as source. Neutrino oscillation parameters can be targeted by using atmospheric neutrinos travelling through Earth and entering the detector at various angles, as their inclination reflects their different path length from

the Earth's surface. This also allows the search for sterile neutrinos, although the precision of the study is naturally outperformed by dedicated oscillation experiments [18].

The search for dark matter is another well explored field of research in the high-energy neutrino observatories, drawing on various theoretical predictions of neutrino production from dark matter interactions. Neutrinos are assumed to be produced by Weakly Interacting Massive Particles (WIMPs) accumulating in massive objects, where their annihilation produces neutrinos. Therefore, the Sun or Earth itself were proposed as sources of neutrinos from WIMP annihilation, as well as the Galactic center or the Milky Way halo, and limits on the neutrino flux from these regions were set by both *ANTARES* and *IceCube* [19].

As the current generation of neutrino observatories is continuously developed further, also additional research goals are explored, extending the agenda from the pure astrophysical focus towards particle physics and new physics goals.

## 2 | The ANTARES detector

### 2.1 Measuring neutrinos

All neutrino detection must rely on secondary products of neutrino interaction. Here, not only the interaction characteristics of neutrinos, but also of particles further down the reaction chain are crucial for a good reconstruction of primary particle properties. These characteristics also define the design of the apparatus to optimize its sensitivity towards this interaction signature. Therefore, the question how to measure neutrinos is covered in the first chapter by first tracing the steps from the neutrino interaction to the Cherenkov photon signature before embarking on a description of the *ANTARES* detector and its data taking in the following chapter.

#### 2.1.1 Neutrino interaction

As weakly interacting particles, neutrinos either exchange a  $W^\pm$  boson in a charged-current (CC) interaction  $\nu_l N \rightarrow l X$ , or a  $Z^0$  in a neutral current (NC) interaction  $\nu_l N \rightarrow \nu_l X$ , see Figure 2.1. Here, NC interactions will lead to the renewed emission of a neutrino with lower energy, a CC interaction produces a charged lepton. While interacting in deep inelastic scattering with the nucleon quarks, both interaction also causes a hadronic particle cascade alongside the neutrino or lepton. Therefore, the interaction vertex of a neutrino can in all cases be detected as charged particle cascade.

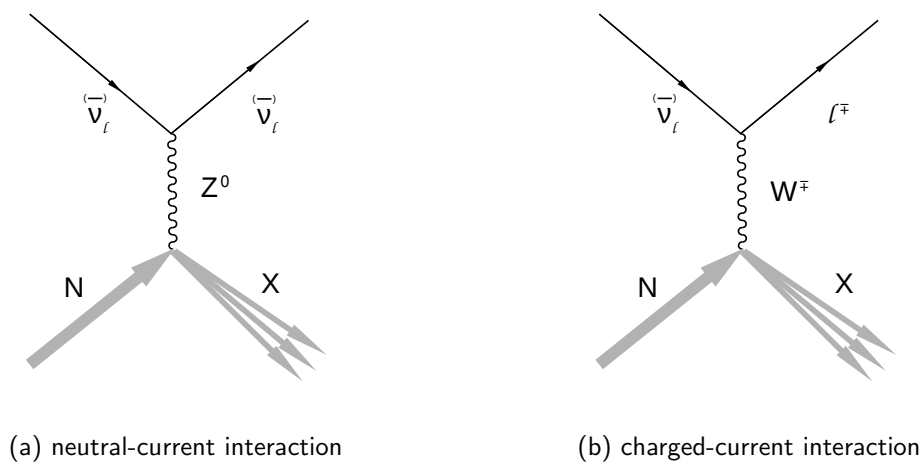


Figure 2.1: Feynman graphs of neutrino  $\nu_l$ ,  $l = e, \mu, \tau$  interaction through  $W^\pm$  or  $Z^0$  exchange with quarks of a hadron  $N$ .



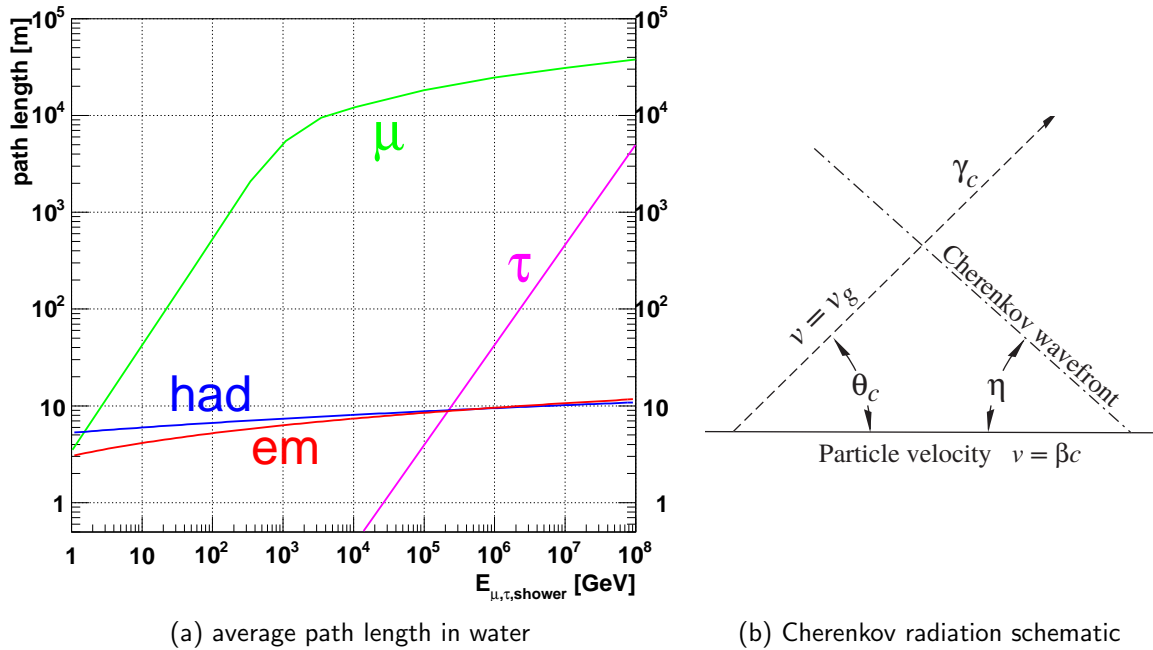


Figure 2.3: Path length of neutrino interaction products, i.e.  $\mu$ ,  $\tau$  and electromagnetic and hadronic cascades, in water, from [21], and schematic illustration of the Cherenkov radiation mechanism, from [22].

and thus give rise to an electromagnetic shower, or decay to cause a  $\nu_\tau$  and a hadronic shower through e.g.  $K$  or  $\pi$  production.  $\tau$  events are therefore either detected as muon events when initial interaction happens outside the detection volume of the detector, as simple cascades in case of a short  $\tau$  track, or as so-called "double-bang" events when the  $\nu_\tau$  interaction causes a hadronic cascade and the  $\tau$  travels a relevant distance before producing the second shower when decaying.

The reconstruction approach for the direction and energy of the incident neutrino depend heavily on their path length in the detector and light production mechanisms, which will be further explained in the following chapter. A comparison of the average path length for the secondary particles can be seen in Figure 2.3a.

**Resonant interactions** On top of the standard NC and CC interactions, resonant scattering processes enter the neutrino cross-section, see Figure 2.2. Of those, the most dominant is the Glashow resonance [23], produced by the interaction  $\bar{\nu}_e + e^- \rightarrow W^-$  at an energy of 6.3 PeV. Decaying, amongst other channels, as  $W^- \rightarrow \bar{\nu}_l l^-$ , all before mentioned event signatures can stem from these resonant interactions, including hadronic cascades.

### 2.1.2 Propagation of charged particles

The detection of charged particles at high energies relies on Cherenkov radiation produced by charged particle passage through a medium above its speed of light. Therefore, sources of Cherenkov radiation are not only the charged leptons and the direct interaction secondary

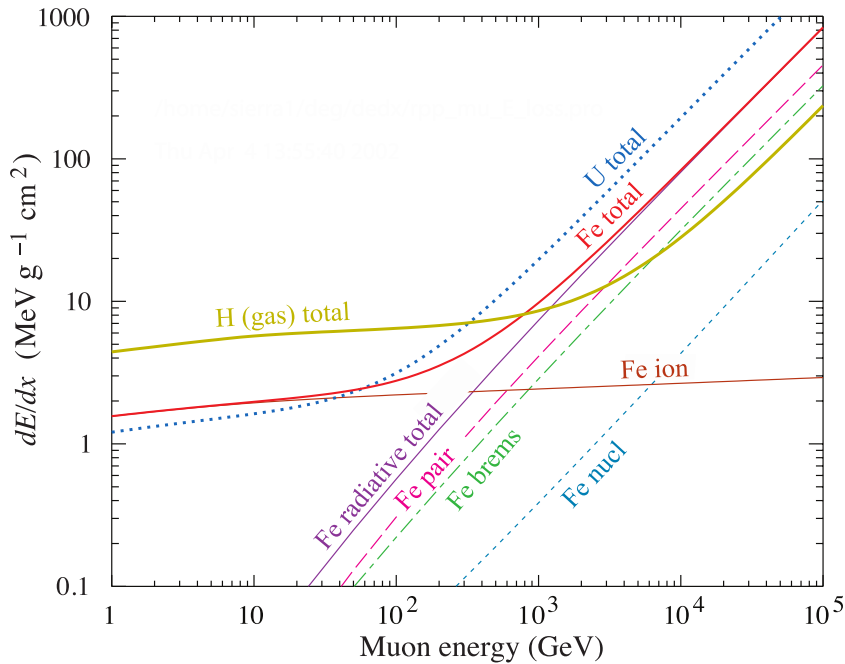


Figure 2.4: Average energy loss by muons passing through hydrogen, iron and uranium through radiative processes and ionization. From [22].

particles, but any charged particles of sufficient energy emerging from electronic and hadronic vertex cascades or from energy loss process of the neutrino-induced lepton.

### Cherenkov radiation

Cherenkov radiation is emitted in the ambient medium of a charged particle through which it passes at a velocity  $\beta$  surpassing the phase velocity  $v_p$  of electromagnetic waves of the medium [22]. It stems from the short-term polarisation of ambient atoms by the charged particle, which thus emit electromagnetic waves which in turn interfere constructively due to the faster passage of the particle than the light speed. The resulting radiation is produced in a conical shell with its vertex at the particle path, propagating as a photon front with cone opening angle  $\eta$ , see Fig 2.3b.

With the opening angle being dependent on the refractive index of the medium,  $n$ , and the velocity of the passing particle,  $\beta$ , the Cherenkov angle  $\theta_C$  can be calculated as  $\cos \theta_C = 1/n\beta$ . For the use in high-energy neutrino detection, the particle velocity can almost always be assumed to be close to the speed of light in vacuum, i.e.  $v \approx c$ . As the refractive index of water as target material is  $n_{\text{H}_2\text{O}} = 1.33$ , Cherenkov radiation is here produced at  $\theta_C = 41.2^\circ$ . The number of photons emitted at pathlength  $x$  and wavelength  $\lambda$  by a charge  $e$  is then given as

$$\frac{d^2N}{dx d\lambda} = \frac{2\pi\alpha}{\lambda^2} \left(1 - \frac{1}{\beta^2 n^2}\right), \quad (2.1)$$

with  $\alpha$  the electromagnetic coupling constant. Considering the light absorption properties of water favouring the propagation of visible light, especially of blue light, and the decreasing photon density of Cherenkov radiation with increasing wavelength, the best trade-off between

transparency of the medium and intensity of the radiation lead to the use of blue to violet light in the experiment. Therefore, the construction of photon detection devices in *ANTARES* is optimized to the according wavelength.

### Energy loss processes

All charged particles suffer energy loss from various mechanisms and are sources of Cherenkov radiation until the particle velocity becomes smaller than the speed of light of the medium. However, in case of *ANTARES*, energy loss processes are best demonstrated with regard to muons as the golden detection channel, where the measurement of the muon path length or Cherenkov emission of energy loss processes along the path can be used to reconstruct the initial muon energy with increased precision.

Energy loss processes for muons in the relevant GeV range undergo a significant transition from a fairly constant energy loss below a critical energy  $E_{crit}$ , stemming from ionization, towards energy-dependent energy loss mechanisms above the critical energy caused by radiative processes, see Fig 2.4. Therefore, muon energy loss is generally approximated as

$$-\frac{dE_\mu}{dX} = a(E) + b(E)E_\mu, \quad (2.2)$$

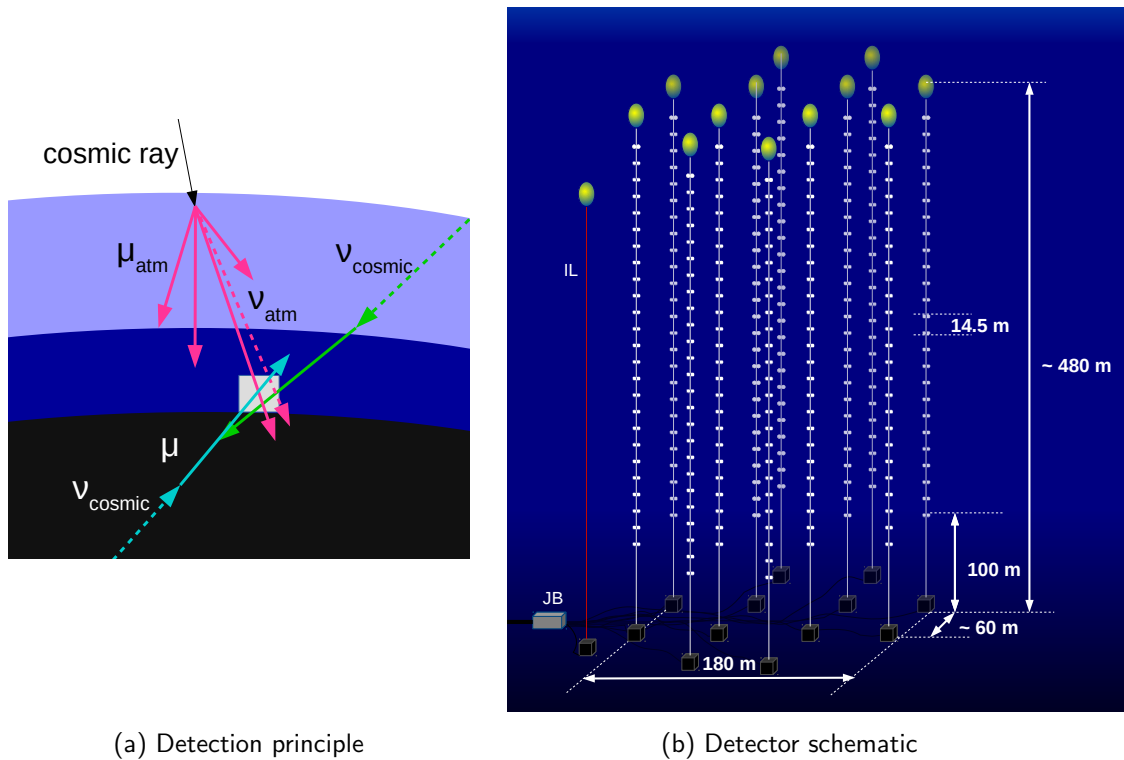
with constants  $a(E)$  describing the ionization loss component, and  $b(E)$  originating from bremsstrahlung,  $e^+e^-$  pair production and photonuclear processes [22]. These latter radiative processes are characterized by stochastically distributed energy losses along the muon's trajectory overall increasing in intensity and decreasing in frequency for higher particle energies. These can lead to sizeable electromagnetic showers along the path for sufficiently high muon energies and are, but for the continuous muon track, hardly distinguishable from electromagnetic or hadronic vertex showers. From Equation (2.2), the critical energy, which is the boundary between the dominance of constant and energy-dependent energy losses, can be expressed as  $E_{crit} = a(E)/b(E)$ . In water,  $a(E)_{H_2O} = 2.67 \times 10^{-3} \text{ GeV cm}^2 \text{ g}^{-1}$  and  $b(E)_{H_2O} = 3.40 \times 10^{-6} \text{ cm}^2 \text{ g}^{-1}$  [24] lead to a critical energy of  $E_{crit,H_2O} = 785 \text{ GeV}$ . For large-scale neutrino telescopes, muon energies from several GeV up to PeV are of relevance and therefore energy reconstruction strategies need to draw on these the different energy loss characteristics depending on the relevant energy range.

## 2.2 Building a high-energy neutrino detector

The primary goal of *ANTARES* lies the detection of high-energy cosmic neutrinos through Cherenkov emission from their charged lepton counterpart, as introduced above. Therefore, the construction of the detector calls for a transparent abundant medium for detection which allows single photon measurement to high precision and minimizes the influence of other photon and particle sources. The design decisions taken to optimize *ANTARES* for this purpose are introduced here and can be found to greater detail in [25].

### 2.2.1 Detection principle

The optimal detection of Cherenkov emission calls for the employment of optical detection units with single photon sensitivity in the relevant wavelength and high timing resolution, which must



(a) Detection principle

(b) Detector schematic

Figure 2.5: Schematic view of the detection principle, with solid lines symbolising charged particles, dashed lines neutrinos; and schematic view of the detector layout.

withstand the environmental conditions of the deep sea. The spacing between the detection unit is then optimized thus that the reconstruction results from Cherenkov radiation from the relevant neutrino sources are optimized.

The reduction of the number of background particles, primarily from atmospheric muons, motivates the employment of the detector in the deep sea to maximize atmospheric particle absorption, decay and energy-loss before they enter the detector. However, even the employment of *ANTARES* at 2.5km sea-depth in the Mediterranean Sea leads to an approximate ratio of  $1 : 10^6$  between neutrino-induced and atmospheric muons entering the detector from above. Therefore, filtering of atmospheric muons is mostly achieved by introducing Earth as a particle filter. While neutrinos can mostly penetrate Earth depending on their energy, atmospheric leptons are here completely shielded. Therefore, the detector is optimized to detect Cherenkov radiation of particles entering the detector from below, see Figure 2.5a.

## 2.2.2 Components and Layout

### Geometry

The 885 optical detection units, the so-called Optical Modules (OMs) of *ANTARES*, are distributed along twelve detection lines and situated in groups of three OMs in one Optical Module Frame (OMF) containing a Local Control Module (LCM), see Figure 2.6b. The orientation of the individual OMs shows a  $45^\circ$  inclination downwards from the horizontal axis, with the three OMs per storey facing in opposite directions by  $120^\circ$ . While OMs within a storey are deployed

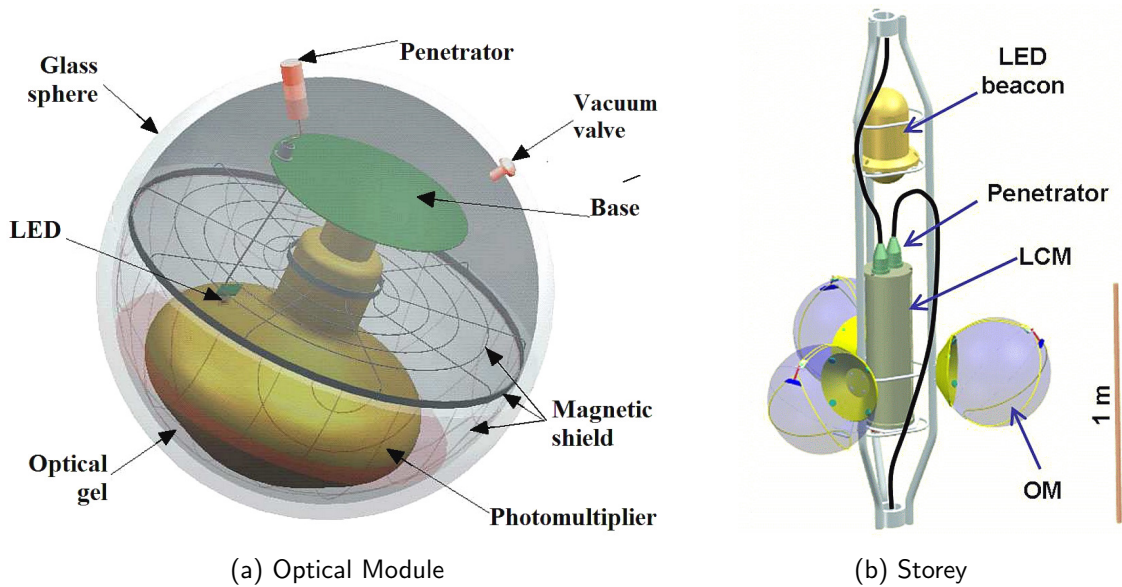


Figure 2.6: Schematic view of an Optical Module (OM) and a single storey of 3 OMs. From [25]

at a relative distance of  $\approx 1$  m, successive storeys per detection line are spaced by 14.5 m along the Electro-optical mechanical cable, which is held upright by a buoy and anchored to the sea floor. The relative dimensions can be seen in Figure 2.5b. *ANTARES* also contains an acoustic neutrino detection system which replaces the upper five storeys of a detection line and includes several acoustic sensors on the additional Instrumentation Line (IL) holding additional instrumentation for environmental control. All lines are connected on the sea floor to the Junction Box (JB) for power supply and data transmission, linking the detector along a single cable to the shore.

### Photon detectors

Each of the 885 OMs (see Figure 2.6a) contains one 10-inch photomultiplier tube (PMT) which is placed within a pressure-resistant glass sphere withstanding up to 700bar, with the intermittent space covered by optical gel. A single incident photon on the photo cathode area is detected with a collection efficiencies above 90% within  $\pm 45^\circ$  towards the PMT axis [26]. The incident photon leads to an electron cascade inside the PMT with a gain of  $5 \times 10^7$  at less than 2000V supplied voltage.

The transit time spread (TTS) of this single photon pulse is at about 1.3ns, which lies at the same magnitude as the chromatic time dispersion in water [27]. A magnetic shield is implemented using a grid of wires around the PMT bulb to decrease the effect of Earth's magnetic field, which would increase the TTS. A relevant impact on reconstruction is also to be expected from so-called pre-pulses and after-pulses stemming from rebounding or misdirected electrons in the electron cascade, which are limited to a maximum of 1% and 15% respectively in order to ensure optimum timing measurement of single photons. Additionally, each OM also contains an internal LED for calibration purposes.

### 2.2.3 Signal read-out

#### Collection and transformation of photon signals

Within each OMF holding three OMs, further signal processing is performed within the LCM, which contains various instruments: the local power box, a clock reference signal, the ARS (analogue ring sampler) motherboard holding the front-end electronic of the OM, the DAQ slow-control for local processing and memory and a compass system. Within an ARS, the digitization of the charge and timing information of the PMT photon pulses takes place using an Amplitude-to-Voltage converter (AVC) and Time-to-Voltage converter (TVC) before digitizing the voltage through an analog-to-digital converter (ADC). Each motherboard contains two alternately operating ARSs in a token-ring scheme in order to minimize the dead time, which leads to a minimum of 15 ns dead time between two consecutive ARS readouts. As each ARS integrates PMT charge over a 25 ns time window, the data from one ARS readout is the basic photon detection unit and is called a photon hit, which after calibration of the ARS read-outs can be assigned a hit time and amplitude. After a hit, an ARS requires 250 ns recovery time until the next possible hit detection.

All signals of the OMs are further transferred along the electro-optical cable of the detection line and through the connection of the line base to the Junction Box (JB), which bundles the signal and forwards it to the shore following an all-data-to-shore principle.

#### Calibration and additional sensors

In addition to the main photon detection infrastructure, several additional instruments complement the detector, ranging from instruments for timing and OM position calibration over various instruments for sea sciences to an acoustic neutrino detection system for ultra-high energy neutrino detection.

The OM positions are evaluated every two minutes using an acoustic beacon system with signalling acoustic transceivers at the line base and receiving hydrophones at various storeys along the line. This information is correlated with the calculated line indentation from sea current measurements, which serves as basis for the positioning of the OMFs. OM orientation within the OMFs is finally determined with the help of the compass system within the LCMs.

Calibration of the time measurement and clock system utilizes two beacon systems employing either Laser or LED as light sources. While LEDs are here used between storeys for short-distance correlations, lasers are used to bridge the distance between the line bases and the OMs for determination of the timing calibration along a line.

Further information about environmental conditions like sea current direction and velocity, and water temperature are measured with according instruments on the instrumentation line, which also hosts hydrophones for acoustic neutrino detection and instruments for sea science.

## 2.3 Detector operation in the deep sea

After setting up the detector in the Mediterranean Sea, several additional obstacles have to be overcome to successfully detect neutrinos. First of all, the atmospheric particle background has to be well understood in order to suppress it, as well as environmental conditions influencing

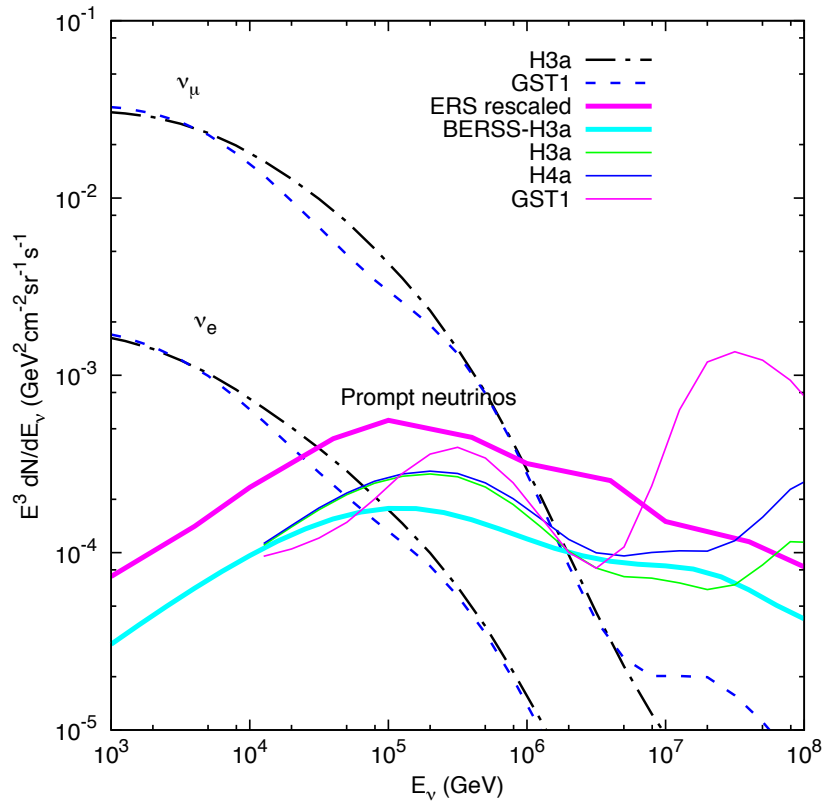


Figure 2.7: Estimates of prompt atmospheric neutrino fluxes (solid lines, thick ones using the H3a conventional model as basis) compared to conventional atmospheric neutrino flux estimates for  $\nu_e$  and  $\nu_\mu$  (broken lines). From [28]

photon detection in the deep sea need to be studied. From the understanding of these additional photon sources, event triggering mechanisms are developed to maximise the yield of neutrino detections.

### 2.3.1 The atmospheric particle background

The largest number of leptons detectable in any high-energy Earth-bound detector generally stems from interactions of cosmic rays with particles in Earth's atmosphere. In the search for neutrinos of cosmic origin, the most relevant background particles are atmospheric muons and atmospheric neutrinos. They are produced in cosmic ray cascades involving pions  $\pi^\pm$ , kaons  $K^\pm$  and heavier hadrons, which in turn decay to form the relevant background. In order to establish the spacial and energetic distribution of muons and neutrinos, the primary cosmic ray spectrum has to be convoluted with a summed contribution from these interaction channels, which reflects the different energy dependence, decay kinematics and branching ratios [3].

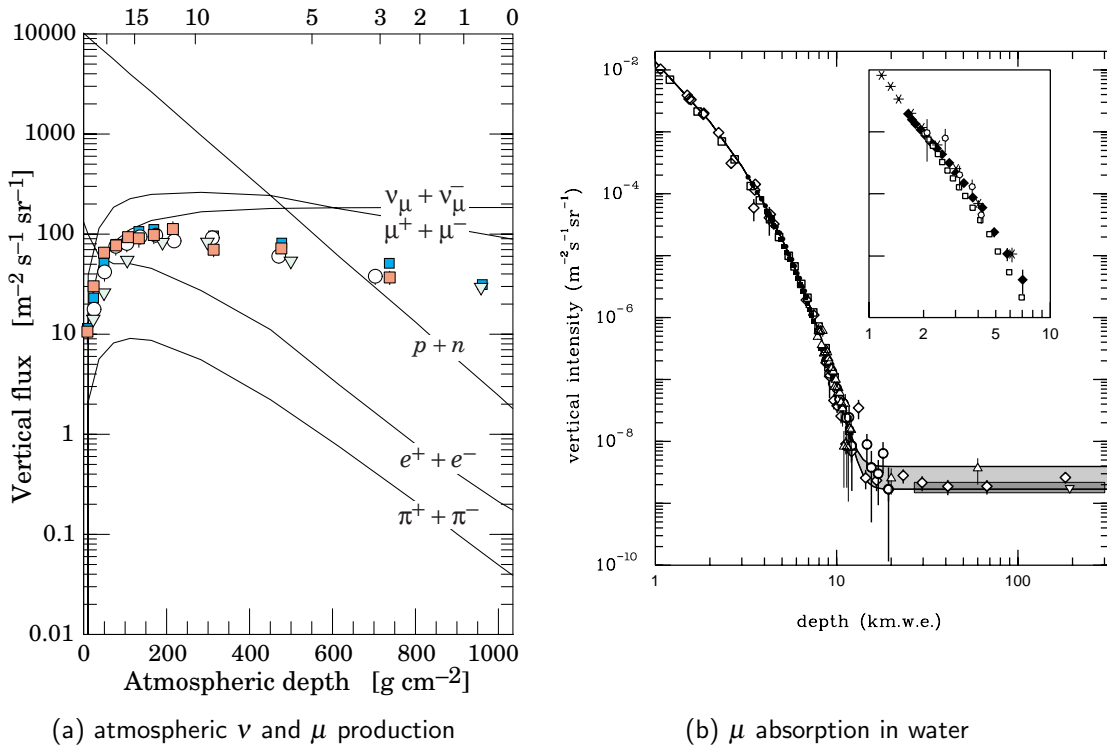


Figure 2.8: Production of atmospheric neutrinos and muon in the atmosphere, and absorption of atmospheric muons after passage through water. From [2]

### Conventional atmospheric neutrinos

The "conventional" part of the atmospheric muon and neutrino spectrum stems from meson decay, i.e.  $\pi$  and  $K$ , which were produced from interaction of cosmic rays in the atmosphere, predominantly protons and heavier nuclei. From this, the atmospheric neutrino spectrum is generated as a superposition of  $\nu$  and  $\mu$  contributions following the spectral distribution of the primaries, convoluted with the subsequent decay channel dynamics. Here, the kaon channel plays an important role and accounts for 80% of muon neutrinos in the TeV range, producing a spectrum that follows the spectral index  $\lambda$  of the primary spectrum as  $\alpha = 1 + \lambda$ .

While the decay dynamics are comparatively well known, larger differences arise from the assumption of the spectral distribution and composition of the primaries, e.g. two used models from the Bartol group [29] and Honda et al. [30]. In addition to that, the hadronic interaction model is constantly improving by integrating current research from the Large Hadron Collider in the flux calculations. In Figure 2.7, spectra for a conventional neutrino flux can be seen, displaying the differing outcome of calculations including a differing spectral cut-off for each primary nucleus group (H3a) and a proton-dominated primary spectrum above  $\sim 10^7$  GeV (GST1). It should be noted that due to the different path lengths of interaction chain particles in the atmosphere, the angular distribution of neutrinos is not isotrop but follows a  $\sec \theta$  distribution with an increasing rate of high energy neutrinos at large zenith angles [2].

### Atmospheric muons

Muons from cosmic ray interaction are produced high in the atmosphere and, together with neutrinos, are the only interaction products able to reach a deep-sea detector. Their energy distribution there reflects the effects of the primary production spectrum, energy loss and decay. At the surface, the energy spectrum of high-energy atmospheric muons above 1 TeV shows a spectral index steeper by one power than the primary cosmic ray spectrum [2], following the atmospheric neutrino spectrum. Here, the integral intensity of vertical muons above 1 GeV/ $c$  lies at  $\sim 70 \text{m}^{-2} \text{s}^{-1} \text{sr}^{-1}$ , with recent measurements favouring a lower normalization by 10 – 15%, and approximating a  $\sec \theta$  distribution for  $\theta < 70^\circ$  [2].

A small contribution from charm interactions and heavier nuclei at high energies can also be taken into account, however, in this work the small contribution of this decay channels will be neglected due to the larger overall normalization error of the muon flux. At sea level, muons and neutrinos are the dominant contribution of atmospheric cascades, see Figure 2.8a.

As already discussed in Section 2.1.2, muons lose energy through ionization and radiative processes, which leads to a shift in the energy spectrum depending on the matter depth of the measurement. While this process flattens out the spectrum at smaller energies, the spectrum at more than 2.5 km w.e. still reflects the surface spectrum for  $E_\mu > 0.5 \text{TeV}$  with a normalization reduced by two orders of magnitude compared to sea level, see Figure 2.8b.

### Prompt neutrinos from charmed hadrons

The contribution to the atmospheric neutrino and muon flux from charmed hadron interactions is negligible for the largest part of the energy range as charm interactions are much rarer than kaon and pion interactions. However, in high-energy neutrino astronomy, the energy range of the cosmic neutrino signal which is largely devoid of conventional atmospheric neutrinos, still contains a non-negligible charmed component, called "prompt" neutrinos. The crossover energy at which the prompt component becomes dominant over the conventional lies at about 10 – 100 TeV for  $\nu_e$  and 1 – 3 PeV for  $\nu_\mu$  with a nearly equal magnitude of  $\nu_e$  and  $\nu_\mu$  prompt neutrinos [28].

The prompt component can be estimated from modelling the charm production in the atmosphere relying on the different models of cosmic ray compositions similar to the conventional flux. In Figure 2.7, the two main models are based on a QCD calculation developed by Enberg, Reno and Sarcevic (ERS) and extended in [31] to BERSS. Changes to the critical energies for charmed hadron interaction can severely influence the model outcome, which can be seen in the alternate spectra of the BERSS model shown with the thin solid lines.

In the ERS model, the uncertainty range cited lies at about 50%, which together with the varying assumption of the primary spectrum, also shows the general uncertainty on the prompt atmospheric flux. As the analysis presented here predates limits and measurements made by *IceCube* which lead to this recent remodelling of the prompt flux, a simplified version of the ERS model with higher normalization was used.

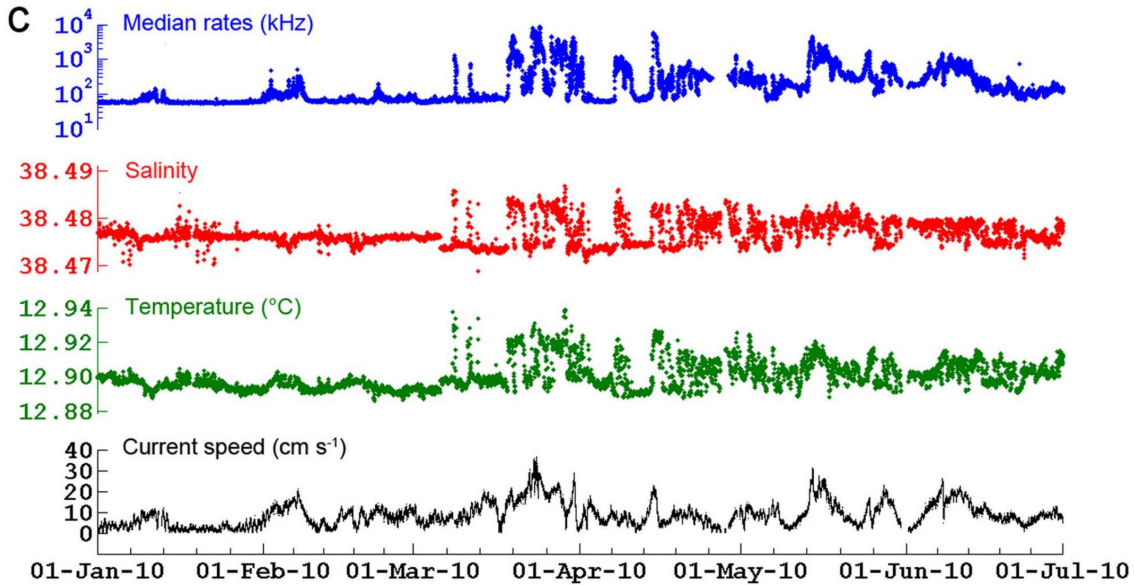


Figure 2.9: PMT mean rate, salinity, temperature and sea current measured at at the instrumentation line in 2010. From [32]

### 2.3.2 Environmental conditions

In addition to photons from charged particles of atmospheric origin passing the detector, also the influence of background photons produced inside the detection volume has to be minimized. These background photons stem from either radioactive decay of  $^{40}\text{K}$  in the sea water, or bioluminescence from bacteria or larger organisms.

#### $^{40}\text{K}$ decays

The radioactive decay of  $^{40}\text{K}$  isotopes in the saline sea water leads to the emission of an electron above the Cherenkov threshold in  $^{40}_{19}\text{K} \rightarrow ^{40}_{20}\text{Ca} + e^- + \bar{\nu}_e$ . This creates a fairly constant background of Cherenkov photons in the vicinity of the OMs which produce, inter alia, coinciding hits in neighbouring OMs. Apart from being a nuisance to photon hit selection in event identification, this background can serve as natural calibration light source to estimate the OM efficiency, light attenuation and relative timing offset between neighbouring OMs.  $^{40}\text{K}$  decays can, in addition to these calibration methods, also be used to estimate the light absorption by sea water [33], assuming an isotropic distribution of the isotope.

#### Bioluminescence

The largest contribution to background photon hits in *ANTARES* stems from luminous deep-sea organisms, with micro-organisms causing single photon hits and macroscopic animals leading to so-called photon bursts from their signalling organs. It was shown that the activity due to bioluminescence exhibits seasonal as well as short-term variations which relate to the sea current, salinity of the water and temperature [32], see Figure 2.9, which is driven by convection processes refuelling the deep seawater with cooled winter water from the surface.

The large variation of background photon numbers poses not only a challenge to hit selection procedures, but also leads to a constantly varying photon sensitivity of the detector's OMs, as photon bursts saturate PMT light yield to the maximum with subsequent periods of insensitivity during the according dead times of the OMs.

These challenges are addressed by a constant measurement of detector status indicators and the OM mean hit rates, which is also included in a detailed simulation of *ANTARES* data taking as it is a strong indicator of data quality. In addition to that, various quality parameters have been introduced, which help to estimate the general data taking conditions for any given period of measurement. One of these quality parameters is displayed in Figure 2.9, namely the detector mean rate, which is calculated the mean hit rate for all active OMs in the detector.

### 2.3.3 Neutrino event triggering

Photon patterns generated inside the detection volume have to be quickly identified as stemming from relativistic charged particles and not environmental sources, and, depending on the physics aim of the measurements, by their probability to originate from a lepton having entered the detector from below. To this end, triggering mechanisms to identify the various event classes within *ANTARES* have been introduced, which run online on a computer farm onshore, selecting relevant fragments of the data stream as so-called events.

The triggering schemes usually draw on time and spacial proximity of hits, e.g. the standard muon trigger, called 3N trigger, uses the possible causal relation between hits in neighbouring OMs to identify potential event signal hits [25]. To be considered for the triggers, hits must coincide in OMs of the same storey within 20ns or be large pulses of more than three photo-electrons (p.e.). Five of these potential signal hits fulfil the trigger criterion if they are neighbouring or causally related considering their timing, distance and speed of light. This trigger is sensitive to lepton events from all directions and shows a high purity with triggers due to random coincidences less than 1%. In addition to the 3N trigger, additional schemes rely on either looser or stricter coincidence or photon spacial distribution criteria, or include a directional preference of the photon pattern to especially target neutrinos from the Galactic centre.

A challenge to *ANTARES* event triggering and reconstruction arises from the fact that trigger rates can vary strongly due to bioluminescence, and photon sensitivity of the OMs change over time due to ageing and exposure to the environment. In order to balance out these effects and deal with the limited storage capacity for data, triggers are usually switched on or off to keep trigger rates at a constant level of a few Hertz.

### 2.3.4 Operational challenges

Ageing effects of the detector and occasional malfunctioning of OMs might also cause problems in data analysis. In the search for high-energy neutrinos, any occurrence of a flash of light within the detection volume could be misinterpreted as event. Indeed, flashes can be produced by OMs themselves when suffering from a high-voltage surge, causing sparks, which has proven to pose a problem in earlier analyses. These fake "sparking events" can be identified by their position and the timing of the arrival of light [16] and need to be successfully suppressed in a cosmic neutrino search.

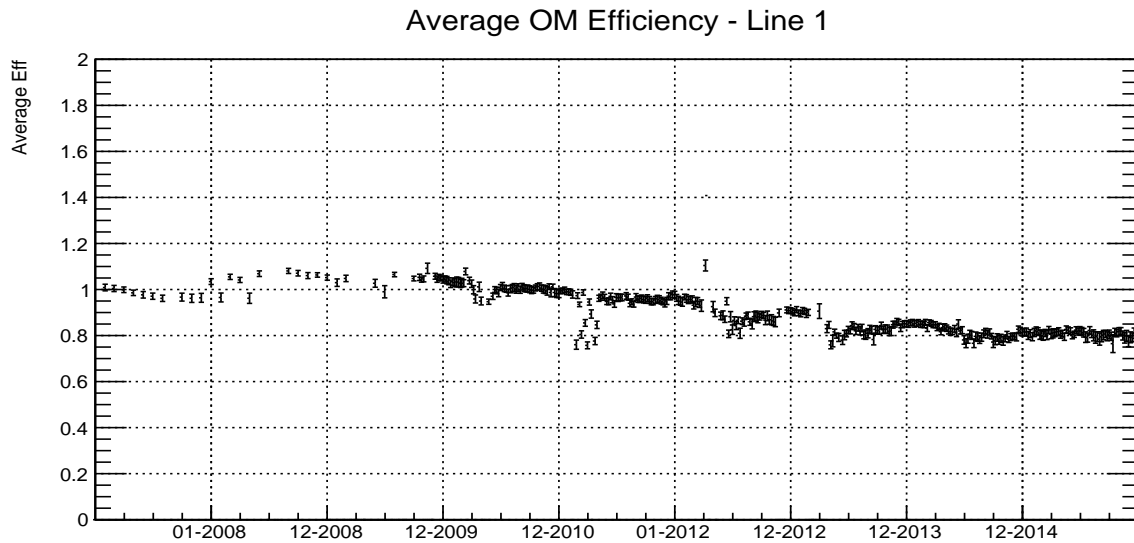


Figure 2.10: Average OM efficiency for detection line 1 over nine years of data taking. From [34]

Another effect that has to be dealt with over the long run time of *ANTARES* is the ageing of the OMs. This is on the one hand addressed by re-calibrating the voltage and readout of the PMTs, on the other hand even this cannot prevent the loss of hit efficiency in the OMs in the long run. The coincident photon rate from  $^{40}\text{K}$  decays is calculated by a Gaussian fit to the relative timing distribution of hits in neighbouring OMs [34]. The peak height here indicates the coincidence rate which can be used as a proxy to OM efficiency, while the relative offset of the peak gives the relative timing offset between OMs. The coincident rate for a fully functioning pair of OMs lies at about 16 kHz, however, over the span of several years a gradual drop in the coincident rate can be observed, which is due to the diminishing OM photon detection capacity. This drop of efficiency can be seen in Figure 2.10, and has to be modelled accurately in simulations, a task that at the time of this analysis was not yet progressed far enough.

**Part II**

**Toolbox**



## 3 | Monte Carlo Simulation

A wide range of computational and mathematical tools is needed in the set-up of this analysis. The methods range from a very detailed Monte Carlo simulation of particle interactions and the *ANTARES* detector response, discussed in Chapter 3, to event reconstruction algorithms as standard equipment of *ANTARES* analysis in Chapter 4. While these simulations and reconstructions are widely used in *ANTARES* analyses, an integration of specific reconstructions of the different neutrino event types to a new combined approach is called for to specifically tune the analysis to a high sensitivity for a diffuse cosmic neutrino flux. To this end, a short toy analysis study of the question how to actually include various event signatures in an overall cosmic neutrino search is presented in Chapter 5 before completing the toolbox by adding relevant analysis-specific classifiers and estimators to it in Chapter 6.

The standard *ANTARES* simulation chain can best be introduced by a close look at its most common implementation, the run-by-run simulation chain. This simulation procedure reflects the complexity and temporal variance of environmental processes at the *ANTARES* site and takes changes into account in OM status, background photon activity and the varying detector geometry. The natural technical data taking cycles of the *ANTARES* detector, the so-called runs, are dependent on the data writing procedures and are the time frames for which data quality estimates are calculated. Both atmospheric muon background simulation and neutrino event generation are provided for each run, including the full simulation of charged-current and neutral-current neutrino events in the  $\nu_e$  and  $\nu_\mu$  channel as well as atmospheric muons [35]. The main steps of the simulation chain are handled by different software packages, which will be described in more detail below and are shown in Figure 3.1. The chain includes

- Generation of neutrinos or atmospheric muons with generation flux  $\Phi_{\text{Gen}}$  at the surface of a generation volume around the detector, using the GenHen and MUPAGE software packages,
- Propagation of the particles towards the detector and production of secondary particles and Cherenkov photons (KM3 package),
- Simulation of the detector position and incidence of photons in OMs (KM3),
- Simulation of the detector response for these photons (TriggerEfficiency), leaving only triggered events based on hits and
- Standard event reconstruction (SeaTray).

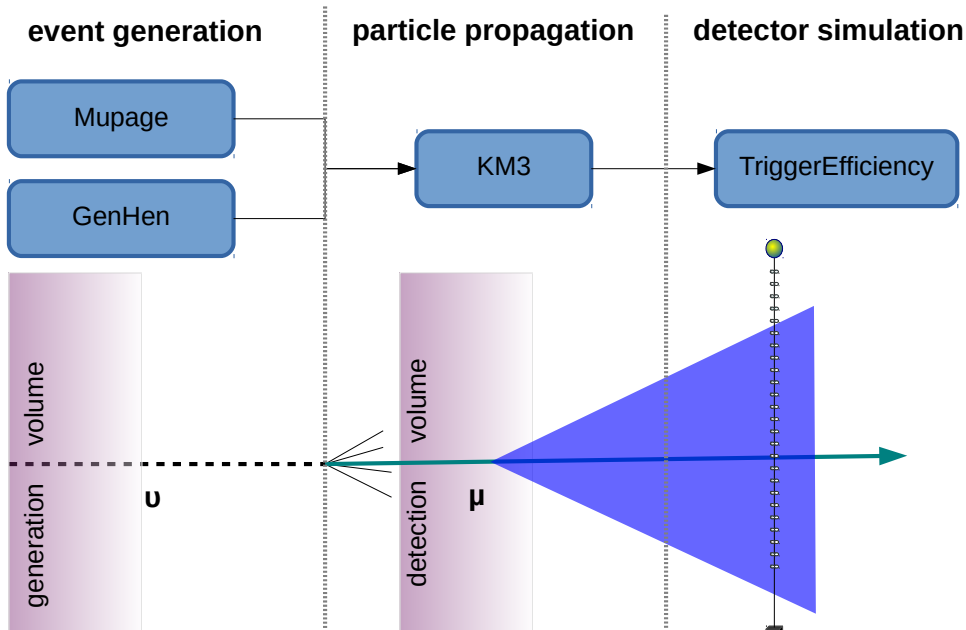


Figure 3.1: Schematic view of the simulation chain.

As these software packages are regularly updated to improve their agreement with the data and follow the changing data taking conditions, different versions of the run-by-run simulations exist, at the time of the analysis version 2 and 3.

## 3.1 Particle Generators

### 3.1.1 Neutrino generation with GenHen

Neutrinos are generated using GenHen [36], a package which produces interacting neutrinos according to a given generation spectrum  $\gamma$  within a generation volume around the detector, with the size of the volume depending on the neutrino energy, neutrino flavour and interaction type. Of those events, the neutrinos producing muons reaching the can, which is defined as cylindrical space around the detector within which light from particles is likely to reach the instrumented volume, are processed further, including those neutrinos interacting within the can, .

For the propagation of particles towards the can, both scattering of the particles and the properties of the propagation media (water or rock) around the detector are taken into account. If a particle reaches the can or if a neutrino interacts within it, the secondary particles produced at the interaction vertex are stored and propagated until they exit the can, decay, or their energy drops below the Cherenkov level.

While  $\nu_e$  and  $\nu_\mu$  events are part of the standard production, most  $\nu_\tau$  interaction channels were only implemented recently. This poses a problem for an all-flavour analysis which will be addressed by introducing a specialized  $\nu_\tau$  production and estimation procedure in Chapter 7.2.1. Each detectable event is assigned a generation weight  $w_2$  for easy recalculation of the event's contribution to an arbitrary neutrino flux.

**Generation weight** The calculation of  $w_2$  is based on the neutrino energy  $E$  and zenith angle  $\theta$ , which is viewed within the generation of an overall flux with spectral index  $\gamma$  [37]. It takes the can volume  $V$  or, in case of  $\nu_\mu$  generation, the effective surface  $w_1$  and effective muon range  $R_\mu$  as  $V = w_1 R_\mu$  into account. The generation weight  $w_2$  is then given for a given angular and energy phase space as

$$w_2 = V \times 2\pi(\cos \theta_{\max} - \cos \theta_{\min}) \times \frac{(E_{\max}^{1-\gamma} - E_{\min}^{1-\gamma})}{1-\gamma} E^\gamma \times \sigma(E) \times \rho N_A \times P_{\text{earth}} \times N \quad (3.1)$$

with  $\rho N_A$  giving the number of target nuclei per cubic metre, and a normalization factor  $N$ . The weight  $w_2$  can now be used to reweight the event distribution for any given differential flux  $\Phi(E)$  given in units of  $\text{GeV}^{-1} \text{sr}^{-1} \text{s}^{-1} \text{m}^{-2} \text{year}^{-1}$  before penetrating Earth by assigning the weight  $w_3 = w_2 \times \Phi(E)$ .

**Atmospheric fluxes from parametric formulae** The calculation of neutrino event weights for standard and prompt atmospheric fluxes is performed by applying parametric formulae [38] of the flux models introduced in Chapter 2.3.1. The relative neutrino event probabilities are tabled according to neutrino type, energy and zenith angle, and actual event weights are interpolated from neighbouring entries in the table. As this weight calculation is available as stand-alone software package<sup>5</sup>, it can also be applied at a later stage starting from the  $w_2$  weight of the event, allowing for the testing of a wide range of different flux models and the addition of new flux assumptions.

**Particle propagation: Music** A simulation for muon propagation in media is applied using the MUSIC code [39]. It contains all relevant processes of muon interaction, including the angular deviation and lateral displacement of muons due to multiple scattering, and stochastic simulation of radiative loss processes like bremsstrahlung, pair production and inelastic scattering. As shown in Chapter 2.1.2, energy losses of muons can generally be viewed as a superposition of a roughly constant energy loss through ionization and an energy-dependent loss through radiative processes. Therefore, the simulation treats the energy loss  $-\langle \frac{dE}{dx} \rangle = \alpha(E) + \beta(E)E = -\langle \frac{dE}{dx} \rangle_{\text{const}} - \langle \frac{dE}{dx} \rangle_{\text{stoc}}$  in two parts, with the stochastic processes added randomly according to the established characteristics depending on the muon energy on top of the constant ionization loss, which is calculated from the Bethe-Bloch formula. The two energy loss parts are generally added per muon path segment, using

$$\left\langle \frac{dE}{dx} \right\rangle = E \frac{N}{A} \int_0^{\nu_{\text{cut}}} d\nu \nu \frac{d\sigma}{d\nu} + E \frac{N}{A} \int_{\nu_{\text{cut}}}^1 d\nu \nu \frac{d\sigma}{d\nu} \quad (3.2)$$

with  $A$  being the mass number of the material,  $N$  the Avogadro number,  $\nu$  the fraction of the transferred muon energy and  $\frac{d\sigma}{d\nu}$  the cross-section of the process. The muon cut energy is chosen as  $\nu_{\text{cut}} = 10^{-3}$ , which is taken from a trade-off between simulation accuracy and duration. Differences in the choices of simulation parameters lead to variations in muon reach, which are explored further in [39] and describe parametric uncertainties in the simulation of energy loss processes.

<sup>5</sup>The neutrinoFlux package, [http://icecube.wisc.edu/~tmontaruli/neutrinoFlux/NeutrinoFlux\\_Teresa.html](http://icecube.wisc.edu/~tmontaruli/neutrinoFlux/NeutrinoFlux_Teresa.html)

### 3.1.2 Muon generation using MUPAGE

In the simulation of high-energy atmospheric muons, only particles with a primary energy above 500 GeV are considered as only those would reach the *ANTARES* site. While a full particle-tracking simulation of atmospheric showers using the CORSIKA simulation code [40] can be used to produce atmospheric neutrino as well as atmospheric muon events, the full simulation of atmospheric showers is time consuming for *ANTARES* due to the need of run-by-run simulation. Therefore, the MUPAGE code [41] was introduced, in which muon events are generated according to energy and zenith distributions from parametrizations of a full shower simulation. Here, the parametric formulae are derived according to vertical depth, zenith angle and multiplicity of the air shower from a full simulation of primary cosmic ray interactions above the sea surface, drawing largely on MACRO data<sup>6</sup>. For muons exceeding a threshold energy of 500 GeV, the particles were propagated through water using MUSIC.

Although this simulation method is quick, the atmospheric muon simulation is also limited by storage capacity and processability, as atmospheric muon events constitute the predominant event class in data taking by about  $1 : 10^6$ . This makes it mandatory to understand the topology of atmospheric muon events well in order to issue a reliable estimate of the atmospheric muon contribution in low statistics analysis.

In the standard run-by-run production, atmospheric muon simulation does not include muon bundles with high multiplicity  $m$ , i.e. muons originating from the same atmospheric shower, but is limited to muon bundles of  $m \leq 200$ . This necessitates the introduction of a specialized atmospheric muon production in this analysis for events with multiplicity  $m > 200$ , for which simulation details can be found in Appendix A.1.2. Muon simulations for *ANTARES* are described in more detail in [42].

## 3.2 Particle Propagation and Photon Production

Having produced all primary particles and propagated to the detection volume, the photon yield from the particle, its production of secondary particles and the probability to actually measure photons from them needs to be added to the chain. The simulation of the full photon yield from passing particles is implemented in the KM3 code. As single photon tracking would call for massive parallel computing which is not available at the current stage, the distributions of Cherenkov photons and induced by energy loss processes of passing  $\mu^\pm$  are drawn from pre-produced photon tables. Thus, for each optical module, the number of incident photons is calculated, taking the relative distance of the OM from and orientation towards the muon track or electromagnetic shower into account.

**Water properties** Photon propagation in sea water is subject to absorption and scattering processes off its molecules and macroscopic particles in the water. The simulation of these effects is implemented using the 'partic' model, which lists both absorption and scattering length  $L_{\text{abs}}$  and  $L_{\text{scat}}$  for sea water for a given wavelength  $\lambda$ , as well as allows for the application of scattering length of light in sea water separately for water  $L_w$  and immersed particles  $L_p$  [43], considering the relative proportion of ions in the water. The scattering parameters used can be

<sup>6</sup>see M. Ambrosio et al., Phys. Rev. D56 (1997) 1407, 1418 and Phys. Rev. D60 (1999) 032001.

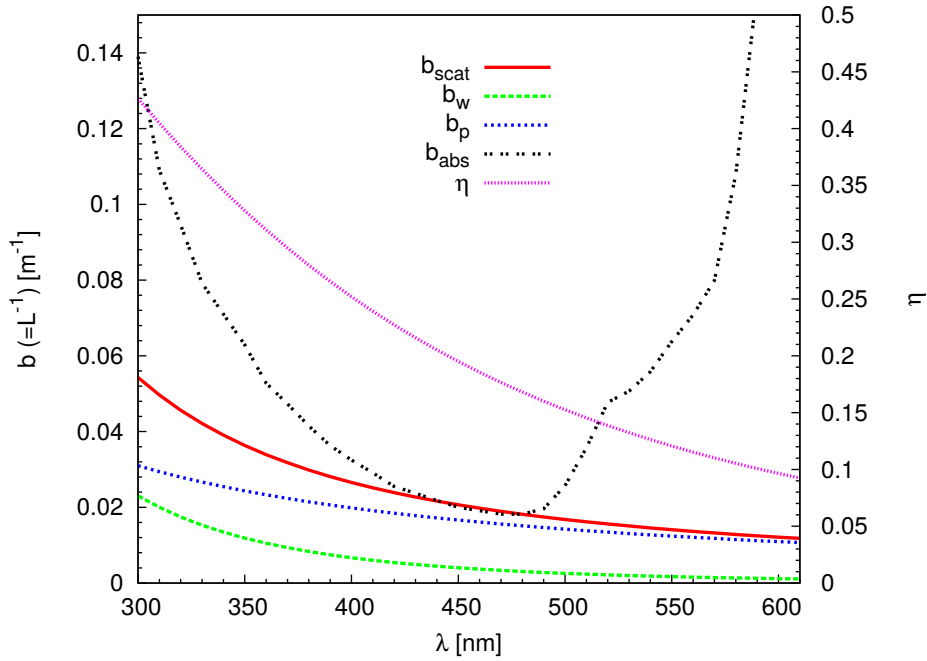


Figure 3.2: Scattering parameters of the 'partic' model, with scattering and absorption parameters  $b_{\text{scat}} = 1/L_{\text{scat}}$  and  $b_{\text{abs}}$ , and water and particle scattering parameters  $b_w$  and  $b_p$ , and fraction of scattering due to sea water  $\eta$ ; from [43].

seen in Figure 3.2. The accuracy of this water model has been re-evaluated various times using in-situ optical properties measurements, e.g. in [44], showing uncertainties in absorption and scattering length at the order of 10-15%.

**Optical module acceptance** For the calculation of the detected number of photons per OM, the glass and gel absorption of photons and the angular and quantum efficiency of the PMT have to be taken into account. The relevant parameters were determined from OM measurements before deployment of the detector. The total photon acceptance per angle is then simulated by directly applying the measured values for quantum and angular efficiency (see Figure 3.3), and by calculating glass and gel absorption from their respective thickness along the optical path.

### 3.3 Detector Response

At this stage, the incidence of single photons at the PMT in each optical module has been generated, leaving the simulation of PMT effects, analogue-digital conversion and processing of the individual signals by the triggering software to produce data that fully mimics the actual measurements. The effects of the PMT readout, addition of further sources of PMT hits from optical background and technical effects, and the processing of this data through the *ANTARES* read-out and triggering scheme is implemented as part of the TriggerEfficiency program [45], which delivers 'events' in a similar format for both simulations and the actual *ANTARES* data taking procedure. These events are in both cases reconstructed by the same algorithms, which are implemented in the SeaTray analysis framework [46] and will be discussed in Chapter 4.

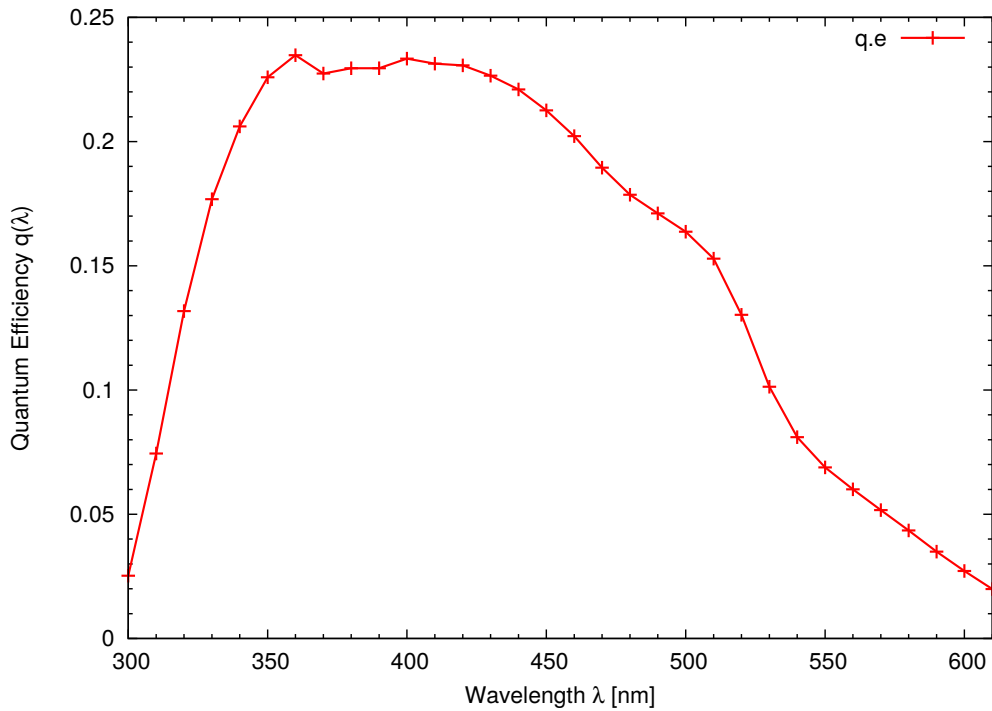


Figure 3.3: Logarithmic angular efficiency and quantum efficiency of the optical modules as simulated in KM3. From [43].

**PMT effects** Within the PMT, the incident photon causes an electron cascade which is dependent on the applied voltage and PMT quantum efficiency and leads to an electronic pulse best simulated as a Gaussian distribution. The pulse magnitude is fairly proportional to the number of simultaneously registered photons for a small number of photons, while a large number of photons leads to a saturation of the PMT available charge. Therefore, photons in the PMT are simulated by mapping the hits to a Gaussian distribution of equivalent charges, which are then time-smearred according to the transition-time spread (TTS) of the PMT. Optionally, a relative quantum efficiency can again be applied at this stage.

PMT effects also include so-called after-pulses, which originate from stray electrons from the PMT electron cascade, or from slow-moving ions in the PMT. These early or late after-pulses can be added optionally as 0.5% and 1% contribution of hits respectively. The charge of these fake hits is adapted according to black box measurements of OMs<sup>7</sup>.

**Digital conversion through ARS simulation** During the now following simulation of the ARS digital readout, the charge from all hits arriving during the gate time of one ARS are integrated. Here, the walk-effect due to the delay of the crossing of the charge threshold for ARS readout originating from the Gaussian smearing of the charge pulse is taken into account in calculating the timestamp and TVC time interpolation. The digitized charge value from the AVC is determined by applying the charge calibration of the ARS.

<sup>7</sup>see Creusto, A. and Gauchet, L., *Black box set-up and first results on the ANTARES optical module*, internal ANTARES note ANTARES-OPMO-2012-001, 2012

**Background photon addition** While the simulation chain so-far processes explicitly photons originating from the generated particles, the photon background present in measurements has to be added as well. For this, various strategies exist, the easiest of which is the addition of single hits with a random distribution in time following from the observed single rate of the PMT, assuming that the rate was caused by K40 decays and bioluminescence. Here, it has to be taken into account that late after-pulses are also part of this photon background due to their timing which makes correlation to the original hits difficult, and they have to be considered as part the rate. However, as the photon background also contains bursts of lights as shown in Chapter 2.3.2, the exact simulation of environmental effects is difficult, which lead to the inclusion of background hits with varying charge which is derived from the observed hit charge distribution at the time of the measurement. This ensures a relatively accurate depiction of the random photon background.

**Adaptation to detector conditions** Experience showed that a detailed adaption of the simulation to both environmental conditions and changing technical parameters of the detector is necessary to reach a solid agreement between simulation and measurement. The adaptation of the background hit rates, ARS calibration and PMT efficiency to the specific detector conditions provides an adaptive and meticulous simulation of the temporal variation during data taking. It will be seen later that the accuracy of this part of the simulation chain has a high impact on the viability of the analysis.



## 4 | Event Reconstruction

The triggered events from both data taking and simulation are starting point for a series of reconstruction techniques for various event type hypothesis. While muon track reconstruction algorithms were the first to be developed in *ANTARES* and are therefore well established, various cascade and energy reconstruction methods have been introduced in recent years. As their wide range of parameters which enhances relevant features for this analysis is an asset that will have to be used in the following tool development, a short but not exhaustive overview over the various reconstruction algorithms is given here.

### 4.1 Muon track reconstruction

Muon track reconstruction techniques generally rely on the hypothesis of photon emission under the Cherenkov angle along the straight muon track. They usually involve a first rough guess of the track location drawing on a strongly restricted hit selection of hits of high charge or coincidence most likely originating from a passing muon and employ, in a second step, a more sophisticated reconstruction of the track parameters involving refined hit selections and often a minimization of parameter probability functions. In *ANTARES*, two muon reconstruction methods of long standing, Aafit and BBFit, are employed in most analyses, although additional reconstructions have been developed lately.

#### 4.1.1 Aafit

**Strategy** The Aafit reconstruction strategy is described in [47] and [48] and consists of a prefit on large hits only and a full likelihood fit taking a larger hit selection into account. The algorithms draw on the time residual of hits  $r$  which is defined as the difference between the actual measured time of the hit and the theoretical arrival time of photons from a given track under the assumption of Cherenkov emission,  $t_{\text{res}} = t_{\text{measured}} - t_{\text{expected}}$ . The prefit stage builds on an M-estimator fit which varies the  $\chi^2$  fit using  $\chi^2 = \sum_{N_{\text{hits}}} t_{\text{res},i}^2$  by assigning lower weights to large residuals.

While this prefit delivers good results close to the actual track, the full likelihood fit using the likelihood  $\log L = \sum_{N_{\text{hits}}} \log P(t_{\text{res},i})$  of the probability density function for the residuals  $P(t_{\text{res}})$  can increase accuracy significantly when using the prefit results as starting assumptions. Nine different starting tracks are entered into the pre-final fit, the track with the largest likelihood is finally passed to an improved pdf fit considering even background hits to produce the final reconstruction.

**Hitselection** The preselection of hits is done starting from the hit of the highest charge and includes all hits within a time window of  $|\Delta t| \leq \frac{d}{v_{c,\text{group}}} + 100\text{ns}$ . For further use, all hits occurring on an OM within 300ns are merged into one hit at the time of the first hit, but the information on the magnitude of the pulse is not used any further [49], leaving the following steps less sensitive to errors in the modelling of the hit charges and after-pulses.

**Quality parameters** The quality parameter  $\Lambda$  is deduced from the final likelihood  $L$ , the number of agreeing fits  $N_{\text{comp}}$  and the number of degrees of freedom  $N_{\text{dof}}$  as  $\Lambda = \log L / N_{\text{dof}} - 0.1(N_{\text{comp}} - 1)$ .

The angular error estimate  $\beta$ , on the other hand, is calculated from the error matrix of the directional reconstruction by using  $\beta = [\sigma_{\theta}^2 + \sigma_{\phi}^2 \sin^2(\theta_{\text{rec}})]^{1/2}$ .

### 4.1.2 BBFit

**Strategy** The BBFit reconstruction algorithm [50] is suited to reconstruct both shower- and track-like events. The algorithm distinguishes between single- and multiline events and per default attempts both a track and a so-called bright-point fit. The fitting procedure relies on a simple  $\chi^2$ -fit including the hit amplitude and either a single point or line of photon emission. In case of the track reconstruction, a linear pre-fit is used as starting point for the track  $\chi^2$ -minimization, which is done for each line. In case of more than one detection line with selected hits, these individual results are combined to a common solution for the multiline fit. An example can be seen in Figure 4.1.

**Hitselection** The hits considered for the reconstruction undergo a merging procedure for all hits on one storey. To this end, all hits occurring within 20 ns on the OMs of the same storey are merged to one and a bonus charge is added if hits stem from different OMs. If this storey hit exceeds a charge of 2.5 p.e. photo-electron equivalent, it is selected if fulfilling the coincidence criterion which demands hits on adjacent or next-to-adjacent floors (T3). Starting from these T3 hits, additional hits are added to the selection if they could have originated from the same track. If the number of found hits exceeds 5, the minimization of the line fit including hit positions and timing is started.

**Quality parameters** The quality parameter of the strategy is the resulting  $\chi^2$  of the final fit steps, namely  $Q = \sum_{N_{\text{hit}}} (t_{\text{exp}} - t_i)^2 / \sigma_i^2 + N$ , with N including information of the hit charge and travel distance and timing uncertainty  $\sigma_i$ .

### 4.1.3 Additional track reconstructions

Two additional track reconstruction methods, based on the grid search algorithm FilteringFit, have been implemented in *ANTARES* more recently [51]. While GridFit optimizes its performance for low-energy events, KrakeFit targets mostly high energy events. In both cases, FilteringFit is preceded by a hit selection, and followed by an M-estimator fit using the photon probability density functions as implemented in AAFit. The main difference between the two methods lies in the hit and track selection algorithms. In both cases, the final quality parameter

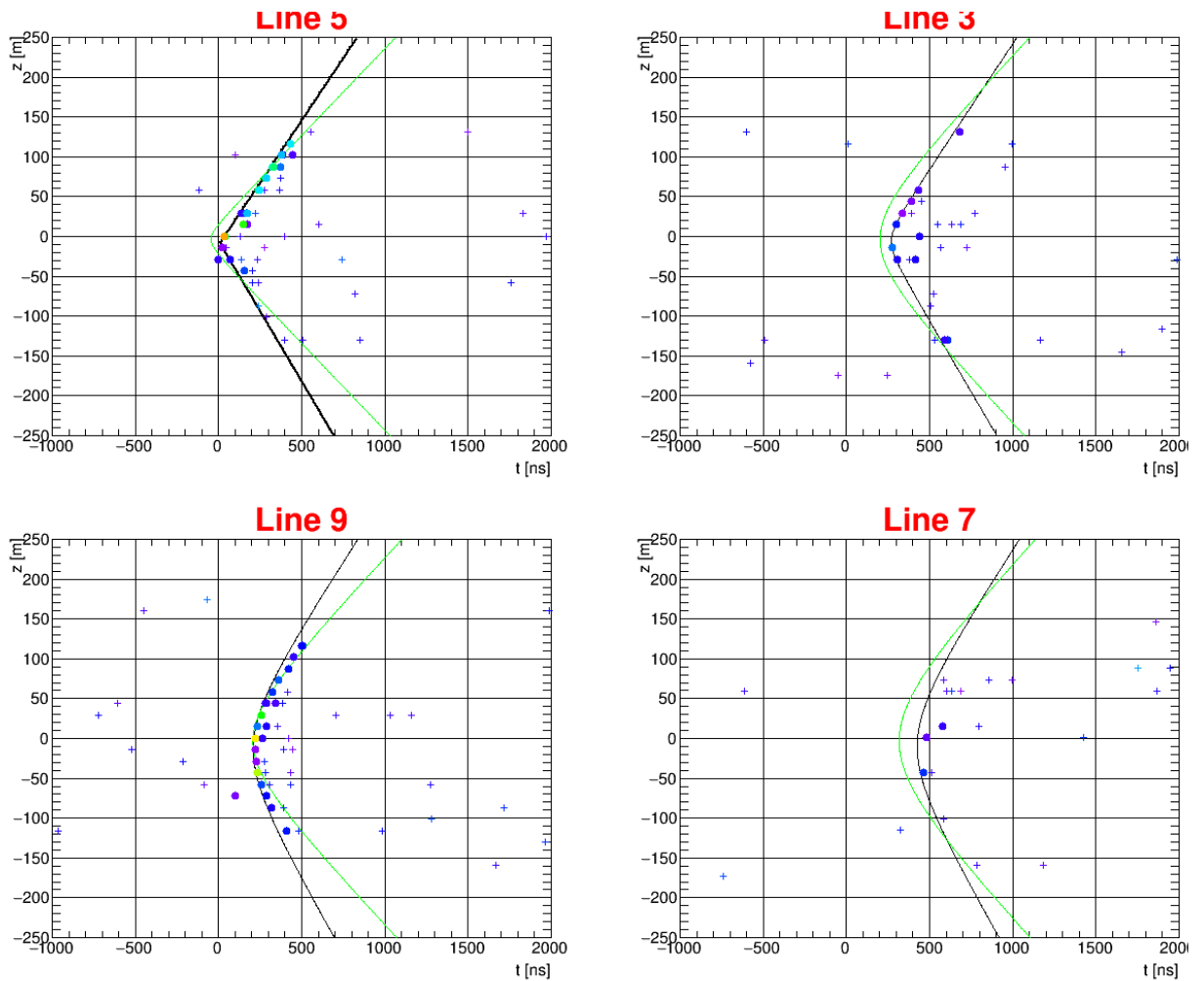


Figure 4.1:  $z$ - $t$ -graphs of hits on four detection lines with  $z$  giving the vertical distance from the centre of the line (crosses - unselected hits, bulletmarkers - triggered hits), solid lines showing reconstruction result, i.e. best fitting hit time and location expected for Cherenkov photons for BBFit track (black) and cascade (green) reconstruction.

is called  $r \log L$  variable, the reduced log-likelihood of the final step likelihood, which is defined by the final likelihood value  $L$  divided by the number of degrees of freedom of the fit  $N_{\text{dof}}$

**GridFit quality** An additional quality parameter is introduced in GridFit. It is conceptually close to the angular error estimate  $\beta$  of Aafit, but uses the width of the minimum (WOM) of the result of the directional fit, which as approximated by an ellipse.

**Muon suppression parameter: Ratio** Due to the comparatively long processing time of the fit, a precut for atmospheric muons had to be introduced. It compares the number of hits in the upper half of the detector to those in the lower half, defining  $R_{\text{Grid}} = \Sigma N_{\text{up}} / \Sigma N_{\text{down}}$ .

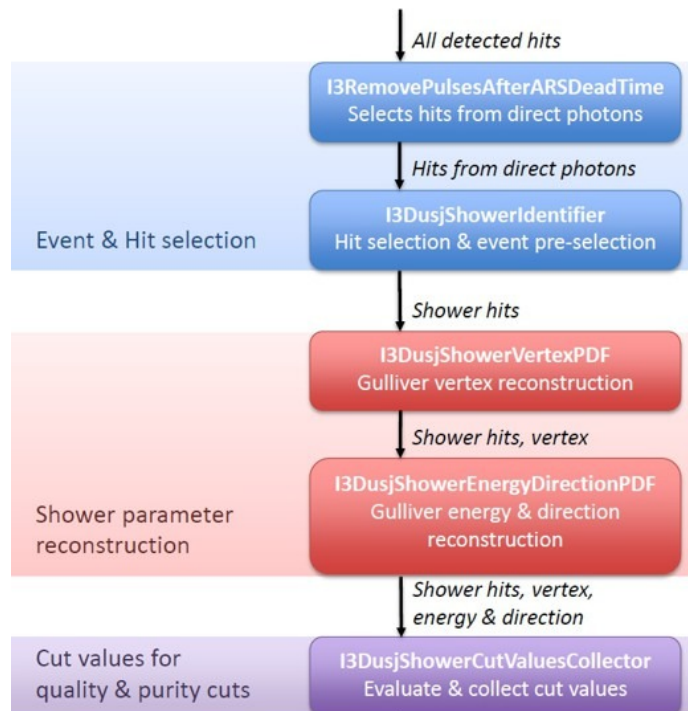


Figure 4.2: Overview over the work flow for the DUSJ cascade reconstruction. From [16].

## 4.2 Cascade reconstruction

In contrast to muon track reconstructions, a cascade reconstruction has to deal with a source extending only over a few meters, which usually is assumed to be point-like in the first reconstruction step. Therefore, a cascade fit generally involves a vertex position and a directional fit. In *ANTARES*, two cascade reconstruction algorithms have previously been used for a diffuse neutrino flux search, called DUSJ and Q strategy.

### 4.2.1 DUSJ cascade reconstruction

The DUSJ strategy [16] consists of three main steps: A first, a hit selection is applied, followed by two consecutive maximum likelihood fits for first the vertex position and interaction time and second the direction and energy of the shower, before finally various quality parameters are calculated, see Figure 4.2.

**Quality parameters** Again, likelihood-based parameters are deduced from the different fitting steps, like the  $r \log L$  for the vertex fit which is here called vertex log-likelihood (VLLH), and the corresponding degrees of freedom of the fit  $N_{\text{dof}}$ . Also, an estimate of the fit quality is introduced from  $\chi^2 = \frac{1}{N_{\text{hits}}} \sum_{N_{\text{hits}}} t_{\text{res}}^2$  parameter, which evaluates the time residuals  $t_{\text{res}}$  of the photons, i.e. their actual compared to their expected arrival time. Finally, the quadrupole moment of the hit distribution is calculated, which serves as an estimate for the elongation of the shower hit distribution.

### 4.2.2 Q-Strategy and BBFit Bright Point

The Q-strategy [52] also relies on a consecutive fitting of firstly the vertex position (here using an M-estimator) and a further hit selection, starting from that vertex, to finally reconstruct the shower direction. The energy reconstruction is here performed separately. This strategy also provides a likelihood-parameter from the directional fit.

Although not performing a complete shower fit, the BBFit bright point fit [53] follows closely the procedure of the BBFit track fit regarding hit selection and optimization procedure, but assumes a point-like source of light. Its output includes the time and position of the bright point and is therefore comparable to the vertex fit of the full cascade reconstruction chain. Its quality parameter is again the  $\chi^2$ -based quality parameter calculated in analogy to the BBFit track reconstruction, see above.

## 4.3 Energy reconstruction

Energy reconstruction of events can only be achieved by analysis of photon distribution and number within the detector and depends strongly on the neutrino event signature. For muon tracks, energy reconstruction is largely achieved by measuring the fraction of light emitted by radiative processes for particles with energies above a few TeV [54] along a part of the track, see Figure 4.3. Energy reconstruction for cascades mostly relies on Cherenkov photons from secondary particles, where the detector can serve as a calorimeter to measure the total amount of light produced in the neutrino interaction.

### 4.3.1 Number of Hits and Timing Structure

**Number of hits** A first estimate of neutrino energy can be calculated from total amount of photons measured in the detector, as high energy leptons produced inside or passing through the detector emit a comparatively larger amount of photons. Naturally, this number is highly dependent on the detector geometry and localization of the neutrino event within the detector. However,  $N_{\text{hits}}$  has so far served in many analyses as an energy proxy as well as a selection criterion for well reconstructible neutrino events.

**Time residuals and R parameter** Regarding the delay of the OM hits with respect to the expected photon arrival time of Cherenkov photons from the reconstructed lepton track, the *time residual*  $t_{\text{res}} = t_{\text{true}} - t_{\text{Cherenkov}}$  already introduced above, can also serve as basis for the calculation of event energy. For cascade events, the larger lateral distribution of particles from radiative processes in high-energy events leads to a larger amount of photons with large time residual. For muon tracks, the photons of radiative processes, which can be regarded as cascades along the muon track, lead to a similar contribution of late photons. This fact is exploited in the *R* parameter estimate, a muon energy estimate which sets the number of hits detected in the successive readout cycles of the photo-multipliers in relation with the overall number of OMs with hits by calculating  $R = N_{\text{hits}}/N_{\text{OM}}$ . As two readout cycles are separated by a dead-time of 250 ns, this parameter is most effective for high-energy events.

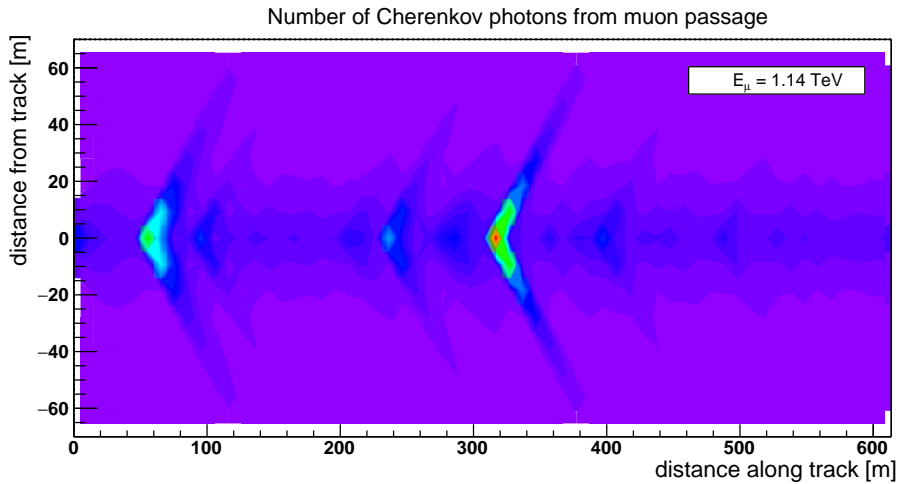


Figure 4.3: Number of Cherenkov photons from the primary particle and radiative processes along an exemplary muon track as modelled using the KM3 code.

### 4.3.2 $dE/dx$ and ANNergy

Two more sophisticated muon energy reconstructions are used in *ANTARES*, on the one hand the energy-loss estimator  $dE/dx$  [55] and the ANN energy reconstruction [56] involving artificial neural networks.

**Energy loss estimator  $dE/dx$**  The energy loss is calculated by relating the total charge produced by the photon hits in the PMTs,  $\sum A$ , to the number of PMT readouts and the effective track length  $L_{\text{eff}}$  of the muon track within the detector, which is given by the length of reconstructed track passing through a cylinder around the instrumented volume of *ANTARES*. It is also scaled by the overall efficiency  $\varepsilon$  of the detector towards Cherenkov photons from the given track, taking into account the angular acceptance and distance of the individual optical modules from the muon track. With this, the energy loss  $\rho$  is then given by  $\rho = \frac{1}{N_{\text{hits}}} \frac{\sum A}{L_{\text{eff}} \varepsilon}$ , from which the mean energy of neutrinos leading to an equivalent energy loss is calculated.

**Neural network estimator ANN** The non-linear function approximation achieved in an artificial neural network is mostly dependent on the input parameters and their according preprocessing, as will be elaborated in Chapter 6. For the ANN energy estimator, over 50 different input parameters are used which range from parameters describing the distribution of hits in the detector by their time, location and charge, to track-related parameters like average time residuals. The training was performed on a charged-current muon neutrino simulation and several neural networks were trained to take into account the varying detector conditions. Therefore, as these events also include vertex cascades of muon neutrinos, the estimator can also be used to reconstruct the energy of cascade events, although not being optimized for this purpose.

### 4.3.3 Cascade energy reconstruction

Energy reconstruction for cascades is included in the same reconstruction packages as the directional and vertex reconstruction. The approach to modelling the light emission from the

vertex can be divided into two extreme cases, either assuming that the photons only originate at the Cherenkov angle from a track along the shower direction, or assuming to come from an isotropically radiating photon point source. For Dusj [16], the assumption of an isotropic point source is used, which, together with a restrictive hit selection, creates a relatively stable algorithm. However, the  $Q$  strategy evaluates the by weighting the total charge of all selected hits according to the summed distance of the hits from the bright point, leading to a less robust algorithm [52].

## 4.4 Further useful parameters

**Random Decision Forest** A Random Decision Forest (RDF) package was introduced in *ANTARES* [57] to serve for the classification of various event types. Apart from the output parameters of the RDF giving the percentage of trees in the forest agreeing on the same classification, the standard RDF for the classification of neutrino-induced signal events from atmospheric background events also comes with over a hundred predefined input variables, of which some are tested for use in the following analysis.

**Hit distribution parameters** Both track and shower reconstructions employ their own hit selection algorithms which, depending on the aim of the reconstruction, range from very loose hit selection criteria to very stringent selections. Parameters derived from hit selections therefore contain information on both the topology of the event, and the energy deposited inside the detector. For the various hit selections, the total number of hits  $N_{\text{hits}}$ , the number of lines with hits  $N_{\text{lines}}$ , the number of hits with single hit charge  $A > 2.5$  p.e. and the total charge of the hits  $A_{\text{total}}$  will be considered.



## 5 | Analysis approach

The main goal of any diffuse flux analysis lies in reaching a high sensitivity towards the cosmic neutrino flux, which is achieved by effectively de-selecting background events from signal events while maintaining a high signal number. As previous analyses only targeted one neutrino event type and these analyses already showed that the *ANTARES* sensitivity for a diffuse neutrino flux can be improved by sophisticating the analysis method, two questions must be answered concerning the strategic approach to the analysis: First, should the optimization aim rather for a rejection of the background-only hypothesis while expecting not to reach a sensitivity high enough to discover a signal, thus setting an upper limit on the actual flux assumption, or should it primarily aim to discover a given flux? This decision will influence the choice of the optimization parameter.

Secondly, how should the event selection be approached? One could either first select well-reconstructed track and cascade events according to the established signature-specific event selection strategies and then combine the resulting events, or introduce common event selection criteria which are sensitive to high-energy neutrino events regardless of their event signature. Depending on the quality of this selection technique, the second approach could extend the selection to include formerly discarded events. This section addresses these two questions before the specific tools for the combined analysis are introduced.

### 5.1 Analysis goal and optimization parameters

With the foreknowledge of both theoretical models of cosmic neutrino generation and flux predictions at Earth and the actual measurements from IceCube available, both the setting of an upper flux limit for the Southern Hemisphere and aiming for high signal detection efficiency are equally interesting targets for the analysis. While the second strategy employs the model discovery potential  $\mathcal{D}(n_{\text{sig}}, n_{\text{bkg}})$  to calculate the optimum relation between the number of background events  $n_{\text{bkg}}$  and signal events  $n_{\text{sig}}$  in the event selection for a signal flux  $\Phi$ , the first approach uses the model rejection factor  $\mathcal{R}(n_{\text{sig}}, n_{\text{bkg}})$ . In analysis steps which call for lesser accuracy but higher computational speed, a simple optimization parameter  $\mathcal{S}(n_{\text{sig}}, n_{\text{bkg}})$  will be used to substitute these two parameters.

**Model discovery potential** The model discovery potential as considered in [58] assumes the existence of a flux, which should be measured with the confidence level  $1 - \beta$  with a certainty that leaves the probability of error comparatively small. The probability of measuring a number of events  $n_{\text{obs}}$  is then calculated by the Poissonian probability  $P(n_{\text{obs}} | n_{\text{sig}} + n_{\text{bkg}})$ . The least

detectable signal of this flux is then defined by the number of events  $\bar{n}_{\text{lds}}$  for which the condition

$$1 - \beta = P(n \geq n_{\text{obs}} | \bar{n}_{\text{lds}} + n_{\text{bkg}}) \quad (5.1)$$

is met. The model discovery potential is then defined as

$$\mathcal{D}(n_{\text{sig}}, n_{\text{bkg}}) = n_{\text{lds}} / n_{\text{sig}}. \quad (5.2)$$

**Model rejection factor** The model rejection technique [59] assumes that the chance of measuring a theoretical flux is small, and therefore the method seeks to set the most stringent limit on a given flux assumption, which should be excluded at a confidence level  $l$ . For this, the average upper limit is calculated by using the Feldman-Cousins confidence interval upper limit  $\mu_l(n_{\text{obs}}, n_{\text{bkg}})$  which describes the probability of a measured number of events  $n_{\text{obs}}$  being in agreement with a background-only measurement, and weighting the possible observations by their Poissonian probability

$$\mu_l(n_{\text{bkg}}) = \sum_{n_{\text{obs}}=0}^{\infty} \mu_l(n_{\text{obs}}, n_{\text{bkg}}) \frac{n_{\text{bkg}}^{n_{\text{obs}}}}{n_{\text{obs}}!} e^{-n_{\text{bkg}}}. \quad (5.3)$$

The model rejection factor is then defined by

$$\mathcal{R}_l(n_{\text{sig}}, n_{\text{bkg}}) = \mu_l(n_{\text{bkg}}) / n_{\text{sig}}. \quad (5.4)$$

As the full calculation requires a comparatively long computing time, a simplified extrapolation from tabled values has been used during the development of the analysis, described in detail in the Appendix A.2.1.

**Simple Optimizer** Instead of the sophisticated model rejection or discovery methods, a simple function approximating the behaviour of the two cut optimizing function was introduced, which was already employed at the development stages of the classification methods and which was also used in the cut optimization procedure as comparative parameter. This simple optimizer is defined as

$$\mathcal{S}(n_{\text{sig}}, n_{\text{bkg}}) = \frac{2\sqrt{n_{\text{bkg}}}}{n_{\text{sig}}} \quad (5.5)$$

A comparison of the enumerator of all three cut optimization functions is shown in Figure 5.1.

## 5.2 Analysis strategy study

In the previous analyses targeting either only cascade neutrino events [16] or only muon track events (e.g. [17]), the analysis approach was an obvious one: depending on the reconstruction methods, a combination of reconstruction quality and zenith angular selection was used to suppress the background of downgoing atmospheric muons against the upgoing neutrino events, followed by a selection of high-energy events to emphasize the cosmic neutrino candidates against the atmospheric neutrino background, see Figure 5.2.

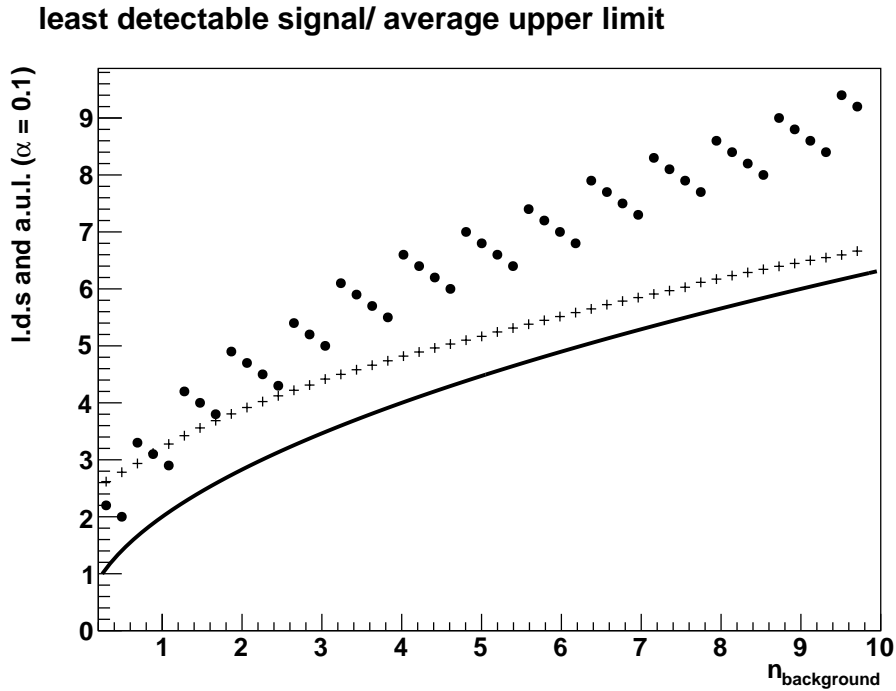


Figure 5.1: Comparison of least detectable signal (dots), average upper limit (crosses) and  $f(x) = 2\sqrt{n}$  (solid line), the cut optimization functions used in the following procedure.

These two tasks of atmospheric muon suppression and high-energy neutrino selection stay the same for an analysis addressing all neutrino flavours. The selection strategy could combine the two individual analyses, if the data set can be separated easily enough into a track-dominated and a shower-dominated sample, to which the signature-specific selection procedure is applied, and then adding up the remaining events. This approach would obviously select those events which are either well-reconstructed showers or tracks and focus on clearly distinguishable signatures. As an alternative approach, multivariate parameters for atmospheric muon suppression and high-energy neutrino selection could be introduced, focusing the cut optimization on common event features for both tracks and showers.

In order to choose one of the two approaches, a toy analysis was performed to estimate the potential of the two analysis chains.

**Toy analysis** Based on simulated runs equivalent to 39 days of data taking, event numbers were scaled to equal 1600 days, which is close to the expected amount of data for this analysis. The test flux was set as  $\Phi_{\text{test}} E^2 = 1.1 \times 10^{-8} \text{ GeV}^{-1} \text{ sr}^{-1} \text{ s}^{-1} \text{ cm}^{-2}$ . In the following section, a comparison is performed between a shower analysis (S) and track analysis (T) based on previous *ANTARES* analysis, a combined analysis using a combination of these two chains (C1) and a combined analysis involving multivariate tools (C2). In both combined analyses, the actual cut values were found by optimization on the model rejection factor, leading to a quite different outcome of the combined analyses in comparison to the previous signature-specific analysis chains. Also, the combined analyses were performed on simulation equivalent to 100 days, as the multivariate tools had to be trained on a sufficiently large subset of the test data.

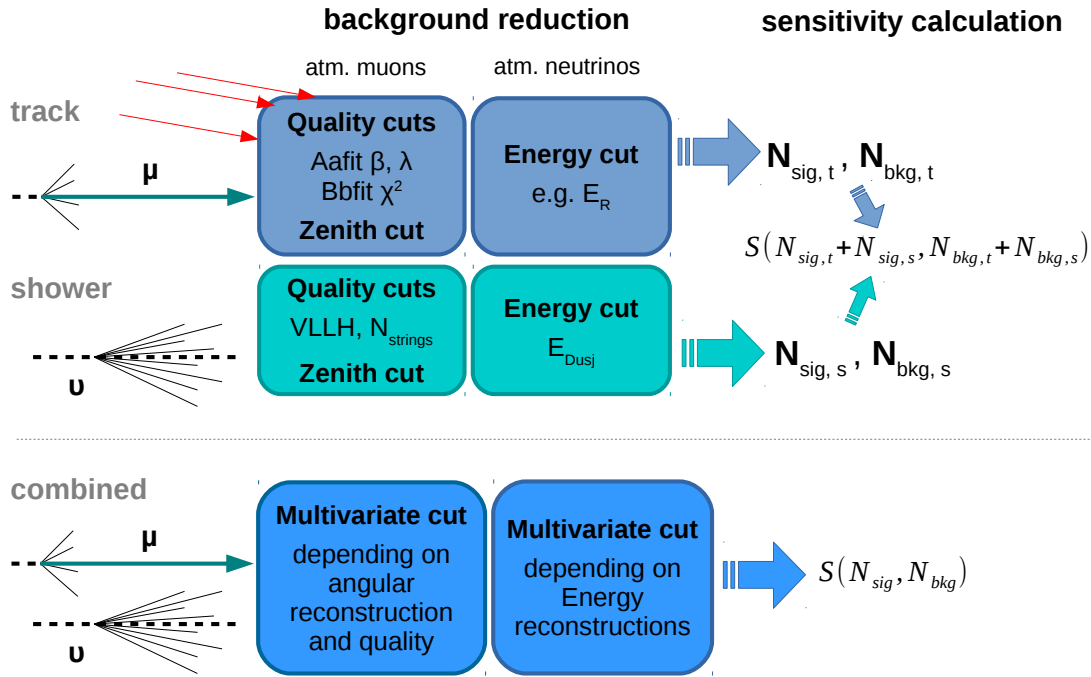


Figure 5.2: Schematic displaying the options for the combination of track and shower analyses.

### 5.2.1 Separate track and shower analyses

**Toy track analysis (T)** The previous track studies have been performed on one [15] up to four years of data (see [60], [61] and [17]). Although all analyses use slightly different approaches, in the end they generally rely on the Aafit reconstruction algorithm and a corresponding error estimate. Therefore, the toy track analysis here uses the reconstruction agreement between Aafit and Bbfit zenith angle reconstruction  $\Delta\theta = |\cos\theta_{\text{Aafit}} - \cos\theta_{\text{Bbfit}}|$  and the difference between the track and shower quality parameter  $\Delta\chi^2 = |\chi_{\text{track}}^2 - \chi_{\text{bright}}^2|$  as introduced in [17]. As energy estimate both the  $R$ -parameter and  $dE/dx$  energy estimate are used in the optimization, leading to two different comparison results. The contribution of atmospheric muons is calculated from a fit to the energy reconstruction parameter distribution of atmospheric muon events to extrapolate the low statistic sample to the cut value. The model rejection factor minimization leads to

**Track quality cuts**  $\Lambda_{\text{Aafit}} > -6.2$ ,  $\beta_{\text{Aafit}} < 0.3^\circ$ ,  $\Delta\chi^2 > 3$ ,

**Zenith angle**  $150^\circ > \theta_{\text{Aafit}} > 81^\circ$  with reconstruction agreement  $\Delta\theta < 0.2$  and

**Energy cut**  $\log_{10}(E_{dEdx,R}/\text{GeV}) > 4.9$ .

While, in [17], a sensitivity of  $3.6 \times 10^{-8} \text{ GeV}^{-1} \text{ sr}^{-1} \text{ s}^{-1} \text{ cm}^{-2}$  is given for 933 days lifetime, this toy analysis would reach  $2.7 - 4.0 \times 10^{-8} \text{ GeV}^{-1} \text{ sr}^{-1} \text{ s}^{-1} \text{ cm}^{-2}$  for the equivalent time and is therefore compatible to this latest analysis. For 1600 days of equivalent data taking, a sensitivity of  $2.0 - 2.9 \times 10^{-8} \text{ GeV}^{-1} \text{ sr}^{-1} \text{ s}^{-1} \text{ cm}^{-2}$  could then be reached.

	T with dEdx	T with R	S	C1	C2
$N_{\mu\text{atm}}$	12.2	8.2	2.4	10.3	2*
$N_{\nu\text{track}}(\text{Bartol})$	2.4	6.11	0.86	7.43	2.6
$N_{\nu\text{shower}}(\text{Bartol})$	0.0	0.0	1.1	0.9	1.1
$N_{\nu\text{track}}^\dagger$	3.0	4.4	0.06	5.5	2.4
$N_{\nu\text{shower}}^\dagger$	0.0	0.0	3.3	3.8	3.6
$\mathcal{R}_{90\%}^\dagger$	2.6	1.8	1.5	0.94	0.90

Table 5.1: Event numbers and model rejection factor of the toy analyses, tested on simulation sample of 39 days (T,S) or 100 days (C), and scaled to 1600 d livetime, with (\*) estimated atmospheric muon contribution ( $\dagger$ ) on a test flux of  $\Phi_{\text{test}}E^2 = 1.1 \times 10^{-8} \text{ GeV}^{-1} \text{ sr}^{-1} \text{ s}^{-1} \text{ cm}^{-2}$

**Toy shower analysis (S)** Although other studies targeting shower-like events have been performed before, the most sensitive and well validated analysis has been put forward in [16]. Therefore, the model shower analysis follows closely the cuts used therein, though hugely simplified to the main cut steps and disregarding muon contamination estimates, the filter introduced for sparking events,  $\nu_\tau$  contribution and other finer details. The close outcome of the test analysis in this process is a good indication for the validity of these model analyses, with  $\Phi E^2 = 2.2 \times 10^{-8} \text{ GeV}^{-1} \text{ sr}^{-1} \text{ s}^{-1} \text{ cm}^{-2}$  given in [16] for 1247 days and  $\Phi E^2 = 2.0 \times 10^{-8} \text{ GeV}^{-1} \text{ sr}^{-1} \text{ s}^{-1} \text{ cm}^{-2}$  reached here with these cuts:

**Shower quality cut**  $\text{Dusj VLLH} < 7.9$ , number of strings with hits  $N_{\text{string}} > 2$

**Zenith angle**  $\theta_{\text{Dusj}} > 94^\circ$

**Energy cut**  $\log_{10}(E_{\text{Dusj}}/\text{GeV}) > 4.0$

For 1600 days, the shower analysis would therefore reach a sensitivity of about  $\Phi E^2 = 1.6 \times 10^{-8} \text{ GeV}^{-1} \text{ sr}^{-1} \text{ s}^{-1} \text{ cm}^{-2}$ .

## 5.2.2 Combining tracks and showers

Combining now these two analysis chains introduces the challenge of combining two relatively distinct sets of parameters describing different event topologies. While the one approach emphasises the distinct differences between track and shower signatures in following the two signature-specific analysis chains, the other relies on features that are common to both signatures in comparison to background events. Considering the relative small size of *ANTARES* and common features of subshowers in both track and shower events, both approaches might have their advantages.

**Using initial event classification (C1)** An initial event classification can easiest be introduced by utilizing a reconstruction quality parameter. Here, the vertex likelihood VLLH of the Dusj shower reconstruction is used to split the data set into a shower dominated and a track dominated subset using

- for the track subset  $\text{VLLH} > 7.9$  and  $\text{VLLH} < 7.9$  for showers,

leading to relatively pure subsets. On the shower subset, the further cuts of the above toy shower analysis were applied, as were the toy track cuts on the track set. For higher accuracy, simulation of 100 days data taking was used. In the end, event numbers from both analysis branches were again added up, shown as C1 in Table 5.1. This kind of analysis would reach a sensitivity of  $\Phi E^2 = 1.0 \times 10^{-8} \text{GeV}^{-1} \text{cm}^{-2} \text{sr}^{-1} \text{s}^{-1}$ .

This kind of combination would therefore increase the sensitivity compared to a separate track or shower approach.

**Using multivariate classification (C2)** In order to estimate the feasibility of a multivariate approach, some out-of-the-box multivariate tools were trained using the ROOT TMVA package [62], which is introduced in more detail in the following section, on part of the available simulation. As the signature specific event selection takes place in the first analysis step addressing the atmospheric muon rejection, all atmospheric muon suppression parameters from the T and S toy analysis were used to train a Boosted Decision Tree (BDT), a neural network, Fisher discriminant and a Likelihood discriminator, which are also explained in the following section. In combination with each of the above used energy estimates, a two-dimensional parameter scan on the multivariate tool and the energy estimate using model rejection was performed to find the cut value combination leading to the lowest model rejection factor. The results for the best cut combination on the Fisher discriminant and  $E_{dEdx}$  is shown as C2 in Table 5.1. As scanning yielded an atmospheric muon contribution of 0, but with low statistical accuracy, an atmospheric muon contribution of 2 was assumed, as a single atmospheric muon in the simulation carries a weight of 3. With these assumptions, the multivariate analysis would outperform the combined analysis with initial event classification. Within a reasonable margin of error allowing for e.g. a larger muon contribution, these two analysis chains reach at least the same sensitivity.

These toy analyses showed a number of key points for a combined analysis: Firstly, an event type combination for the diffuse cosmic neutrino search should increase the sensitivity in comparison to the separate searches. Secondly, a multivariate approach to combination seems to offer at least the same sensitivity as pursuing separate analysis chains for track and shower events, as the above multivariate classification was far from optimized on the specific task. Last but not least, the previous analysis chains offer a starting point for the development of the classifiers by suggesting parameters which are specifically useful for the two main tasks of atmospheric muon and atmospheric neutrino suppression. The development of these tools will therefore be taken up in the next section.

## 6 | Multivariate Tools development

Finding the ideal separation between signal and background events can be viewed as searching for the boundary layer in a multidimensional space spanned by the features, i.e. observables and reconstruction parameters derived from them. Various methods ranging from simplistic linear cuts to sophisticated functional structures have been developed to this end, such that the search for the best cut parameters turns into the tuning of a multivariate tool adapted to the requirements of the task at hand. In this section, the development process of multivariate tools is first introduced before applying it to the tasks of background suppression for the diffuse flux analysis.

The TMVA package [62] offers a comprehensive collection of multivariate methods which are suited to break down the high-dimensional task of background suppression and signal optimization to a simple final cut on the output of a multivariate classifier. The performance of the multivariate classifier depends on the input parameters to the method, the method's capability of modelling the functional dependence between the input and the required output of the method, and the properties of the set of data from which the model is derived. A short introduction to the methods here tested is given in the first subsection. In the subsequent sections, the optimization criteria and methodology is developed before finally the performance of the optimized multivariate techniques is evaluated.

### 6.1 Multivariate classification methods

#### 6.1.1 Statistical approaches to parameter modelling

In general, the classification problem can be described as assigning an event of class  $\omega_i$  to the correct class with probability  $p(\omega)$ , such that the error of this assignment is minimal when considering a vector of observables  $\mathbf{x}$  of the event. This is expressed in Bayes' rule for minimum error [63] of classifying events in  $C$  classes as

$$p(\mathbf{x}|\omega_i)p(\omega_i) > p(\mathbf{x}|\omega_k)p(\omega_k) \quad k = 1, \dots, C; k \neq i. \quad (6.1)$$

In order to minimize the classification error, two approaches can be chosen. The respective probability density function (pdf)  $P(\mathbf{x})$  can either be reconstructed through functional modelling of the pdf, or a decision boundary between the classes is constructed disregarding the actual functional dependence. In the first case, parametric and non-parametric pdf modelling methods are employed, where either a prior assumption of the pdf is used as starting point in parametric modelling, or no prior assumption is available to use in non-parametric modelling. In the second

case, a decision boundary between the classes is constructed in a discriminant analysis which disregards the actual form of the pdf but models the decision boundary purely from the observed parameter correlations. In the simplest case, the boundary can be assumed as linear, in more complex cases various discriminant functions and/or a combination of various discriminators are included.

For all different TMVA methods, the actual adaption of the method lies in the minimization of the error between model and true pdf as found in a given set of data. This so-called training data provides the reference for the true dependencies between the observables and the classification classes. In case of pdf modelling, an adaption of the model is achieved through training algorithms employing (6.1).

**Parametric modelling** Parametric modelling involves foreknowledge of the functional dependence between the observables  $\mathbf{x}$  and the class probability  $p(\omega_i)$ . The free parameters  $\mathbf{a}$  of the function  $p(\omega) = f(\mathbf{a}, \mathbf{x})$  are then adapted by minimizing the error for a given dataset. Typical functions employed contain linear or quadratic functions and are considered as Gaussian classifiers. Due to their design, these classifiers encounter problems if the function assumed does not fit the actual classification problem and if the observables show high covariance. As the problem at hand is too complex for analytical pdf estimation, these methods will play no further role here.

**Non-parametric modelling** If no prior knowledge of the functional dependence is available, the pdf can still be modelled e.g. by employing spline function modelling to parameter histograms, as implemented in the TMVA package as *Likelihood* method. Another approach is the *k-nearest-neighbour* method, see Fig. 6.1a, in which the probability density is estimated by calculating the volume  $d\mathbf{x}$  around each event containing the  $k$  events nearest to it in the parameter space and evaluating the fraction of events of the given classes  $C$  within this volume. These methods thus also adapt to event distributions which exhibit irregular features not easily captured by parametric modelling.

**Linear discriminants** In linear discriminant analysis, the aim is to find a weight vector  $\mathbf{w}$  applied to the parameter vector such that  $\mathbf{w}^T \mathbf{x} + \mathbf{w}_0 > (<) 0$  if the event is part of class  $\omega_1$  ( $\omega_2$ ). The simplest application of this can be found in a single perceptron where the error of the weight vector is calculated as the distance of misclassified events to the decision boundary. In the *Fisher* criterion, the decision boundary is chosen by evaluating the ratio of the between-class over the within-class variance,

$$J_F = \frac{|\mathbf{w}^T(\mathbf{m}_1 - \mathbf{m}_2)|^2}{\mathbf{w}^T \mathbf{S}_W \mathbf{w}}, \quad (6.2)$$

where  $\mathbf{m}_1$  and  $\mathbf{m}_2$  are the group means and  $\mathbf{S}_W$  the pooled within-class covariance [63]. In concept similar methods are the *H-matrix* calculation, which assumes a Gaussian distribution of the input variables, and *support vector machines (SVM)*, see Fig. 6.1d, for which few support events are used to construct a hyperplane which maximizes the distance of the events to this plane according to the linear discrimination criterion.

On the boundary between linear and non-linear methods lies the *functional discriminant analysis*

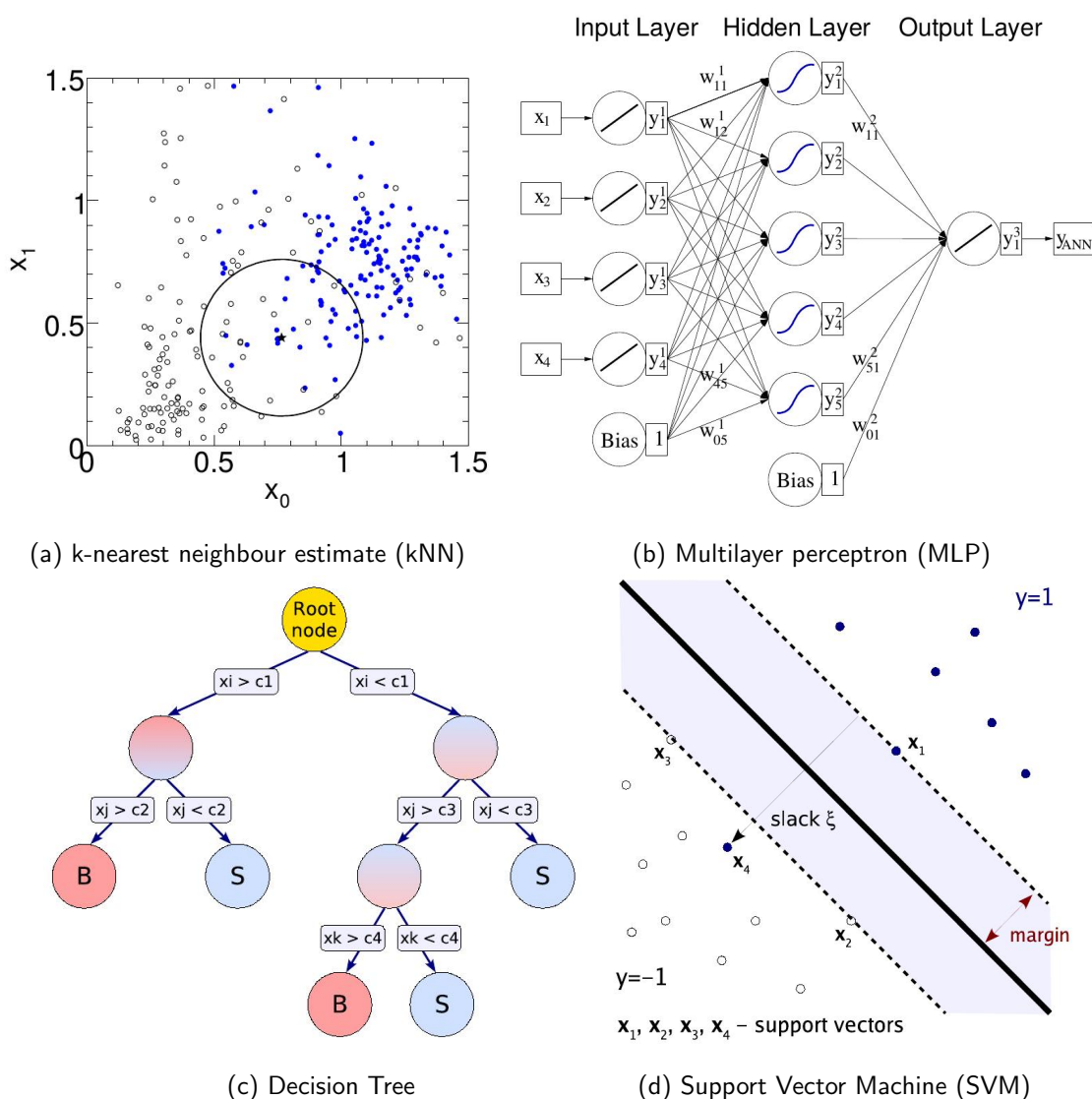


Figure 6.1: Schematic of various multivariate methods, from [62]

(*FDA*), in which the discriminant function can be chosen not only to involve linear terms, but also terms of higher order polynomials or other functional dependences.

**Non-linear discrimination** The step from linear to non-linear discrimination is that of a single decision boundary to a multitude of decisions which are performed either in parallel and/or consecutively. In *multi-layer perceptrons* (*MLP*, also known as artificial neural networks, see Fig. 6.1b), decision units, so-called perceptrons, perform linear discrimination of  $y = f(\mathbf{wz})$  depending on the perceptron input  $\mathbf{z}$ . Each perceptron either passes their output value  $y$  to perceptrons in the consecutive layer, which provide their decisions based on the weighted combined input of the previous layer's output, or the last layer single perceptron provides the decision. These arrays of perceptrons are thus able to adapt to highly non-linear decision boundaries.

A simpler construction of decision boundaries is performed in the nodes of a decision tree, see Fig. 6.1c. Here, each tree node deals only with the decision on one parameter  $x_i \leq c_i$  with

classification boundary  $c_i$ , where each layer after the first node contains maximum  $2i$  nodes, each node classifying only one subgroup of events with similar classification in the previous layers until a stop criterion is met. While this single tree structure naturally reaches only a limited accuracy, the parallel training of many trees as in *random decision forests (RDF)* or *boosted decision trees (BDT)* however provide a method to enhance the concept to high precision, as the decision on the class then is drawn from the overall result from differently trained trees.

**Additional techniques** Some additional methods are offered by the TMVA package which are either not suitable for the problem at hand or cannot be sorted into the categories above. Of these, two methods were considered in the analysis which lie on opposite ends of multivariate methods regarding complexity: on the one hand, *Rectangular Cut* optimization implements minimization rules for finding the optimal one-dimensional cuts  $\mathbf{c}$  in the parameter space such that  $\mathbf{x}_i > \mathbf{c}_i$ . It can thus be compared to the classical analysis approach implementing independent cuts on observables. On the other hand, the *Rulefit* algorithm employs a multitude of different decisions drawn from the nodes of a RDF trained on data subsamples, which are recombined according to an optimization criterion.

In addition to these methods, most methods can also be boosted in order to increase their separation power, meaning they are repeatedly applied, where the output of previous application of the method serves as input to the next application, sometimes with increased weights to misclassified events to emphasize their characteristics. Apart from boosting, bagging is also used to increase classifier stability. Here, the training data is re-sampled for parallel trained methods, and the result given as the average of the various method representations.

CRITERIA		MVA METHOD									
		Cuts	Likeli- hood	PDE- RS / k-NN	PDE- Foam	H- Matrix	Fisher / LD	MLP	BDT	Rule- Fit	SVM
Perfor- mance	No or linear correlations	*	**	*	*	*	**	**	*	**	*
	Nonlinear correlations	o	o	**	**	o	o	**	**	**	**
Speed	Training	o	**	**	**	**	**	*	*	*	o
	Response	**	**	o	*	**	**	**	*	**	*
Robust- ness	Overtraining	**	*	*	*	**	**	*	* <sup>39</sup>	*	**
	Weak variables	**	*	o	o	**	**	*	**	*	*
Curse of dimensionality		o	**	o	o	**	**	*	*	*	
Transparency		**	**	*	*	**	**	o	o	o	o

Table 6.1: Comparison of properties of the different TMVA methods, from [62]

### 6.1.2 Data preprocessing

In order to adapt parameters for use in multivariate methods, the parameter can be normalized, sets of parameters decorrelated or parameters transformed to different distributions. While normalization is a straight-forward scaling of the parameter range to fit within  $[-1, 1]$ , variable

decorrelation and transformation can be performed in various ways.

**Variable decorrelation** In *linear decorrelation*, the covariance matrix  $C$  is used to transform the set of parameters to a decorrelated set by employing a diagonal matrix  $D$  and unitary matrix  $S$  to  $D = S^T C S$  such that  $C' = S \sqrt{D} S^T$ . The decorrelation is then performed as  $\mathbf{x} \mapsto (C')^{-1} \mathbf{x}$  [62]. In *principal component decomposition*, the decorrelation is applied such that the input parameters  $x_l$  are transformed to principal components  $x_{PC,k}$ , which are ordered according to their variance in the sample and obtained by employing the data sample means  $\bar{x}$  and eigenvectors  $\mathbf{v}^{(k)}$  as

$$x_{PC,k} = \sum_{l=1}^{n_{\text{var}}} (x_l - \bar{x}_l) v_l^{(k)}, \quad \forall k = 1, n_{\text{var}}. \quad (6.3)$$

Here, the matrix of eigenvectors  $V$  follows the relation  $C \cdot V = D \cdot V$ . For Gaussian distributed variables, this transformation eliminates linear correlations [62].

**Variable transformation** As decorrelation works best on uniformly and Gaussian distributed variables, the input distribution is transformed into a *uniform distribution* by smoothing out its histogram. If *Gaussian transformation* is required, the input variable  $x$  is then transformed from the probability density function  $\hat{x}$  employing

$$x \mapsto \sqrt{2} \cdot \text{erf}^{-1} \left( 2 \cdot \int_{-\infty}^x \hat{x}(x') dx' - 1 \right). \quad (6.4)$$

Whether data preprocessing is required not only depends on the method, but also on the number and correlation of the input parameters employed. The following search for a well-performing MVA method therefore considers different preprocessing options as well as different methods.

### 6.1.3 The pattern recognition cycle

The step between the theory of multivariate methods to the reality of the adapted tool lies in a repeated application of what is called the pattern recognition cycle, which can be seen in Figure 6.2. After definition of the aim of the multivariate tool, the available data is explored in order to find suitable parameter candidates for this task. Here, reliability of the parameters as well as their relevance for the task are crucial and will be explored in the following section. This is followed by the actual cycle of feature extraction and preprocessing of the data used for the training of the classifier, the actual training and an assessment of the trained tool to re-enter the parameter adapting and selection. Here, a quality criterion has to be chosen to compare the performance of the multivariate tools before restarting the cycle by optimizing the parameter selection, preprocessing the parameters and training the tools.

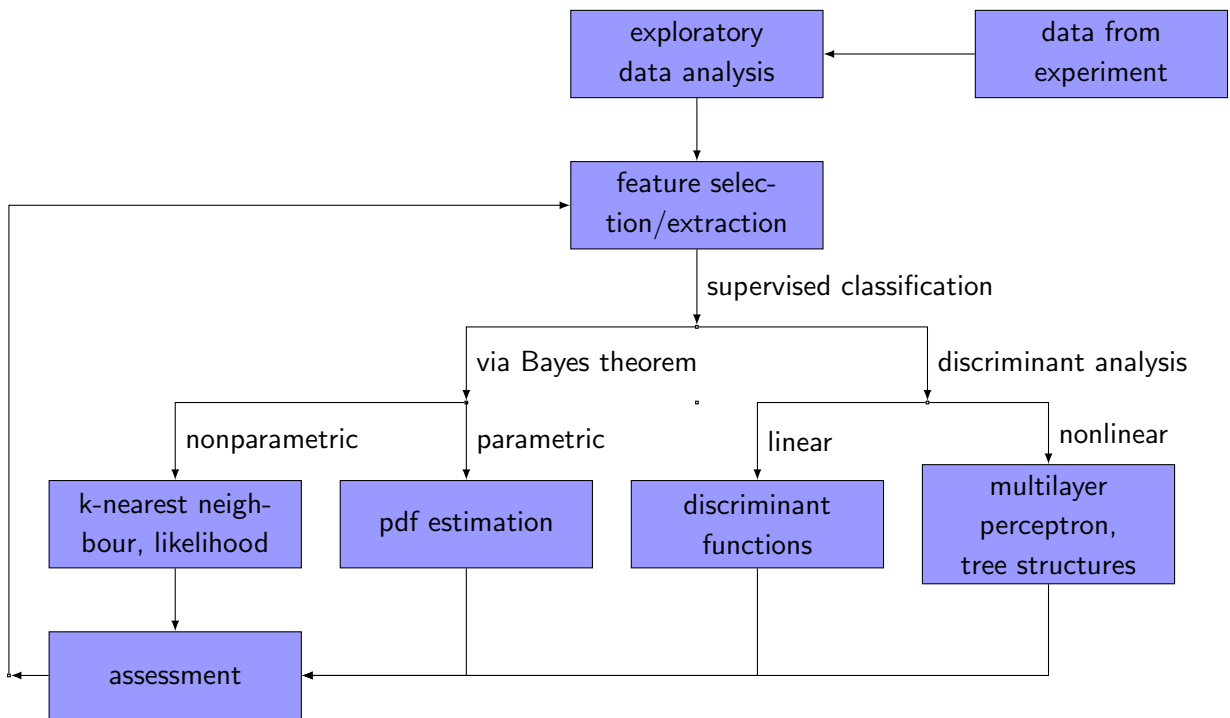


Figure 6.2: Overview over multivariate methods (adapted from [63]) and the pattern recognition cycle.

## 6.2 Parameter selection

The parameter selection process consists of three steps: Firstly, the number of candidate parameters is extended to encompass the feature space as widely as possible. Starting from the extended set, the choice is secondly limited by evaluating the stability of the parameters, their suitability for the tasks and their correlation. Thirdly, candidate parameters for atmospheric muon suppression and cosmic signal selection are chosen according to their suitability for the task and serve as a basis for the construction of multivariate tools in the following chapter.

### 6.2.1 Expanding the parameter space

In order to systematically approach the vast possibilities for input parameters to the multivariate tools, they are here introduced as grouped according to their function and former use. A full list of parameters considered within the selection process can be found in the Appendix A.4.1.

**"Classical" parameters** All parameters used in the previous diffuse neutrino flux analyses were introduced as parameter candidates, which included mainly quality parameters of the track and shower reconstruction methods (and combinations of them such as  $\Delta\chi^2$  as difference between track and shower quality in BBFit, see [17]) as well as the event's reconstructed direction and reconstruction quality, and several energy reconstruction parameters and estimates.

**Additional reconstruction parameters** In addition to the parameters used in previous analyses, basically all quality parameters of the event reconstruction methods were considered,

as well as some input parameters to the multivariate methods used in the RDF directional selection and ANNergy energy reconstruction.

**Parameters employing hit selections** Both track and shower reconstructions employ their own hit selection algorithms which, depending on the aim of the reconstruction, range from loose correlation criteria to quite stringent filters. Parameters derived from these hit selections contain information on both the topology of the event, depending on the selection, and the energy deposited inside the detector. For the various hit selections the total number of hits  $N_{\text{hits}}$ , the number of lines with hits  $N_{\text{lines}}$ , the number of hits with more than single hit charge  $N(A > 2.5 \text{ p.e.})$  and the total charge of the hits  $A_{\text{total}}$  was included in the parameter candidate list.

**Topological parameters** In order to estimate the reconstructability of an event from its position inside the detector volume, two coverage parameters were introduced. Assuming an idealized shape for track and shower events, the first parameter uses a cone from the reconstructed shower vertex with an opening angle equalling the Cherenkov angle and variable length  $s$ , the second assumes a cylinder of radius  $r$  around the track hypothesis. For both shapes, the percentage of active optical modules within this event boundary is calculated. It can thus be used as weight parameter to the hit selections introduced above. However, these parameters later proved to be not well represented within the simulation.

**Parameters for track enhancement** During training of the MVA method for atmospheric neutrino suppression, it became apparent that additional parameters are needed to increase the method sensitivity towards high-energy track signatures. To this end, the ANN energy reconstruction [64] was applied on various hit selections and Aafit and Dusj directional estimates. The input parameters used for the neural net in ANN evaluate hit timing and amplitude of the used hit selection in relation to the reconstructed track and include parameters like the number of hits and their amplitude within a given distance from the track estimate, number of storey and strings with hits from the hit selection and mean and RMS of arrival times and distances towards the tracks for the hit distributions. All parameters are described in detail in in [56].

### 6.2.2 Evaluating the parameter space

In this step, the above list of parameters needs to be reduced to a manageable size, which was achieved deselecting parameters according to quality criteria introduced in this step.

Due to the large variation of detector conditions, those parameters used in the multivariate tools should be comparatively stable towards these changes, and be well represented within simulation. Therefore, a sample of 56 runs<sup>8</sup> was used for basic performance tests of the observables. Observables showing a good representation in simulation and a stable agreement between simulation and measurement (**P1**) are then analysed in subgroups of similar parameters types (e.g. directional parameters, energy related etc.). The goal of this step lies in firstly finding parameters which by themselves show a different distribution for signal and background, and which will

<sup>8</sup>sample of runs with run numbers ending in 0, taken at approximate equal intervals between 2007 and 2012, for which run-by-run v2 simulation is available

secondly add additional information to the parameter set as no strong linear correlation exists to the well classifying parameters in the subgroup (**P2**).

Therefore, each parameter to be considered as candidate parameter is judged and (de)selected according to the following criteria:

**P1: Simulation reliability** The observable distribution must be well represented in simulation and therefore show a good agreement between data and simulation in MUPAGE from run-by-run simulation version 2 [35], and a stable performance throughout the runtime must be seen.

**P2a: Separation power** The observable must discriminate by itself well between signal and background events using the simple optimizer  $\mathcal{S}$  or/and

**P2b: Orthogonality** Within a given parameter set, the observable must add valuable information, i.e. show a reasonable orthogonality towards the remaining parameters in a principal component analysis.

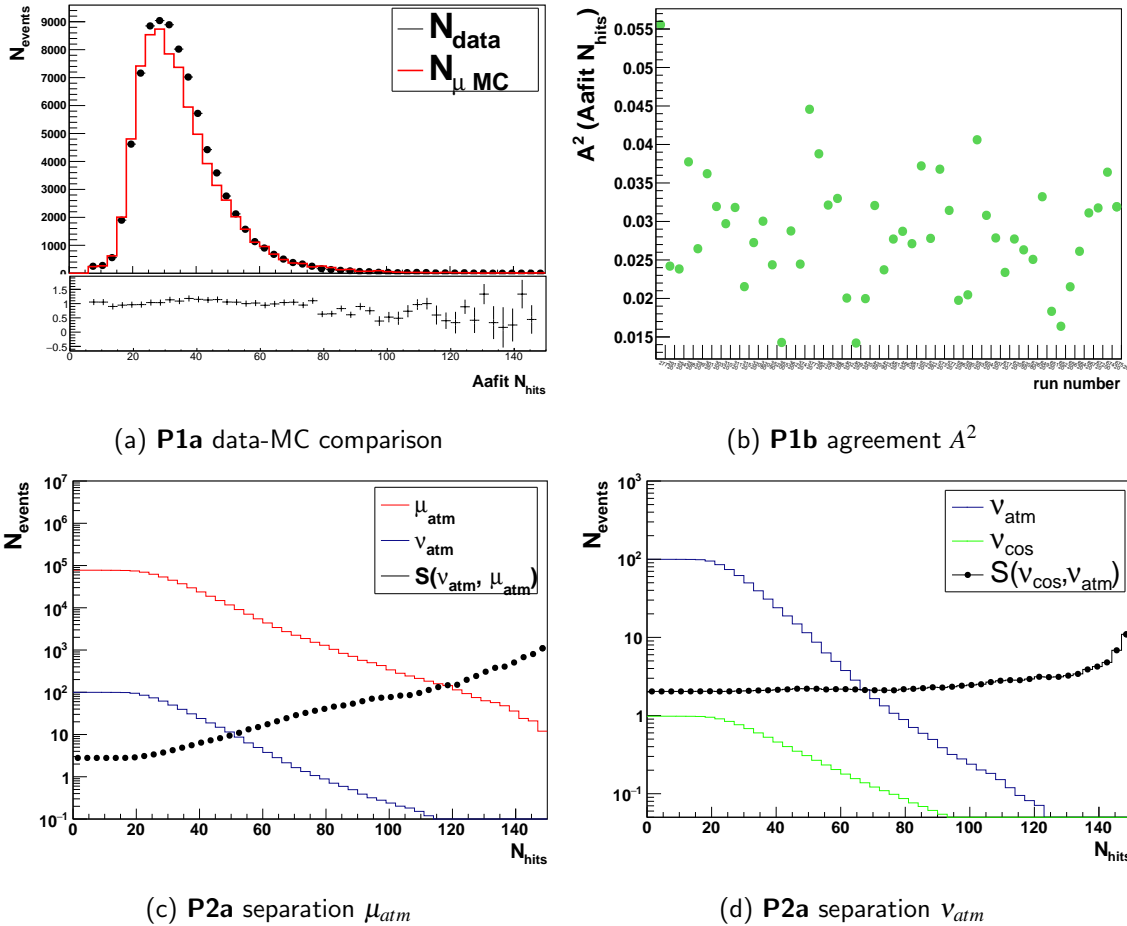


Figure 6.3: Selection criteria for parameter candidates evaluated using 56 runs, here with  $N_{hits,Aafit}$ : a) general data/MC agreement b) data/MC agreement for all runs in the test sample c) simple optimizer for neutrinos from atmospheric muon background, scaled to 1600 days d) simple optimizer for cosmic neutrinos from atmospheric background, scaled.

**Agreement in data and simulation (P1)** Firstly, the one-dimensional parameter distribution is viewed for muon simulation and data of all sample runs and a by-eye evaluation of the agreement is performed, see Figure 6.3a, rating the agreement between good and unsuitable for analysis. Then, the distribution is compared for simulated atmospheric muons and data for each of the test runs separately and the run-by-run histogram agreement  $A^2$  is calculated as

$$A^2(x_{\text{data}}, x_{\text{sim}}) = \sum_{i=1}^{n_{\text{bin}}} \sum_{j=i}^{n_{\text{bin}}} \frac{(n_{di}/N_d - n_{sj}/N_s)^2}{(j-i+1)^2}, \quad (6.5)$$

assuming two histograms of the distribution of parameter  $x$  from data and simulation, of the same number of bins  $n_{\text{bin}}$  and the same parameter range holding the events  $N_d$  and  $N_s$  with entries  $n_{di}$  and  $n_{sj}$  for bin  $i$  respectively. In Figure 6.3b, one can therefore judge the stability of data and simulation agreement for the different detector conditions. Later in the development of the TMVA tools, this comparison is also performed on a small sample of runs already available from run-by-run simulation version 3, which lead to the deselection of formerly selected parameter candidates.

**Separation power (P2a)** To evaluate the suitability of the observable for distinguishing between the cosmic signal and the atmospheric muon and neutrino background, the cumulative distributions for the test sample for atmospheric muons, atmospheric neutrinos and cosmic neutrinos is plotted, and for each bin  $\mathcal{S}(N_{v,\text{atm}}, N_{\mu,\text{atm}})$  and  $\mathcal{S}(N_{v,\text{cos}}, N_{v,\text{atm}})$  calculated. Parameters achieving a comparatively low value in  $\mathcal{S}$  are then added to the parameter candidate list, as this indicates that a single parameter cut would already increase the sensitivity of a signal selection based singly on this parameter.

**Orthogonality (P2b)** Parameters of similar function (e.g. event directional estimates, energy estimates etc.) passing **P1** are allocated to a subsample and a Principle Component Analysis (PCA, documented in [62] as preprocessing method) is performed for events of the simulated muon sample and neutrino sample. The PCA here serves firstly to identify the parameter of the subgroup mostly representing the relevant feature, which is that of the largest eigenvalue. Secondly, its covariance matrix can be used to identify correlation between parameters. Here, a different two-dimensional behaviour between two observables for muons and neutrinos can be used as indication to include both parameters on the ground of their combined event discrimination power. This was evaluated by calculating the difference in covariance  $\Delta C = |Cov(x_i, x_j)_{\text{sample1}} - Cov(x_i, x_j)_{\text{sample2}}|$  for the background and signal sample as shown for one subgroup in Figure 6.4b. In this example, this would lead to the selection of the reconstructed zenith of the BBFit track reconstruction, as it by itself shows a large  $\Delta C$  compared to the other reconstructions. Having selected BBFit track, the Krake fit shows the largest  $\Delta C$  compared to BBFit track, but relatively good agreement with other reconstructions, and is therefore selected to complement the information gained from the BBFit track.

Later in the process, the various preprocessing transformations introduced in Section 6.1.2 were used to evaluate parameter correlations within the sample of input parameters for the multivariate tool. These correlation measures here only serve as indicators, as basically all parameters show higher importance in one or more preprocessing scenarios, as seen in Figure 6.4a, which makes it difficult to abandon any with this observation alone.

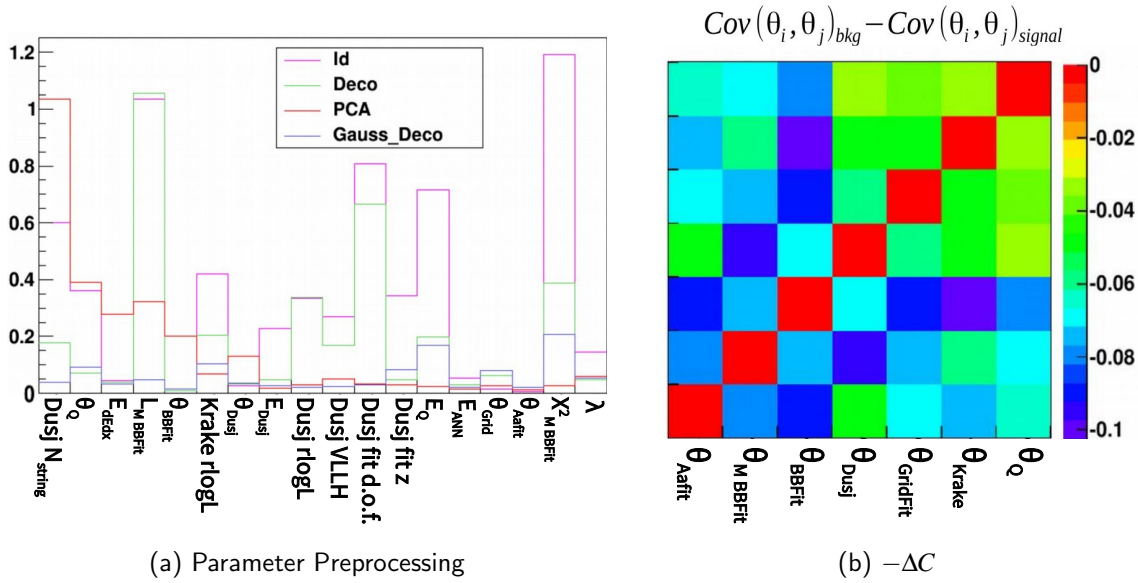


Figure 6.4: Input parameter evaluation by a) comparing parameter importance for different preprocessing scenarios (identity transformation, linear decorrelation, principle component decomposition, Gaussian decoupling and decorrelation) and by b) calculating  $\Delta C$  for a subsample of parameters.

### 6.2.3 Reducing the parameter space

After application of the aforementioned quality criteria, parameters were mostly selected according to their estimated performance, although these criteria were used as a guideline rather than a strict rule. In order to ensure continuity with formerly performed analysis, parameters used before were therefore included although their performance might not have been as good as those of newly added parameters. Also, the necessity to add parameters emphasizing features of high energy track events over shower events arose during multivariate tool development, which lead to the inclusion of such parameters without evaluation of their performance in the P2 criteria, as they were obviously needed to cover an afore neglected part of the parameter space. These considerations lead to the list of parameter candidates given in Table 6.2. A full record of the selection process results for all parameters can be found in Appendix A.4.1.

<sup>9</sup>*methods*: Cuts=rectangular cut optimization, Likelihood=Likelihood method, PDERS=multidimensional likelihood estimator, KNN=k-nearest-neighbour, HMatrix=H-Matrix, LD=linear discriminant, Fisher=Fisher discriminant, BoostedFisher=boosted application of Fisher discriminant, MLP=multi-layer perceptron, FDA=functional discriminant analysis, SVM=support vector machine, BDT=boosted decision tree, RuleFit=Rulefit, combination of various techniques, see 6.1.1; *preprocessing*: D=linear decorrelation, PCA= principle component decomposition, G=Gaussian transformation see 6.1.2; *specification* depending on the method; *optimization task*: 1=atmospheric muon suppression, 2=atmospheric neutrino suppression

parameter type	atm. $\mu$ suppression	atm. $\nu$ suppression
directional	Aafit $\theta$ <sup>cs</sup>	Aafit $\theta, \varphi$ <sup>s</sup>
	BBFit $\theta$ <sup>cs</sup>	Dusj $\theta, \varphi$ <sup>s</sup>
	Dusj $\theta$ <sup>cs</sup>	BBFit $\theta$ <sup>s</sup>
	GridFit $\theta$ <sup>s</sup>	
energy-like	$E_R$ <sup>s</sup>	$E_R$ <sup>cs</sup>
	$E_{ANN}$ <sup>s</sup>	$E_{ANN}$ <sup>cs</sup>
	Aafit $N_{\text{hits}}$ <sup>c</sup>	$E_{dEdx}$ <sup>cs</sup>
	Dusj $N_{\text{hits}}$ <sup>cr</sup>	$E_{Dusj}$ <sup>cs</sup>
	(ANN $\langle A \rangle$ all hits) <sup>s3</sup>	(Dusj $\sum A$ ) <sup>s3</sup>
		Aafit $N_{\text{hits}}$ <sup>n</sup>
	Dusj $N_{\text{hits}}$ <sup>n</sup>	
categorization	Aafit $\lambda$ <sup>c</sup>	GridFit width of min <sup>sr</sup>
	Aafit $\beta$ <sup>c</sup>	Dusj fit d.o.f <sup>s</sup>
	(BBFit track $\chi^2$ ) <sup>cd</sup>	
	(BBFit bright $\chi^2$ ) <sup>cd</sup>	
	Dusj VLLH <sup>c</sup>	
	Gridfit ratio <sup>s</sup>	
	Krake rlogL <sup>sr</sup>	
(Dusj shower $r\chi^2$ ) <sup>s3</sup>		
topological	Dusj convergence $z$ <sup>s</sup>	(ANN track length) <sup>s3</sup>
	dE/dx track length <sup>s</sup>	(ANN event duration) <sup>s3</sup>
	ANN $RMS(d_{\text{cher}})$ <sup>s</sup>	

Table 6.2: Parameter candidates for the analysis according to the following selection criteria:  $c$  = classical from former analysis,  $s$  = for good separation power,  $r$  = as good representation for parameter subsample,  $n$  = new parameter for track enhancement,  $d$  = deselected later because of data/MC discrepancy, 3 = deselected for disagreement with run-by-run simulation v3

### 6.3 Tools assessment

After obtaining the parameter candidates, the tools development was performed in two stages, the first of which involved general testing of the MVA methods and comparison of their performance on a comparatively small event sample from 50 runs. At the second stage, the best performing parameters and methods from this broad scanning were retrained on a sample of about 5% of the available simulated data under conditions close to the final set-up. In both cases, the tools and parameter quality criteria introduced here were used. For details on the training and evaluation, see Appendix A.5). In the following part, a short-hand for the individual setup of the classifiers will be used, calling a method as "method name + preprocessing + specifications (+ optimization task)" <sup>9</sup>.

**Precuts** After testing the reliability of possible cut parameters, some primary cuts on the parameters were introduced in order to reduce the parameter space to the relevant part, i.e. reducing the contribution of atmospheric muons without relevant impact on neutrino events.

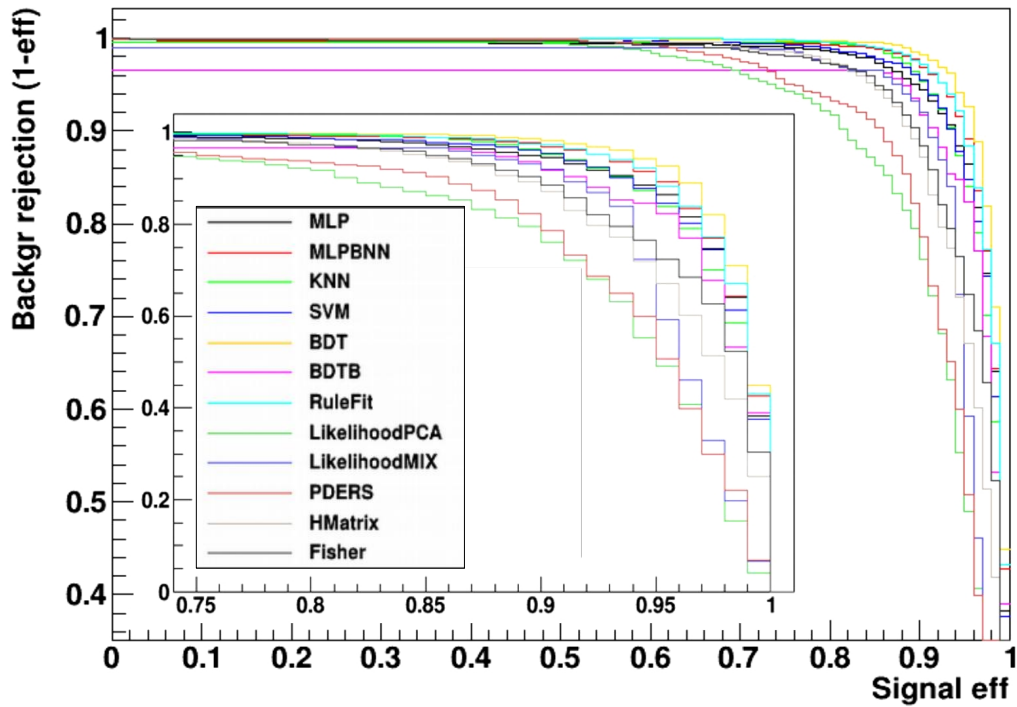


Figure 6.5: ROC curves for various methods in first test training.

This was accomplished for the following testing phase of TMVA methods by more restrictive cuts on reconstructed zenith angles.

**Precut test1**  $D_{usj} \theta > 0.2\text{rad}$

**Precut test2**  $A_{afit} \theta > 1.2\text{rad}$ ,  $Gridfit \theta > 1.2\text{rad}$ ,  $Krakefit \theta > 1.2\text{rad}$ ,  $BBFit \theta > 1.2\text{rad}$

These cuts were only used for the testing and replaced later during the optimization process for the final analysis classifiers by optimized cuts. Note that at the tools development stage also more parameters were considered than listed as final candidate parameters in Table 6.2 to evaluate the reliability of the methods independent of the more concrete input parameter choice.

### 6.3.1 Method evaluation

At the first stage, the method evaluation parameters consisted of their ROC curves and separation power using the simple optimization function  $\mathcal{S}$ .

The ROC(Receiver Operator Characteristics)-curves show the background rejection versus the signal efficiency of the classifiers. Here, curves reaching closest to (1,1) in both background rejection and signal efficiency obviously perform best. In addition to that, the simple optimization function  $\mathcal{S}$  (Eq. 5.1) is used to evaluate the discrimination power of the optimizers for various cut values in a cut value scanning, see Figure 6.5. This parameter has already been used in the evaluation of the separation power of single parameters, where a low value of  $\mathcal{S}$  here indicates a good separation of signal from background for the specific method at the selected cut, see Figure 6.6.

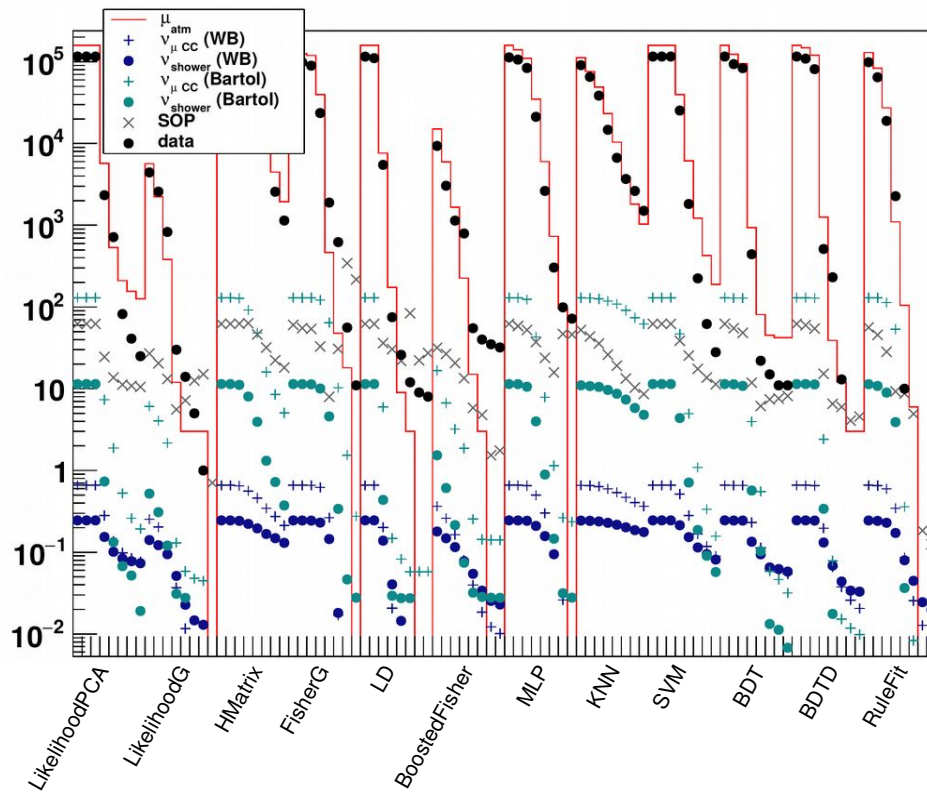


Figure 6.6:  $N_{\text{events}}$  and  $\mathcal{S}$  of various methods at different cut values.

**First method deselection** Some first conclusions were drawn from these tests. Firstly, linear discriminants did not necessarily perform worse than non-linear methods at this stage, which shows that a larger part of the input parameters performs (at least after parameter preprocessing) such that these simple and easy-to-train methods can be used further. Secondly, methods involving probability density function modelling like PDERS did not work well and would need far more consideration of the parameter space. Furthermore, multi-layer perceptrons did partially perform well, but here a lot more fine-tuning would have to be invested to show the method's full capabilities, which in such a broad scan proves disadvantageous. Last but not least the k-nearest neighbour method did not, even with this small training sample, manage to suppress all background events at the highest possible accuracy and therefore was also not considered further.

Also, a reduction of the number of input parameters to the methods was tested, which showed a better performance of the pdf modelling methods for smaller sets of input parameters (e.g. 7 parameters), while non-linear methods like boosted decision tree did not alter their behaviour much with different numbers of input parameters.

### 6.3.2 Method-based parameter selection

After a rough selection of multivariate tools suitable for this analysis, the question has to be addressed which parameters of the above selected are actually necessary and relevant within the multivariate tool. As both linear and non-linear classifiers show potential for the task, the

selection of the most suitable parameters for each method go hand in hand with the optimization of the classifier set-up themselves. As different input parameters are needed for the different classification tasks, quality parameters  $Q(y)$  will be defined according to the task of atmospheric muon suppression and atmospheric neutrino suppression in the next section. They will be used to evaluate the suitability of the classifiers and the relevance of parameters within the given parameter set. As some methods are computationally more demanding, the parameter set was specified on two quickly trainable methods. Within the group of non-linear classifiers, the BDT was chosen, while the Fisher linear discrimination could be used to evaluate the classification gain from assuming linear correlations within the parameters.

**Parameter selection procedure 1: building up the parameter space** Employing the parameter  $Q(y)$  as quality criterion of a classifier  $\mathbf{x} \mapsto y$  with classification output variable  $y$ , the following parameter selection procedure on a parameter vector  $\mathbf{x}$  of length  $n$  was introduced using the BDT classifier. In this procedure, the parameter set is build up starting with one single parameter and adding parameters, until the best performance is reached.

1. For all  $x_i$ ,  $Q(y = x_i)$  is evaluated, and the parameters ranked by  $Q(x_i) > Q(x_{i+1})$ .
2. The quality  $Q(x_0)$  of parameter  $x_0$  with best performance is set as benchmark. Each remaining parameter  $x_{i>0}$  is paired with  $x_0$  as  $\mathbf{x}_{\text{test},i} = (x_0, x_{i \neq 0})$ .
3. The TMVA method is trained on  $\mathbf{x}_{\text{test},i}$  and  $Q(y(\mathbf{x}_{\text{test},i}))$  is evaluated.
4. The parameter  $x_i$  with largest  $Q(y(\mathbf{x}_{\text{test},i}))$  is added to the parameter list  $\mathbf{x}_{\text{opt}} = (x_0, x_i)$ , if  $Q(y(\mathbf{x}_{\text{test},i})) > Q(x_0)$ .
5. The process is repeated by training the method now on  $\mathbf{x}_{\text{test}} = (x_{\text{opt}}, x_j)$  for the remaining parameters and comparing their quality, adding the best performing parameter to  $\mathbf{x}_{\text{opt}}$  and so forth.
6. The process is stopped if no increase in quality can be achieved by adding another parameter.

It has to be noted that this process is, due to computational limitation, only performed with a small subsample of runs, and BDT performance might vary slightly for successive trainings. Also, in order to avoid a bias on the initial parameter  $x_0$ , the process has to be redone starting from e.g.  $x_1$ .

**Parameter selection procedure 2: reducing the parameter space** For linear classifiers, a similar procedure was adapted as described above for the non-linear method, with the exception that, due to the bad performance of these classifiers for less than three parameters, the scanning started using the full parameters list  $\mathbf{x}$  without prior parameter ranking, and the list of parameters was successively reduced.

1. The TMVA method is trained on  $\mathbf{x}_{\text{test},i} = (x_0, \dots, x_{n-2})$  excluding each one parameter  $x_i$  in turn.
2.  $Q(y(\mathbf{x}_{\text{test},i}))$  is evaluated and the parameter  $x_i$  deselected to arrive at  $\mathbf{x}_{\text{opt}} = (x_0, \dots, x_{n-3})$  for  $x_i$  with  $Q(y(\mathbf{x}_{\text{test},i})) < Q(\mathbf{x}_{\text{test},j \neq i}) \forall j$ .
3. The process is repeated with the reduced parameter vector until the maximum quality  $Q(y(\mathbf{x}_{\text{opt}}))$  is found.

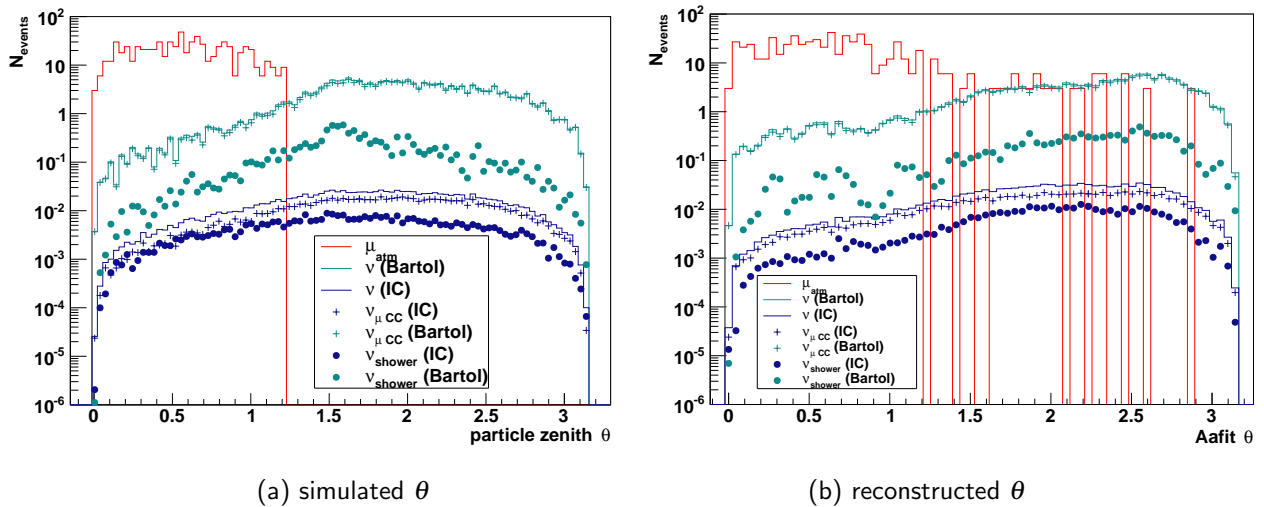


Figure 6.7: Angular distribution of events in simulation and reconstructed by Aafit before cuts for 40 runs.

## 6.4 Atmospheric muon classifier

### 6.4.1 Some heuristic considerations

Atmospheric muon suppression is, due to the design of the detector, largely achieved by accurate estimate of the arrival direction, deselecting track-like events originating from above. As can be seen in Figure 6.7, the largest problem then lies in deselecting those atmospheric muons which have falsely been reconstructed as upgoing. For these events it can be considered helpful that atmospheric muons generally arrive at the detector at energies which lie below the threshold for catastrophic energy losses, producing mostly primary Cherenkov radiation and ionization. If, at the same time, these events only pass the detector, the amount of light deposited is comparatively low, which makes them distinguishable from high-energy neutrinos.

Two signatures from atmospheric muons pose the largest problems: on the one hand muons with zenith angles close to the horizon might, if only slightly wrongly reconstructed, enter the selected event sample. On the other hand muon bundles with higher multiplicity produce muons entering the detector closely together, which can produce patterns that are not easily identifiable as single track event any more. While the first issue is targeted during the development of the classifier, the issue of high multiplicity muon events will be explored at another stage of the analysis.

It should be noted that atmospheric muons are generally not assigned a good reconstruction quality by shower reconstructions due to their different event topology. Also, track reconstructions generally reaches lower quality parameter values for muons entering the detector from above due to the downwards oriented OMs which gather less light from these events. Therefore, both track and shower reconstruction qualities serve as muon indicators.

parameter $x$	$Q(x)$ (single)	parameter $x$	$Q(x)$	discarded
Aafit $\beta$	1.83	Aafit $\beta$	1.83	Dusj VLLH
Aafit $\lambda$	1.47	+ Gridfit ratio	5.92	Dusj $\theta$
Gridfit ratio	0.69	+ Aafit $\theta$	8.66	Aafit $\lambda$
Gridfit $\theta$	0.51	+ Dusj shower $r\chi^2$	9.89	BBFit $\theta$
... Aafit $\theta$	0.17	+ Gridfit $\theta$	10.74	$E_{\text{ANN}}$
$E_{\text{R}}$	0.08	+ $E_{\text{R}}$	11.65	Dusj position $z$
... ANN $RMS(d_{\text{cher}})$	0.002	+ ANN $RMS(d_{\text{cher}})$	12.1	Krake rlogL
Dusj shower $r\chi^2$	0.0001	+ dE/dx track length	12.8	Aafit $N_{\text{hits}}$
dE/dx track length	$1.1 \times 10^{-5}$	+ Dusj $N_{\text{hits}}^*$	13.6*	

Table 6.3: Scanning results for atmospheric muon suppression. On the left, ranking of single parameters according to their bulk separation  $Q(x)$ , on the right  $Q(x)$  for the BDT output parameter (\*) after adjusting precuts.

**Optimization parameter Q** For the suppression of atmospheric muons, the aim of the parameter optimization is the general deselection of atmospheric muon events for a larger part of the feature space. At the same time, the remaining neutrino events should be selected effectively and still be distributed over a large part of the remaining feature space. The output variable of the multivariate classifier should exhibit a large bulk separation between the TMVA output parameter distribution for signal and background events. The quality parameter therefore selected to describe the separation is

$$Q(x) = \frac{|\mu(x_{\text{sig}}) - \mu(x_{\text{bkg}})|}{|RMS(x_{\text{sig}}) + RMS(x_{\text{bkg}})|}. \quad (6.6)$$

Here,  $\mu(x)$  is the mean of the parameter distribution and  $RMS(x)$  its spread calculated as root-mean-square.

#### 6.4.2 Feature extraction

**Precuts** In order to focus on the most important part of the feature space, additional cuts on the parameters specifically relevant for atmospheric muon reduction were introduced as part of the preprocessing for the input parameters of the classifier. They were also used to exclude regions of bad agreement between data and simulation. Note that, during preprocessing of the simulated events, missing angular reconstructions were assigned  $\theta_{\text{reco}} = 4$  in order not to exclude an event due to only one missing reconstruction.

**Precut 1** Dusj  $\theta_{\text{Dusj}} > 1.2$

**Precut 2** Aafit  $\theta_{\text{Aafit}} > 1.4$

**Precut 3** Gridfit  $\theta_{\text{GridFit}} > 1.4$

**Precut 4** Aafit  $\beta < 0.1$

**Precut 5** Gridfit ratio  $0 < g < 2.5$

**Precut 6** Dusj Shower identifier  $r\chi^2 < 3000$

**Scanning setup** Using  $Q(x)$ , the parameters listed in Table 6.2 for muon suppression were ranked by their bulk separation calculated from a test sample, with atmospheric muon events

considered as background and atmospheric neutrino events as signal. Subsequently, a parameter selection process was performed as described in Section 6.3.2 as procedure 1, starting from the best separating parameter and adding to the parameter set until the optimal performance was reached.<sup>10</sup>

**Scan runs** Table 6.3 shows the best result of the training after repetitive trials including tests of several precuts on input parameters like Precut 1-6. The application of parameter precuts increased the overall performance of the best result of the parameter scanning process from  $Q_{\text{nocuts}} = 9.8$  to  $Q_{\text{precuts 1-6}} = 12.8$ , clearly showing the necessity for this step.

As the analysis aims to maximise the number of both track and shower events after this muon suppression cut, the scanning was also performed using only track or only shower events as signal. Although these specialized classifiers probably focus on areas of the feature space more specific to the two event topologies (the shower selection e.g. focusing more on a vertex reconstruction, the track more on reconstruction precision), both classifiers performed worse than a classifier trained for both event types simultaneously. It can be expected that this classifier in the end also selects events that show large similarities between track and shower events, e.g. track events that show a large subshower from radiative processes which can be interpreted as shower by itself.

For cross-validation, the same scanning was also performed starting with Gridfit ratio as first scanning parameter, which selected the same parameters.

**Result** As can be seen in Table 6.3, nine parameters were selected for the BDT. These included two track zenith angle estimates, one track and one cascade reconstruction quality parameter, a track energy estimate and the number of photon hits measured in all PMTs in a cascade, one atmospheric muon suppression parameter and two geometrical parameters describing the extension of the event within the detector and the time residual distribution of the photons. Although being the result of an automated process, this selection makes sense if seen in the context of 'classical' muon suppression methods. The agreement between zenith estimates helps in the deselection of wrong directional reconstructions, the quality parameters test the agreement with a neutrino-like event, the track length puts the  $N_{\text{hits}}$  parameter into context while the two parameters measuring the time residuals of photons to the track hypothesis (which is also the case for the R energy estimate) give information on both the energy of the event and presence of (sub-)showers. GridFit ratio naturally is a atmospheric muon suppression parameter and adds to the task as such.

### 6.4.3 Method tuning and final training

**Method selection** Various methods were tested using the before selected nine input parameters. While likelihood estimators, the kNN method as well as multilayer perceptrons failed to achieve a good separation, linear discriminant estimators, RuleFit and boosted decision trees showed a better performance. As the performance of these three methods reached roughly the same level, BDTs were chosen as method for further fine-tuning, as linear discriminants do not

<sup>10</sup>The classifier used for this testing was a standard BDT without parameter preprocessing and 600 trees with a depth of 3.

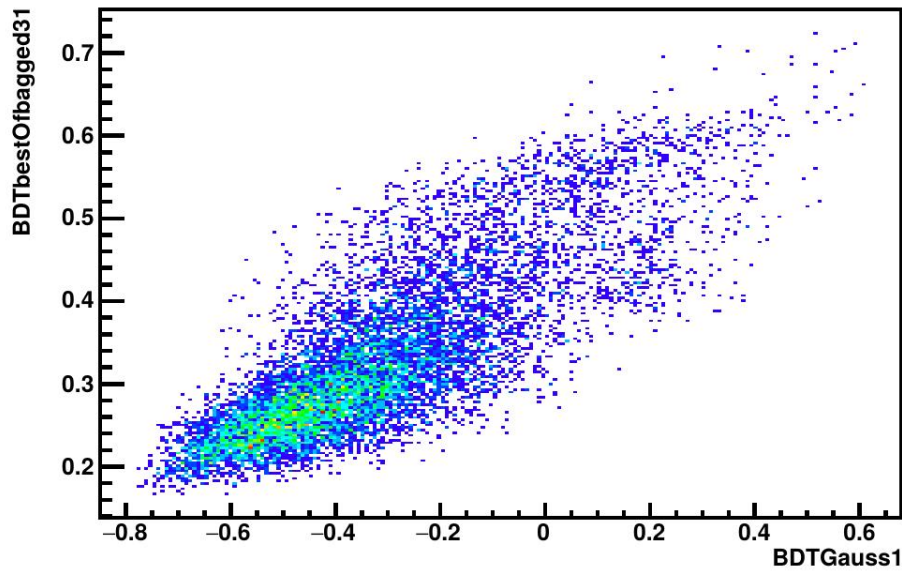


Figure 6.8: Correlation between two different BDT setups for muon events from the test sample.

offer many optimization options except for preprocessing and boosting and the optimization of RuleFit proved difficult.

**BDT tuning** The design of a BDT can be changed by using different tree structures, node setup and minimizers, which were tested and optimized in repetitive trainings and which are given in detail in Appendix A.5.2. Here, apart from the separation  $Q(x)$  also the signal efficiency  $\epsilon_{0.02\%}$  at a muon suppression of  $2 \times 10^{-4}$  is considered, as not only bulk separation, but also signal efficiency at nearly no background is needed. The testing lead to the following conclusions:

**preprocessing** Both PCA and Gaussian decoupling as parameter preprocessing increase the signal efficiency, a combination of both does not further increase performance, therefore a Gaussian decoupling is used.

**separation type** The separation function used in the tree nodes shows no impact on BDT performance.

**boost type** Bagging improves separation and is used. AdaBoost, an adaptive boost algorithm emphasizing misclassified events in repetitive trainings was used, employing a higher learning rate with larger number of grid points (50) in parameter range performs best.

**tree depth and number** An increase in tree depth and number of trees increases separation due to the increased accuracy of training adaption and is fixed to  $N_{\text{tree}} = 1200$  with a depth of 7 each after repetitive trials.

Note that generally the signal efficiency of the various set-ups did not vary significantly, however, bulk separation is largest for these BDT choices. As the method performing best on its own for atmospheric muon suppression does not necessarily have to be the best choice when used in combination with a cosmic neutrino selector, various BDTs using similarly successful set-ups were trained for later comparison.

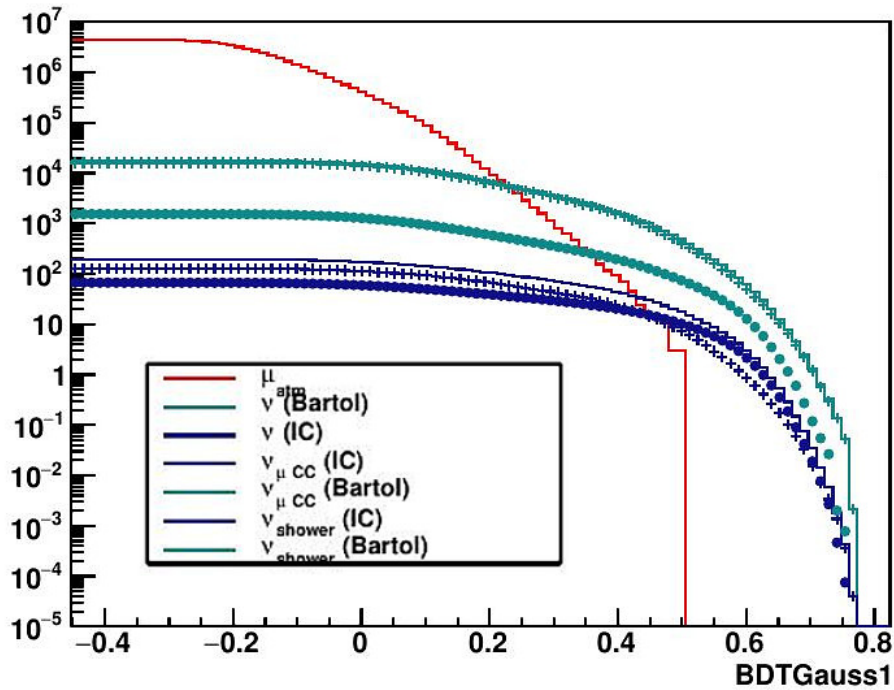


Figure 6.9: Output parameter of BDTGauss1 method on 1490d lifetime.

**Final training** The various versions of the BDTs were trained on a set of randomly selected runs from the run-by-run production v2.x.1 with roughly 40 days of lifetime, after application of the aforementioned precuts. Atmospheric muons produced using MUPAGE [41] were used as background, while the signal was formed by GenHen [36] events including all event types from  $\nu_e$  and  $\nu_\mu$ , which were weighted according to the Bartol atmospheric neutrino flux [29]. An exemplary output of the muon suppression BDTs can be seen in Figure 6.8.

**Performance** The resulting muon suppression (Figure 6.9) outperforms all single parameter cuts which could be applied to the sample, of which the most effective in this context was GridFit ratio. For GridFit, no parameter cut can be found which completely reduces atmospheric muons, which is the case for the BDT\_1 methods.

The BDT set-ups selected for the final training naturally lead to roughly similar classification, as can be seen in Figure 6.8, but also certain differences are apparent. It shows that muons reconstructed with high signal likeness i.e. high BRT output value, seem to be interpreted differently in the various BDTs, which emphasizes the necessity to try various versions of the atmospheric muon suppression methods in combination with the cosmic neutrino selector.

The BDTs favours neither the shower or track topologies when deselecting atmospheric muons below the level of the atmospheric neutrino component. It should be noted however that in the region of high event energies where the cosmic neutrino signal will be dominant in the analysis, high-energy shower neutrino events are starting to dominate against the muon events, see Figure 6.9.

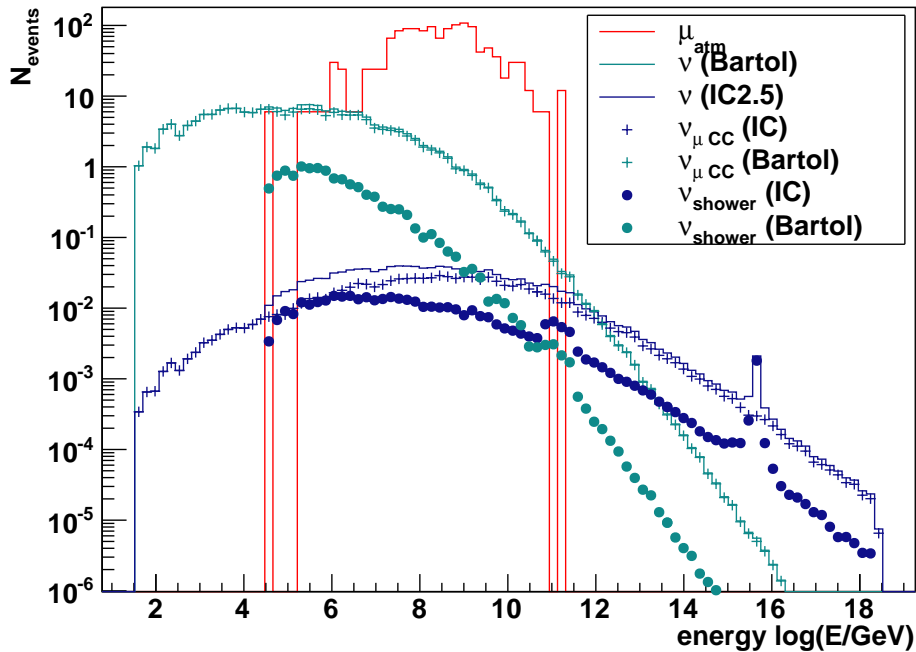


Figure 6.10: Simulated event energy and number of hits from the Aafit selection as exemplary energy estimate.

## 6.5 Atmospheric neutrino classifier

### 6.5.1 Again heuristic considerations

Atmospheric neutrino suppression can only be achieved by estimating the respective event energy, as particle energy is the main characteristic distinguishing neutrinos of atmospheric origin from those of cosmic origin (see Figure 6.10). As various sophisticated energy estimators were developed within *ANTARES* for the different event types, this estimator should draw on the capacity of these established methods. Nonetheless it is not limited to these methods, and can include further energy- and event type related parameters to serve as generalized cosmic neutrino classifier.

Energy-related parameters must draw on the particle energy deposited in the detector from neutrino interactions, which is seen as additional light yield originating from photons from either the Cherenkov emission from secondary particles at the interaction vertex or as radiation from energy loss processes along the muon track. Additionally topological parameters describing extension of the event and direction, and parameters evaluating its compatibility with track and shower hypothesis could prove useful to put the light yield into perspective with regard to the event topology.

**Optimization parameter Q** The task of signal extraction demands a high purity in the final event sample. As experience with former analyses shows that the model rejection or discovery procedure leads to event samples with a few remaining background events over which the

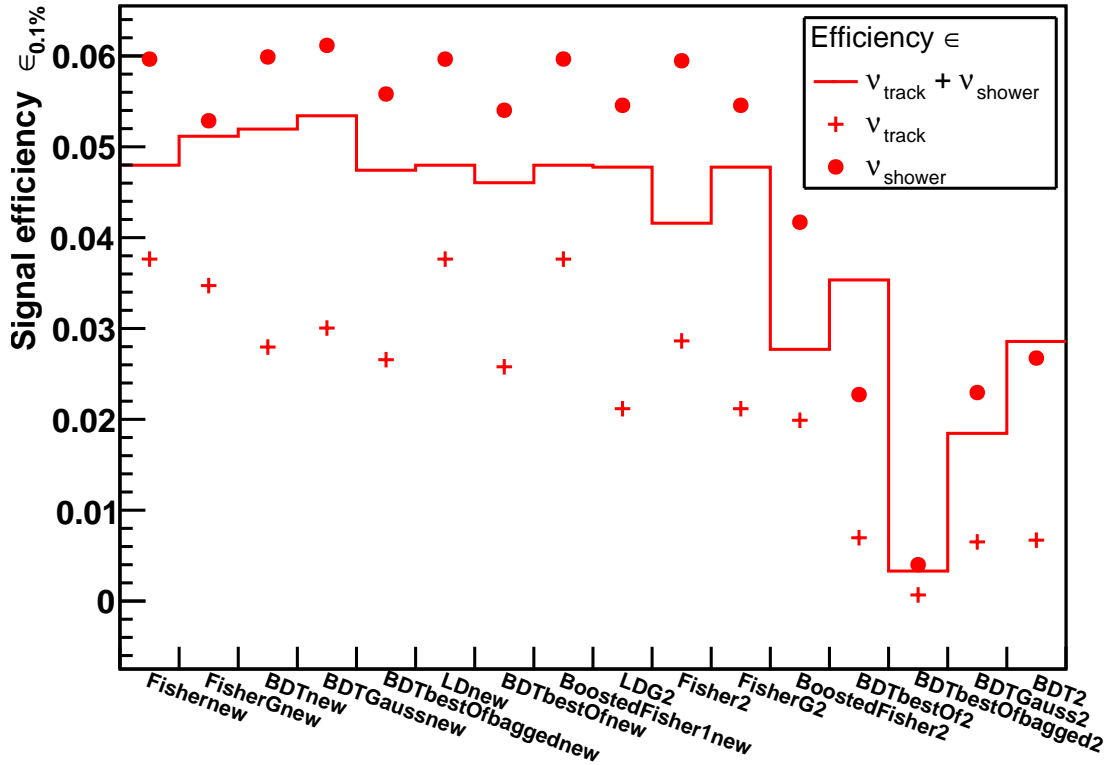


Figure 6.11: Signal efficiency  $\varepsilon_{0.1\%}$  comparison of final TMVA methods for atmospheric neutrino suppression; methods trained including additional parameter cuts as listed in Table 6.4 are labelled 'new' or 'alt'.

contribution of cosmic events is evaluated, the signal efficiency  $\varepsilon$  is introduced as optimization parameter  $Q$  in the tools development cycle. For a given parameter  $x$ , the signal efficiency is defined as the fraction of signal events which fulfil the condition to be selected by a cut  $x_{\text{cut,pbkg}}$  over the total number of signal events  $N_{\text{sig}}$ . The cut value  $x_{\text{cut,pbkg}}$  is defined by the parameter value for which a fraction of the background events  $p_{\text{bkg}}$  are selected.

$$\varepsilon_{p_{\text{bkg}}}(x) = \frac{N(x_{i,\text{sig}} > x_{\text{cut,pbkg}})}{N_{\text{sig}}}. \quad (6.7)$$

The background is chosen such that a handful of atmospheric events would remain with  $p_{\text{bkg}} = 0.001$ , as this corresponds roughly to the area of the cut value for the given sample. The quality criterion is therefore set as  $Q = \varepsilon_{0.001}$ . The use of this quality criterion reflects the difference of the task of cosmic neutrino selection to the previous development of an atmospheric muon classifier, where a rough overall separation of the signal and background distributions was called for. Here, the enhancement of the signal contribution in the tail of the event distribution is the goal of the following multivariate tool development.

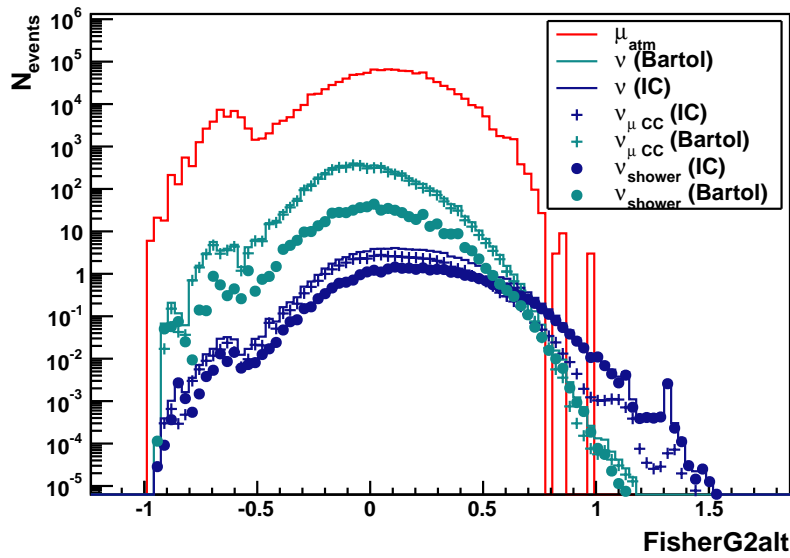


Figure 6.12: Fisher discriminant output for 1490 days lifetime.

### 6.5.2 Feature extraction

**Preprocessing** To enhance the parameter space for energy estimation, various input parameters of the ANN energy estimator [56] are added, applied on hit selections from the Dusj and Aafit reconstruction. These are the following:

- P1** the number of triggered hits
- P2** the number of all hits within a time window of  $[-20, +300]$  ns around the triggered hits
- P6** the number of storey layers with hits of the Dusj hit selection
- P7** the number of strings with hits of the Dusj hit selection
- P15** time difference between first and last hit of Dusj hit selection
- P19** fraction of Dusj hits arriving with time residual from shower assumption within  $[-10, +250]$  ns
- P21** the average amplitude of Aafit selected hits arriving with time residuals from the reconstructed track within  $[-10, +40]$  ns, measuring the amplitude of direct hits.

In order to ensure easier interpretation of the relevant input parameters, the below listed cuts and transformations were applied on the training sample after testing their effect on a BDT performance. Setting energy-related parameters to logarithmic scale enhances the onset of energy loss processes at higher energies, facilitating a better training of the classifier on these relevant features. Last but not least, the additional cuts mainly exclude regions in the feature space with non-relevant neutrino contribution and help to easily purify the sample.

**Replacing missing parameter values** for failed reconstructions:  $\theta_{\text{Dusj}} = 2$ ,  $\text{VLLH} = 11$ ,  $\lambda = -6$ ,  $P6 = 4$

**logarithmic**  $x' = \log(x)$ : P1, P2, P21, VLLH,  $E_{\text{ANN}}$ ,  $E_{\text{Dusj}}$ ,  $E_{\text{dEdx}}$

**additional cuts**  $\theta_{\text{BFFit}} > 1.4$ ,  $\lambda > -8$ ,  $\text{VLLH} < 30$

**Scanning procedure** First training of multivariate tools on the parameters in Table 6.2, here called  $\mathbf{x}_1$ , showed a strong emphasis on the selection of shower events. In order to increase

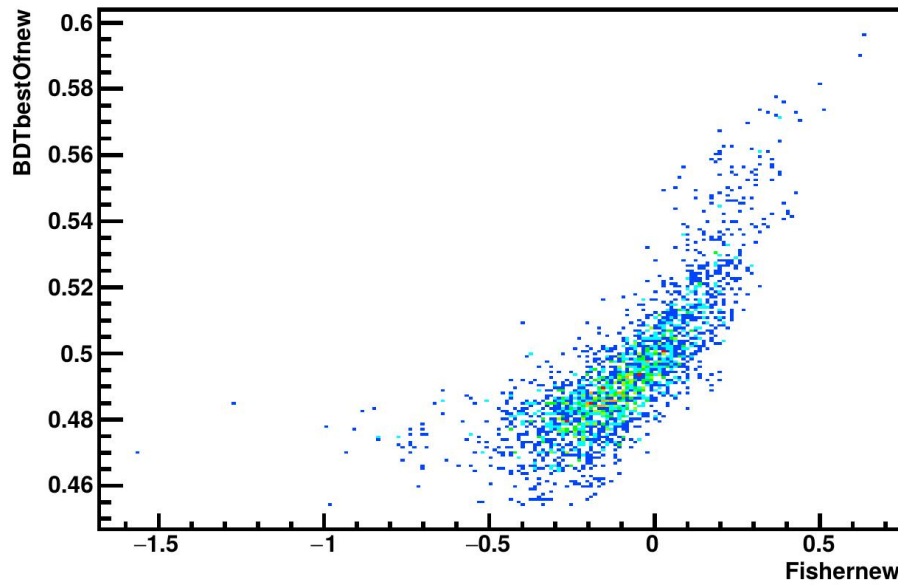


Figure 6.13: Correlation of two well-performing Fisher discriminants.

the chance of well separated track-like events,  $\mathbf{x}_1$  were combined with additional parameters showing a high signal efficiency for track-like events  $\mathbf{x}_{t+}$  introduced in the previous paragraph. The scanning process was repeated for the extended set  $\mathbf{x}_{\text{ext}} = (\mathbf{x}_1, \mathbf{x}_{t+})$ , which resulted in a better overall performance of the final parameter set. As a separation of track- and shower-like event signatures could also be considered at this stage, the parameter selection was repeated separately including only parameters related to a track event hypothesis  $\mathbf{x}_{\text{ext,track}}$ , and those related to shower reconstruction  $\mathbf{x}_{\text{ext,shower}}$ , and the combined signal efficiency calculated for events classified as signal by either or both of the classifiers. However, this procedure resulted in a lower signal efficiency compared to the training on a final selection form a combined parameter set  $\mathbf{x}_{\text{ext}}$ . For the final parameter set, scanning procedure 2 from Section 6.3.2 was used in a first scanning including only  $\mathbf{x}_1$ , resulting in a parameters set which was joined by those parameters which remained after scanning procedure 2 on the extended parameter set  $\mathbf{x}_{\text{ext}}$ , ensuring that a robust overall classifier on  $\mathbf{x}_1$  was further enhanced by those additional parameters which increase the performance from the extended set  $\mathbf{x}_{\text{ext}}$ .

**Result** The resulting parameter set of 10 input parameters, see Table 6.4, again reflects well the task at hand. Not only are three different energy estimators,  $E_{\text{ANN}}$ ,  $E_{\text{Dusj}}$  and  $E_{\text{dEdx}}$  selected, but also three parameters related to the amount of light detected, namely P1, P2 and P21 as introduced above, which are part of the  $x_{t+}$  parameters. In addition to that, the Dusj zenith angle estimate  $\theta_{\text{Dusj}}$  contributes directional information, while the number of storeys P6 add information about the extension of the event inside the detection volume. Finally, as was the case in the atmospheric muon suppression parameters, two reconstruction quality parameters are added, with Aafit  $\lambda$  expressing the track-likeness of the event, and Dusj VLLH its agreement with a shower hypothesis.

### 6.5.3 Method tuning and performance

First training with a wide range of different classifiers showed that, in addition to BDTs, likelihood methods performed well for this task, which lead to further tests of the input parameter preprocessing with these likelihood methods. However, after parameter preprocessing and scanning, discriminant methods like the Fisher discriminant or H-matrix outperformed the likelihood methods. Both BDTs and Fisher discriminants were therefore selected as main methods and tested with different set-ups, which already have been described for the BDT for atmospheric muon suppression.

**Fisher discriminant optimization** In the case of linear discriminants, the possibility of method optimisation is much more limited. The different parameter preprocessing options were tried, as well as changing the probability density function modelling by using different spline function options. Finally, a varying number of Fisher discriminants was boosted. In order to compare the effects of the above introduced parameter transformations on the classifier performance, the methods were trained both without and including the these transformations.

As linear discrimination is only one of the simplest cases of functional discriminant analysis, several other functions were tested to replace the linear function inherent to the Fisher discriminant. However, the application of higher order functions proved to be difficult and no discriminator was found that outperformed the simple Fisher discriminant.

**Tool performance** As with the atmospheric muon discriminator, all selected methods were trained on simulated events equivalent to about 40 days data taking. One example of correlation between the trained methods can be found in Figure 6.13. It should be noted that the atmospheric neutrino classifier can serve to an extent for atmospheric muon suppression, as atmospheric muons also possess generally lower energies, which gives a good starting point for the combination of both classifiers in the following section.

An overview over all parameters, processing steps and trained methods can be seen in Table 6.4.

	<b>atmospheric muon suppression</b>	<b>cosmic neutrino selection</b>
input parameters	Aafit $\beta$ Aafit $\theta$ Gridfit muon estimate $g$ Dusj Shower identifier $r\chi^2$ Gridfit $\theta$ R energy estimate $E_R$ dE/dx track length estimate $l_{dEdx}$ Dusj number of selected hit $N_{hits,Dusj}$ ANN $RMS(d_{Cherenkov})$	Dusj energy estimate $E_{Dusj}$ Dusj $\theta$ ANN energy estimate $E_{ANN}$ Aafit $\lambda$ Dusj shower $r\chi^2$ Aafit $N_{hits}$ all event hits $N_{hits}$ all event hits $\langle A \rangle_{tcher < 40ns}$ dE/dx energy estimate $E_{dEdx}$ Dusj number of storeys $N_{storey}$
transformations	Aafit $\theta$ if nan, $\theta := 4$ GridFit $\theta$ if nan, $\theta := 4$ all parameters if nan, $x := -1$ all energies if nan, $E := 100$ $E'_x = \log(E_x / \text{GeV})$	Dusj VLLH if nan, $VLLH := 11$ $VLLH' = \log(VLLH)$ Aafit $N'_{hits} = \log(N_{hits})$ Aafit $\lambda$ if nan, $\lambda := -6.0$ Dusj $\theta$ if nan, $\theta := 2$ all event hits $N'_{hits} = \log(N_{hits})$ all hits $\langle A \rangle'_{tc < 40ns} = \log(\langle A \rangle_{tc < 40ns})$ $E'_{Dusj} = \log(E_{Dusj})$
parameter cuts	Dusj $\theta > 1.2$ Aafit $\theta > 1.4$ Gridfit $\theta > 1.4$ Aafit $\beta < 0.1$ Gridfit muon estimate $0 < g < 2.5$ Dusj Shower identifier $r\chi^2 < 3000$	BBFit $\theta > 1.4$ Aafit $\lambda > -8$
TMVA methods	BDT BDTGauss BDTbestOf BDTbestOfbagged BDTbestOfbaggedCross BDTbestOfbagged3	Fisher FisherG BDT BDTGauss BDTbestOfbagged BDTbestOf boosted Fisher discriminant

Table 6.4: Input parameters, parameters transformations and TMVA classifiers for atmospheric muon suppression and cosmic neutrino selection



**Part III**

**Analysis**



## 7 | Event selection and simulation additions

Data taking and simulation for *ANTARES* have already been introduced in Chapter 2 and Chapter 3, respectively. Now, for the task of searching for a diffuse flux of cosmic neutrinos, this data needs to be filtered such that known variations in detector conditions are manageable and accounted for when applying the event selection for the diffuse search. In order to assure agreement between simulation and measurement, on the one hand, data quality evaluation and selection are necessary, while on the other hand the standard simulation has to be extended to include all event types and those contributions which, at that point, are not included in the standard simulation.

To meet the first concern, a data quality assessment on top of the standard quality parameters in *ANTARES* was introduced in order to include considerations in the quality assessment based on the parameter space relevant for the multivariate tools. For the second part, a  $\nu_\tau$  simulation and estimate was added, high multiplicity muon bundles simulated, the atmospheric muon contribution modelled and a prompt neutrino flux added.

Depending on the availability of measurements and their respective simulation, *ANTARES* data from the years 2007-2013<sup>11</sup> is considered in this analysis. It should be noted that for 2013 a version upgrade took place in the simulation, leading to a heterogeneous mixture of run simulations for the complete period.

### 7.1 Data selection

The run selection had to address the fact that firstly not all available data runs were suitable for analysis, depending on detector conditions or possible technical problems, and secondly that for those runs not necessarily a full run simulation was available. Starting from the full number of runs available in the data base and deselecting only those which were acoustic or bio-camera runs, the remaining runs were assigned analysis-specific quality estimates in addition to the not always available classical *ANTARES* data quality flags and selection categorizations. In contrast to the standard run quality classification in *ANTARES*, which relies on detector conditions like bioluminescence indicators and OM availability, the quality indicators here are based specifically on the distribution of the relevant observables for the analysis in the simulation. This assumes that even runs which showed difficult detector conditions can still be well included in the analysis if the relevant parameters are well enough represented in the simulation.

---

<sup>11</sup>runs 25656 - 74348

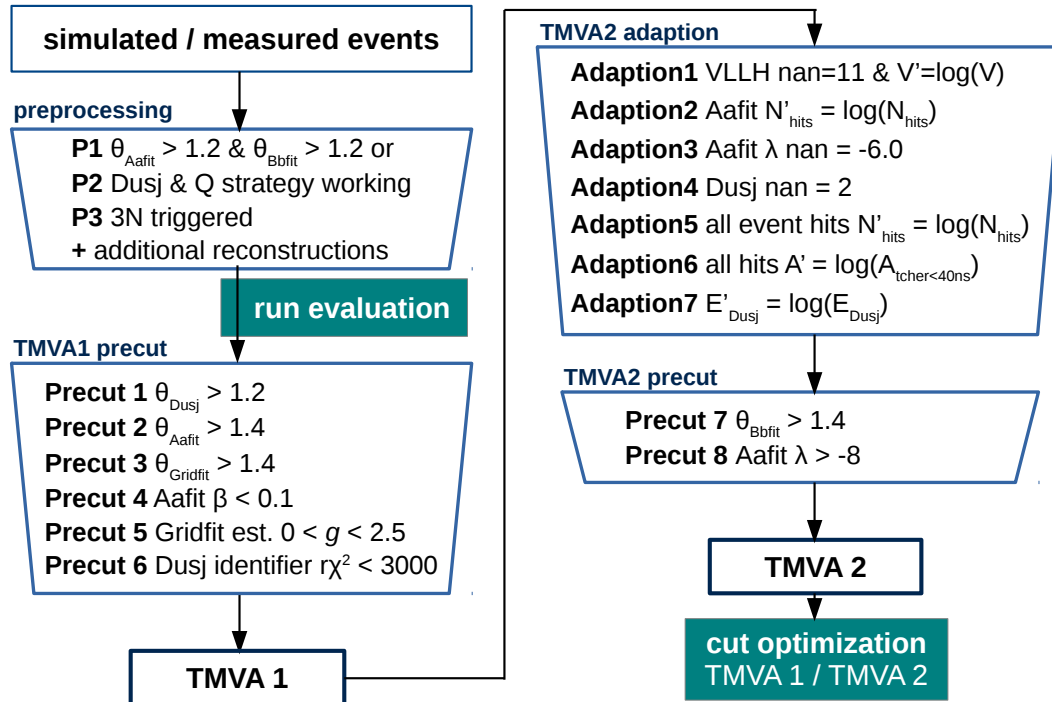


Figure 7.1: Schematic overview over the event selection, parameter transformation and multivariate tool application.

### 7.1.1 Preselection from the full data sample

In order to reduce both data and simulated events to a manageable amount, those events were discarded at a first processing of the fully reconstructed runs which were unlikely to enter the analysis. As only well reconstructed upgoing neutrino events are looked for, only those are selected which are either reconstructed as upgoing by the two track reconstruction methods Aafit and BbFit, or which are reconstructed by both cascade reconstruction methods. Due to the larger neutrino direction uncertainty of the cascade reconstruction, no angular criterion is applied for reconstructed showers. So, in the following procedure only events are considered for which

- P1** either  $\theta_{\text{Aafit}} > 1.2$  and  $\theta_{\text{BbFit}} > 1.2$
- P2** or Dusj and Q strategy are successful.

As well-reconstructable high-energy events should be easily recognised also by a strict triggering algorithm, the events considered for the analysis was restricted to

- P3** only 3N triggered events,

a trigger which is described in more detail in Section 2.3.3. After this event selection, the additional reconstructions needed for the expansion of the parameter space for the multivariate tools as introduced in Section 4 is applied to the event samples before entering the run quality evaluation.

### 7.1.2 Data quality assessment

The following quality assessment builds on both standard *ANTARES* run quality parameters, and the introduction of the data-Monte Carlo ratio and  $A^2$  parameter as additional analysis-specific parameters.

**Standard parameters** At the core of the standard run quality assessment, described in [65], lies the introduction of a data quality flag, the quality basic  $Q_{\text{basic}}$ , which assumes a value between minimum 1 and best 4 according to the environmental conditions measured by the baseline and burst fraction for the given run, which are determined from a Gaussian fit to the distribution of rates for all OMs as median and fraction above a given threshold. This parameter is also dependent on the number of active OMs in the detector  $N_{\text{OM}}$ , which naturally decreases as the detector ages. Also, an estimate for the bioluminescence activity in the detector can be assumed to be relevant for the data quality. Here, the mean rate  $F_{\text{hits}}$  of hits averaged over all active OMs in the detector is used.

**Data-simulation ratio**  $N_{\text{data/MC}}$  As the Monte Carlo simulation is done on a run-by-run basis, a first criterion for the accuracy of the simulation is given by the ratio between the number of data events and the number of simulated events  $N_{\text{data/MC}} = N_{\text{evts,measured}}/N_{\text{evts,simulated}}$  after the three preprocessing cuts **P1-P3**<sup>12</sup>. Keeping in mind that this can only provide information about the good representation of atmospheric muons due to the small number of neutrinos in a single run sample, the restriction to  $3N$  triggered events ensures a relatively stable performance of this parameter.

**Standardized parameter histograms** In order to evaluate the agreement of observable behaviour in data and simulation for each run, several quality parameters based on the binned data were introduced. The quality parameter follows the idea of bin-per-bin comparison of two histograms introduced in Equation 6.5. As this selection criterion should reach roughly the same sensitivity to discrepancies between measurement and simulation, but shape and distribution of the observables varied largely, the binning of the individual histograms was adjusted using the spread  $\xi(x)$  of the observable histogram for standardization.

The spread  $\xi$  and mean  $m$  of the distribution of observable  $x$  is evaluated from the number of bins  $N_{\text{bins}}$ , with bins  $i$  holding a number of entries  $x_i$  such that

$$m(x) = \frac{\sum_{N_{\text{bins}}} ix_i}{\sum_{N_{\text{bins}}} x_i} \quad (7.1)$$

$$\xi(x) = \sqrt{\frac{\sum_{N_{\text{bins}}} (i - m(x))^2 x_i}{\sum_{N_{\text{bins}}} x_i}}. \quad (7.2)$$

The binning and range of the relevant parameters in the histograms was then adjusted thus that a comparable spread of the distribution was achieved for all observables.

<sup>12</sup>This parameter was corrected for runs from the 5-line period for the "trigger bug" in the measurements for this time period.

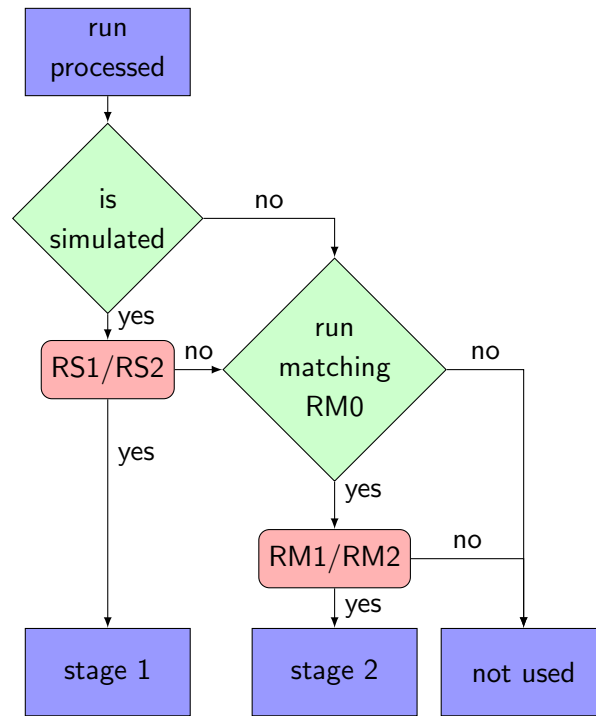


Figure 7.2: Data processing schematic

	not used	stage 1	stage 2a	stage 2b
measurement	1163 (113.2 d)	8676 (913.5 d)	5267 (557.9 d)	1388 (286.1 d)
genhen $v_{\mu CC}$ v2	770 (74.1 d)	8676 (913.5 d)	4232 (451.5 d)	597 (69.7 d)
genhen $v_{e, \mu NC}$	689 (66.0 d)	8676 (913.5 d)	3641 (384.0 d)	526 (61.6 d)
mupage v2	717 (68.7 d)	8676 (913.5 d)	3659 (385.8 d)	534 (62.0 d)
mupage v3	475 (64.7 d)	4556 (473.9 d)	2465 (270.0 d)	840 (212.8 d)
$N_{3Ntriggered}$	$6.9 \times 10^7$	$2.7 \times 10^8$	$1.5 \times 10^8$	$1.0 \times 10^8$

Table 7.1: Number of runs and lifetime for measurements and simulation sets selected by the run matching process for simulation of run-by-run simulation version 2 (v2) and 3 (v3).

**Area difference** In order to evaluate the agreement of the one-dimensional distribution of each input parameter between data and simulation, the histogram comparison estimate  $A^2(x_{data}, x_{MC})$  (Equation 6.5) introduced already for the investigation of parameter performance stability in the previous chapter is applied here as well.

Here, some parameters proved to be more sensitive to detector alterations than others, with all parameters showing a generally good agreement. At this level, some discrepancies were found especially for the  $dE/dx$  energy estimate, but were considered to have a minor impact on the overall agreement of the final classifiers. For all other observables, a good agreement was found for the majority of runs, which lead to the discarding of a given run only if  $A^2$  deviated from the average any of the remaining observables by a given percentage.

### 7.1.3 Primary selection: data and simulation agreement

These quality parameters were now used in the run matching procedure, see Figure 7.2. Starting from all runs of which processed data is available, at first all those runs should be used for which both data and simulation exist and are well in agreement. Agreement is here defined by

$$\mathbf{RS1} \quad a \quad 0.75 < N_{\text{data}/\text{MC}} < 1.25$$

$$\mathbf{RS2} \quad \text{For all relevant parameters, } A^2(x_{\text{data}}, x_{\text{MC}}) < 0.2.$$

The relevant parameters here include those that enter the analysis by serving as input parameters to the later discussed multivariate tools or which are used during the processing steps. If these run selection criteria **RS** are met, the according run in data and simulation is selected as *stage 1* run. As runs without simulation from run-by-run version 2 are not considered, stage 1 runs contain no runs from 2013.

### 7.1.4 Secondary selection: run matching

If a data run is not selected, the rest of available simulations is used as a database to find a matching simulation run. A run counts as similar if its number of active OMs  $\bar{N}_{\text{OM}}$  and optical mean rate  $\bar{F}_{\text{hits}}$  averaged over the whole run are similar within a given margin. The number of events in the mupage sample of the matched simulated run with duration  $d'_{\text{MC}}$  is then scaled to the duration  $d_{\text{data}}$  of the search run by  $d_{\text{scale}} = d_{\text{data}}/d'_{\text{MC}}$ . The scaled simulation is then compared to the data run by the same criteria as the original run simulation would have been. For the run matching procedure, the run matching criteria **RM** therefore are

$$\mathbf{RM0} \quad |\bar{N}_{\text{OM}} - \bar{N}'_{\text{OM}}| < 85 \quad \text{and} \quad |\bar{F}_{\text{hits}} - \bar{F}'_{\text{hits}}| < 30 \text{kHz}$$

$$\mathbf{RM1} \quad 0.75 < N_{\text{data}}/(N'_{\text{MC}}d_{\text{scale}}) < 1.25 \quad (\text{like RS1})$$

$$\mathbf{RM2} \quad \text{For all relevant parameters, } A^2(x_{\text{data}}, x'_{\text{MC}}) < 0.2$$

If the criteria are fulfilled, the data run is added to the selected sample, while at the same time the weight of events in the comparison Monte Carlo run is scaled to add the additional lifetime of the matched data run. These additional runs are considered as *stage 2* selected runs.

In order to reduce computing time, this matching process was first performed between runs within a data taking interval of several month, i.e. within 500 neighbouring runs (*stage 2a*). Only then, the remaining unmatched runs from these subgroups were compared to simulation with a larger time distance to the original data taking run, i.e. 2500 runs (*stage 2b*). This second matching included all runs from 2013, as no simulation from 2013 was available, see Figure 7.3. On the other hand, no *stage 2b* could be assigned for the early data taking period with 5 active lines, as criterion **RM0** could not be fulfilled for runs involving a different number of detection lines.

The number of runs and their according lifetime selected at the two stages, with the two different time windows for matching in *stage 2* denoted as *2a* and *2b*, can be seen in Table 7.1.

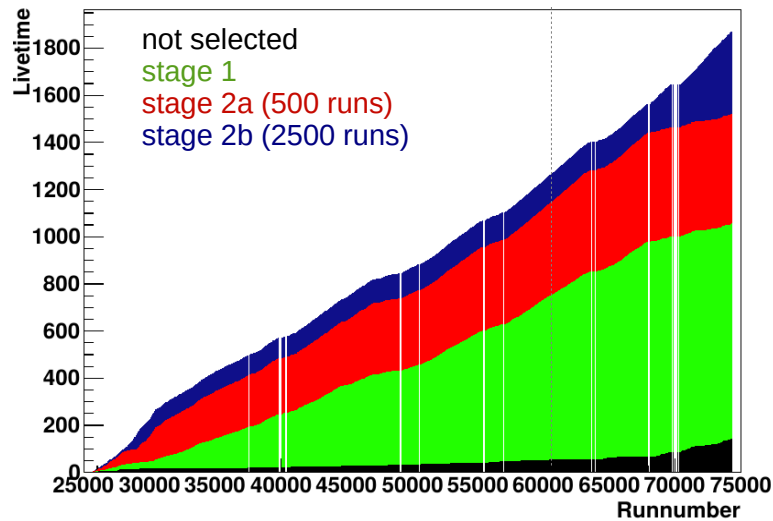


Figure 7.3: Accumulated data taking livetime in days over runnumber.

## 7.2 Simulation extensions and adaptations

In the standard simulation, some event contributions are either under-represented or missing, as the full simulation would either be too computationally extensive or has not yet been implemented. These unavoidable deficits are addressed in the following part before entering a full parameter cut optimization procedure for the complete analysis chain in the next chapter.

Firstly, the event contribution from  $\nu_\tau$ -induced events has only been implemented during the finishing stages of the analysis and was therefore not available in the regular simulation. As an estimate for the  $\nu_\tau$  contribution was already introduced in [16], two approximations of it are available and used here, namely the earlier estimate from  $\nu_e$  and  $\nu_\mu$  simulations and the extrapolation from a small  $\nu_\tau$  simulation.

Secondly, two limitations of the atmospheric muon simulation have to be overcome. Here, the equivalent lifetime of the atmospheric muon simulation covers only 1/3 of the data taking, which makes an interpolation of the atmospheric muon number in the area of low statistics for the classifier distribution necessary. In addition to that, quite rare muon bundles from the same atmospheric shower producing more than 200 atmospheric muons are not simulated in the standard production and have to be added from a specialized mupage simulation.

Last but not least, although measurements from *IceCube* point towards a comparatively low flux of prompt neutrino events, the contribution from prompt atmospheric neutrinos as introduced in Section 2.3.1 is added as conservative estimate.

### 7.2.1 $\tau$ neutrinos

The two estimates available for the number of  $\nu_\tau$  events both lack the precision of the full simulation, on the one hand due to the rough estimates of used for the extrapolation from  $\nu_e$  and  $\nu_\mu$  simulation, on the other hand due to lack of some interaction processes and a partially faulty implementation of  $\nu_\tau$  interactions in *genhen*. Therefore, the difference between the outcome of the two methods is introduced as estimate of the error on the  $\nu_\tau$  contribution, while

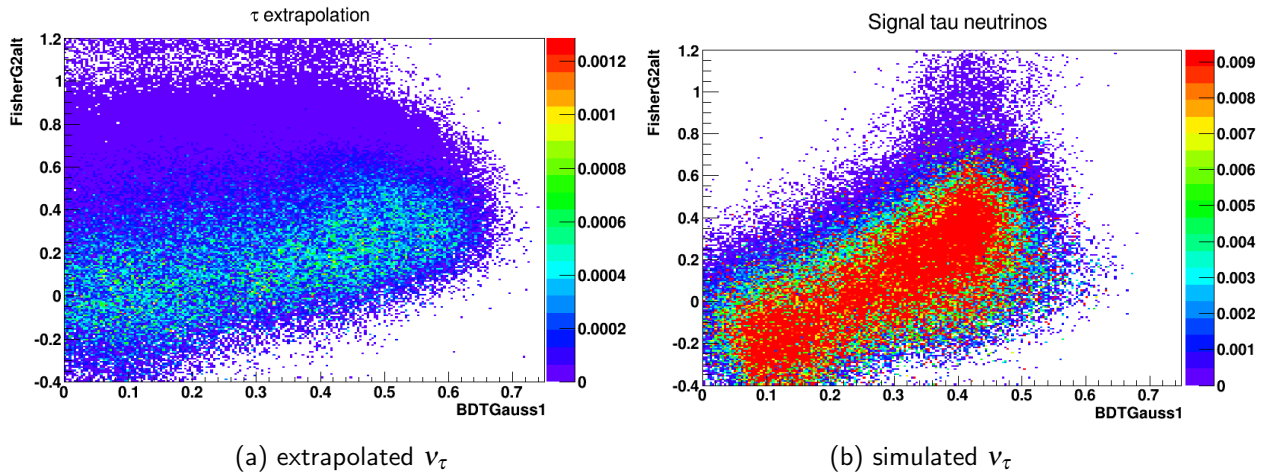


Figure 7.4: Distribution of cosmic tau neutrinos  $\nu_\tau$  for two classifiers, either as extrapolated from  $\nu_e$  and  $\nu_\mu$  or as simulated by a toy simulation. Due to an error in the weighting of events in the simulation, the total number of events per bin is overestimated.

choosing the interpolation as estimate basis due to its smoother distribution at low statistics. A comparison of the distribution of events for two classifier parameters can be seen in Figure 7.4.

**Extrapolation of  $\nu_\tau$  estimate from  $\nu_e$  and  $\nu_\mu$  simulation** Before any  $\nu_\tau$  simulation became available in ANTARES, the estimation of this event class from the existing neutrino simulation had been used in the prior shower analysis [16]. While the estimation procedure there showed a high degree of sophistication, a simplified version of this method will be implemented here, as the results can be checked against the small simulation sample.

**Cosmic  $\nu_\tau$  events** As the ratio between the different neutrino flavours of the cosmic flux is  $\nu_e : \nu_\mu : \nu_\tau = 1 : 1 : 1$  due to neutrino mixing, the cosmic  $\nu_\tau$  contribution from neutral-channel (NC) events can be approximated as average of the  $\nu_e$  and  $\nu_\mu$  channel,

$$N_{\nu_\tau \text{ NC}} = (N_{\nu_e \text{ NC}} + N_{\nu_\mu \text{ NC}})/2. \quad (7.3)$$

The same is generally true for the charged-current (CC) channel. However, the Glashow resonance leading to an excess in the  $\bar{\nu}_e$ -channel by a branching ratio  $\eta_{\text{Glashow}}$  has to be taken into account. Furthermore, the  $\tau$  lepton can decay both producing only a shower, or an additional muon in the reaction  $\tau^- \rightarrow \mu^- + \bar{\nu}_\mu + \nu_\tau$ . This occurs at a branching ratio of 17.4%, with showers making up  $\eta_{\tau, \text{shower}} = 82.6\%$  of the events. Therefore, shower events from  $\nu_\tau$  CC-interaction occur approximately with

$$N_{\bar{\nu}_e \text{ CC}} = N_{\bar{\nu}_e \text{ CC}}(1 - \eta_{\text{Glashow}})\eta_{\tau, \text{shower}} \quad \text{and} \quad N_{\nu_\tau \text{ CC}} = N_{\nu_e \text{ CC}}\eta_{\tau, \text{shower}}. \quad (7.4)$$

Depending on its energy, the tau's lifetime allows it to travel only a few meters before the second interaction. These events resemble neither a shower nor an extended track, which makes it more challenging to add these events here. However, as a preliminary  $\nu_\tau$  simulation was available for the analysis allowing to study these events, no further estimate for these decay channels is added here. Also, the deficit in energy transferred to the shower in case of  $\nu_\tau$  production is considered negligible for this estimation.

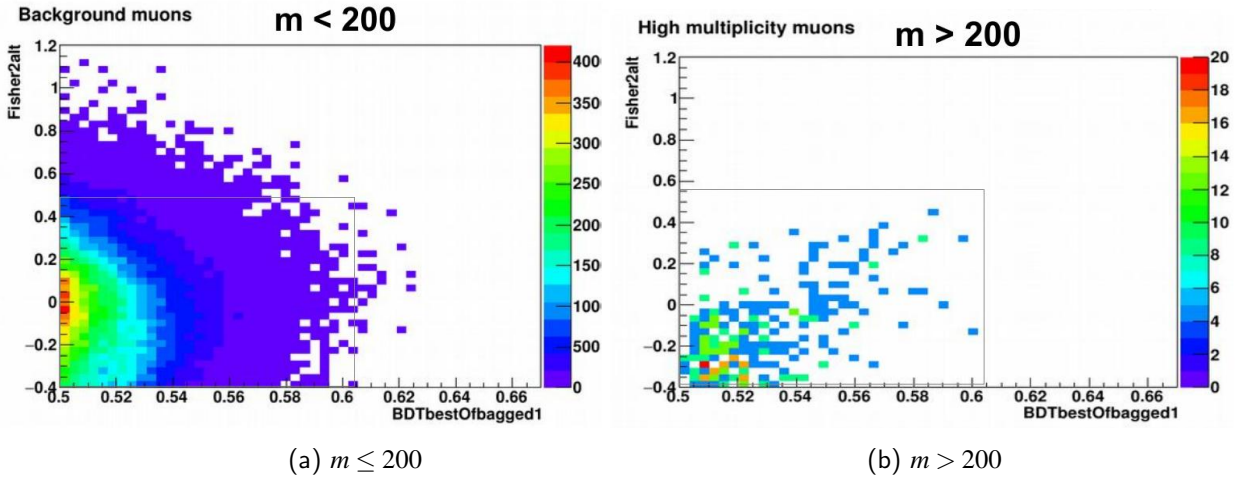


Figure 7.5: Distribution of atmospheric muon events in the two classifier types, with multiplicity  $m$  above and below 200. The box indicates the classifier cuts established later in the analysis chain.

**Atmospheric  $\nu_\tau$  events** The same considerations as for the cosmic  $\nu_\tau$  contribution are also viable for the atmospheric component, with the exception that no events from standard atmospheric showers are expected. However, the prompt component would contribute events with an expected magnitude of  $\nu_e : \nu_\tau \approx 17 : 1$ , which, considering the initially low contribution of the prompt atmospheric flux, would result in such a low event number that it is neglected here.

Following the above described approach, the  $\nu_\tau$  contribution was calculated in the following steps for the number of events  $N_{\nu_\tau}$  after a given classifier cut resulting in  $N_{\nu_e}$  electron and  $N_{\nu_\mu}$  muon neutrinos.

- $N'_{\nu_{\tau\text{NC}}} = (N_{\nu_{e\text{NC}}} + N_{\nu_{\mu\text{NC}}})/2$
- Scaling events in the energy range of the Glashow resonance to even out the Glashow peak, thus that  $N'_{\nu_{\tau\text{CC}}} = f(N_{\nu_{e\text{CC}}})$ , see above.
- $N_{\nu_{\bar{\nu}_{\tau\text{CC}}}} = N_{\nu_{\tau\text{CC}}} + N'_{\nu_{\tau\text{CC}}}$
- Reduce by event number decaying to muons  $N'_{\nu_{\tau\text{CC}}} = N_{\nu_{\bar{\nu}_{\tau\text{CC}}}} \cdot \eta_{\tau, \text{shower}}$
- This leads to the final  $N_{\nu_\tau} = N'_{\nu_{\tau\text{NC}}} + N'_{\nu_{\tau\text{CC}}}$ .

Obviously, this estimate has to be considered as a rough approximation only. Future analysis will be able to rely on a full  $\nu_\tau$  simulation, making this estimate obsolete.

**$\tau$  simulation** Implementation of  $\tau$  neutrino decay channels was improved during the course of this analysis, so that the run production of 119 runs can be used to test the contribution of these events. Seven decay channels were implemented here, see Appendix A.1.2. However, as the event weights allocated here contained some faulty functions, the sample cannot be seen as

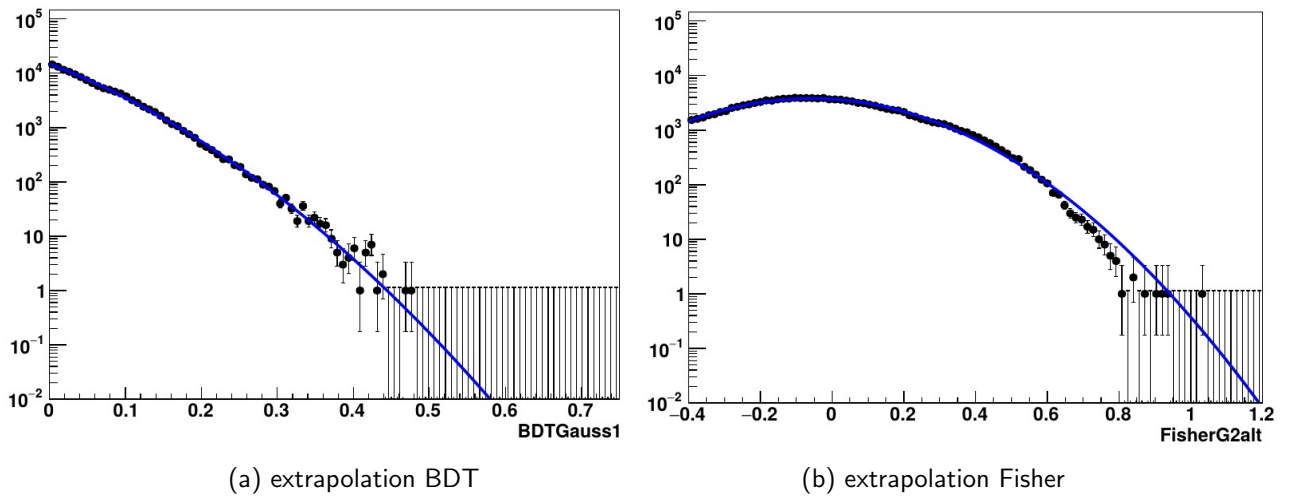


Figure 7.6: Distribution of number of atmospheric muon events and  $2d$  Gaussian fit to the distribution for the BDT and Fisher discriminant.

reliable. Although a correction to the weights was manually added which shifts faulty excessive weights close to the expected values, the simulation at this stage needs the comparison to the extrapolation to arrive at a more reliable conclusion. It can be seen in Figure 7.4 that some differences exist between the estimate from  $\nu_e$  and  $\nu_\mu$  and the simulation, especially in the distribution in the relevant parameter area. Therefore both an extrapolation from the small  $\tau$  run sample and from the extrapolation procedure are applied and their difference taken into account as error. Due to the large uncertainties, the estimate will only be added after the optimization procedure.

## 7.2.2 Atmospheric muons

**High multiplicity muon bundles** In former track-based diffuse cosmic neutrino searches, the contribution of high multiplicity muon bundles was considered relevant, as these bundles would lead to bright events easily mistaken as high-energy neutrino events. Therefore, a mupage sample was produced using the run-by-run version 3 chain, which consisted only of events with multiplicity  $m > 200$  and  $E_{\text{primary}} > 3\text{TeV}$ , see Appendix A.1.2. The mupage livetime of the 119 runs was increased to generate the equivalent of 1 year of high multiplicity mupage events, and the TMVA methods and their corresponding pre-cuts were applied on this simulation as introduced above. The resulting high multiplicity events were added into the atmospheric muon estimate, scaling the corresponding weights to match the full sample. As can be seen for two examples from Figure 7.5, events with high multiplicity show a similar two-dimensional distribution in the classifiers as those events with lower multiplicity and do not reach the area of potential event selection cuts.

**Extrapolation of atmospheric muon number** As the atmospheric muon simulation covers only  $1/3$  of the actual livetime of the runs, the contribution from atmospheric muons has to be extrapolated by a fit procedure. As the search for final selector cuts relies solely on the atmospheric muon classifier  $x_1$  and atmospheric neutrino classifier  $x_2$  developed above, a

simultaneous fit of the atmospheric muon contribution as a product probability density function using two Gaussian functions  $g(x, m, \sigma) = \frac{1}{\sqrt{2\pi}\sigma} \exp(-(x - m)^2 / 2\sigma^2)$  for the two selectors is introduced. The fit procedure to the function

$$P(x_1, x_2) = g(x_1, m_1, \sigma_1) \times g(x_2, m_2, \sigma_2) \quad (7.5)$$

also provides an error estimate for the atmospheric muon contribution taken from the errors of the fit procedure on the Gaussian mean  $m$  and width  $\sigma$ . The error on the number of atmospheric muons is then calculated by varying the parameters  $m$  and  $\sigma$  by their error from the fit procedure and assuming the difference between the original fit and the variation as error on the atmospheric muon number. An exemplary fit result used later in an analysis on 10% of the full sample can be seen in Figure 7.6. In this approach, the two-dimensional fit might be strongly determined by muon events with high classifier values, leading to a more conservative estimate due to an overestimation in one particular classifier dimension, see Figure 7.6b. For the final fit, all available muon events from run-by-run simulation version 2 and 3 and the extra sample of high multiplicity events was used to increase the accuracy of the estimate.

### 7.2.3 Prompt atmospheric neutrinos

As introduced in Chapter 2.3.1, an additional and energetically harder flux above the standard atmospheric neutrinos is expected to stem from charmed interactions. This contribution of prompt neutrinos has not yet been observed, and in [66], the model by Naumov<sup>13</sup> predicting a comparatively high flux was already excluded. Due to the disputed contribution on neutrinos from prompt atmospheric interactions [67], the following analysis chain was first set up without a prompt neutrino estimate. Only in the final parameter scanning, a prompt contribution following the model by Enberg, Reno and Sarcevic [31] is used as estimate.

---

<sup>13</sup> E. Bugaev, V. Naumov, S. Sinegovsky, and E. Zaslavskaya, *Il Nuovo Cimento C* 12, 41 (1989).

## 8 | Search for cosmic neutrinos

The rough procedure of the diffuse cosmic neutrino flux search could already be seen in the toy analyses carried out in Chapter 5. Now, with tools for the suppression for atmospheric muons and atmospheric neutrinos available, a choice of the measurements and simulations used for the analysis having been made and the simulated event samples adjusted such that all relevant event contributions are included, the search for the best event selection parameters and cut value can be finalized. As before, this optimization includes both the model rejection and model discovery factor as optimization parameters. An overview of the event contributions from the different simulation sets entering the analysis can be seen in Figure 8.1.

In Chapter 6, the training of a set of classifiers for the two selection task was described, with small variations in the multivariate tool setup between the individual classifiers. In order to select of the best performing classifiers, a smaller and simplified simulation sample was used for computational reasons, before the final event classifier cuts were set using the full simulation. Having found the event selection cuts, the error of the various event contributions is estimated. In order to cross-check the congruency of the final procedure optimized on the simulation with measurements, the analysis is tested on a sub-sample of roughly 10% of the data to ensure the validity of the procedure regarding known differences between simulation and measurement.

### 8.1 Classifier selection

The classifier selection procedure relies on a two-dimensional cut parameter optimization on model discovery  $\mathcal{D}$  and model rejection  $\mathcal{R}$  on a simplified set of simulations equivalent to 88 days data taking. Here, each possible combination of an atmospheric muon classifier and an atmospheric neutrino classification parameter  $(x_i, y_j)$  is tested, using six atmospheric muon classifiers and 15 atmospheric neutrino selectors. A list of all classifiers and summary of the simulated event set can be seen in Table 8.1.

**Scanning procedure** In Figure 8.1, the distribution of classifier values of event numbers of the various signal and background contributions is shown for an exemplary set of classifiers  $(x_i, y_j)$ . In the simplified optimization procedure, only simulated  $\nu_e$  and  $\nu_\mu$  events and the full sample of atmospheric muons without any extrapolation are considered.

For each classifier, a range of event selection cuts  $\bar{c}$  was tested, and the remaining simulated event numbers  $N_{\text{sig}}(x > c_i, y > c_j)$  and  $N_{\text{bkg}}(x > c_i, y > c_j)$  obtained. From these, the model rejection factor  $\mathcal{R}_{ij}(\hat{N}_{\text{sig},ij}, \hat{N}_{\text{bkg},ij})$  and model discovery potential  $\mathcal{D}_{ij}(\hat{N}_{\text{sig},ij}, \hat{N}_{\text{bkg},ij})$  were calculated for each cut parameter combination. For comparability, the resulting event numbers were

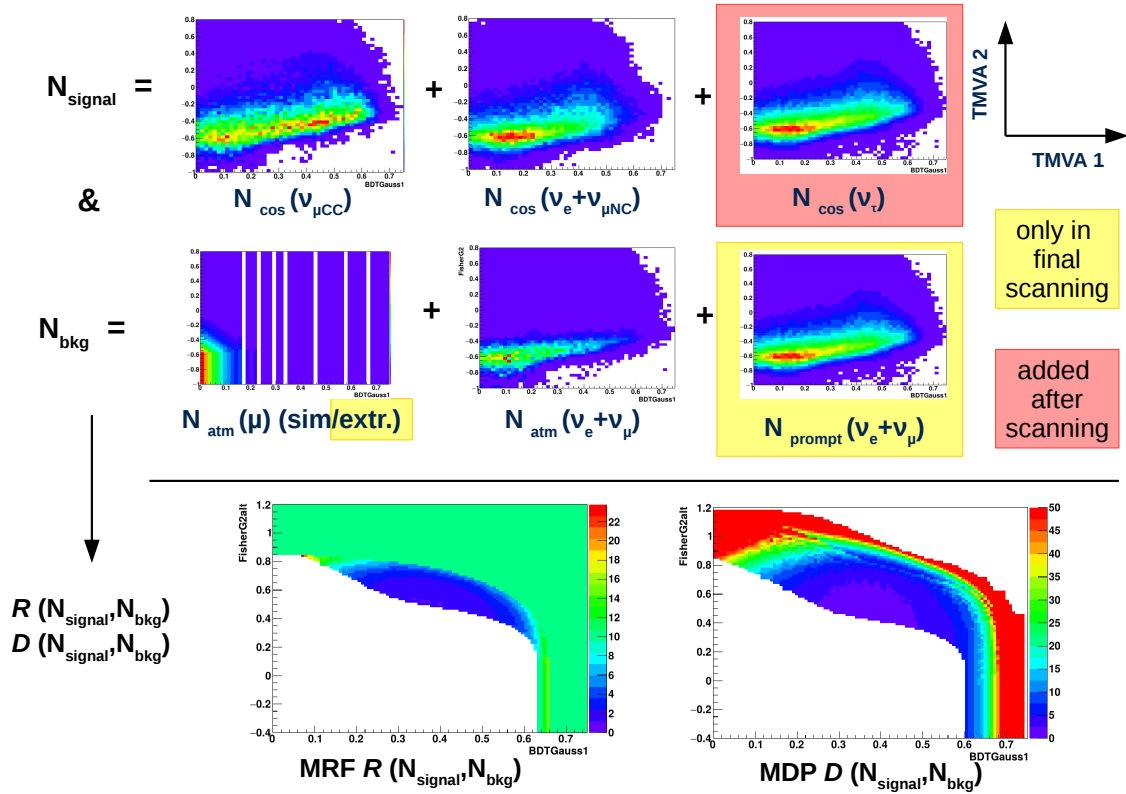


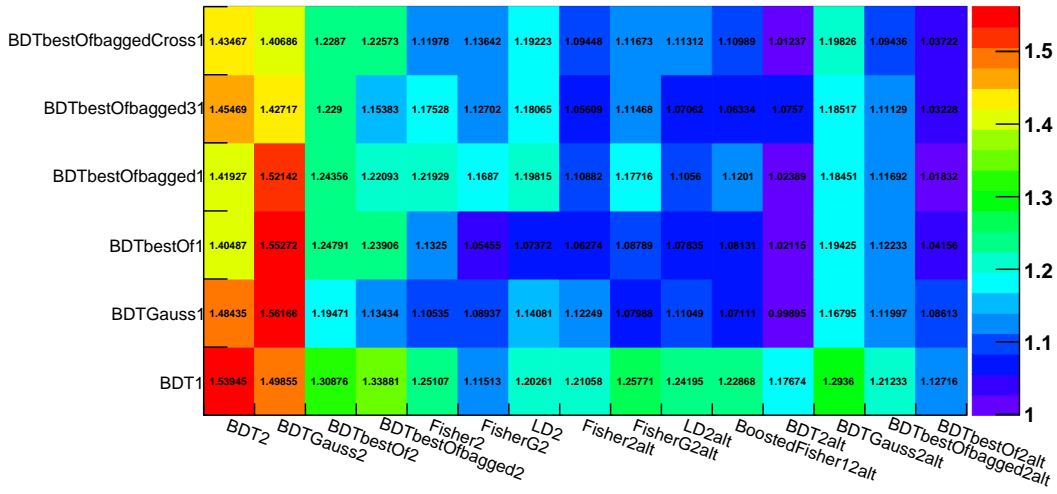
Figure 8.1: Schematic overview over the model rejection and discovery optimization scanning. Each bin entry in the histograms above the line shows the number of events for the given classifier values shows and simulation sample, those in histograms below the line show the optimizer results calculated from the sum of the above shown event numbers, integrated for all bins lower than the given bin. The prompt atmospheric muon component and muon extrapolation were only added in the final cut parameter optimization, and the  $\nu_\tau$  component after the scanning.

scaled to an equivalent of 1600 days data taking,  $\hat{N} = N \times d_{1600\text{d}}/d_{\text{simulation}}$ .

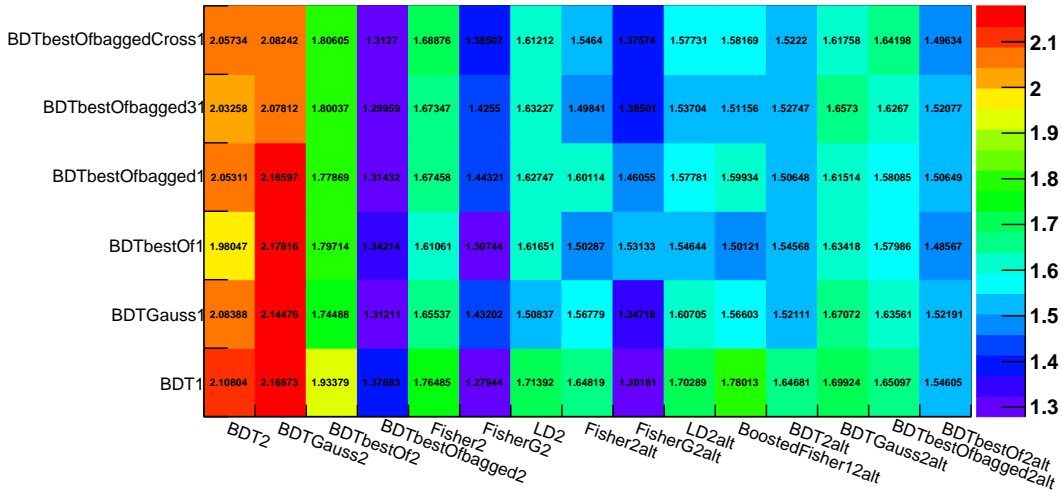
After discarding all cut combinations resulting in a number of muon background events too large for calculation of the optimizers, or leaving a too low number of cosmic neutrino events  $\hat{N}_{\text{sig}} < 0.5$ , the minimum values  $\mathcal{D}^{\text{min}}$  and  $\mathcal{R}^{\text{min}}$ <sup>14</sup> for the best classifier combination were extracted to compare their performance.

**Scanning results** The minimal model discovery  $\mathcal{D}^{\text{min}}$  and rejection  $\mathcal{R}^{\text{min}}$  for each classifier combination can be seen in Figure 8.2. Firstly, it can be seen that some classifiers generally perform worse in combination with others (BDT1, BDT2, BDTGauss2, BDTbestOf2, BDTGauss2alt) and are therefore discarded. For the remaining methods, performance between model discovery and rejection vary. Regarding the atmospheric neutrino classifiers, shown along the x-axis in Figure 8.2, it should be noted that the linear classifiers like Fisher discriminant perform at least equally well as the mathematical more complex BDTs. This can be seen as indication

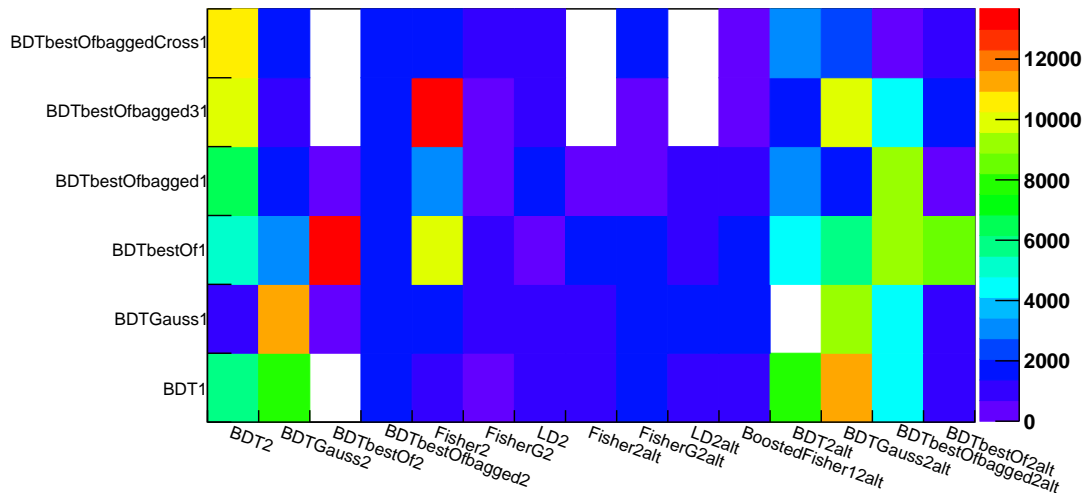
<sup>14</sup>For computational speed, the MRF extrapolation, see Appendix A.2.1, was used.



(a) MRF  $\mathcal{R}^{\min}$



(b) MDP  $\mathcal{G}^{\min}$



(c) cut distance  $\Delta N^2$

Figure 8.2: Result of the cut optimization procedure for classifier selection.

TMVA method 1 x	TMVA method 2 y	simulation details
BDT1	BDT2, BDTGauss2	$d_{\text{genhen}} = 88 \text{ d}$
BDTGauss1	BDTbestOf2, BDTbestOfbagged2	$d_{\text{mupage}} = 1430 \text{ d}$
BDTbestOf1	Fisher2, FisherG2	$d_{\text{reference}} = 1600 \text{ d}$
BDTbestOfbagged1	Fisher2alt, FisherG2alt	$\Phi_{\nu, \text{bkg}} = \Phi_{\text{Bartol}}(\nu_e + \nu_\mu)$
BDTbestOfbagged31	LD2, LD2alt	$\Phi_{\nu, \text{sig}} = \Phi_{\lambda=2.5}(\nu_e + \nu_\mu)$
BDTbestOfbaggedCross1	BoostedFisher12alt, BDT2alt BDTGauss2alt, BDTbestOf2alt BDTbestOfbagged2alt	

Table 8.1: Methods list and simulation details for the classifier scanning. For more details on the simulation, see Appendix A.6.1, for details on the TMVA methods used, see Appendix A.5.2.

that the complex BDT does generally not uncover non-linear correlations between the input parameters that enhance the classification result above that of linear classifiers.

Several classifier combinations show good results for both  $\mathcal{D}$  and  $\mathcal{R}$  and therefore a suited for the analysis. However, even if the results for both optimization parameters are good, they also need to agree on the cut values, as a single pair of cut values should at the same time optimize both parameters. Therefore, the squared difference of signal and background events remaining after the optimal model rejection and model discovery cut  $\Delta N^2 = (\hat{N}_{\text{signal}}^{\min \mathcal{D}} - \hat{N}_{\text{signal}}^{\min \mathcal{R}})^2 + (\hat{N}_{\text{bkg}}^{\min \mathcal{D}} - \hat{N}_{\text{bkg}}^{\min \mathcal{R}})^2$  for a signal flux with  $\lambda = 2.5$  is used as an estimate of the cut agreement between both methods, see Figure 8.2c. Last but not least, a by-eye-comparison of the distribution agreement between simulation and measurement for the considered parameters added to the decision process for the final classifier selection.

**Classifier selection** Starting the selection from the atmospheric neutrino classifiers and regarding their result of  $\mathcal{R}^{\min}$  in Figure 8.2a, most Fisher-classifiers seem suitable, but the best performance here can be seen with some alternatively trained BDTs. The latter, however, show no good result in  $\mathcal{D}^{\min}$  in Figure 8.2b. Of the Fisher methods, both FisherG2 and FisherG2alt perform well for both optimizers.

Following the same priorities, the atmospheric muon classifier that performs well model rejection in combination with the FisherG2 and FisherG2alt classifiers are the BDTGauss1 and BDTbestOf1. Comparing results for the four possible combinations of these four classifiers, it can be seen that both (BDTbestOf1, FisherG2) and (BDTGauss1, FisherG2alt) could serve as well-performing classifiers. As the BDTGauss1 classifier generally shows a better agreement between data and simulation, the combination  $(c_1, c_2) = (\text{BDTGauss1}, \text{FisherG2})$  is preferred, keeping in mind that the alternative combinations reach a similar performance and could replace this selection, should problems arise later in the analysis.

## 8.2 Application to the full simulation

The definite setting of the parameter cuts now utilised the full simulation of stage 1 runs as introduced in Chapter 7. The atmospheric muon simulation was replaced the numerical estimate drawn from the two-dimensional Gaussian fit of the muon distribution using all available mupage

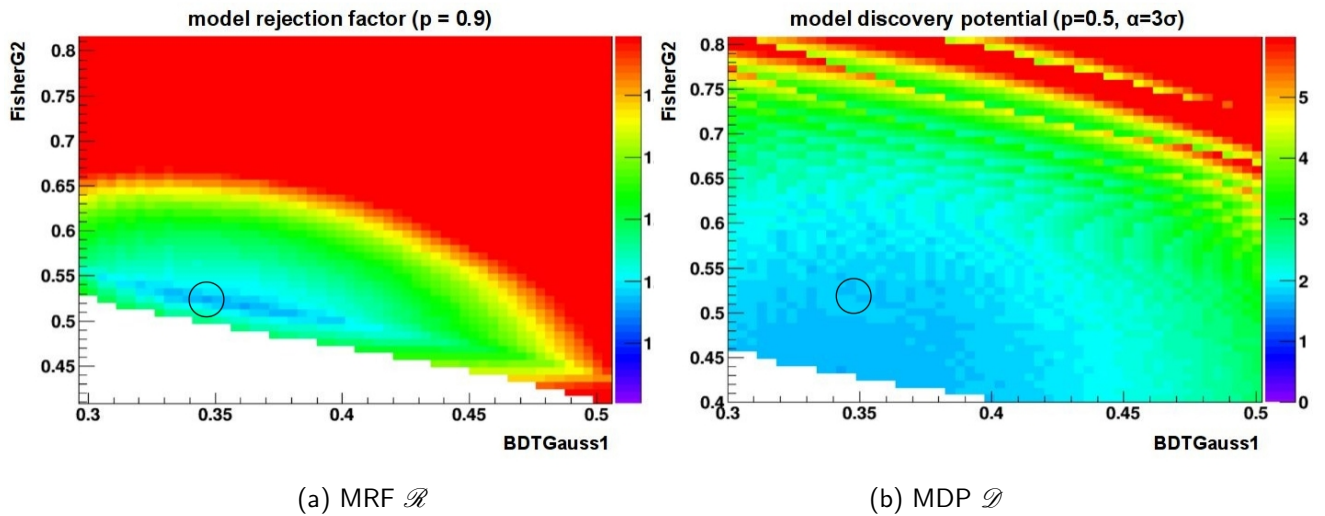


Figure 8.3: Model rejection factor and discovery potential (for  $3\sigma$  at 50%) for various parameter cut configurations. The compromise was set at  $\text{BDTGauss1} > 0.345$  and  $\text{FisherG2alt} > 0.52$

samples, and a prompt component was added, see Table 8.2. With smaller intervals between the tested cut values, the full minimization of  $\mathcal{D}$  and  $\mathcal{R}$  was run as shown in Figure 8.1. In this procedure,  $(\text{BDTbestOf1}, \text{FisherG2})$  reaches the best model discovery, while  $(\text{BDTGauss1}, \text{FisherG2alt})$  yields the minimum in model rejection. Together with the considerations given in the last paragraph,  $(\text{BDTGauss1}, \text{FisherG2alt})$  were therefore selected as definitely final optimizers used in the analysis chain.

For this final classifier combination, the optimizer landscapes seen in Figure 8.3 allow slight variations for the final cut values, as  $\mathcal{D}^{\min}$  is reached for  $(c1 = 0.345, c2 = 0.43)$  within a wider range of parameter cuts leading to roughly similar values, and the best model rejection  $\mathcal{R}^{\min}$  lies at  $(c1 = 0.345, c2 = 0.52)$ . Leaning towards a strong model rejection, and seeing that model discovery  $\mathcal{D}$  for the optimal rejection cut is not far from the minimum, the final parameter cuts were set as

**TMVA1**  $\text{BDTGauss1} > 0.345$  and

**TMVA2**  $\text{FisherG2alt} > 0.52$ .

The resulting event numbers when applying these cuts to the full set of simulations including stage 2 runs are shown below in Table 8.3. For these event selection cuts, a sensitivity towards the IceCube-like test fluxes  $\Phi_{\text{IC}2.0}$  and  $\Phi_{\text{IC}2.5}$  with an unbroken power law spectrum with  $\lambda = 2.0$  and  $\lambda = 2.5$  can be reached at the level of the flux itself:  $\Phi_{90\% \text{C.L.}, \text{IC}2.0} = 1.03 \Phi_{\text{IC}2.0}$  and  $\Phi_{90\% \text{C.L.}, \text{IC}2.5} = 0.97 \Phi_{\text{IC}2.5}$ .

### 8.3 Error estimates

Uncertainties in the event number estimate can stem from various sources: limited accuracy of the flux model, omissions or inaccuracies in the simulation chain, and errors of the methods used in the analysis chain. The probability to measure the given event number is assumed to be

TMVA method 1 x	TMVA method 2 y	simulation details
BDTGauss1	FisherG2alt	$d_{\text{genhen}} = 913 \text{ d}$
BDTbestOf1	FisherG2	muon extrapolation
		$d_{\text{reference}} = 1728 \text{ d}$
		$\Phi_{\nu, \text{bkg}} = \Phi_{\text{Bartol+Enberg}}(\nu_e + \nu_\mu)$
		$\Phi_{\nu, \text{sig}} = \Phi_{\lambda=2.5}(\nu_e + \nu_\mu)$

Table 8.2: Method and simulation details for the parameter cut scanning.

Gaussian distributed, leading to the addition of uncertainties  $\varepsilon_i$  following the standard deviation as  $\varepsilon = \sqrt{\sum \varepsilon_i^2}$ . As the exercise to account for all types of uncertainties can naturally be driven to great detail, only the leading errors known at the time of the analysis will be considered here, with the resulting errors shown in Table 8.3. In all cases, the more conservative assumption leading to a larger background contribution or including the larger error was chosen. Considering this conservative approach, also correlations between the various errors are not considered.

### 8.3.1 Atmospheric $\nu_e$ and $\nu_\mu$

**Flux uncertainties** The atmospheric neutrino flux models mostly diverge on the spectrum of the primary particles used, as was already seen in Figure 2.7. Here, the models of Honda et al. [30] and the Bartol group [29] are used. The error on the flux model can therefore be derived from the difference in expected event numbers in the selection. Note that while the cut optimization shown above was performed using the Bartol flux, the procedure was also cross-checked using the flux model from Honda, which yielded comparable event selection cuts.

Considering the prompt component of the atmospheric neutrino flux, the assumption from Enberg, Reno and Sarcevic was included in the final scanning above, although in [14], a 90% C.L. limit on the prompt flux is set at  $0.5 \times \text{ERS}$ . The error on this flux considered here therefore lies at the same level as the assumed signal.

**Detector simulation** The detector simulation has been tested in many comparisons between measured events and simulation and errors can be assumed to be relatively small. As the reliance on the hit timing and, more difficult to reproduce, amplitude is crucial especially to high-energy neutrino searches, the effect of water properties on the hit distribution and number is evaluated with a specialized toy-simulation, the details of which are listed in Appendix A.1.2. In [68], the absorption length  $\lambda_{\text{abs}}$  and scattering length  $\lambda_{\text{scat}}$  measurements allow for an error of roughly 10%, which was implemented in the toy simulation and simulation sets were produced using run-by-run simulation version 3 with  $\lambda_{\text{abs/scat}} = 1 \pm 0.1 \lambda_{\text{abs/scat}}$ . As the event numbers above are drawn from run-by-run simulation version 2 and only few runs were used, only the absolute difference between  $\Delta N_{\text{abs/scat}} = N_{1.1 \lambda_{\text{abs/scat}}} - N_{0.9 \lambda_{\text{abs/scat}}}$  is used as error as  $\varepsilon_{\text{abs/scat}} = 1/2 \Delta N_{\text{abs/scat}}$ , scaled and assumed symmetrical around the expected event number. It should be noted here that, while the absorption length shows direct proportionality to the number of photons detected, a change in the scattering length has rather an effect on the containment of photons within the detection volume. The effect of a shorter absorption length can approximately mimic a reduced photon sensitivity, which has to be assumed over the long run-

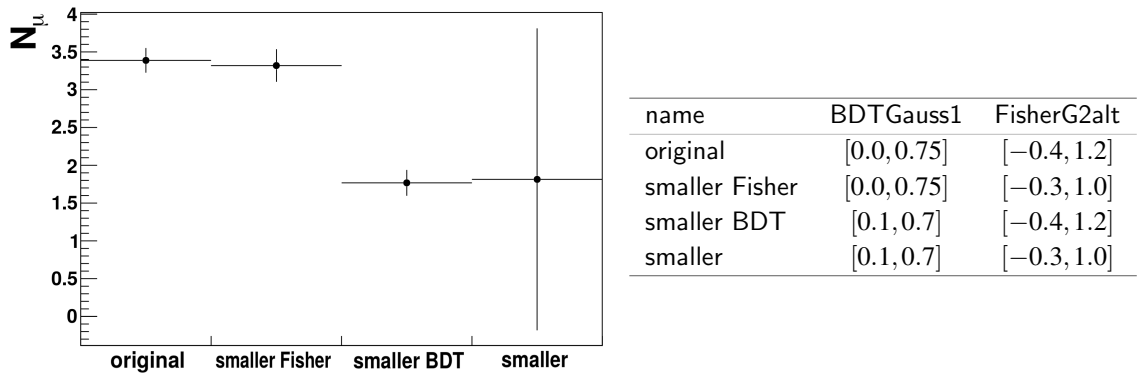


Figure 8.4: Extrapolated muon number and error for different fit intervals.

time of the detector, but for which no implementation in simulation is yet included in this study. It can be seen that error from absorption length variations is by far the largest, and although comparisons between simulation and measurement below show that the simulated absorption length is probably more accurate, the scale of the error estimate shows that inaccuracies in photon absorption and photon detection efficiency play a large role for the neutrino detection sensitivity.

**Analysis procedure** As the analysis procedure mostly relied directly on the simulation, errors either stem from uncertainties in the simulation chain itself, or from the additional estimates or steps in the analysis procedures not directly relying on the simulation. Here, the run matching procedure introduced to use data runs without matching simulation has to be considered. An error for the run matching procedure introduced by scaling the event numbers for selection 1 or 2 respectively to the full livetime,  $N_{1/2\text{only}} = N_{1/2} \times d_{\text{full}}/d_{\text{select}1/2}$ , giving an estimate of how large the event number would be for an selection 1/2 - only sample. This gives an indication for the effect of the different run conditions allocated to the respective samples and their impact on the overall event numbers. The error is then calculated as  $\epsilon_{1/2} = |N_{1\text{only}} - N_{2\text{only}}|$ .

### 8.3.2 Atmospheric muons

Using the MUPAGE program [41], the choice of the atmospheric muon flux model is fixed to the parametrization from full atmospheric cascade simulation that served as the basis for the initial program development, dating back roughly a decade. Certainly, different flux models and measurements would allow a more precise parametrization according to newer information, which might vary around 10 – 15% in normalization from the original formula, see Chapter 2.3.1. However, comparison between measurement and simulation have shown that the far greater uncertainty in the atmospheric muon count stems from environmental variations and data taking conditions. In the relevant high-energy tail of the atmospheric muon spectrum, the fact that the simulation only amounts to 1/3 of the full event sample certainly gives the leading error stemming from the low statistics and the resulting modelling of the atmospheric muon distribution in the analysis chain. The error from the muon estimate is therefore the only error considered for atmospheric muons.

Flux type	$N_{\text{events}}$	$\epsilon$	$\epsilon_i$
$N^{2.5} \nu_{\mu, \text{CC}}$	2.60	1.21	$0.2^d + 0.88^{c1} + 0.81^{c2}$
$N^{2.5} \nu_{\mu, \text{NC}}, \nu_e$	4.85	2.24	$0.5^d + 1.65^{c1} + 1.43^{c2}$
$N^{2.5} \nu_{\tau}$	1.63	0.99	$0.99^f$
$N^{2.0} \nu_{\mu, \text{CC}}$	3.38	1.32	$0.3^d + 0.57^{c1} + 1.15^{c2}$
$N^{2.0} \nu_{\mu, \text{NC}}, \nu_e$	4.02	1.85	$0.3^d + 1.21^{c1} + 1.37^{c2}$
$N^{2.0} \nu_{\tau}$	1.11	0.8	$0.8^f$
IceCube 2.5 $N_{\text{cos}}$	9.08	4.44	
IceCube 2.0 $N_{\text{cos}}$	8.51	3.97	
$N_{\text{Honda}} \nu_{\mu, \text{CC}}$	10.27	7.51	$1.13^a + 0.2^d + 6.96^{c1} + 2.57^{c2}$
$N_{\text{Honda}} \nu_{\mu, \text{NC}}, \nu_e$	3.85	2.73	$1.47^a + 1.52^d + 1.73^{c1} + 0.11^{c2}$
$N_{\text{Enberg}} \nu_{\mu, \text{CC}}$	0.46	0.46	$0.46^b$
$N_{\text{Enberg}} \nu_{\mu, \text{NC}}, \nu_e$	1.0	1.0	$1.04^b$
$N_{\mu, \text{atm}}$	3.19	1.52	$1.52^e$
atmospheric	18.77	13.22	
$\Phi_{90\% \text{C.L.}}$ IceCube 2.5	0.97		
$\Phi_{90\% \text{C.L.}}$ IceCube 2.0	1.03		

Table 8.3: Signal and background expectation including error estimates for 1757.5 days of *ANTARES* lifetime, and sensitivity towards the test fluxes. Signal event numbers are given for an IceCube-like flux with  $\lambda = 2.5$  (IceCube 2.5) and  $\lambda = 2.0$  (IceCube 2.0), see Appendix A.3.1. Error estimates are drawn from a) difference between the atmospheric muon model by Honda et al. and the Bartol group, b) the assumption of a non-existing prompt component, c1) error from absorption length variation  $\epsilon_{\text{abs}}$ , c2) error from scattering length variation  $\epsilon_{\text{scat}}$ , d) difference between selection 1 and selection 2 estimates  $\epsilon_{1/2}$ , e) variation from muon model fit processes and f) the difference between  $\nu_{\tau}$  estimate and simulation

**Error from muon estimate** To account especially for the high-energy contribution for atmospheric muon events, high multiplicity muon bundles have been added to the simulated sample to increase the statistical representation of this contribution and to include it in the atmospheric muon model used in the analysis. The error of the model can be derived from the fit errors on the fit function parameters, which are relatively small for the used fit. However, the choice of the fit parameter interval has a far larger effect on the muon model and therefore estimated muon number. In Figure 8.4, the effect of varying fit intervals can be seen on the muon estimate. As this error is by far larger than the actual fit error, the largest deviation of the muon number estimate of an alternative muon distribution fit to the number from the original model is used as error, i.e.  $\epsilon_{\mu \text{ atm}} = N_{\text{original}} - N_{\text{smallerBDT}}$ .

It should also be noted that, of the simulated atmospheric muon sample, exactly one muon survives the event cuts, giving a muon estimate from simulation of  $N_{\mu \text{ atm sim}} = 3$ , which is well in agreement with the muon model estimate for the given cut value and indicates a suitable fit model.

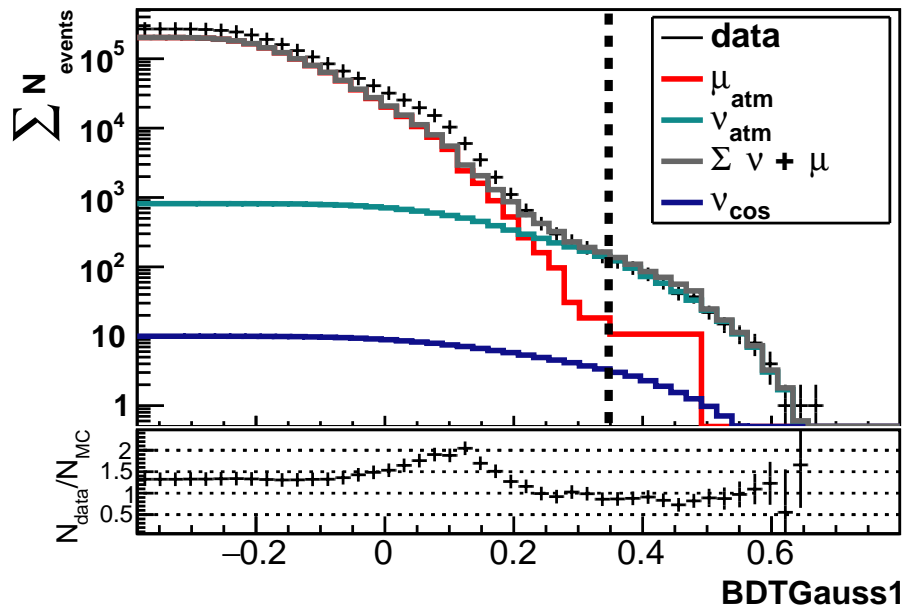


Figure 8.5: Comparison between measurement and simulation in the test sample for the atmospheric muon suppression parameter after primary cuts.

### 8.3.3 Tau neutrinos

As the missing  $\nu_\tau$  component in the simulation has to be replaced by either the extrapolation procedure or toy simulation introduced above in Section 7.2.1, and both lack accuracy either due to the estimation process or the simulation challenges (see Appendix A.1.2), the method producing the lower signal estimate, i.e. the extrapolation method, is used to obtain the event number, while the difference to the number obtained from the toy simulation is used as error.

## 8.4 Test on a data subsample

Before applying the cuts on the full data sample, the reliability of the method with regard to deviations between the simulation and data has to be shown within reasonable boundaries. As this analysis was developed as blinded analysis on simulation only, roughly 10% of the data is selected to be compared to the simulation as test sample. In order to ensure a good representation, only runs with run numbers ending in 0 were selected, which amounted to 155.8 days. In this test, the expected event distribution for the classifiers as well as for the input parameters to the multivariate tools enter the comparison between simulation and the test data sample. Finally, the number of detected events within the test sample is compared to the expectation.

### 8.4.1 Reduced event samples for measurements and simulation

As the cut for atmospheric muon suppression is set such that only very few atmospheric muon events remain, the application of the cuts should lead to an almost pure atmospheric neutrino sample. Therefore, the BDTGauss1 parameter should foremost show a good agreement in

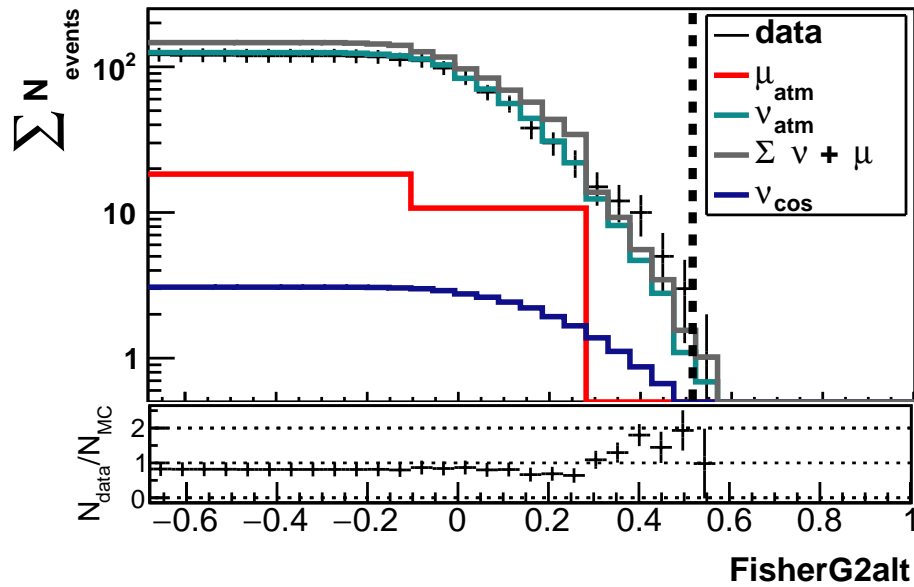


Figure 8.6: Comparison between measurement and simulation in the test sample for the atmospheric neutrino suppression parameter applying  $\text{BDTGauss1} > 0.345$

magnitude and slope of the parameter distribution around the cut value, while the FisherG2alt is required to exhibit a good agreement where cosmic neutrino events become dominant at high classifier values. In Figure 8.5, the comparison between measurement and simulation can be seen for the complete test sample for BDTGauss1, showing a satisfactory agreement around the intended cut value, and in Figure 8.6 the distribution of the FisherG2alt parameter for the remaining neutrino events. Here, a slight underfluctuation can be observed for high parameter values in the atmospheric neutrino classifier. As this estimate relates strongly to neutrino energy, it shows a tendency in measured events to lead to a lower reconstructed energy than in simulation. However, as the purpose of the analysis is the general discovery of a cosmic neutrino signal and comparison between measurement and simulation is still within reasonable boundaries, it can be regarded as more conservative estimate and was therefore approved for unblinding. In the test sample, two events were found, which showed normal unexpected input parameters or hit distributions, and are most probably neutrino-type events. This cross-check was also used to rule out the influence of so-called sparking events, which is explained in the next paragraph.

#### 8.4.2 Representativeness of the subsample

As the test is performed to check the plausibility of the results of the analysis for this small subset, the adequacy of the test sample to represent the complete sample has to be confirmed first. One indicator for the good representation of the test sample can be seen in an agreement of the classifier cut values if the cut optimization procedure performed above for the complete simulation set would be restricted to the simulation of the test sample. Indeed the optimization arrived at the same parameter cut values as using the full simulation set. In the test sample, two data event were found after applying all parameter cuts. Assuming a 10% contribution

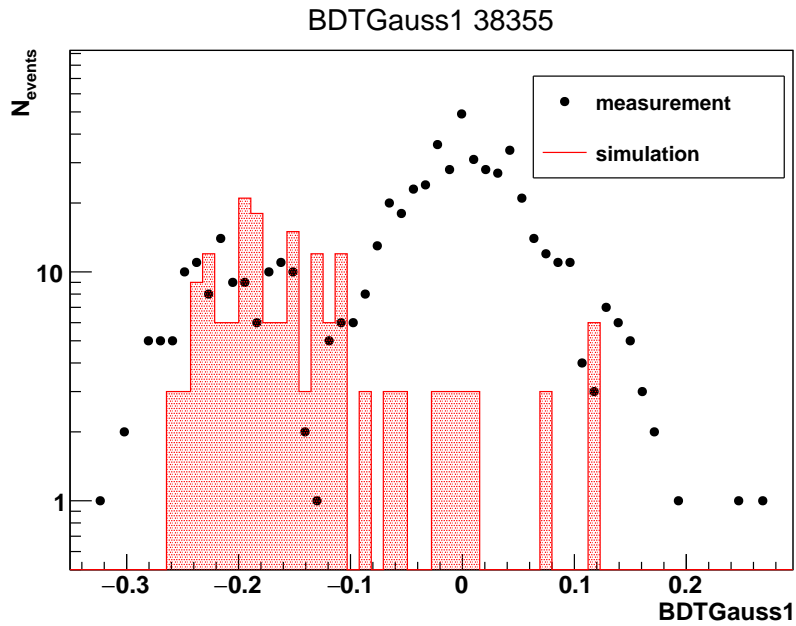


Figure 8.7: Events from run 38355, classified as *sparking* for the atmospheric muon classifier, compared to expectations from simulation.

from Table 8.3, 2 events from background would be expected. With a 27% probability of this outcome in a Poisson-distributed variable, the result is not the most probable, but surely within reasonable expectations. Therefore, the analysis was considered reliable enough to be extended to the full set of measurements.

### 8.4.3 Detector malfunction: "sparking" events

Events triggered by sparking optical modules posed a problem in previous analyses, most of all to the shower analysis. A spark produced in a failing OM lights up a large part of the detector, and therefore leads to a triggered hit pattern interpreted as "event" with a large number of photons. Depending on the reconstruction, these pseudo-events can be misinterpreted as high-energy neutrino events. In order to avoid the introduction of an additional filter criterion for the sparking events, a short investigation was carried out to ensure no influence of the phenomenon on the analysis. The influence of sparking events on this analysis was evaluated on the one hand by excluding those runs from the test sample which were already identified as containing sparking events, and on the other hand by reconstructing four sparking events identified in a previous shower analysis. Of these four events, none could successfully be reconstructed with both classifiers, as either BFit or Aafit reconstruction did not succeed or result in a reconstructed zenith angle  $\theta < 1.2$ , leading to deselection of the event. In the runs containing sparking events, the majority of sparking events was naturally assigned a high value for the FisherG2alt-parameter. However, as can be seen in the exemplary run in Figure 8.7, these events are not classified as neutrino-like by the BDTGauss1-parameter. Overall, no event was found in the known sparking runs that would not be selected as neutrino-like by the atmospheric muon classifier.



## 9 | Analysis results

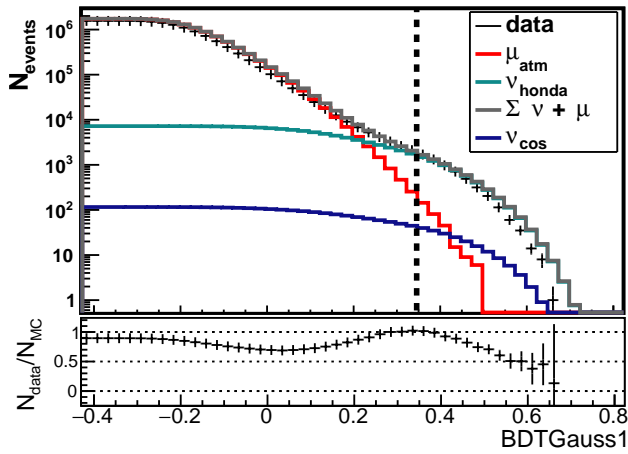
After the validation of the analysis with a subsample of data runs, the analysis chain was applied to the full set of measurements. It will be seen that a far lower number of events is found in the full sample than previously expected. Therefore, a closer look is taken at the events remaining after the final cuts, and the cause for this deficit is traced and considered as a result of the run matching process introduced above. Following this assumption, the analysis was finally reduced to the selection 1 subsample, which is used to set a limit on the assumption of the cosmic neutrino flux.

### 9.1 Results from the full sample

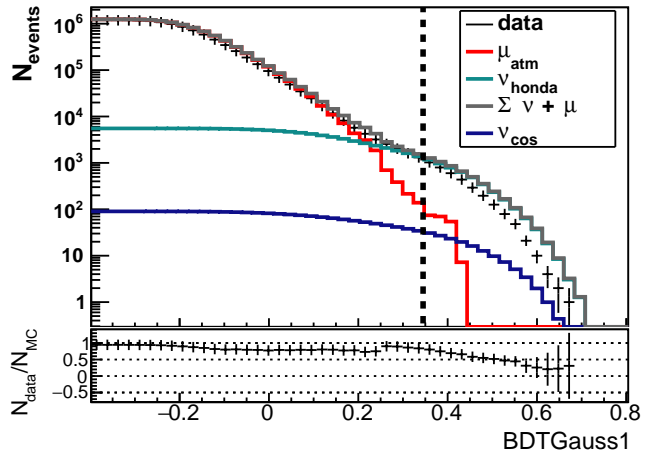
The full set of measurements, subdivided in sample 1 and 2 with 913.5 days and 557.9 days of data taking, was subjected to the full analysis chain, see Figure 8.1. For the main cut steps, i.e. the preprocessing selection focusing on well-reconstructed upgoing events, the application of both the atmospheric muon classifier and the atmospheric neutrino classifier separately to evaluate their specific impact, and the complete set of cuts can be seen in Table 9.1.

**Selection parameter distribution** It is well known for diffuse neutrino searches in *ANTARES* that a crucial element in the solidity of the analysis lies in the agreement between simulation and measurement especially regarding the luminosity of an event or its related energy estimates, which has caused problems already in earlier analyses. Therefore, the agreement between simulation and measurement should indicate a reliable representation of the cut parameters at least around the cut value. In Figure 9.1, the classifier distributions can be seen to fulfil that requirement quite well, especially for the selection 1 runs. It can also be seen that, firstly, the atmospheric muon classifier cut leads to a generally lower number of events in the neutrino-dominated sample of selection 2, which indicates a worse representation of high-energy events in this sample, as can also be seen in Table 9.1 and in the increasing discrepancy between simulation and data for large classifier values in Figure 9.1c.

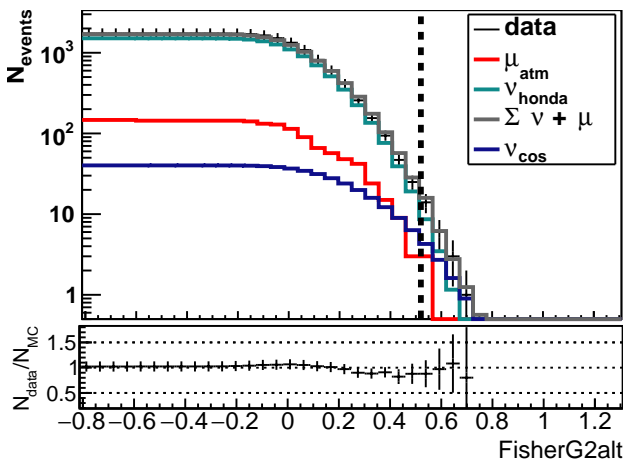
In Table 9.1, the effect of the application of the atmospheric neutrino classifier without prior application of the atmospheric muon classifier is also shown, which leads to an atmospheric muon dominated sample focusing on high energy events. Here, at least for atmospheric muons, a tendency of the classifier is exhibited to identify less high-energy events than expected in data, especially in the selection 2 runs. While this cut step was not part of the investigation before unblinding, it brings ex post an indication towards a deficit of high-energy event identification.



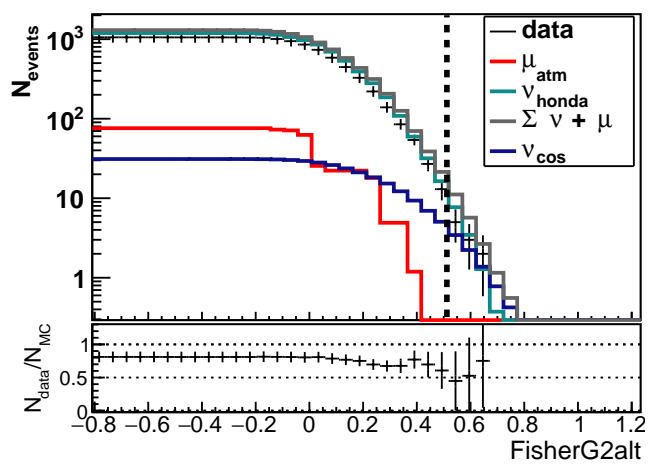
(a) BDTGauss1 selection1



(b) BDTGauss1 selection2



(c) FisherG2alt selection1



(d) FisherG2alt selection2

Figure 9.1: Agreement between data and simulation for all events from data selection 1 and 2 for the BDT method for atmospheric muon suppression and the Fisher discriminant for cosmic neutrino identification after a cut on  $\text{BDT} > 0.345$ .

Event type	prep. P1-3	TMVA 1	TMVA 2	all cuts
$N^{2.5} \nu_{\mu,CC}$	74.0 (57.4)	23.3 (17.8)	2.93 (2.53)	1.40 (1.13)
$N^{2.5} \nu_{\mu,NC}$	42.0 (32.8)	17.1 (13.3)	4.68 (4.00)	2.64 (2.27)
$N_{\text{Honda}} \nu_{\mu,CC}$	$6.51 (4.94) \times 10^3$	$1.35 (1.06) \times 10^3$	12.6 (11.9)	5.27 (4.83)
$N_{\text{Honda}} \nu_{\mu,NC}$	717 (597)	164 (133)	3.87 (3.83)	2.37 (2.32)
$N_{\text{Enberg}}$	16.3 (16.8)	9.2 (5.86)	1.41 (0.97)	0.79 (0.53)
$N \mu_{\text{atm}}$	$1.73 (1.25) \times 10^6$	147 (76)	$13.5 (13.0) \times 10^3$	3 (0)
measured	$1.56 (1.18) \times 10^6$	$1.74 (1.05) \times 10^3$	$9.73 (5.19) \times 10^3$	12 (5)
$N_{\text{data}}/N_{\text{sim}}$	0.90 (0.94)	1.04 (0.83)	0.70 (0.40)	1.05 (0.65)
$N_{\text{data}}/N_{\text{sim}}$ total	0.92	0.95	0.56	0.89

Table 9.1: Event number expectations from simulation and measurement after different cut stages for all selection 1 (selection 2) runs. A cut on the atmospheric neutrino selector alone was not part of the analysis chain and is added here for comparative purposes.  $N_{\text{data}}/N_{\text{sim}}$  is calculated for background simulation only, which lacks the  $\nu_{\tau}$  estimate.

**Final selected events** In total, 17 events were found after application of the final event selection cuts, of which some reconstruction parameters can be seen in Table 9.2, with event displays and a longer parameter list given in Appendix A.7. In selection 1 runs, 12 events were found with a background-only expectation of 9.51 events from atmospheric fluxes after addition of all atmospheric neutrino flavours and the muon number extrapolation, see Table 9.3. However, overall only 17 events were discovered, which is actually less than the 18.8 events expected for background only events for the full sample, see Table 8.3. Therefore, while the selection 1 result matches expectations for the emergence of a cosmic neutrino flux quite well, the selection 2 casts serious doubt on the reliability of the representation of these measurements in simulation. This calls for a closer investigation of the resulting events selection, their properties and the cause for the observed deficit. As a first indication, it is noteworthy that no events were found after run 68234, which was taken in December 2012, leaving the whole year 2013 without any selected event. Therefore, an actual change in the observables used in the analysis can be suspected for these late data taking periods which leads to a deterioration of the selection quality. As the drop is not seen in the simulation, this change is most likely not represented in the matched runs, which generally stem from an earlier data taking period.

## 9.2 A closer look at the final events

When the properties of the final events are explored further, it should be noted that conclusions drawn from the final event sample on the one hand lack statistical significance, and on the other hand properties of this sample are naturally result of the design of the study and reflect in some aspects rather the set-up of the analysis chain than general properties of neutrino measurements in ANTARES. It should be noted that some of the selected events have already been included in the cosmic neutrino candidates of former analysis, especially the latest diffuse flux search based on shower-like events and the latest point-source search.

	$r$	$\theta_{\text{Dusj}}$	$\theta_{\text{Aafit}}$	$E_{\text{Dusj}}^a$	$E_{\text{ANN}}^a$	$\lambda$	VLLH	BDT	Fisher	ref.
1	26397	3.05	2.08	4.0	662.3	-5.04	7.93	0.36	0.55	[16] (2)
2	33176	2.46	2.51	1.1	187.6	-4.96	7.91	0.43	0.57	
3	35473	1.24	1.73	4.7	190.5	-4.71	10.36	0.35	0.52	
4	35958	2.25	2.12	1.4	183.5	-4.95	8.62	0.43	0.54	
5	40213	2.29	2.47	0.6	166.0	-5.71	8.06	0.35	0.55	
6	46195	2.0	2.2	6.4	233.0	-5.86	8.01	0.38	0.65	
7	46852	2.15	2.48	17.6	62.1	-5.34	7.87	0.43	0.61	[16] (2)
8	47679	2.55	2.38	3.6	206.1	-5.49	7.8	0.43	0.63	[16]
9	49425	1.75	1.93	10.9	164.7	-5.25	7.71	0.35	0.66	[16] (2)
10	51140	1.96	2.23	4.0	13.0	-5.86	7.86	0.35	0.61	
11	52092	2.03	2.68	43.5	101.6	-4.9	8.31	0.43	0.54	PS
12	54320	1.72	1.62	12.0	89.1	-4.46	8.82	0.35	0.54	PS
13	57495	2.55	2.36	13.1	35.7	-5.68	8.22	0.38	0.58	
14	58428	1.77	1.7	1.9	79.3	-5.53	8.09	0.39	0.54	
15	60058	2.04	2.22	2.3	269.8	-5.5	8.46	0.42	0.62	(2)
16	61055	1.72	1.75	1.4	11.8	-5.35	8.22	0.4	0.53	
17	62834	2.06	2.42	16.5	197.3	-5.16	7.64	0.45	0.7	[16] (2)

Table 9.2: Reconstruction parameters of the events found in the full data sample, giving the run number  $r$ , the zenith reconstruction of the Dusj shower reconstruction and Aafit track reconstruction, energy estimates ( $^a$  in [TeV]) of Dusj and the ANNergy estimator, Aafit track quality  $\lambda$ , Dusj shower quality VLLH, and the multivariate classifiers. The reference column indicates events also found in previous shower analysis [16] or previous point-source searches (PS), and events from stage 2 runs (2).

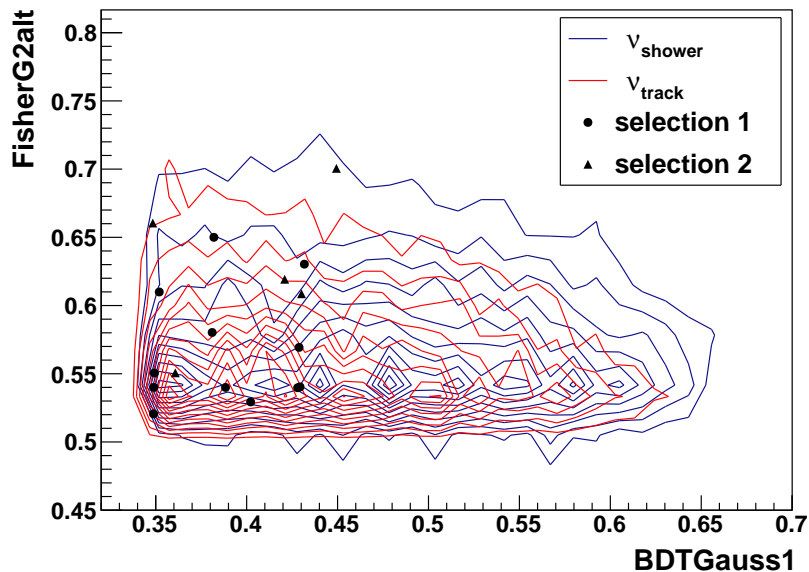


Figure 9.2: Classifier parameters of the final events, compared to the expected distribution of atmospheric shower- and track-like neutrino events.

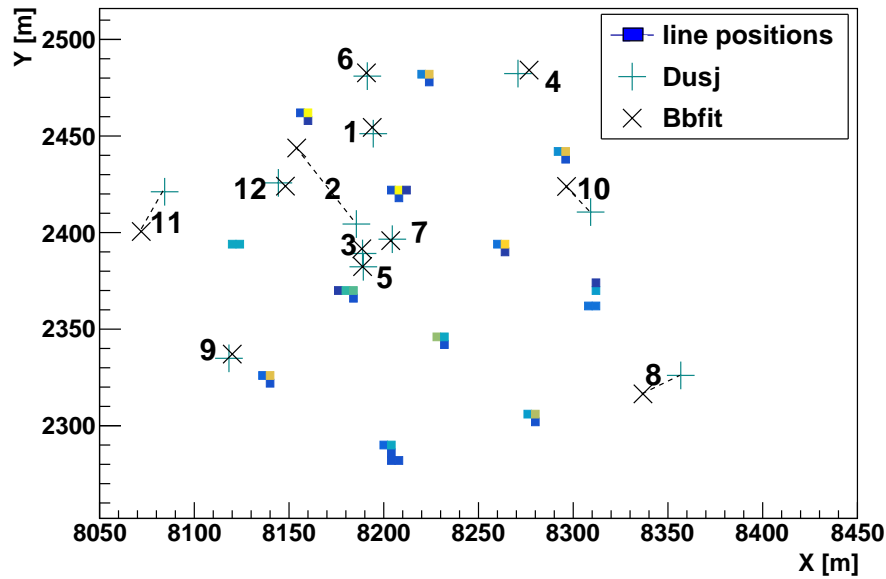


Figure 9.3: Shower vertex positions as reconstructed by the BBFit Bright Point fit and the Dusj reconstruction for the 12 events of selection 1.

**Cosmic neutrino classification** In Figure 9.2, the distribution of the multivariate selection parameter values of the final events can be seen. It is interesting to note that none of the events shows a high parameter value for the atmospheric muon classifier, i.e. the identification of neutrino events in the high-energy region is not as clear as simulation indicates. Considering the input parameters to the classifier, one can only speculate as to the source of that deficit, which might stem from e.g. inaccuracies on the timing structure of the photon distribution, e.g. through scattering. Surprisingly, this deficit is not seen for the cosmic neutrino classifier. Here, the clear identification of high-energy neutrinos which therefore are considered cosmic candidates works well, with one event, number 17, being identified by both classifiers as high-energy neutrino.

**Event topology** The events studied in this analysis generally exhibit similar event topology which allows each to be reconstructed as both track and cascade events. As the events are found to be either interacting close to the detector or inside the instrumented volume, the number of photons measured by the detector is generally large. A vertex can be reconstructed for all events, and both the BBFit Bright Point fit and the Dusj shower reconstruction largely agree on the vertex position, see Figure 9.3, where those markings coinciding actually belong to the same events. This indicates that even for the track-like events, the sub-showers from radiative processes of the muon energy loss are well-identifiable as showers within the detection volume. This reflects the initial intent of the analysis to draw on generalizable event properties for all neutrino flavours.

**Angular reconstruction** The zenith angle reconstruction seen in Figure 9.4a shows the general agreement of direction reconstruction for both shower and track direction reconstruction. As the direction reconstruction accuracy of the Dusj method is quoted in [69] to be between

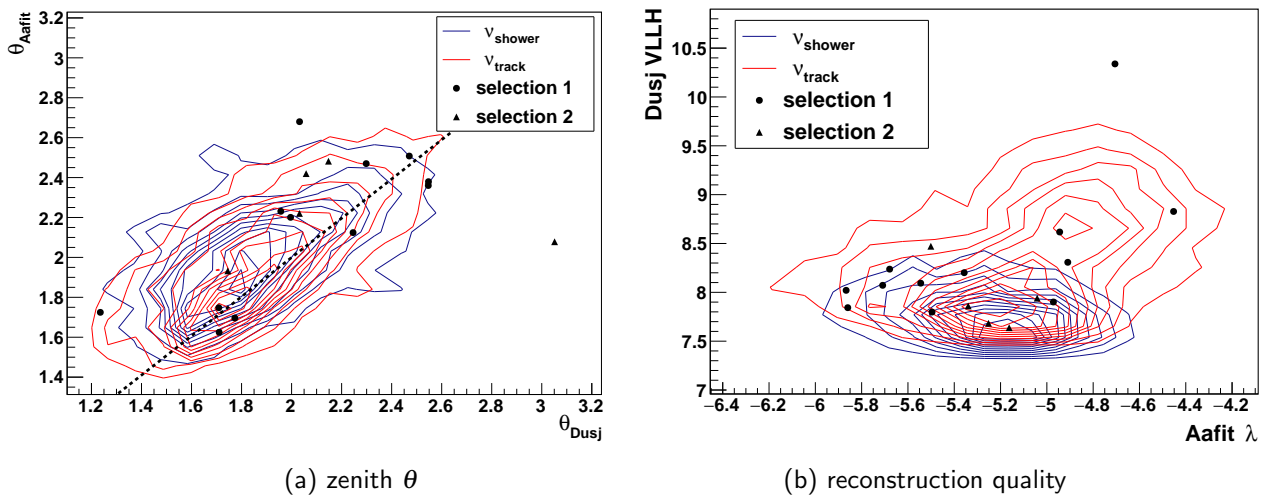


Figure 9.4: Reconstruction parameters for the selected events from run selections 1 and 2 compared to the expectation of track- and shower-like atmospheric neutrino events; 9.4a reconstructed zenith angle from Dusj and Aafit reconstruction and 9.4b the cascade likelihood from the Dusj VertexLogLikelihood parameter and Aafit’s quality parameter  $\lambda$ .

$20^\circ - 40^\circ$ , most events show reasonable agreement in zenith angle reconstruction. Assuming that a cascade from radiative energy loss processes is boosted in the direction of the primary muon, it is reasonable that this direction reconstruction yields comparable results. On the other hand, a track-like direction reconstruction of a cascade resembles a one-particle approximation of the cascade and would yield a comparable reconstruction result. However, in these cases the error on the track zenith reconstruction naturally cannot be assumed to be as accurate as the usual  $< 1^\circ$ , as cascade topology generally does not allow for this.

**Reconstruction quality** The comparison of track and shower reconstruction parameters, on the other hand, shows that it is generally difficult to assign each event an easy label of “track” or “shower”. Remembering the hard quality parameter cuts from earlier analyses, which required e.g.  $\text{Dusj VLLH} < 7.9$  or  $\lambda_{\text{Aafit}} > -4.9$  in shower or track diffuse analyses respectively, most events in this analysis are assigned a lesser shower or track quality, with generally higher event quality for the shower reconstruction. This result is actually partially the target of the design of the analysis, as obviously here events are included in the final sample which would not have shown up in a signature-specific analysis, but are still clearly identified as high-energy neutrino events.

**Energy reconstruction** Energy reconstruction for high-energy events is always dependent on the reference event sample used to map the statistical distribution of an energy reconstruction parameter to an actual event energy. Therefore, the reconstructed energies show both the overall brightness of the event in the detector as well as the evaluation of this brightness towards the reference sample of shower and track events. Therefore, the interpretation of a track energy reconstruction assumes a higher overall neutrino energy, as it interprets the cascade as only a part of the overall energy deposition, while the shower reconstruction mostly assumes

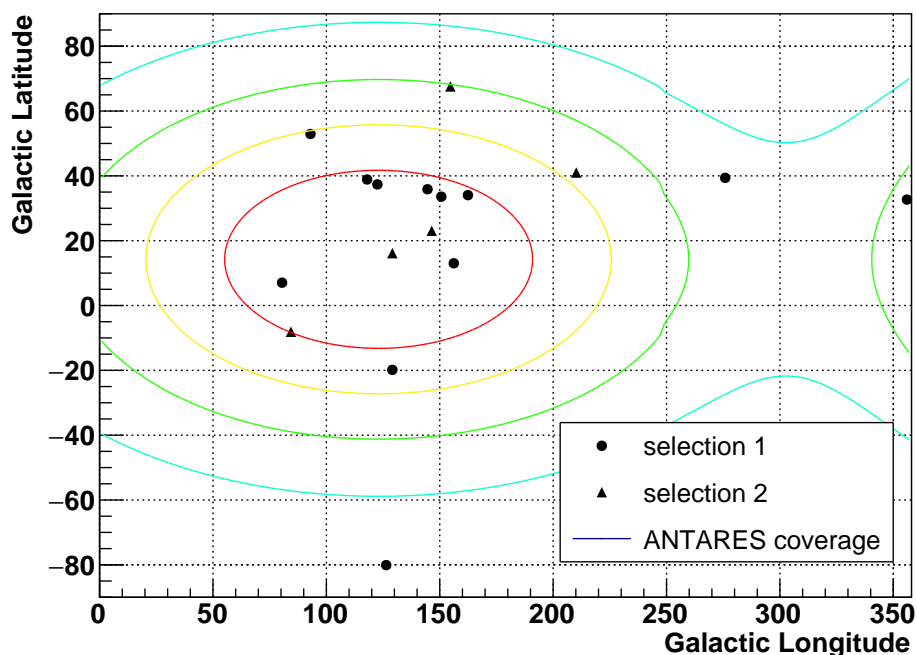


Figure 9.5: Galactic latitude and longitude of the final events as reconstructed by the Aafit track reconstruction. The lines give an approximation of the coverage of *ANTARES* of the full sky from simulation.

a complete energy deposit in the cascade. With energy, an exceptionally bright event would also be most likely a cosmic neutrino candidate independent of the interpretation as track or shower event. Therefore, in Figure 9.9, the *Dusj* reconstructed energy is shown for the final events and compared to simulation, showing no indication of exceptionally high-energy events.

**Galactic coordinates** In Figure 9.5, the neutrino direction of origin as reconstructed with the Aafit algorithm can be seen. As the distinction between cascade and track event is not easily possible and angular reconstructions for *Dusj* and Aafit do not always concur, the attached error in direction reconstruction must be assumed larger than that for a clearly distinguishable muon track. The outlines roughly indicate the *ANTARES* coverage of the sky in this analysis, showing that the event distribution according to Galactic coordinates does match the expectation.

**Event topology** In Figures 9.6 and 9.7, two exemplary neutrino events (12, 17) are shown, one from each selection. Within the final event sample, they show the most extreme versions of what could, by eye, be rather classified as cascade-like or track-like event. This impression is supported by the fact that they are actually included in signature-specific analyses. In Event 12, the comparison between the *Dusj* hit selection and Aafit hit selection shows why simultaneous reconstruction as track and shower works well: due to the comparatively small size of the detector, usually only a few detection lines register hits, with the track reconstruction gathering further hits outside the bulk of clearly distinguishable correlated high-amplitude hits, leading to a clearer interpretation as elongated track. In this case, the direction reconstruction also agrees much better than in cases like event 17, which is clearly a burst of correlated photons, strongly

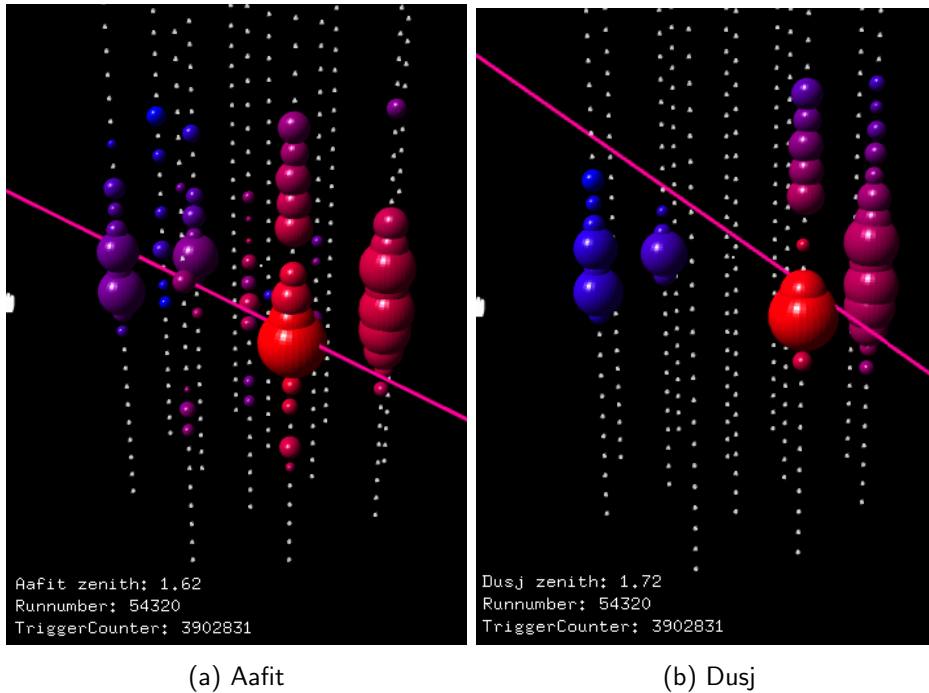


Figure 9.6: Event 12 as shown in a 3D animation using the Aafit and Dusj hit selection and reconstruction, with white dots indicating the position of detection units, bubbles representing hits with diameters proportional to the hit amplitude and colour showing hit time coded from red (early) to blue (late). Red lines show the track or cascade directional reconstruction. This event reaches the highest track quality parameter  $\lambda = -4.46$  and is contained in the point-source search.

illuminating the lower edge of the detector, but with no discernible outlying hits. Here, direction reconstruction shows a larger divergence between the two reconstruction methods. This event was allocated the highest signal probability, and is clearly a neutrino event, however, not very well suited for the classical task of neutrino point-source analysis.

This confirms an impression already indicated in the toy analyses in Chapter 5, in which the cascade-only diffuse flux analysis reached a generally better result compared to track-only analyses. Especially with the compact detector set-up, and no need for a good direction reconstruction, burst-like events which deposit a high number of photons in the OMs are considered as well-identifiable neutrinos.

### 9.3 Results from selection 1

The two data selections resulting from the data-simulations matching process in Chapter 7.1 show widely diverging results: Selection 1, consisting of runs for which the dedicated simulation shows a good agreement according to the established quality parameters, also returns a result that is close to the expectation. Also, these runs had been used in other analyses to success.

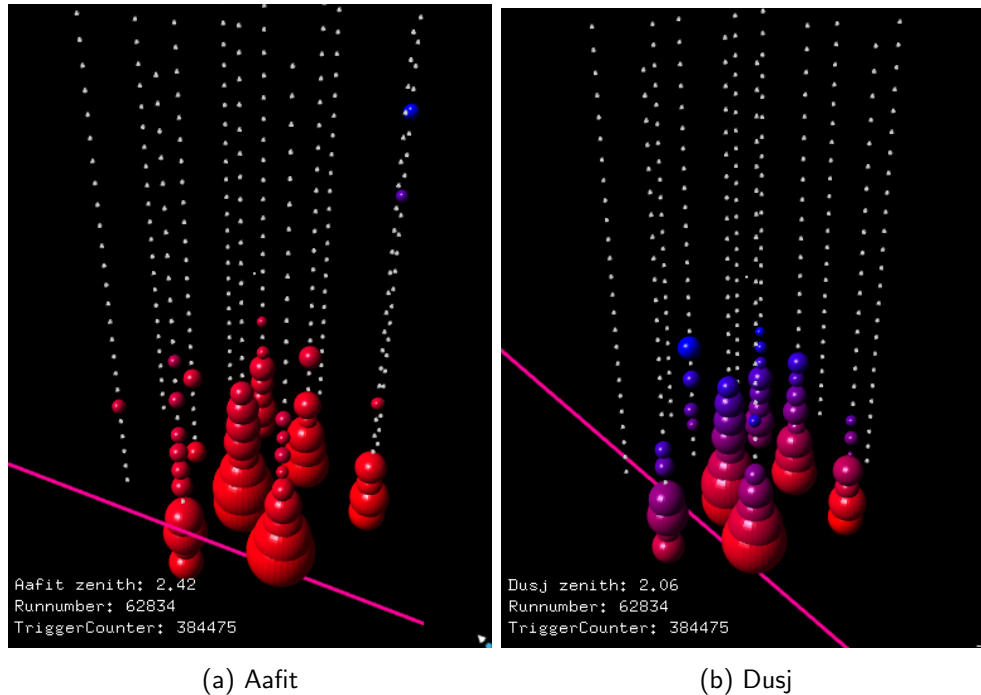


Figure 9.7: Event 17 as shown in a 3D animation using the Aafit and Dusj hit selection and reconstruction. It shows the highest probability as cosmic event (Fisher = 0.7) and is contained in the the shower diffuse flux analysis.

In selection 2, various problematic issues accumulate. They consist of runs for which either the original run simulation did not match well enough according to the criteria, or runs for which no simulation with the same simulation setup was available.

The attempt to bridge this gap of missing simulation, especially for the latest data taking period of 2013, seems not to have had the desired effect. For the sample of selection 2 dominated by atmospheric neutrinos, i.e. after the cut on the atmospheric neutrino classifiers, only 80% of the expected number of events was found, see Figure 9.1d. The deficit actually increases for events with a high probability for cosmic neutrino origin, i.e. high atmospheric neutrino classifier value, which already hints towards the deficit found in the final event selection. While investigating the possible reason for this discrepancy in selection 2 later, a closer look is first taken at the results for the selection 1 events, from which sensitivity estimates for this analysis are drawn. Limiting the analysis to this selection reduces the data taking time to 913.5 days. All additional event contribution estimates were re-evaluated for this sample and the according error estimates calculated, with the results shown in Table 9.3.

### 9.3.1 Sensitivity and energy range

Measurements by *IceCube* have already established the presence of a cosmic neutrino flux, which is reflected in the cosmic neutrino flux models used in this analysis. Therefore, the task of this analysis lies in the confirmation of the measurement within the *ANTARES* data. However, as the

Signal	$N_{\text{events}}$	$\epsilon$	$\epsilon_i$
$N^{2.5} \nu_{\mu, \text{CC}}$	1.4	0.64	$0.47^{c1} + 0.44^{c2}$
$N^{2.5} \nu_{\mu, \text{NC}}, \nu_e$	2.6	1.17	$0.88^{c1} + 0.77^{c2}$
$N^{2.5} \nu_{\tau}$	0.9	0.55	$0.55^f$
$N^{2.0} \nu_{\mu, \text{CC}}$	1.8	0.68	$0.30^{c1} + 0.61^{c2}$
$N^{2.0} \nu_{\mu, \text{NC}}, \nu_e$	2.2	1.0	$0.66^{c1} + 0.75^{c2}$
$N^{2.0} \nu_{\tau}$	0.6	0.43	$0.43^d$
IceCube 2.5 $N_{\text{cos}}$	4.9	$\pm 2.36$	
IceCube 2.0 $N_{\text{cos}}$	4.6	$\pm 2.11$	
Background	$N_{\text{events}}$	$\epsilon$	$\epsilon_i$
$N_{\text{Honda}} \nu_{\mu, \text{CC}}$	5.3	3.87	$0.58^a + 3.59^{c1} + 1.33^{c2}$
$N_{\text{Honda}} \nu_{\mu, \text{NC}}, \nu_e$	2.4	1.42	$0.92^a + 1.08^{c1} + 0.07^{c2}$
$N_{\text{Enberg}} \nu_{\mu, \text{CC}}$	0.2	0.2	$0.2^b$
$N_{\text{Enberg}} \nu_{\mu, \text{NC}}, \nu_e$	0.6	0.6	$0.6^b$
$N_{\text{Enberg}} \nu_{\tau}$	0.01	0.01	$0.01^b$
$N_{\mu_{\text{atm}}}$	1.0	0.48	$0.48^e$
Atmospheric $\Sigma$	9.51	$\pm 6.58$	

Table 9.3: Signal and background expectation including error estimates for 913 days of *ANTARES* lifetime. As cosmic flux, the *IceCube* measurement is used assuming either a spectral index  $\lambda = 2.5$  or  $\lambda = 2.0$ , see Appendix A.3.1. Error estimates are drawn from a) difference between the atmospheric muon model by Honda et al. [30], b) the assumption of a non-existing prompt component, c1) error from absorption length variation  $\epsilon_{\text{abs}}$ , c2) error from scattering length variation  $\epsilon_{\text{scat}}$ , d) the difference between  $\nu_{\tau}$  estimate and simulation and e) variation from muon model fit processes

expected event numbers indicate, neither the confirmation or rejection of the cosmic neutrino flux can be performed to a high statistical certainty, but rather serve as a quality benchmark for an analysis.

**Sensitivity towards the cosmic neutrino flux** In Chapter 5.1, the model rejection factor had been introduced. It serves as the basis to calculate the detection sensitivity  $\Phi_l$  as  $\Phi_l = \mathcal{R}_l \times \Phi_{\text{test}}$ . For the two standard test fluxes  $\Phi_{\text{IC}2.5}$  and  $\Phi_{\text{IC}2.0}$  with  $\gamma = 2.5$  and  $\gamma = 2.0$ , the sensitivity assuming a 90% confidence interval were therefore calculated, and the corresponding energy ranges within which 90% of the events are included are deduced from the according simulation. The two spectral indices generally reflect the range of possible flux assumptions. A diffuse flux with  $\gamma = 2.0$  follows the model of Waxman and Bahcal [70] and was here assumed with a normalization of  $\Phi_{\text{IC}2.0} = 1.1 \times 10^{-8} \text{ GeV}^{-1} \text{ sr}^{-1} \text{ s}^{-1} \text{ cm}^{-2}$  following the magnitude of *IceCube* measurements. In this analysis, a sensitivity towards this flux per flavour of  $\Phi_{90\% \text{IC}2.0} = 1.57 \times 10^{-8} \text{ GeV}^{-1} \text{ sr}^{-1} \text{ s}^{-1} \text{ cm}^{-2}$  is reached, valid within 16.4 TeV to 7.1 PeV.

On the theoretical other end of flux assumptions and well within the *IceCube* measurements presented in Chapter 1.3.2, a flux of  $\Phi_{\text{IC}2.5} = 4.1 \times 10^{-6} \text{ GeV}^{-1} \text{ sr}^{-1} \text{ s}^{-1} \text{ cm}^{-2}$  would be detected with a sensitivity of  $\Phi_{90\% \text{IC}2.5} = 1.35 \Phi_{\text{IC}2.5}$  per flavour, valid between 6.74 TeV and 1.12 PeV.

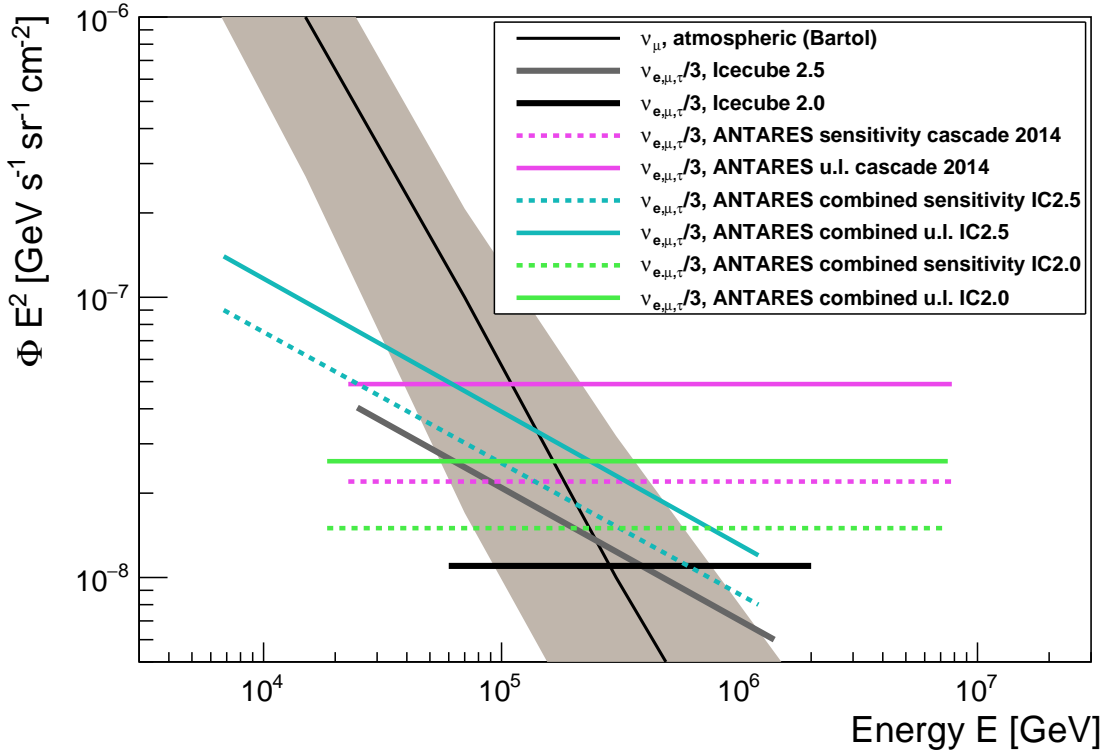


Figure 9.8: Flux limits for the last track and cascade analyses in ANTARES, the *IceCube* result and limits and sensitivity and upper limits of this analysis.

### 9.3.2 Upper limit and discovery

An upper limit to a given flux can be introduced as Feldman-Cousins upper limit  $\mu_{90\%}$ , see Chapter 5.1. However, this construction does not allow to take into account the systematic uncertainties of signal and background event number estimates. In order to compensate for this omission, a frequentist construction of confidence intervals with Bayesian treatment of systematic uncertainties was developed and implemented in the POLE program [71], which will be used here to calculate the upper limit on the flux assumptions.

In this construction, the confidence belt is searched for a number of observed events  $n_{\text{obs}}$  with an assumption of background events  $b$  and signal events  $s$  such that a confidence belt  $[n_1(s+b, \alpha), n_2(s+b, \alpha)]$  for a confidence level  $1 - \alpha$  is covered with  $\sum_{n=n_1}^{n_2} p(n)_{s+b} = 1 - \alpha$  for a Poisson distribution of events. To allow for uncertainties, the probability  $p(n)$  is extended to the conditioned probability  $q(n)$  by including a Gaussian distribution with uncertainty  $\sigma_\varepsilon$  of the detection efficiency  $\varepsilon$  relative to the nominal efficiency and uncertainty  $\sigma_b$  of the background event number,

$$q(n)_{s+b} = \frac{1}{2\pi\sigma_b\sigma_\varepsilon} \int_0^\infty \int_0^\infty p(n)_{b'+\varepsilon's} e^{-(b-b')^2/(2\sigma_b^2)} e^{-(1-\varepsilon')^2/(2\sigma_\varepsilon^2)} db' d\varepsilon', \quad (9.1)$$

In addition to that, the symmetrical calculation of the limit is adjusted such that for  $n < n_{\text{obs}}$  the consideration is included the actual number of background events  $b$  cannot be larger than  $n_{\text{obs}}$ , shifting the confidence belt construction.

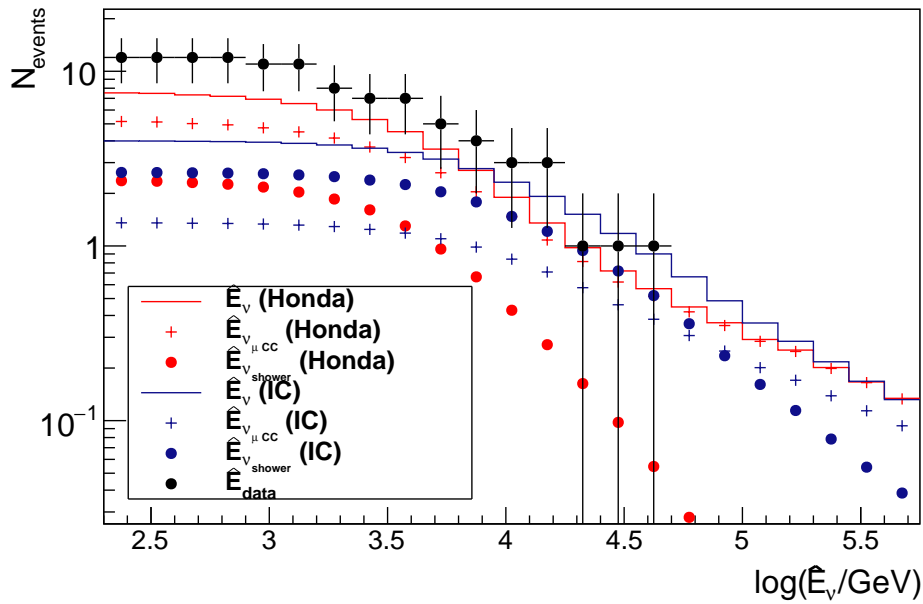


Figure 9.9: Integrated energy distribution for the events found in 913 days, giving the reconstructed neutrino energy  $\hat{E}_{\text{Dusj}}$  of the Dusj reconstruction for data and simulated  $\nu_e$  and  $\nu_\mu$  contributions.

Using the construction including error estimates, upper limits on the respective fluxes can be set as  $\Phi_{90\%u.l.IC2.5} = 4.1\Phi_{IC2.5}$  and  $\Phi_{90\%u.l.IC2.0} = 4.2\Phi_{IC2.0}$  within the same energy ranges as the above quoted sensitivities. Sensitivities, upper limits and the reference fluxes are shown in Figure 9.8.

For completeness it should be noted that the measurement of 12 events while expecting 9.51 background events corresponds in a Gaussian distribution to a deviation by  $0.98\sigma$ , which in scientific terms amounts to nothing noteworthy, and falls short from the expectation of a combined event number of signal and background of about 14 events.

### 9.3.3 Detecting a diffuse cosmic neutrino flux

Comparing the results of this limited combined track and shower analysis to the signature-specific analyses in *ANTARES*, the assumptions from the toy analyses in Chapter 5.2 are confirmed. In the latest track analysis [16], which uses data of 1247 days, a sensitivity of  $2.21 \times 10^{-8} \text{ GeV}^{-1} \text{ sr}^{-1} \text{ s}^{-1} \text{ cm}^{-2}$  is reached, which is the most sensitive benchmark this analysis has to be compared to. As the two analyses were performed on the basis of the same simulation, their sensitivity estimates can be assumed as comparable, even if the above lack of neutrino events in selection 2 indicates a problem in the simulation accuracy for newer measurements. In Figure 9.8, sensitivities and limits from various *ANTARES* analyses are shown in comparison with the results of this analysis. The combined analysis proves to be more powerful than the separate signature-specific analysis or a simple addition of the separate analysis. However, a larger

increase of simulation sensitivity can be expected once the discrepancies between simulation and measurement can be overcome.

**High-energy neutrinos** As the lower number of events in measured data than in simulation most probably stems from a decreasing photon efficiency of the apparatus, it can be assumed that high-energy neutrino events might still be well distinguished in relation to the atmospheric background. In order to distinguish neutrino events with a high possibility of cosmic origin, an energy estimator has to be employed. As no specific energy estimator was included in the analysis, the  $D_{\text{usj}}$  energy reconstruction is displayed in Figure 9.9 to this end. Considering that track events might be interpreted as cascades and a decreasing photon efficiency might not be well modelled within the simulation, it can be assumed that event energy is rather underestimated than overestimated. However, while the energy distribution of the final events follows expectations from simulation, no event with an unexpectedly high energy indicating a large probability of cosmic origin was found.



# 10 | Investigation and Outlook

It was shown in the previous part that the analysis method has its merits in the higher sensitivity towards a diffuse flux, a finding that was underlined by a follow-up analysis [72] using a comparable approach to the one introduced in the toy study in Chapter 5 as C1 with a combination of an initially separated track and shower analysis. Before taking a short look at this new analysis, the shortcomings of the present analysis should be inspected further. One drawback of the analysis are the large errors on simulation parameters which have to be included in the rough estimate used above. Recent investigations of water properties and detection efficiency have helped to reduce this error estimate for the current production of run-by-run simulation, which are shortly outlined below. Above all, the run matching procedure introduced above might be useful to find replacement simulations for neighbouring runs with comparable data taking conditions, but seems to be inadequate for the matching of runs from different data taking periods.

## 10.1 Simulation discrepancies

### 10.1.1 From the run matching procedure

In the run matching procedure, see Chapter 7.1, the matching criteria for runs are primarily the agreement in the parameter distribution for input parameters to the multivariate tools in the atmospheric muons of the runs. Assuming that the variation in data taking conditions from bioluminescence and different detector configurations introduces the largest uncertainty in the agreement between data and simulation, this seemed fitting. However, the outcome of the analysis shows that, on the one hand, the effects on the atmospheric muon sample cannot always be assumed to hold for atmospheric and cosmic neutrino events due to the different event characteristics like average photon yield and particle direction. On the other hand, agreement in the input parameters does not necessarily lead to an agreement of the output parameter of a multivariate tool, as can be seen in Figure 10.1. In the run matching, the agreement of all input parameters to the classifiers was a prerequisite for a match, but not the agreement of the classifiers themselves. While the atmospheric muon classifier still shows a good agreement for most runs, the atmospheric neutrino classifier shows a wide deviation in the measured events of the matched run, although the original run and its simulation still agree well. This shift is not observed for earlier runs matched within a shorter time frame. This shows that a qualitative change has appeared in these later runs which is not represented in the simulation, and that the matching procedure is not useable for runs between which a larger time span elapsed, as long-term effects of measurement seem to have a significant impact on the data taking.

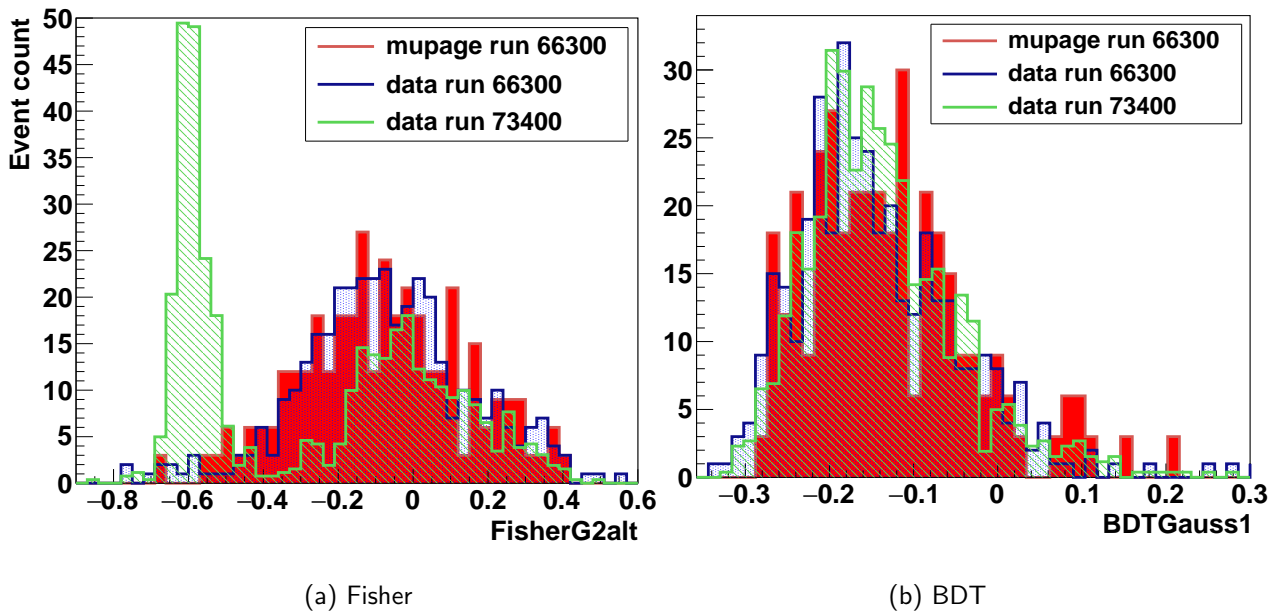


Figure 10.1: Comparison of the parameter distribution for both multivariate parameters for all measured events after application of the TMVA classifiers and connected cuts in a stage 2 run (run 73400, scaled to equal lifetime) and its matched stage 1 run (run 66300) and the mupage simulated events used for both runs.

### 10.1.2 From water properties modelling

As cause for these long-term effects, ageing of the optical modules and a change in the water properties was suspected, so the next step of the run-by-run simulation version 3 already implemented additional changes in the water properties in the simulation software (see Appendix A.1.1), the effect of which is shown in Figure 10.2. The comparison between the distribution of the classifiers for both simulation versions show that the altered water modelling parameters lead to a general shift of the classifier towards lower values, which is true for the whole duration of data taking. It shows that the deficit in the event number estimate not only stems from the run matching procedure but also from the too idealistic assumptions of water properties in the old simulation set, and is therefore not only limited to stage 2 runs, but is, to a lesser degree, also present in the stage 1 runs.

**Further adjustment of the water modelling** The water model was once more revised for the version 4 simulation, and comparisons between measurement and simulation performed using different water models, see Figure 10.3a. For example, the attenuation length was deduced from the photon number over distance for atmospheric muons, see Figure 10.3b. The investigation lead to the application of a model closer to the Nemo water than the former *ANTARES* model.

### 10.1.3 From OM efficiency modelling

Apart from the analysis presented here, also other analyses including newer measurements showed indications of discrepancies between simulation and data which generally could be traced to a lower photon detection efficiency of the detector than was assumed in the simulation. This

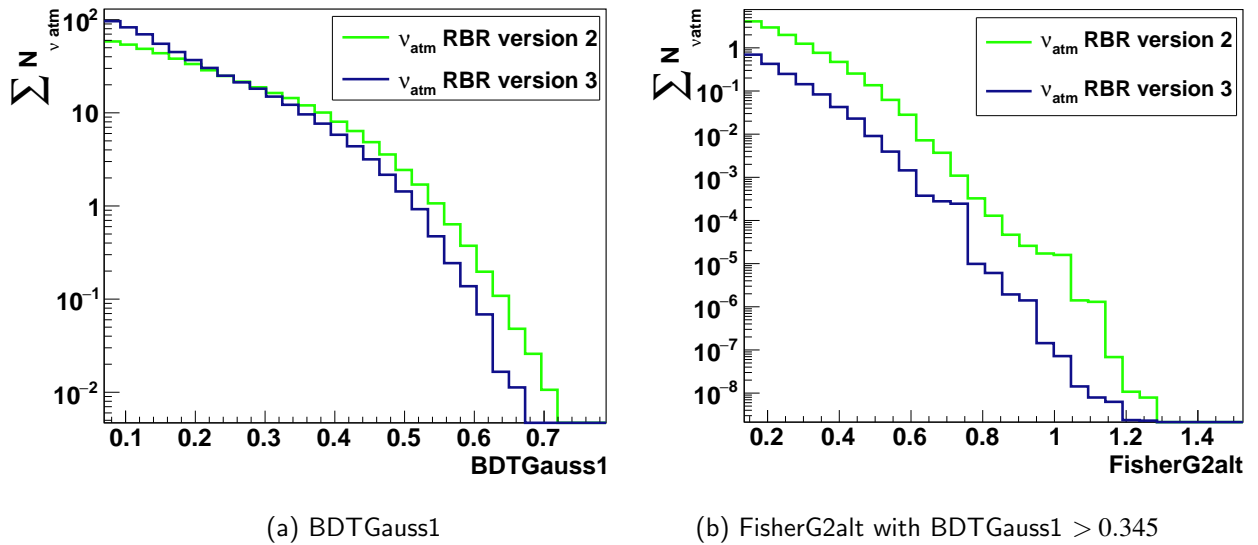


Figure 10.2: Comparison of the parameter distribution of atmospheric neutrinos (Bartol) for the atmospheric muon and atmospheric neutrino classifier for 59 simulated runs from the test sample in run-by-run simulation version 2 and 3. The atmospheric neutrino classifier is shown after the analysis cut on the atmospheric muon classifier.

triggered investigations into the OM photon efficiency and ageing effects especially for the later data taking years starting from 2013.

**OM efficiency** As introduced in Chapter 2.3.2, the OM efficiency is primarily calculated from the K40 coincidence rate in neighbouring OMs. First of all, a reduction of the collection efficiency by 15% was added, as well as an OM-by-OM modelling of the individual efficiency from K40 measurements in 6 day intervals. The higher attenuation length together with the reduced OM efficiency which increases with ageing might partially explain the deficit of well identifiable cosmic neutrinos, as a lower photon yield is measured especially for high energy events compared to atmospheric muon events. However, to prove this point, more detailed studies on the new simulation would have to be performed.

## 10.2 Signature-specific analysis and update

Lately, a combined diffuse flux search has been performed in *ANTARES* with track-specific and shower-specific parameter cuts were applied on 9 years of data [72]. The analysis was able to make use of the updated simulation and 2450 days of equivalent livetime. The sensitivity reached in the analysis for  $\lambda = 2.0$  is  $\Phi_{90\%|C2.0} = 1.2 \times 10^{-8} \text{ GeV}^{-1} \text{ sr}^{-1} \text{ s}^{-1} \text{ cm}^{-2}$ . Also, the error on the background assumption with this simulation is given as about 30%, which outperforms the above used simulation. Comparing the two analyses, the close sensitivity of the above presented combined search approach with less than half the data indicates what potential the analysis approach holds for the full data set and an updated simulation.

Naturally, the cut parameter optimization procedure would have to be repeated for an update including the full simulation. On the other hand, the multivariate tools would not need to

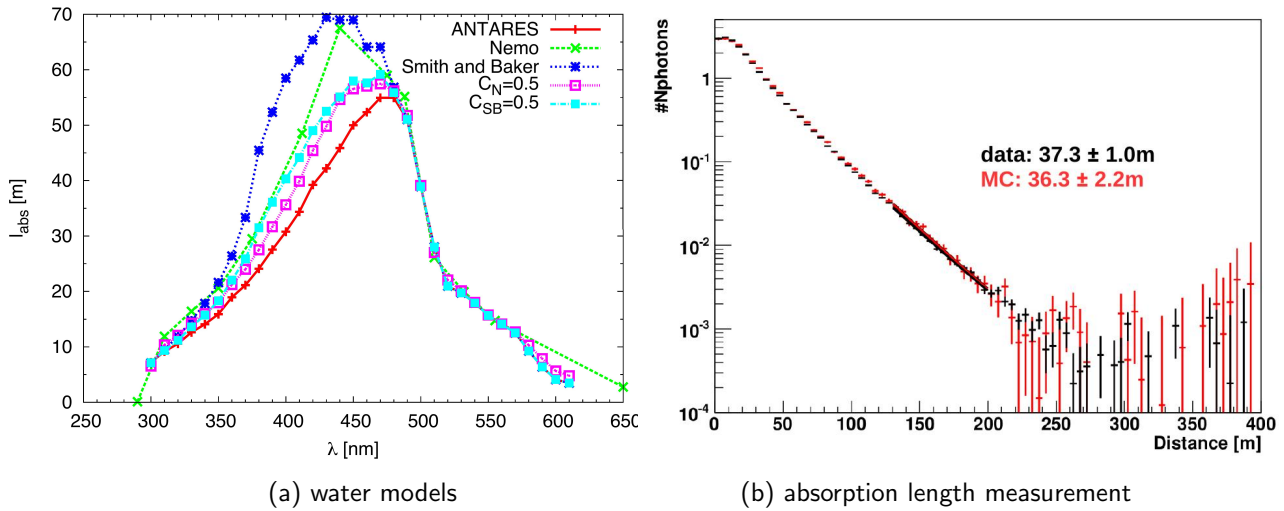


Figure 10.3: Water models tested for the *ANTARES* site, from [73] and measurement of the absorption length from atmospheric muons. From [74].

be readjusted, as they model the intrinsic dependencies between the input parameters rather than depend on their explicit values and have been driven to a level of sophistication where renewed training might only yield little improvement compared to the overall uncertainties in the simulation and the time invested in training.

Also, the subdivision of the full data sample into shorter data taking periods with comparatively stable conditions and a cut optimization for each sub-sample rather than an overall cut on the full data sample would have to be introduced. This would on the one hand circumvent the deficit of events identified as cosmic neutrinos increasing with an ageing detector, as the adapting of the detection threshold for cosmic events could follow the detector's OM efficiency. On the other hand, it would also allow a more detailed monitoring of the influence of detector ageing on the analysis cuts.

Last but not least, the analysis presented here has shown that, especially for a smaller scale detector like *ANTARES*, a combined search for a cosmic neutrino flux which at the first stage disregards the classification of the specific event signature shows at least the potential of a signature-specific search.

# Conclusion

In this analysis, the search for a diffuse cosmic neutrino flux has been pursued for events from all neutrino flavours measured in the *ANTARES* detector as muon tracks or particle cascades.

At the core of the analysis lies the development of two dedicated multivariate tools to target the task of suppression of events from the atmospheric muon background on the one hand and to distinguish the cosmic neutrino signal from atmospheric neutrinos on the other hand in Chapter 6. For these classifiers, observables used in both track and shower neutrino event reconstructions as well as additional new parameters were tested for use in a variety of multivariate tools. For atmospheric muon suppression, the optimization procedure aimed to separate the bulk of atmospheric muons from neutrino-generated events, a task for which a boosted decision tree was found to work best. For the separation of cosmic neutrino events from the atmospheric background, a Fisher discriminant using mostly energy-related features was trained to separate events especially in the high-energy region of neutrino events in the *ANTARES* detector. With these tools, the novel approach of this analysis was implemented, drawing on these two dedicated classifiers designed for the common use on muon tracks and cascade events instead of an event-type specific event selection strategy.

The analysis was optimized for both signal detection and model rejection on a Monte-Carlo simulation explicitly reproducing the specific data-taking conditions at the time of measurement. However, these simulations were still under development, lacking a production for  $\nu_\tau$  generated events and measurements taken after 2012. Therefore, a run matching procedure was introduced for the missing simulation runs relying on similar parameter distributions in atmospheric muons in the matched runs, see Chapter 7, and dedicated low-statistic productions of additional event types were added. After establishing the full event selection chain, cuts and classifiers were tested on 10% of the full set of measurements, for which a good agreement between simulation and measurements could be established. However, on applying the analysis chain to the full set of measurements, a deficit of events from expectation was found especially in the latest run taking period, which can most likely be traced to an overestimation mainly of the detector's photon sensitivity after several years of data taking by disregarding OM ageing. Therefore, the analysis was limited to a data sample of 913 days for which the run matching procedure showed a good agreement between simulation and measurement. For this sample, a sensitivity to an IceCube-like flux with either  $\lambda = 2.0$  or  $\lambda = 2.5$  was reached that shows the advantage of a flavour-combined analysis to a flavour-specific diffuse flux analysis, as a sensitivity of  $\Phi_{90\%|C2.5} = 1.35 \Phi_{|C2.5}$  for  $\Phi_{|C2.5} = 4.1 \times 10^{-6} \text{ GeV}^{-1} \text{ sr}^{-1} \text{ s}^{-1} \text{ cm}^{-2}$  between 6.74 TeV and 1.12 PeV is reached, and  $\Phi_{|C2.0} = 1.1 \times 10^{-8} \text{ GeV}^{-1} \text{ sr}^{-1} \text{ s}^{-1} \text{ cm}^{-2}$  leads to a sensitivity of  $\Phi_{90\%|C2.0} = 1.57 \times 10^{-8} \text{ GeV}^{-1} \text{ sr}^{-1} \text{ s}^{-1} \text{ cm}^{-2}$  valid within 16.4 TeV to 7.1 PeV.

In the 17 events detected for the full event sample, events from both former point-source analysis as well as from a former diffuse cosmic flux search with cascades were included, together with events which would not fit a strict track- or cascade-type event selection. Therefore, the combined analysis identifies both signature-specific cosmic neutrino candidate as well as adds events which are not so easily placeable as shower or track candidate, but still show a high cosmic signal probability. The analysis therefore explores a part of the feature space formerly inaccessible for signature-specific analysis and gains from this an enhanced sensitivity.

The drawback of the analysis lies in its lack of dedicated simulation, which by now has been remedied by the production of follow-up simulations both implementing  $\nu_\tau$  events well and including a more adequate simulation of detector ageing effects. A re-application of the analysis chain to the new simulation is recommended, although it is now longer in the scope of this thesis. The lack of cosmic neutrino candidates for data recorded after 2012 can most likely be avoided by introducing parameter cuts which are optimized within a shorter data taking period than the full sample, as relevant features for the classifier output parameters seem to change within this time span. An analysis approach including common features of both signature types can therefore also be recommended for the future generation of similarly constructed water-based detectors, namely the KM3NeT detector, for which the increased size should allow for a more solid confirmation of the *IceCube* diffuse flux discovery.

# A | Appendix

## A.1 Monte Carlo Simulation Definition

### A.1.1 Run-by-run simulations v2 and v3

The simulation chain for the run-by-run production v2 is given in detail in [35]. It includes the production v2.2, which implements shower-like events. It uses MUPAGE v3r5, GenHen v6r8, KM3 v4r2, GeaSim v4r13 and TriggerEfficiency from 2011-12-19.

In comparison to this, v3 advances to GenHen v7r1, KM3 v5r1 with an updated light propagation code. GeaSim is dropped and a one-particle approximation for showers introduced in KM3. Additional simulations to this analysis were based on the v3 chain.

### A.1.2 Additional simulations

The runs included in the production should be usable for extensive comparisons, therefore they had to be included in the burn-sample of zero-ending runs in order to be usable in data comparisons, and should have a full standard simulation available. Therefore selection criteria for the reference runs are

- only runs with complete data processing
- runs ending in \*10 and \*60
- runs available in run-by-run version 2 and 3

This results in the selection of 119 runs with a total lifetime of 12.7 days.

**Reference runlist** 26710, 26810, 27660, 27760, 28110, 28510, 30060, 30110, 30160, 30310, 31360, 32110, 32160, 32260, 32360, 32710, 33110, 33210, 34560, 34610, 34860, 34960, 35060, 35160, 35910, 36110, 36160, 36210, 36860, 38110, 38610, 39760, 40660, 40710, 40910, 41310, 41560, 43610, 43760, 43860, 44060, 45110, 45210, 45860, 46310, 46360, 46460, 46510, 46610, 46710, 47610, 47710, 49710, 51160, 51710, 51810, 52710, 53510, 53660, 53710, 53860, 53910, 53960, 54060, 54110, 54260, 54610, 54710, 55110, 55210, 55760, 55810, 56610, 56710, 56760, 57260, 57310, 57360, 57560, 57610, 58560, 59110, 59460, 59810, 59860, 59910, 59960, 60060, 60260, 60410, 60460, 60610, 60910, 61160, 61210, 61410, 61710, 61760, 61960, 62110, 62260, 62560, 63060, 64760, 64810, 64960, 65160, 65310, 65360, 65410, 65610, 65760, 66060, 66260, 66310, 66510, 66760, 67360, 68160.

**Runs for  $\tau$  production and water properties studies** 26810, 28110, 31360, 32710, 34860, 36210, 38610, 41560, 46460, 52710, 54110, 55110, 55760, 56760, 57360, 59860, 60460, 60910, 61960, 65610, 66260, 66760, 65160, 53710.

### Mupage high multiplicity muon simulation

**Lifetime calculation** The total sample of high-multiplicity muon bundles should be the equivalent of at least one year data taking. Therefore the lifetime of each run had to be scaled such that the total lifetime of 360 days was reached. Therefore the muon weight for each run in the toy production is  $w_\mu = 1/30$ .

However, since Mupage accepts no direct input of lifetime but only of number of generated events, the equivalent number of events for one year was estimated from a small muon production of 500 events with muon multiplicities  $m$  between 100 and 1000. According to [41], this corresponds to about 3.5 hours of data taking, i.e. 143 events/hour. In this test sample, the ratio between events above and below  $m = 200$  was roughly  $100 < m < 200 : 200 \leq m < 1000 = 4 : 1$  (see Figure 7.5). Therefore the number of simulated events per run with lifetime  $d$  was calculated as  $N_{\mu m > 200} = 143/\text{h} \times 0.2 = 30 \times d/\text{h}$

As each run was finally scaled to reach one year of total lifetime, the number of events simulated per run are  $N_\mu = 30 \times d/\text{h} \times 1/w_\mu$ .

**Changes in comparison to run-by-run version 3** The mupage data card was adapted in the following parameters

**Emin** minimum energy in TeV: 0.02

**Emax** maximum energy in TeV: 500.0

**Ethreshold** minimum energy of threshold in TeV: 3.0

**MULTmin** minimum multiplicity: 200

**MULTmax** maximum multiplicity: 1000

### $\nu_\tau$ simulation

The following decay channels were implemented in Tauola, the part in genhen version v7r3 included for tau production.

decay channel	branching ratio	decay channel	branching ratio
$\tau \rightarrow e \nu_e \nu_\tau$	1.0000	$\tau \rightarrow 3\pi \nu_\tau$	1.0180
$\tau \rightarrow \mu \nu_\mu \nu_\tau$	0.9832	$\tau \rightarrow K \nu_\tau$	0.0405
$\tau \rightarrow \pi \nu_\tau$	0.6217	$\tau \rightarrow K \pi \nu_\tau$	0.0781
$\tau \rightarrow \pi \pi \nu_\tau$	1.4221		

During processing, an error in the weighting of events was found, assigning an obviously too large event weight to some events. The weight of these events was manually adjusted to fit the expected event weight distribution, however, it can be assumed that event numbers from the simulation are slightly too high.

### Changed water property simulations

In order to compare the effect that uncertainties in the water scattering length  $\lambda_{\text{scat}}$  and absorption length  $\lambda_{\text{abs}}$  has, the listed runs were simulated again using the v3 run-by-run chain, with photon tables in the KM3 photon propagation code within genhen changed thus that the assumed scattering length varied by 10%. This resulted in 4 new runs per reference run with  $\lambda_{\text{scat}0.9} = 0.9 \times \lambda_{\text{scat}}$ ,  $\lambda_{\text{scat}1.1} = 1.1 \times \lambda_{\text{scat}}$  and accordingly  $\lambda_{\text{abs}0.9}$  and  $\lambda_{\text{abs}1.1}$ .

## A.2 Mathematical methods

### A.2.1 Simplified MRF calculation

**Interpolation from tabled values** As the calculation of the  $\mu_i$  demands a higher computing time than the comparatively simple model discovery potential, an estimate for the model rejection factor was introduced. It interpolates  $\mathcal{R}$  from its tabled values for the next lower and upper number of signal events  $n_{s> / <}$  and background events  $n_{b> / <}$  by linear interpolation. Using the background distance  $\bar{n}_b = (n_b - n_{b<}) / (n_{b>} - n_{b<})$  and signal distance  $\bar{n}_s = (n_s - n_{s<}) / (n_{s>} - n_{s<})$ , the estimated model rejection factor is calculated as

$$\overline{\mathcal{R}}(n_s, n_b) = \mathcal{R}_{s<, b<} (1 - \bar{n}_s - \bar{n}_b + \bar{n}_s \bar{n}_b) + \mathcal{R}_{s>, b<} (\bar{n}_s - \bar{n}_s \bar{n}_b) + \mathcal{R}_{s<, b>} (\bar{n}_b - \bar{n}_s \bar{n}_b) + \mathcal{R}_{s>, b>} \bar{n}_s \bar{n}_b. \quad (\text{A.1})$$

## A.3 Fluxes

### A.3.1 Test fluxes

The fluxes are quoted as

$$\Phi(E) = \Phi_{\text{astro}} \times 10^{-18} (E/100 \text{ TeV}^{-\gamma_{\text{astro}}} \text{ GeV}^{-1} \text{ sr}^{-1} \text{ s}^{-1} \text{ cm}^{-2}). \quad (\text{A.2})$$

Name	$\Phi_{\text{astro}}$	$\gamma_{\text{astro}}$	published in
IceCube HESE 4 years	2.2	2.58	PoS(ICRC2015)1081
IceCube combined	7.0	2.49	PoS(ICRC2015)1066
IceCube tracks 6 years	0.90	2.13	[14]
IceCube 2015	6.7	2.5	[75]
IceCube discovery	1.2	2.0	[10]
IceCube classical	2.06	2.46	
IceCube 2.5	1.3	2.5	
IceCube 2.0	1.1	2.0	

## A.4 Parameter selection

### A.4.1 Full parameter list

Parameter	DMC	A2	SOP	Parameter	DMC	A2	SOP
Aafit $\phi$	good	0.04	4.8	Dusj vertex rlogL	good	0.04	5.97
Aafit $\theta$	good	0.01	3.99	Dusj convergence energy	good	0.07	5.98
Aafit position x	bad	0.17	5.48	Dusj convergence x	good	0.08	6.0
Aafit position y	bad	0.2	5.48	Dusj convergence y	good	0.08	6.0
Aafit position z	medium	0.12	5.48	Dusj convergence z	good	0.22	2.47
Aafit $\lambda$	medium	0.17	4.76	Dusj horizontal dist2center	good	0.02	6.0
Aafit $\beta$	medium	0.48	5.48	Dusj vertical dist2center	good	0.0	6.0
Bbfit $\phi$	good	0.0	7.95	Dusj $N_{strings}$	good	0.02	5.48
Bbfit $\theta$	good	0.01	3.31	Dusj quadrupole moment	good	0.01	5.98
Bbfit track position x	bad	0.48	5.73	Dusj $t_{res}\chi^2$	medium	0.42	5.99
Bbfit track position y	bad	0.48	5.7	Dusj $A_{total}$	binning	0.2	5.48
Bbfit track position z	medium	0.21	5.38	Dusj showerId horizontal d2c	medium	0.12	5.89
Bbfit track $\chi^2$	medium	0.58	6.0	Dusj showerId vertical d2c	good	0.01	5.89
Bbfit track $N_{lines}$	crap	0.0	5.48	Dusj showerId reduced $\chi^2$	good	0.03	3.8
Bbfit track dist2line	crap	0.0	100.0	energy R	None	-	-
Bbfit track $N_{hits}$	crap	0.0	5.48	R value	good	0.02	4.76
Bbfit bright position x	medium	0.26	6.01	GridFit position x	binning	0.02	4.41
Bbfit bright position y	medium	0.55	6.01	GridFit position y	binning	0.08	4.41
Bbfit bright position z	good	0.03	5.63	GridFit position z	binning	0.0	4.41
Bbfit bright $\chi^2$	medium	0.58	6.0	GridFit zenith $\theta$	not working	0.0	2.81
Bbfit bright $N_{lines}$	crap	0.0	5.48	GridFit azimuth $\phi$	medium	0.0	4.41
Bbfit bright dist2line	crap	0.0	100.0	GridFit ratio	binning	0.55	5.48
Bbfit bright $N_{hits}$	crap	0.0	5.48	GridFit precut ratio	binning	0.59	2.5
Bbfit $\phi$	nan	0.0	7.94	GridFit width of minimum	good	0.05	4.54
Bbfit $\theta$	nan	0.01	3.91	Krake position x	binning	0.21	5.95
Bbfit bright position x	bad	0.06	7.41	Krake position y	binning	0.22	5.95
Bbfit bright position y	bad	0.04	7.04	Krake position z	binning	0.14	5.95
Bbfit bright position z	medium	0.1	6.65	Krake zenith $\theta$	good	0.0	3.21
Bbfit M-est quality	medium	0.01	5.75	Krake zenith $\phi$	medium	0.0	5.95
Bbfit M-est likelihood	medium	0.01	7.94	Krake rlogl	good	0.01	1.98
Bbfit bright $N_{lines}$	crap	0.01	5.48	Q position x	binning	0.33	100.0
Bbfit bright $N_{hits}$	crap	0.01	5.48	Q position y	binning	0.37	100.0
Dusj $\theta$	good	0.01	2.97	Q position z	binning	0.36	100.0
Dusj $\phi$	good	0.0	6.0	Q zenith $\theta$	medium	0.0	3.47
Dusj position x	binning	0.01	6.0	Q azimuth $\phi$	good	0.0	7.31
Dusj position y	good	0.01	5.99	Q energy E	good	0.07	100.0
Dusj position z	good	0.01	5.86	Q likelihood	medium	0.08	100.0
Dusj energy	good	0.48	5.98	Q total A	medium	0.05	100.0
Dusj fit d.o.f.	binning	0.09	5.48	RDF class	None	0.0	29.24
Dusj value fit logL	binning	0.07	6.0	RDF value	good	0.02	5.48
Dusj fit calls	good	0.29	5.48	ANN energy	good	0.59	5.48
Dusj fit rlogL	good	0.01	5.79	ANN background count	good	0.02	4.76
Dusj vertex d.o.f.	good	0.09	5.48	ANN OM count	good	0.01	4.76
Dusj vertex logL	good	0.06	6.0	ANN $N_{OM}$ triggered hits	medium	0.05	5.48
Dusj vertex calls	good	0.02	5.48	ANN $N_{hits}$ triggered hits	binning	0.08	5.48

Parameter	DMC	A2	SOP	Parameter*	DMC	A2	SOP
ANN $N_{\text{hits}}$ all hits	binning	0.05	5.48	Aafit LargeCharges	medium	0.1	5.48
ANN $\langle A \rangle$ triggered hits	good	0.05	4.76	Aafit Slopes	good	0.25	5.48
ANN $\langle A \rangle$ all hits	good	0.06	4.76	Aafit SlopeWithCharge	good	0.47	5.48
ANN RMS(A) triggered hits	binning	0.04	5.48	Aafit SlopeBigCharge	bad	0.45	0.48
ANN $N_{\text{storey}}$ triggered hits	medium	0.02	4.76	BBFit NHits	good	0.12	5.48
ANN $N_{\text{strings}}$ triggered hits	good	0.01	4.76	BBFit NLargeHits	good	0.15	5.48
ANN track eff. length	good	0.04	4.83	BBFit NStrings	good	0.01	5.48
ANN distance to CoG	good	0.04	5.47	BBFit TotalCharge	medium	0.18	5.48
ANN $\langle d_{\text{cher}} \rangle$ hits2track	binning	0.11	4.81	BBFit LargeCharges	medium	0.17	5.48
ANN $RMS(d_{\text{cher}})$ hits2track	good	0.02	4.76	BBFit Slopes	good	0.62	5.48
ANN $\langle t_{\text{res}} \rangle$ hits2track	binning	0.29	5.48	BBFit SlopeWithCharge	medium	1.0	5.48
ANN $RMS(t_{\text{res}})$ hits2track	medium	0.02	4.76	BBFit SlopeBigCharge	medium	0.38	5.48
ANN duration triggered hits	good	0.04	4.99	Dusj NHits	good	-	-
ANN $\langle v^{-1} \rangle$ all hits	binning	0.81	5.48	Dusj NLargeHits	medium	-	-
ANN $RMS(v^{-1})$ all hits	binning	0.59	5.48	Dusj NStrings	good	-	-
ANN track contained length	good	0.06	4.8	Dusj TotalCharge	medium	-	-
dEdx energy	binning	0.68	5.48	Dusj LargeCharges	medium	-	-
dEdx detector eff.	binning	0.59	5.48	Dusj Slopes	good	-	-
dEdx track length	good	0.03	4.39	Dusj SlopeWithCharge	good	-	-
RDF feature:056 $N_{\text{lines}}$	medium	0.0	5.48	Dusj SlopeBigCharge	good	-	-
RDF 064 number L1 hits?	good	0.01	5.48	GridFit NHits	good	-	-
RDF 065 max. storey charge	good	0.08	5.48	GridFit NLargeHits	good	-	-
Aafit hitseries nhits	good	0.03	1.08	GridFit NStrings	good	-	-
Aafit hitseries charge	medium	0.02	0.04	GridFit TotalCharge	good	-	-
Aafit hitseries duration	bad	0.02	1.01	GridFit LargeCharges	medium	-	-
Dusj hitseries nhits	good	0.04	1.08	GridFit Slopes	good	-	-
Dusj hitseries duration	medium	0.08	1.72	GridFit SlopeWithCharge	good	-	-
Dusj hitseries charge	bad	0.1	0.05	GridFit SlopeBigCharge	bad	-	-
GridFit hitseries nhits	medium	0.05	1.08	Krake NHits	good	0.12	26.11
GridFit hitseries charge	good	0.03	0.13	Krake NLargeHits	medium	0.07	26.11
GridFit hitseries duration	bad	0.04	4.76	Krake NStrings	good	0.0	26.1
Bbfit hitseries nhits	good	0.03	1.08	Krake TotalCharge	good	0.09	26.11
Bbfit hitseries charge	binning	0.01	1.19	Krake LargeCharges	good	0.09	26.11
Bbfit hitseries duration	medium	0.04	4.95	Krake Slopes	good	0.41	26.1
Krake hitseries nhits	good	0.05	1.08	Krake SlopeWithCharge	good	0.49	26.08
Krake hitseries charge	binning	0.01	0.3	Krake SlopeBigCharge	bad	0.25	26.09
Krake hitseries duration	bad	0.05	4.42	Q NHits	good	-	-
Q hitseries nhits	good	0.04	1.08	Q NLargeHits	medium	-	-
Q hitseries charge	binning	0.02	1.11	Q NStrings	medium	-	-
Q hitseries duration	bad	0.03	4.69	Q TotalCharge	good	-	-
Aafit hits NHits	good	0.06	4.85	Q LargeCharges	good	-	-
Aafit hits NLargeHits	medium	0.08	5.48	Q Slopes	good	-	-
Aafit hits NStrings	good	0.0	4.77	Q SlopeWithCharge	crap	-	-
Aafit hits TotalCharge	medium	0.08	5.48	Q SlopeBigCharge	good	-	-

\* all parameters are based on the reconstruction's hit selection

## After Data/MC selection and correlation analysis per parameter type

### Direction estimates

Parameter	DMC	A2	SOPmu	SOPnu
<b>Aafit <math>\phi</math></b>	good	0.04	3.48	219.1
Bbfit $\phi$	good	0.0	100.0	2000.0
! Bbfit M $\phi$	not working	0.0	100.0	2000.0
<b>Dusj <math>\phi</math></b>	good	0.0	4.34	221.63
<b>Q azimuth <math>\phi</math></b>	good	0.0	5.33	204.07
<b>Aafit <math>\theta</math></b>	good	0.01	2.92	<b>219.1</b>
<b>Bbfit <math>\theta</math></b>	good	0.01	2.34	<b>214.1</b>
! Bbfit M $\theta$	not working	0.0	100.0	2000.0
<b>Dusj <math>\theta</math></b>	good	0.01	<b>2.2</b>	221.63
GridFit zenith $\theta$	not working	0.01	2.05	224.2
Krake zenith $\theta$	good	0.0	2.37	263.82

BBFit M-Estimator seems unreliable and highly correlated to the BBFit estimate. Aafit shows good angular agreement with both shower reconstruction strategies, while they show less agreement between each other. GridFit and Krake show less agreement in zenith reconstruction with Dusj than Aafit or BBFit. The Shower zenith reconstruction seems to bear more information for muon suppression,

while the track zenith reconstruction is better suited for neutrino signal optimization. Aafit zenith seems to well represent the main feature of this sample.

*Parameter candidates for muon suppression* Dusj  $\theta$ , (Aafit  $\theta$ , Bbfit  $\theta$ )

*Parameter candidates for atmospheric suppression* Aafit  $\theta$ , BBFit  $\theta$ , Dusj  $\phi$ , Aafit  $\phi$ , (Q  $\phi$ )

### Position estimates

Parameter	DMC	A2	SOPmu	SOPnu
<b>Bbfit bright position z</b>	good	0.06	4.11	214.09
Dusj position x	binning	0.01	4.34	221.63
Dusj position y	good	0.01	4.34	221.63
Dusj position z	good	0.01	4.24	221.63
Dusj value convergence x	good	0.08	4.34	221.63
Dusj value convergence y	good	0.08	4.34	221.63
<b>Dusj value convergence z</b>	good	0.22	<b>1.76</b>	221.63

BBFit Bright and Dusj positions in z agree well for both muons and neutrinos. As the convergence position of Dusj promises some separation for atmospheric muons, it will be considered there.

*Parameter candidates for*

*muon suppression* Dusj value convergence z

*Parameter candidates for atmospheric suppression* Bbfit bright position z

### Detector condition parameters

Parameter	DMC	A2	SOPmu	SOPnu
ANN background count	good	0.02	3.46	219.1
ANN OM count	good	0.01	3.45	219.1
dEdx detector eff.	binning	0.57	20.49	1395.72
RDF value	good	0.02	3.97	219.1

These parameters can be used to try to finetune the methods, and will be tried to increased accuracy.

**Event geometry estimats**

Parameter	DMC	A2	SOPmu	SOPnu
Dusj horizontal d2center	good	0.02	4.34	221.63
Dusj vertical d2center	good	0.01	4.34	221.63
Dusj showerld vertical d2center	good	0.01	4.27	219.56
ANN distance to CoG	good	0.04	3.97	219.09
dEdx track length	good	0.04	<b>3.18</b>	219.1
ANN track eff. length	good	0.04	3.5	<b>212.74</b>
ANN track contained length	good	0.06	3.49	219.1
Aafit cylinder $r = 55m$	bad	0.09	-	-
Aafit cylinder $r = 75m$	bad	0.07	-	-
Aafit cylinder $r = 100m$	bad	0.05	-	-
Dusj cone $s = 55m$	medium	0.14	-	-
Dusj cone $s = 75m$	medium	0.1	-	-
Dusj cone $s = 100m$	bad	0.06	-	-

This information can help to classify the type of events.

*Parameter candidates for muon suppression* dEdx track length

*Parameter candidates for atmospheric suppression* ANN track eff. length

**Hit distribution parameters**

Parameter	DMC	A2	SOPmu	SOPnu
Dusj value quadrupole moment	good	0.01	4.33	221.19
ANN $\langle d_{cher} \rangle$ all hits to track	binning	0.11	3.5	219.09
ANN $RMS(d_{cher})$ all hits to track	good	0.02	<b>3.46</b>	219.1
ANN $\langle t_{res} \rangle$ all hits to track	binning	0.28	3.97	219.1
ANN duration triggered hits	good	0.04	3.65	<b>217.11</b>
ANN $\langle v^{-1} \rangle$ all hits	binning	0.62	3.99	219.39
ANN $RMS(v^{-1})$ all hits	binning	0.56	3.49	220.6

quadrupole moment (EV)

*Parameter candidates for muon suppression* ANN  $RMS(d_{cher})$   
*Parameter candidates for atmospheric suppression* ANN event duration triggered hits, Dusj value

**Energy related estimats**

Parameter	DMC	A2	SOPmu	SOPnu
Dusj energy	good	-	-	-
Dusj value convergence energy	good	0.07	4.33	221.63
R value	good	0.02	3.45	189.45
!Q energy E	good	0.43	3.97	214.68
ANN energy	good	0.02	3.45	177.22
dEdx energy	binning	0.08	3.96	176.47

Of the energy estimates, the track energy estimates show a larger potential for signal optimization, although all three methods are also strongly correlated. For muon

suppression, the Dusj energy parameter carries a large part of the information, as does the R-parameter for atmospheric suppression

*Parameter candidates for muon suppression* Dusj energy, ANN energy  
*Parameter candidates for atmospheric suppression* R value, dEdx energy

**Reconstruction quality parameters**

Parameter	DMC	A2	SOPmu	SOPnu
<b>Dusj value fit d.o.f.</b>	binning	0.1	3.97	<b>97.4</b>
Dusj value fit logL	binning	0.09	4.34	101.79
Dusj value fit calls	good	0.46	3.97	219.1
Dusj value fit rlogL	good	0.01	4.19	217.94
Dusj value vertex d.o.f.	good	0.09	3.97	97.6
Dusj value vertex logL	good	0.07	4.34	127.23
Dusj value vertex calls	good	0.02	3.96	219.09
Dusj value vertex rlogL	good	0.04	4.31	201.86
Dusj value showerId reduced $\chi^2$	good	0.03	2.56	219.55
GridFit ratio	good	0.59	0.89	214.06
GridFit precut ratio	good	0.61	0.9	214.0
GridFit width of minimum	good	0.05	3.31	219.1
Krake rlogl	good	0.0	2.06	261.78

GridFit ratio are well usable for muons suppression, although their run-by-run agreement varies. As Dusj logL and d.o.f. are highly correlated, as are GridFit ratios, only one of each should be used per method. *Parameter candidates for muon suppression* GridFit ratio, Krake rlogl (EV), Dusj value showerId red.  $\chi^2$

*Parameter candidates for atmospheric suppression* GridFit width of minimum(EV), Dusj value fit d.o.f (SOP)

**Track enhancing parameter**

These parameters were added to increase the contribution of track events in the atmospheric neutrino suppression step.

Parameter	DMC	A2	SOPmu*	SOPnu*
$N_{hits}$ triggered hits	good	0.04	3.1	1.3
$N_{hits}$ off event	good	0.03	3.1	1.8
$N_{string}$ Dusj hits	good	0.02	3.1	1.7
$N_{storeys}$ Dusj hits	good	0.02	3.1	2.0
Dusj hits event duration	good	0.02	3.1	2.0
Dusj hit fraction $t_{cher} < 250ns$	good	0.025	3.1	2.0
$< A_{Afit} > (t_{cher} < 40ns)$	good	0.025	3.0	1.4

Here, the SOP was scaled compared to the previously investigated parameters. These parameters were not included in the atmospheric muon suppression step.

**Hit charge parameters**

Parameter	DMC	A2	SOPmu*	SOPnu
Dusj value $A_{total}$	binning	0.21	3.97	<b>73.68</b>
ANN $N_{hits}$ triggered hits	binning	0.15	3.97	138.98
ANN $N_{hits}$ all hits	binning	0.05	3.97	179.27
ANN $\langle A \rangle$ triggered hits	good	0.11	3.97	219.1
ANN $\langle A \rangle$ all hits	good	0.18	<b>3.45</b>	176.92
ANN RMS(A) triggered hits	binning	0.33	3.97	219.1
Aafit hits NHits	good	0.05	22.93	926.55
Aafit hits NStrings	good	0.01	22.96	1433.78
BBFit hits NHits	good	0.14	26.1	908.95
BBFit hits NLargeHits	good	0.1	26.11	834.92
BBFit hits NStrings	good	0.01	26.1	974.97
Dusj hits NHits	good	0.04	26.1	876.56
Dusj hits NStrings	good	0.01	26.1	934.99
GridFit hits NHits	good	0.12	20.04	810.08
GridFit hits NLargeHits	good	0.1	21.68	958.34
GridFit hits NStrings	good	0.01	20.5	1472.01
GridFit hits TotalCharge	good	0.1	20.2	1058.07
Krake hits NHits	good	0.12	26.11	1270.74
Krake hits NStrings	good	0.0	26.1	1201.62
Krake hits TotalCharge	good	0.09	26.13	1474.45
Krake hits LargeCharges	good	0.09	26.11	1439.32
Q hits NHits	good	0.09	26.1	1025.95
Q hits TotalCharge	good	0.08	26.1	1010.97
Q hits LargeCharges	good	0.08	26.1	1371.8

\* re-evaluated using smaller livetime  
*Parameter candidates for muon suppression*  
ANN  $\langle A \rangle$  all hits, (ANN  $N_{hits}$  triggered hits)  
*Parameter candidates for atmospheric suppression*  
Dusj value  $A_{total}$ , (GridFit hits NHits, Dusj hits NStrings)

## A.5 TMVA optimization

### A.5.1 Parameter scanning

Results of the parameter scanning procedure for the atmospheric muon suppression can be seen in Table A.1, results for the atmospheric neutrino suppression are listed in Table A.2.

### A.5.2 TMVA method evaluation

#### BDT setup testing for muon suppression

The Boosted Decision Tree (BDT) architecture can be varied as described in [62] by applying a preprocessing to the sample of input events (Gaussian decoupling or Principal Component Analysis), varying the number of trees  $N_{tr}$  and the depth of the individual trees, using different boosting types (Adaptive Boost, Gradient Boost, Bagging) which come with different learning rate functions (Adaptive Boost:  $\beta$ , Gradient Boost: shrinkage) which is increase in position by using a higher number of grid points used for node splitting (nCuts). The separation criterion in node splitting can be varied between cross entropy, Gini index (also with Laplace criterion), misclassification error and  $S/S+B$ . Performance is evaluated using the efficiency  $\varepsilon$  (Chapter 6.7) and separation  $S$  (Chapter 6.6).

Method	Prep	$N_{tr}/\text{depth}$	Boosting(learning, nCuts)	Sep-fkt.	$\varepsilon$	$S(x)$
BDT	none	600/3	Ada(0.5,20)	GiniIndex	0.11	10.5
BDTPCA	PCA	600/3	Ada(0.5,20)	GiniIndex	0.21	11.5
BDTGauss	Gauss	600/3	Ada(0.5,20)	GiniIndex	0.25	11
BDTMisClass	none	600/3	Ada(0.5,20)	ClassError	-	13
BDTCross	none	600/3	Ada(0.5,20)	CrossEntropy	-	13
BDTGiniL	none	600/3	Ada(0.5,20)	GiniLaplace	0.10	10.5
BDThighCut	none	600/3	Ada(0.5,50)	GiniIndex	0.26	11.5
BDTmaxCut	none	600/3	Ada(0.5,-1)	GiniIndex	0.23	11
BDTMMBB	none	1200/5	Ada(0.5,20), Bagged	GiniIndex	-	35
BDTBb	none	600/3	Ada(0.5,20), Bagged	GiniIndex	0.15	12
BDTFisher	none	600/3	Ada(0.5,20), Fisher cuts	GiniIndex	-	14
BDTg	none	600/2	Grad(0.1,20)	GiniIndex	-	4
BDTbeta	none	600/3	Ada(0.8,20)	GiniIndex	0.12	14
BDTNodeP	none	600/3	Ada(0.5,20),purity=0.3	GiniIndex	0	3
BDTrealA	none	600/3	RealAda(0.5,20)	GiniIndex	0.12	23
BDTBag	none	600/3	Bagging	GiniIndex	0.0	2
BDTbestOf	Gauss	1200/7	Ada(0.8,50)	GiniIndex	0.25	16
BDTbestOfbagged	Gauss	1200/7	Ada(0.8,50), Bagged	GiniIndex	0.22	30

parameter $x$	$\varepsilon(x)$ (single)	dropped in round	$\varepsilon(x)$ without parameter
Dusj $A_{total}$	0.040	14	0.054
Dusj $N_{hits}$	0.038	6	0.059
Dusj final fit d.o.f.	0.038	13	0.056
Aafit $N_{hits}$	0.028	(17)	0.057
Aafit $E_{dEdx}$	0.026	11	0.060
Aafit $E_{ANN}$	0.022	(19)	0.051
Aafit $E_R$	0.020	10	0.059
Aafit $\phi$	0.003	3	0.056
Aafit $\lambda$	0.003	(18)	0.055
ANN event duration	0.002	5	0.058
Aafit $\theta$	0.002	4	0.057
Aafit $\beta$	0.002	7	0.059
Dusj shower $r\chi^2$	0.002	1	0.54
ANN track length	0.001	12	0.060
Dusj conv. position $E$	0.001	8	0.059
Dusj $E_{Dusj}$	0.001		
Dusj VLLH	0.001		
Dusj quadrupole moment	0.001	15	0.053
Dusj $\phi$	0.0	2	0.056
GridFit w.o.m.	0.0	9	0.060
Dusj $\theta$	0.0	(16)	0.052

Table A.1: TMVA scanning results for atmospheric neutrino suppression, starting from the full parameter sample reaching  $\varepsilon = 0.048$ . Parameters in ( ) were left in the final parameter sample due to the increased signal efficiency compared to the completely reduced sample.

parameter $x$	$\varepsilon(x)$ (single)	dropped in round	$\varepsilon(x)$ without parameter
Aafit $E_R$	0.038	1	0.071
Aafit $E_{ANN}$	0.037		
ANN P1	0.036		
ANN P2	0.035		
Aafit $E_{dEdx}$	0.035	7	0.071
Dusj ANN P7	0.022	4	0.074
Aafit ANN P21	0.061		
Dusj ANN P6	0.015	5	0.074
Dusj ANN P15	0.007	6	0.074
$E_{Dusj}$	0.006	2	0.074
Dusj ANN P19	0.005	3	0.074
Dusj VLLH	0.001		
Aafit $\lambda$	0.0	8	0.065

Table A.2: TMVA scanning results for atmospheric neutrino suppression using Fisher discriminant, starting from the full parameter sample reaching  $\varepsilon = 0.065$

### TMVA method comparison for atmospheric neutrino suppression

For comparison, some best performing single parameters and their signal efficiency are also listed.

Method	Preprocess	setup	$\epsilon$
PDEERS			0.038
PDEERSPCA	PCA		0.038
FisherG	Gauss		0.041
BoostedFisher			0.036
BoostedFisherG	Gauss		0.038
KNN			0.042
MLPPCA	PCA		0.024
TMIPANN			0.002
RuleFit			0.032
BDTGauss	Gauss		0.038
BDT			0.035
BDTbestOfbagged			0.046
Dusj total charge			0.04
Dusj $N_{hits}$			0.038
Dusj shower d.o.f.			0.038

### Optimization parameters for classifier combinations

Model rejection and discovery potential reached by a given classifier combination can be seen in Figure A.1.

## A.6 Summary of simulation sets used during this work

### A.6.1 Test set for classifier selection

The complete data taking period evaluated in this analysis, 2007-2013, comes with an equivalently large sample of run-by-run simulation. Of these, following sub-samples of simulated run-by-run (version 2 [35], runs from 2007-2012) were used.

**Monte Carlo set for classifier selection** As the complete sample of simulated events per run would unnecessarily prolong the cut optimization, the set for classifier selection met the following criteria.

- run number ending in xxxx0
- data for the run is available and  $0.75 < N_{data}/N_{mupage,w} < 1.25$ , with  $N_{mupage,w}$  being the events weighted to match the run's duration
- some quality criteria for the distribution of input parameters to the classifiers apply (described elsewhere)
- including all available neutrino files ( $\nu_e$  and  $\nu_\mu$ , generated using genhen) and atmospheric muons (mupage)

These criteria resulted in an equivalent of 88 days of data taking.

**Monte Carlo set for final cut scanning** The final scanning was performed on runs selected by the same criteria as above, except for the restriction on 0-ending runs. Including all runs with suitable agreement between data and simulation resulted in an equivalent of 914 days of data taking.

**Cosmic neutrino signal** The IceCube measurements of the cosmic flux [76] allow both the assumption of a cosmic flux with spectral index  $\lambda = 2.0$ , as in the widely-used Waxman-Bahcall model, or an index of  $\lambda = 2.5$ , which better fits the measured event distribution. Therefore, two cosmic signal hypothesis were tested there, namely

$$\Phi_{2.5}E^{2.5} = 4.1 \times 10^{-6} \text{GeV}^{1.5} \text{cm}^{-2} \text{sr}^{-1} \text{s}^{-1} \quad \text{and} \quad (\text{A.3})$$

$$\Phi_{2.0}E^2 = 1.1 \times 10^{-8} \text{GeV}^1 \text{cm}^{-2} \text{sr}^{-1} \text{s}^{-1}. \quad (\text{A.4})$$

**Atmospheric neutrino background** The atmospheric neutrino background consists of the conventional neutrino flux and a prompt component. As the existence and magnitude of the prompt component is still subject of debate, only a conventional atmospheric flux (either according to Honda et al. [30],  $\Phi_{\text{Honda}}$  or from the Bartol group [29],  $\Phi_{\text{Bartol}}$ ) is used in the classifier scanning. As test for a prompt contribution the model by Enberg et al. [31],  $\Phi_{\text{ERS}}$  is applied.

**Atmospheric muon background** For the atmospheric muon background, the largest problem stems from the statistical magnitude of this flux. As simulation is only available for 1/3 of the duration of each run, the complete set of simulated atmospheric muons with an equivalent weighted lifetime of 1430 days was used in all scanning procedures.

Furthermore, it was found in earlier analyses that events originating from a muon bundle, i.e. coincident muons originating from the same atmospheric shower, might play a role for high-energy analyses. As the standard simulation only includes events with a muon multiplicity of  $m < 100$ , a specialized mupage sample using 50 runs scaled to a total lifetime of 340 days was produced with muon multiplicities  $100 \leq m < 1000$ . This sample was included in the final cut optimization only.

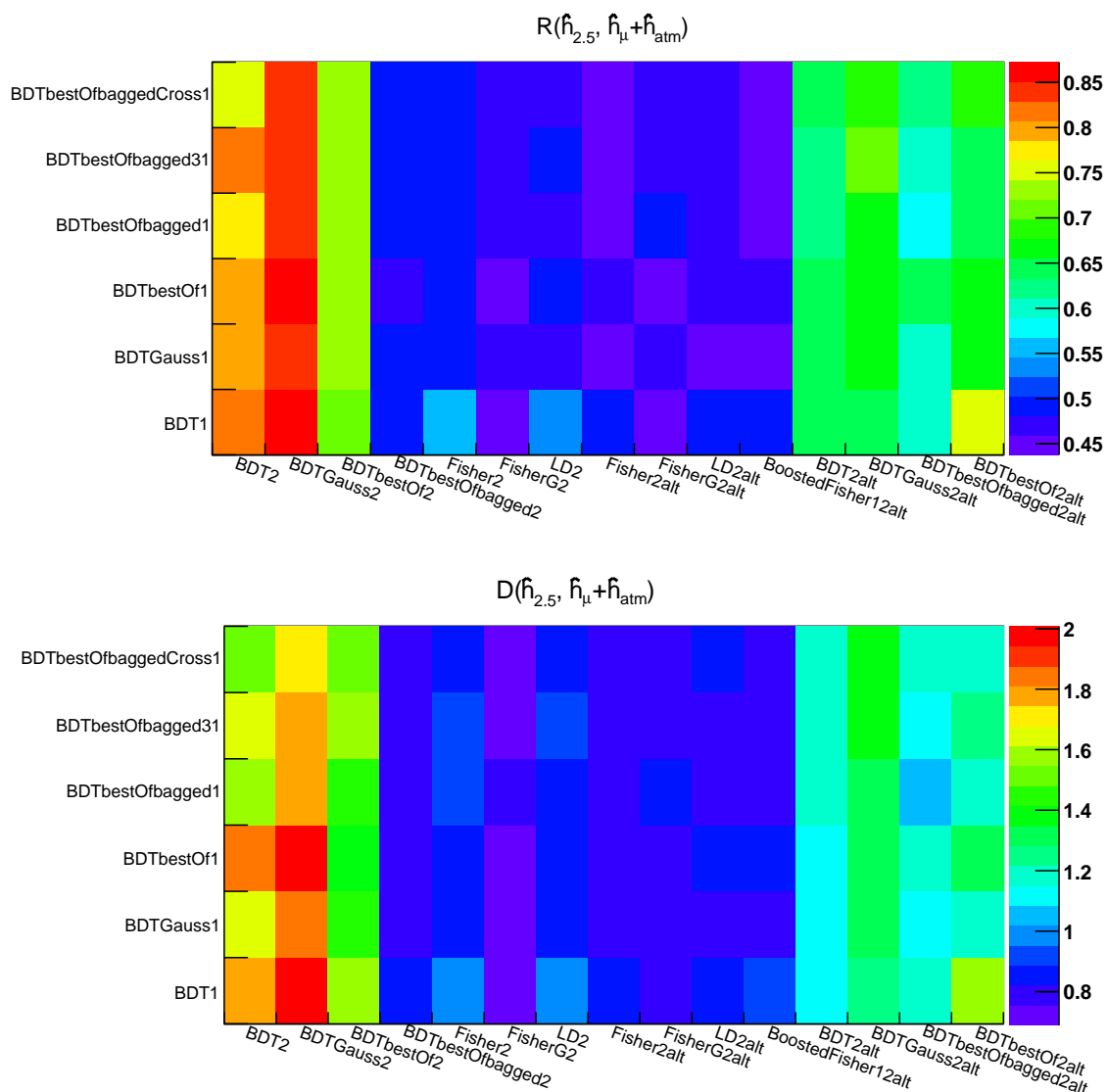
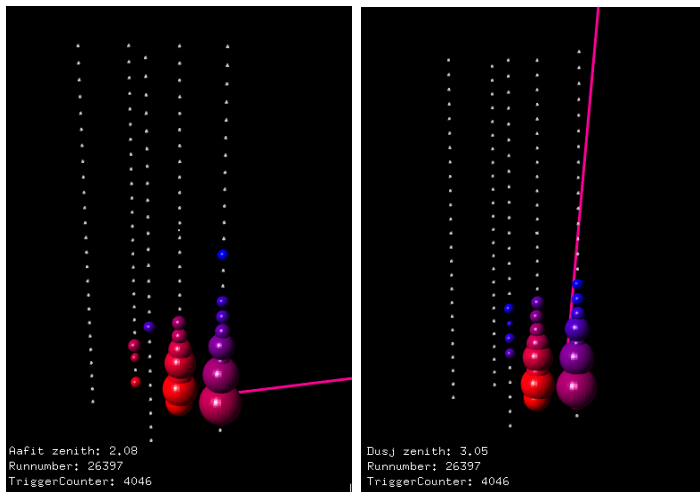
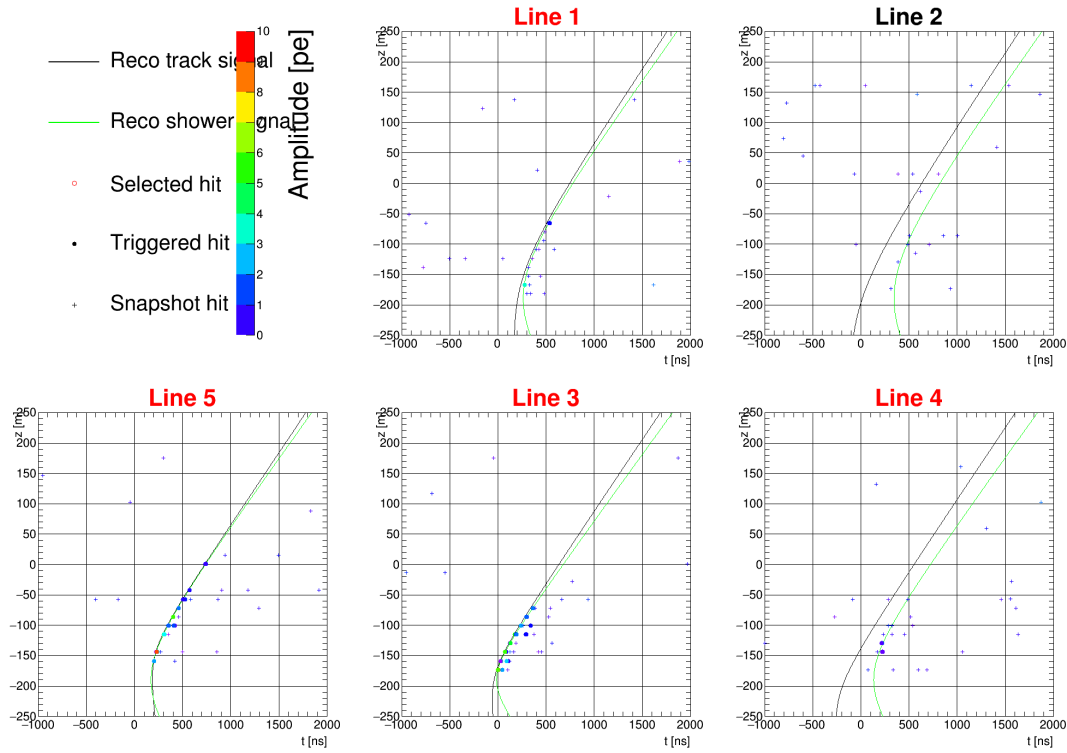
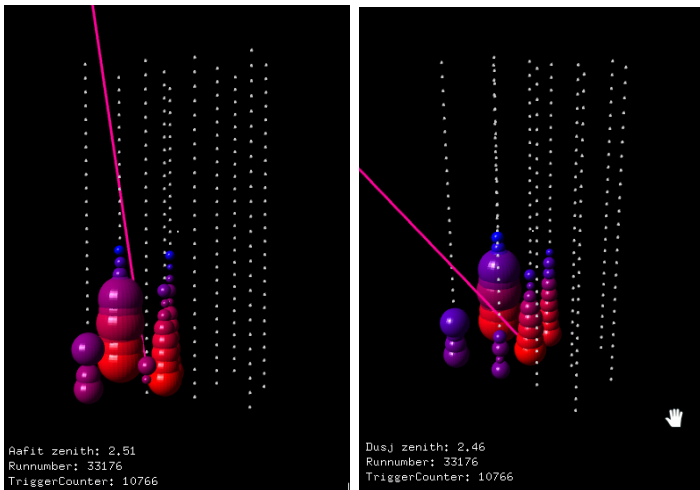
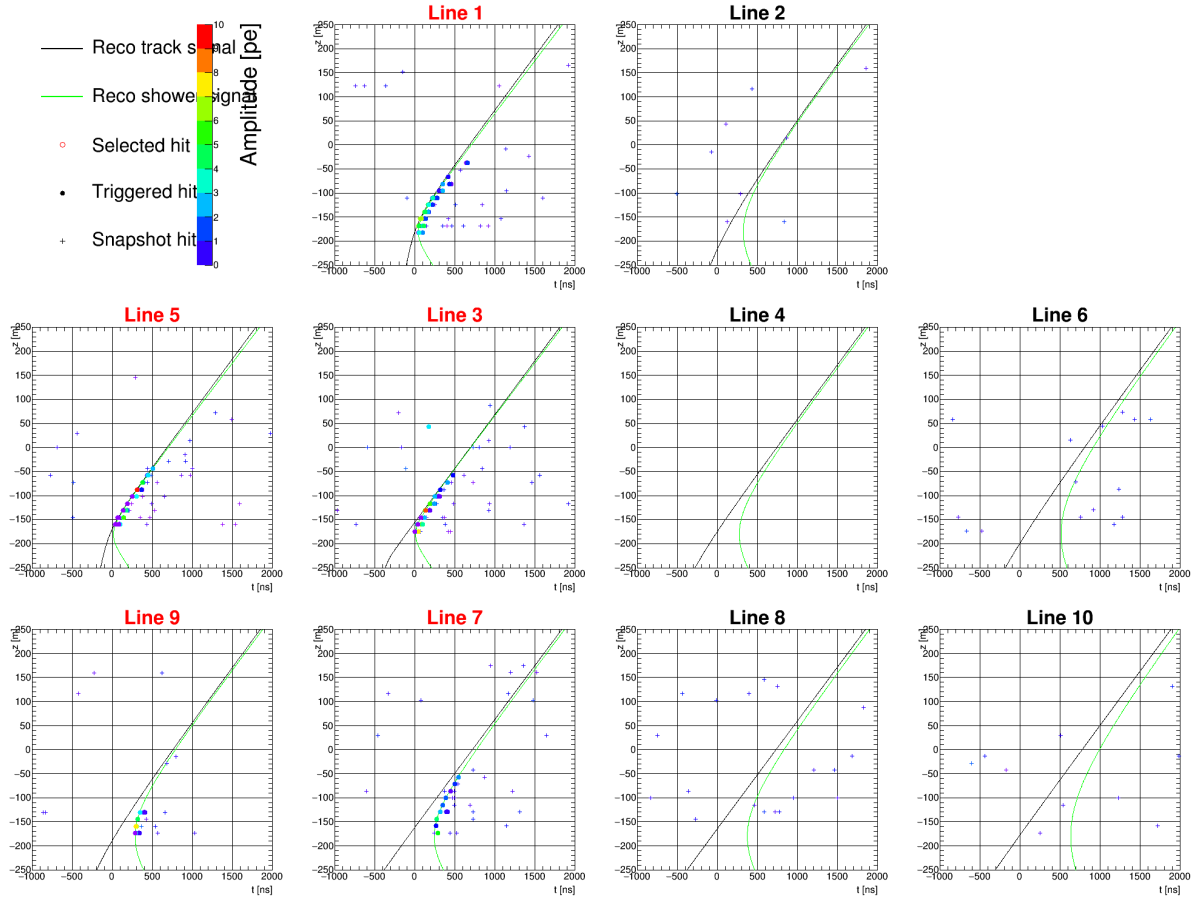


Figure A.1: Best model rejection factor and discovery potential for each classifier combination.

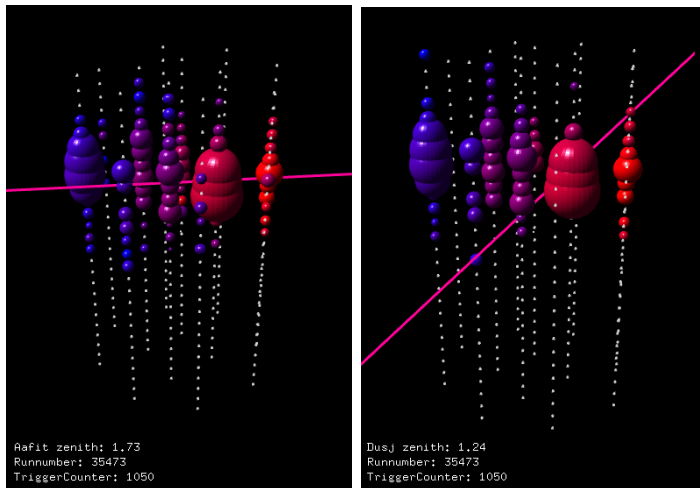
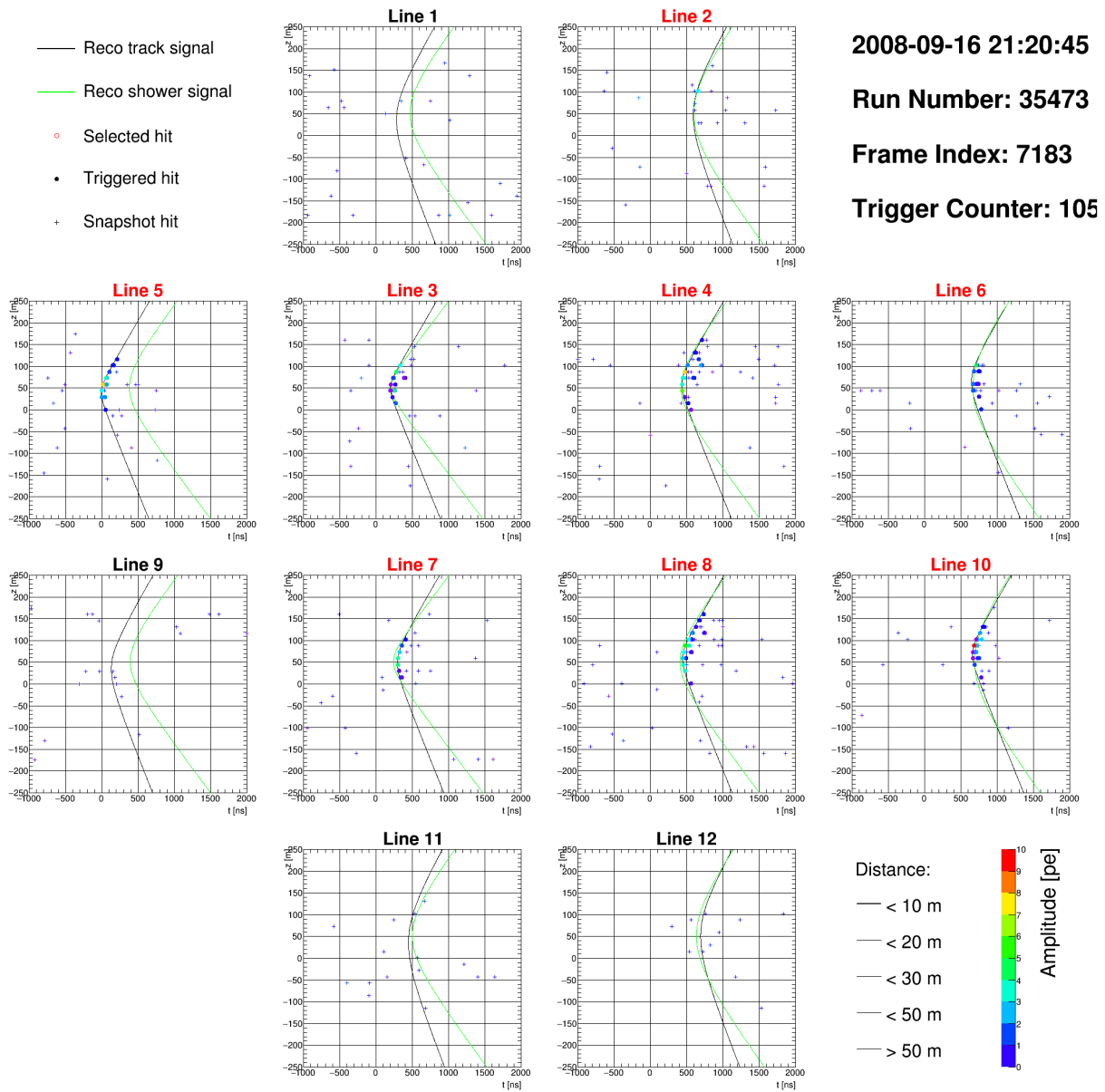
## A.7 Cosmic neutrino candidates



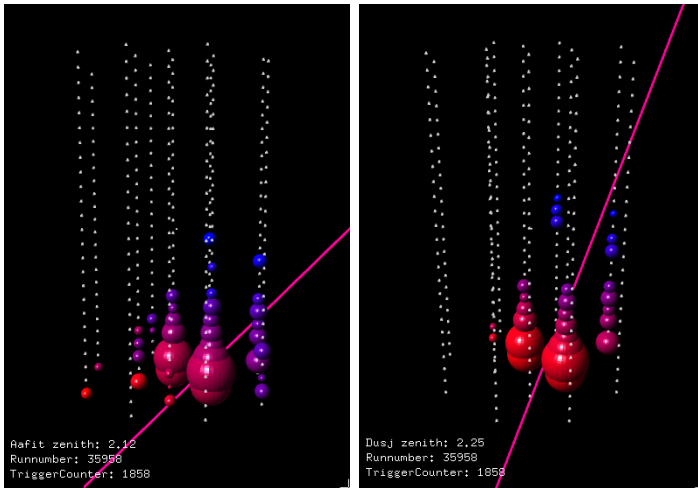
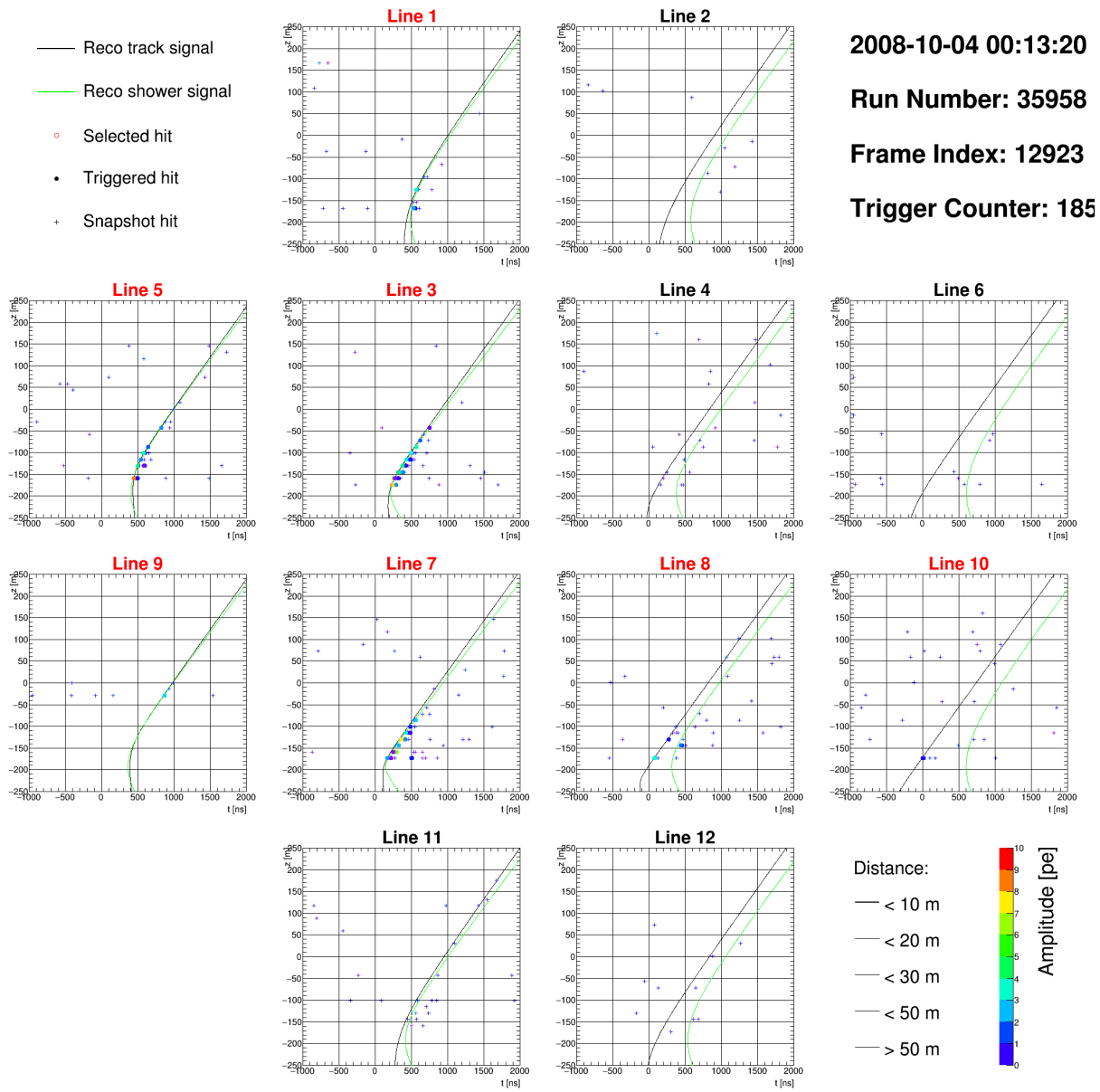
Event	1		
Runnumber	26397	Counter	4046
Event ID	129099	triggers	3D, 3D_SCAN
BDTGauss1	0.36	FisherG2alt	0.55
Aafit $\theta$	2.08	Dusj $\theta$	3.05
Aafit $\phi$	5.61	Dusj $\phi$	3.050.63
Aafit $\lambda$	-5.04	Dusj VLLH	0.9
longitude	154.4	latitude	67.6
Aafit $\beta$	0.02		
BB track $\chi^2$	2.69	BB bright $\chi^2$	2.46
$E_{ANN}$ [GeV]	0.77	$E_{Dusj}$ [GeV]	0.56
$E_{dEdx}$ [GeV]	4.94	$A_{Dusj}$	180.44
$E_R$ [GeV]	5.38		
$N_{Aafit}$	46	$N_{Dusj}$	50
in analysis	shower	selection	2



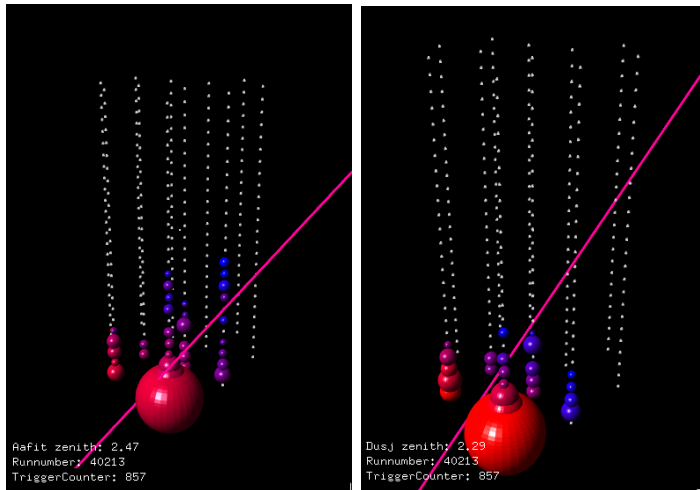
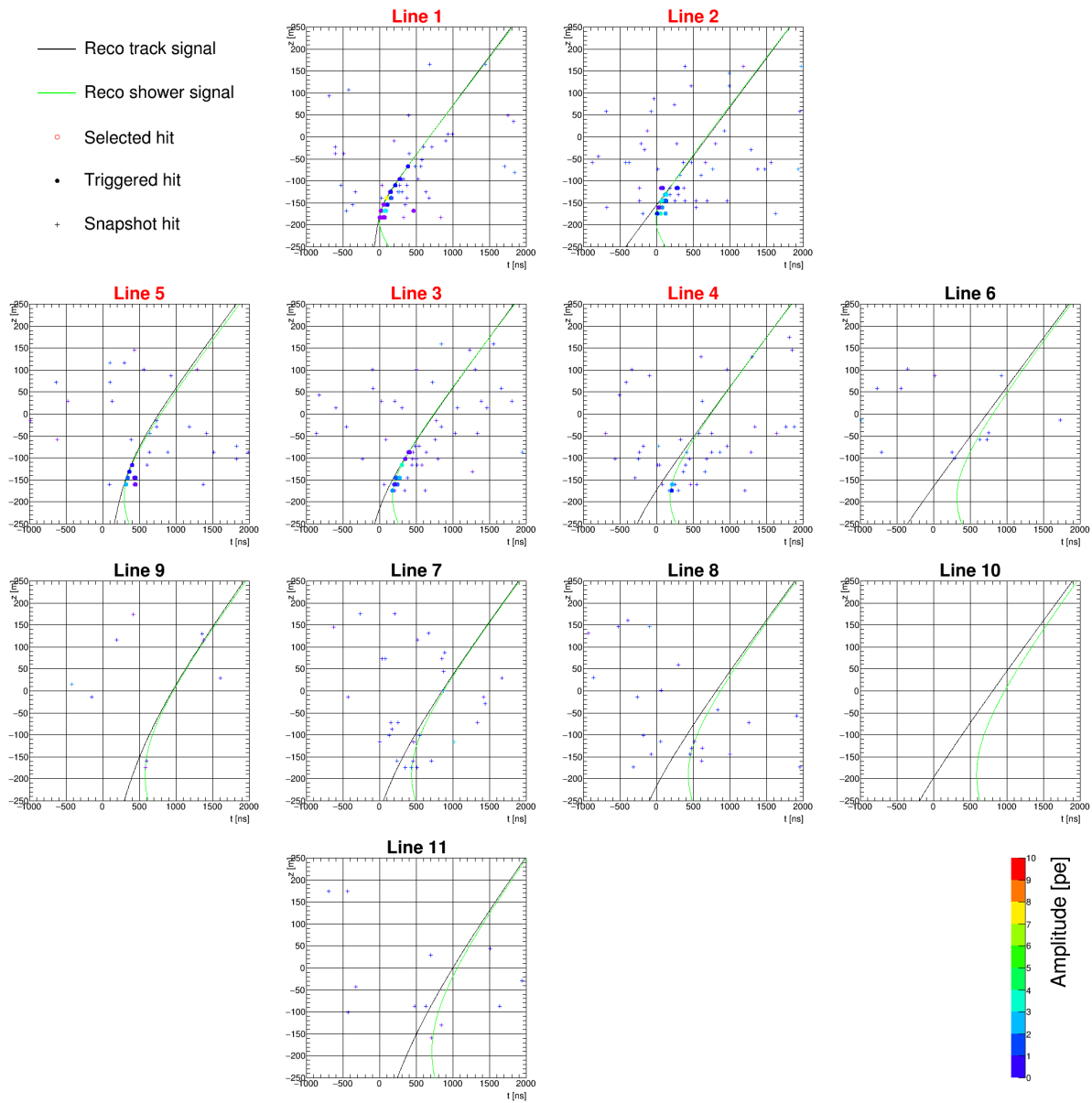
Event	2		
Runnumber	33176	Counter	10766
Event ID	50112	triggers	3D_SCAN, T3
BDTGauss1	0.43	FisherG2alt	0.57
Aafit $\theta$	2.51	Dusj $\theta$	2.46
Aafit $\phi$	4.85	Dusj $\phi$	2.461.06
Aafit $\lambda$	-4.96	Dusj VLLH	0.9
longitude	116.1	latitude	38.7
Aafit $\beta$	0.04		
BB track $\chi^2$	16.91	BB bright $\chi^2$	2.84
$E_{ANN}$ [GeV]	0.72	$E_{Dusj}$ [GeV]	0.48
$E_{dEdx}$ [GeV]	5.38	$A_{Dusj}$	836.03
$E_R$ [GeV]	5.65		
$N_{Aafit}$	81	$N_{Dusj}$	132
in analysis	-	selection	1



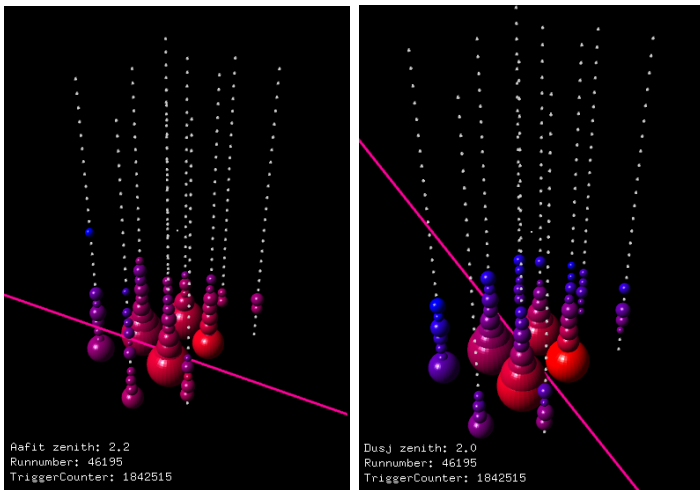
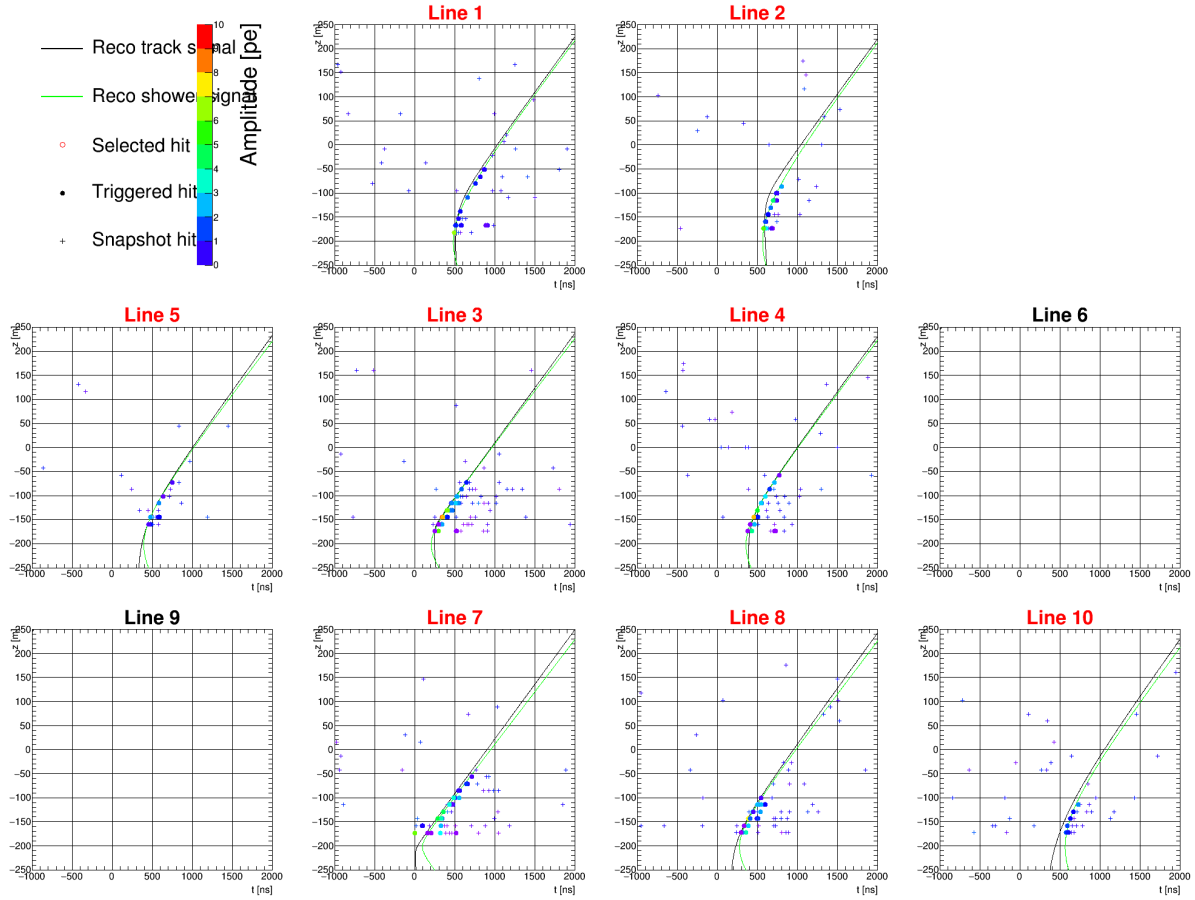
Event		3	
Runnumber	35473	Counter	1050
Event ID	7183	triggers	3D_SCAN, T3
BDTGauss1	0.35	FisherG2alt	0.52
Aafit $\theta$	1.73	Dusj $\theta$	1.24
Aafit $\phi$	2.49	Dusj $\phi$	1.242.92
Aafit $\lambda$	-4.71	Dusj VLLH	1.02
longitude	127.0	latitude	-80.8
Aafit $\beta$	0.0		
BB track $\chi^2$	1.83	BB bright $\chi^2$	17.34
$E_{ANN}$ [GeV]	0.72	$E_{Dusj}$ [GeV]	0.57
$E_{dEdx}$ [GeV]	4.84	$A_{Dusj}$	466.1
$E_R$ [GeV]	4.99		
$N_{Aafit}$	152	$N_{Dusj}$	136
in analysis	-	selection	1



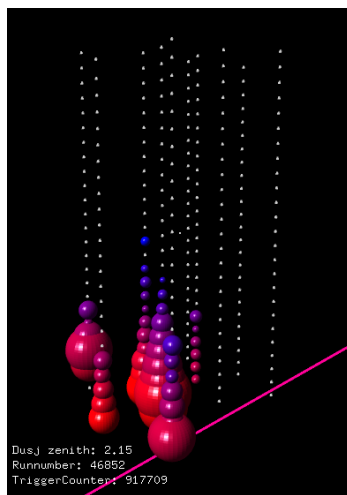
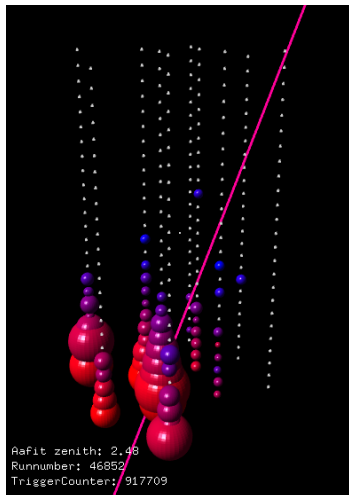
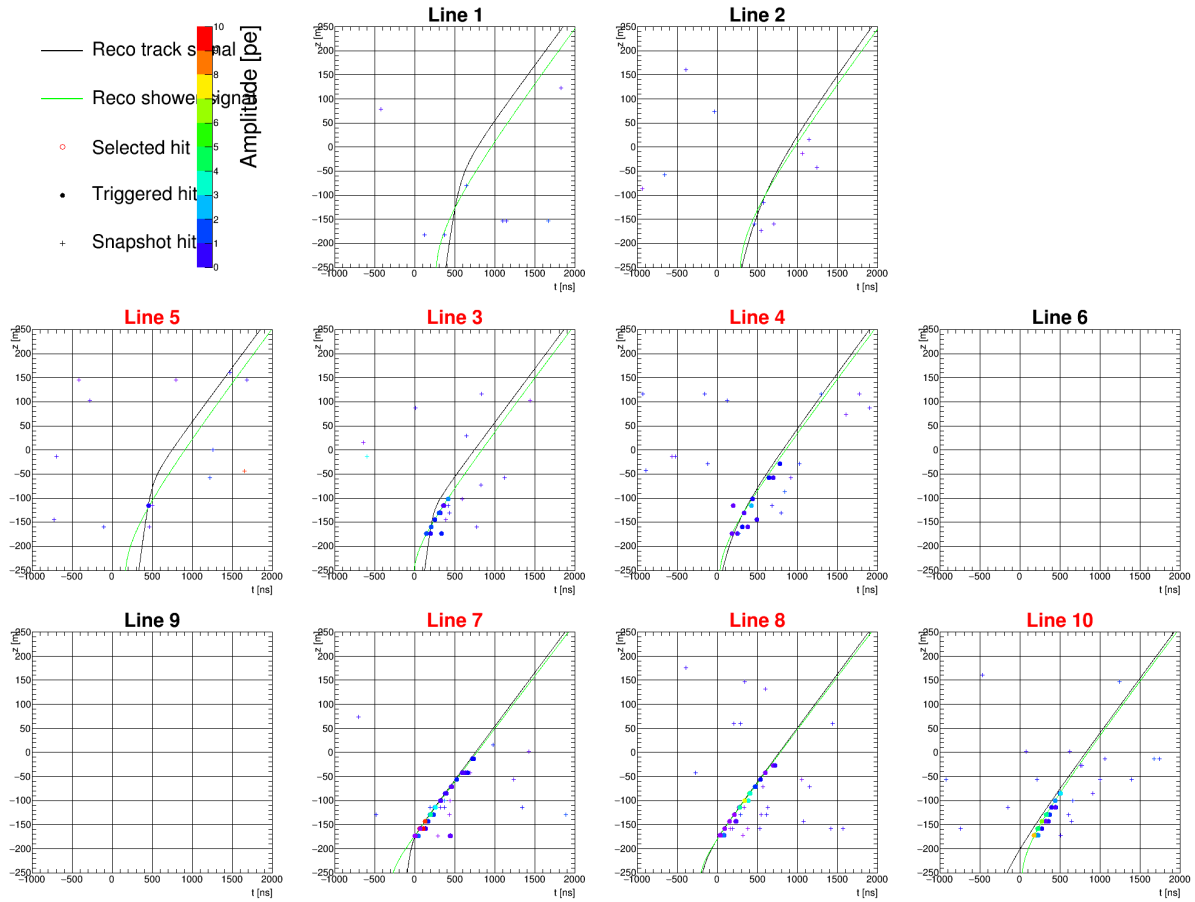
Event		4	
Runnumber	35958	Counter	1858
Event ID	12923	triggers	3D_SCAN, T3
BDTGauss1	0.43	FisherG2alt	0.54
Aafit $\theta$	2.12	Dusj $\theta$	2.25
Aafit $\phi$	5.64	Dusj $\phi$	2.256.03
Aafit $\lambda$	-4.95	Dusj VLLH	0.94
longitude	81.5	latitude	6.6
Aafit $\beta$	0.01		
BB track $\chi^2$	8.53	BB bright $\chi^2$	2.87
$E_{ANN}$ [GeV]	0.72	$E_{Dusj}$ [GeV]	0.5
$E_{dEdx}$ [GeV]	5.14	$A_{Dusj}$	374.07
$E_R$ [GeV]	5.43		
$N_{Aafit}$	78	$N_{Dusj}$	80
in analysis	-	selection	1



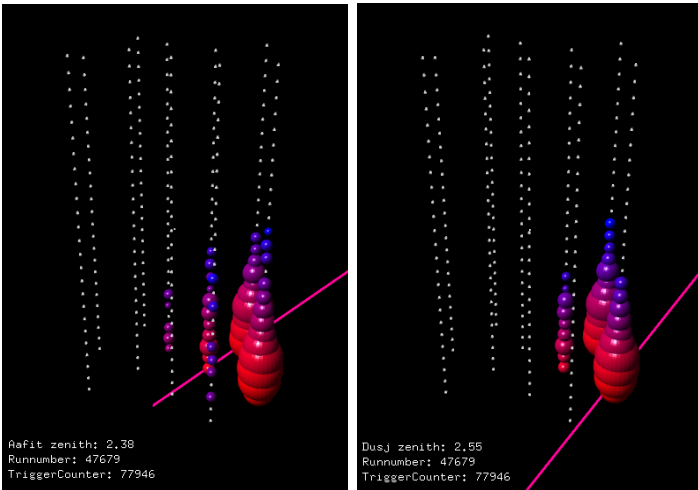
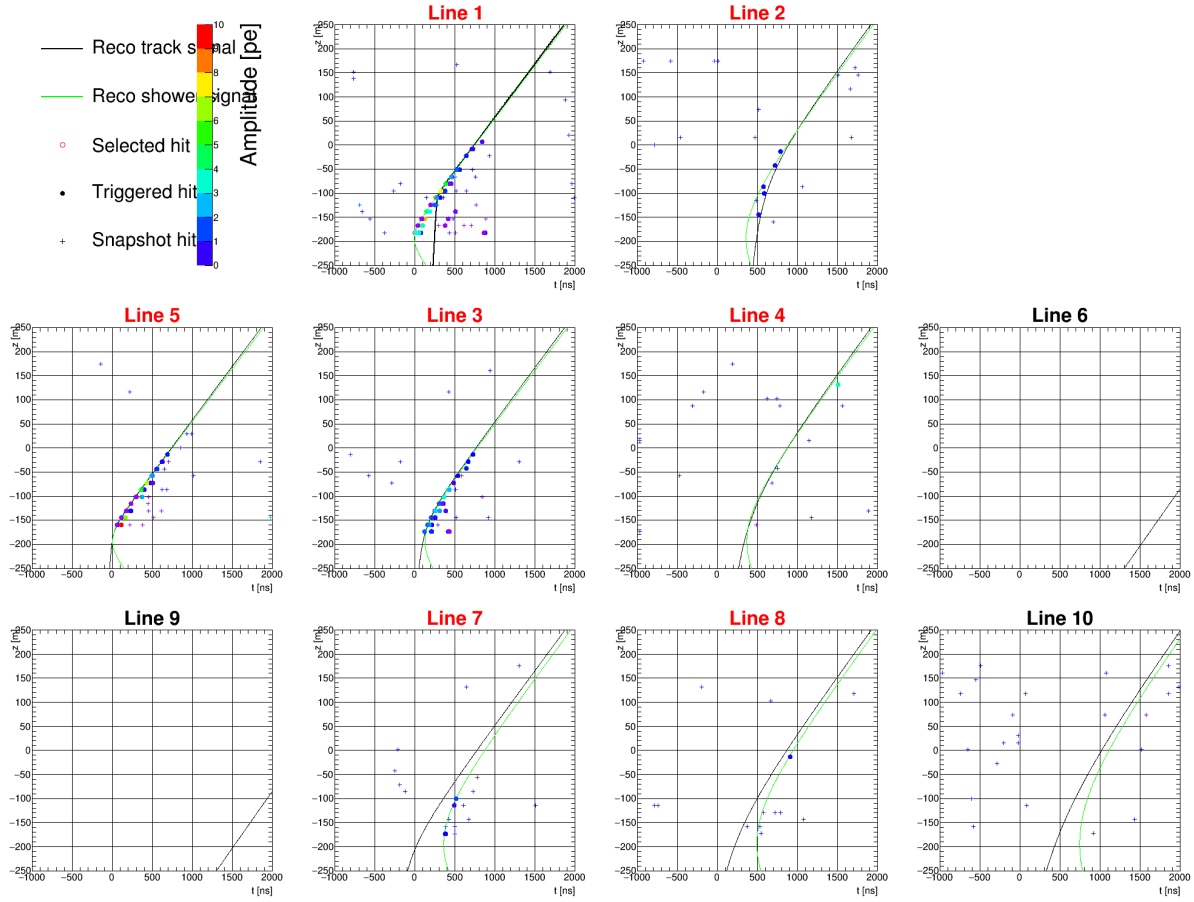
Event		5	
Runnumber	40213	Counter	857
Event ID	67423	triggers	3D_SCAN, T3
BDTGauss1	0.35	FisherG2alt	0.55
Aafit $\theta$	2.47	Dusj $\theta$	2.29
Aafit $\phi$	5.57	Dusj $\phi$	2.290.95
Aafit $\lambda$	-5.71	Dusj VLLH	0.91
longitude	157.1	latitude	12.8
Aafit $\beta$	0.02		
BB track $\chi^2$	6.33	BB bright $\chi^2$	7.44
$E_{ANN}$ [GeV]	0.72	$E_{Dusj}$ [GeV]	0.44
$E_{dEdx}$ [GeV]	4.9	$A_{Dusj}$	358.16
$E_R$ [GeV]	5.42		
$N_{Aafit}$	75	$N_{Dusj}$	70
in analysis	-	selection	1



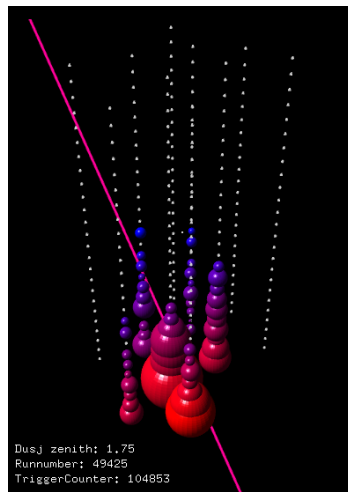
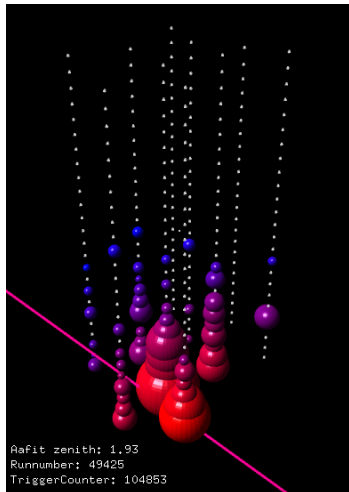
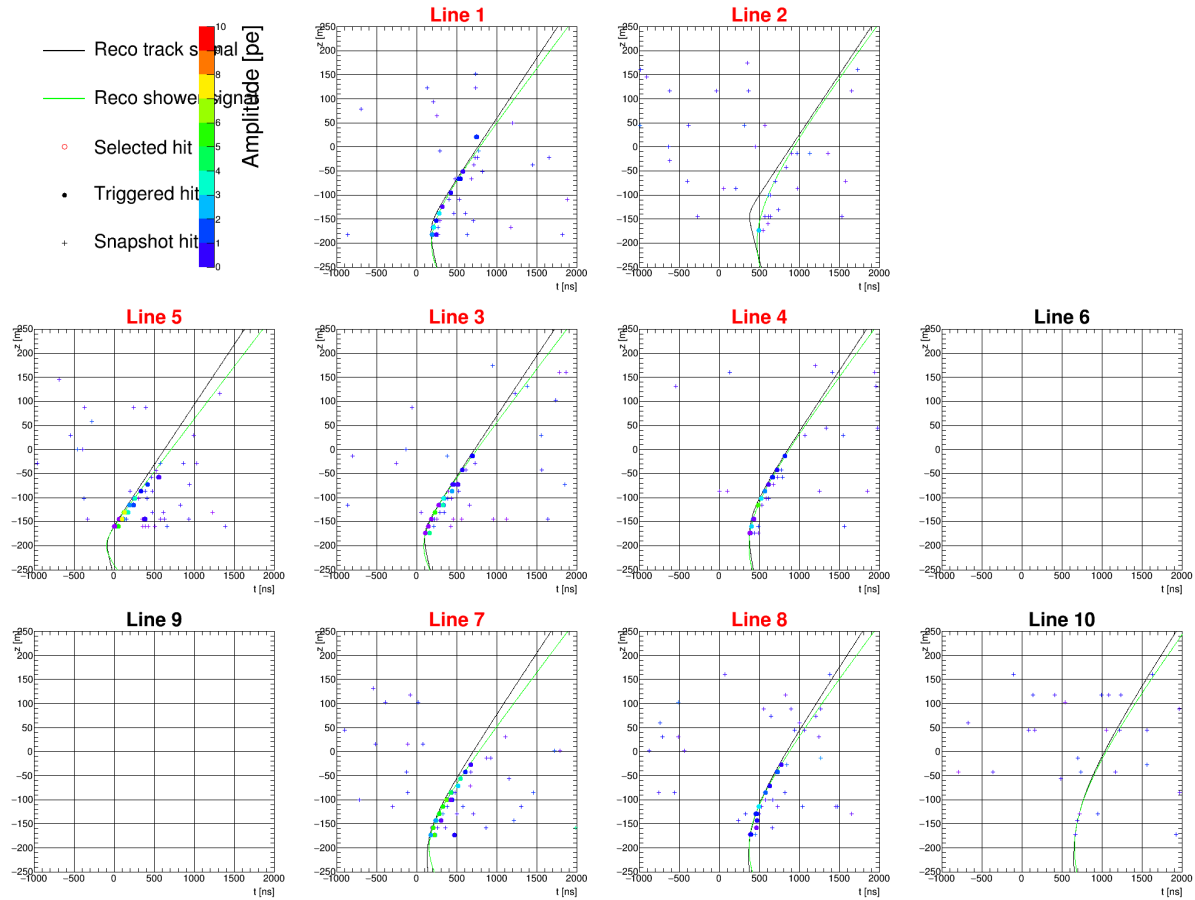
Event		6	
Runnumber	46195	Counter	1842515
Event ID	16436	triggers	3D_SCAN, T3
BDTGauss1	0.38	FisherG2alt	0.65
Aafit $\theta$	2.2	Dusj $\theta$	2.0
Aafit $\phi$	3.9	Dusj $\phi$	2.02.83
Aafit $\lambda$	-5.86	Dusj VLLH	0.9
longitude	92.4	latitude	54.0
Aafit $\beta$	0.01		
BB track $\chi^2$	16.2	BB bright $\chi^2$	6.88
$E_{ANN}$ [GeV]	0.73	$E_{Dusj}$ [GeV]	0.58
$E_{dEdx}$ [GeV]	4.84	$A_{Dusj}$	724.81
$E_R$ [GeV]	5.73		
$N_{Aafit}$	137	$N_{Dusj}$	159
in analysis	-	selection	1



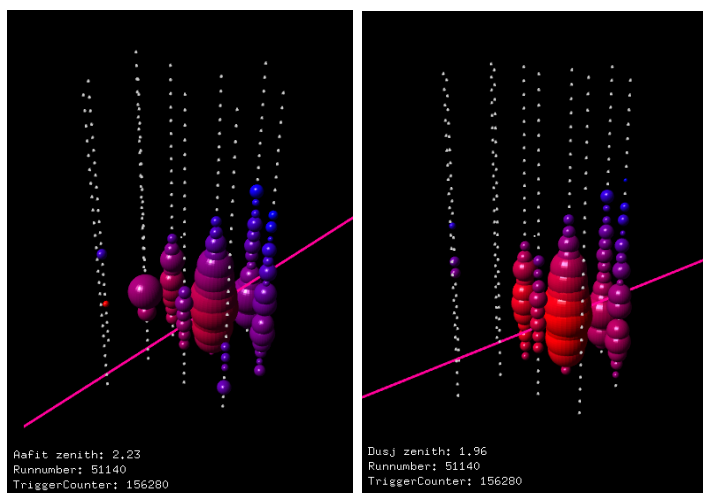
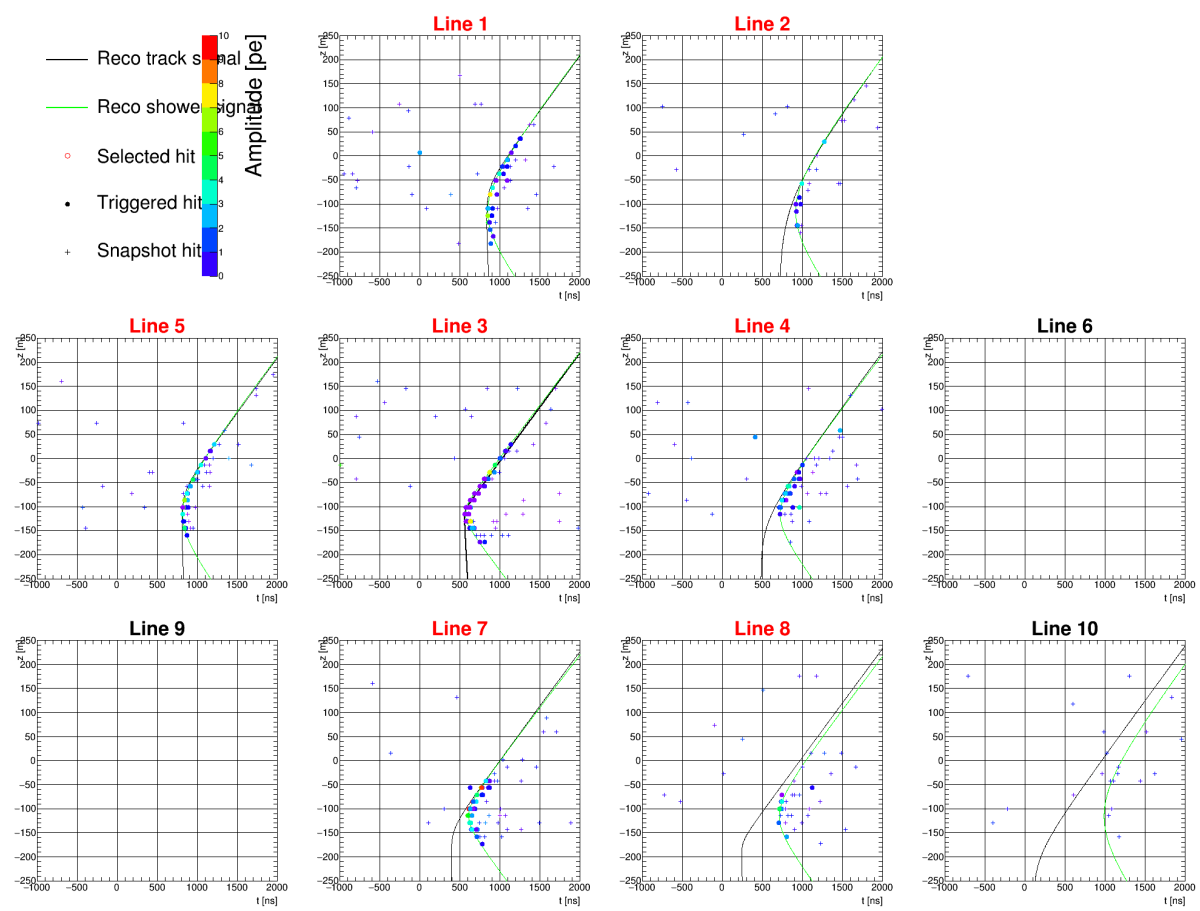
Event		7	
Runnumber	46852	Counter	917709
Event ID	51708	triggers	3D_SCAN, T3, GC, TQ
BDTGauss1	0.43	FisherG2alt	0.61
Aafit $\theta$	2.48	Dusj $\theta$	2.15
Aafit $\phi$	4.83	Dusj $\phi$	2.153.78
Aafit $\lambda$	-5.34	Dusj VLLH	0.9
longitude	129.0	latitude	17.7
Aafit $\beta$	0.01	BB track $\chi^2$	8.03
BB track $\chi^2$	8.03	BB bright $\chi^2$	3.23
$E_{ANN}$ [GeV]	0.68	$E_{Dusj}$ [GeV]	0.63
$E_{dEdx}$ [GeV]	4.56	$A_{Dusj}$	650.59
$E_R$ [GeV]	5.13		
$N_{Aafit}$	122	$N_{Dusj}$	126
in analysis	shower	selection	2



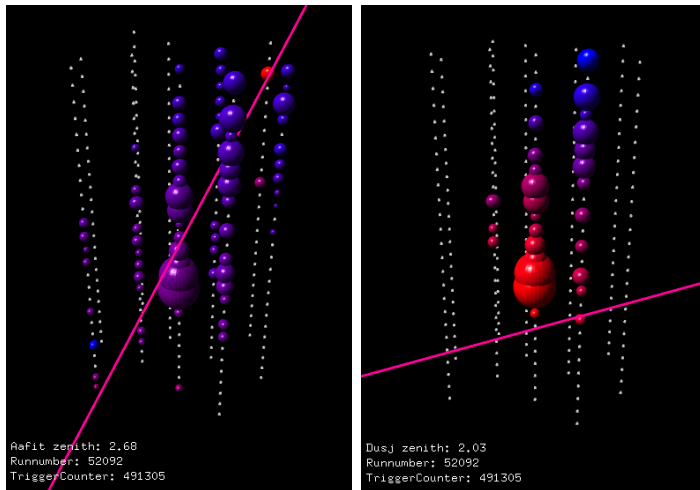
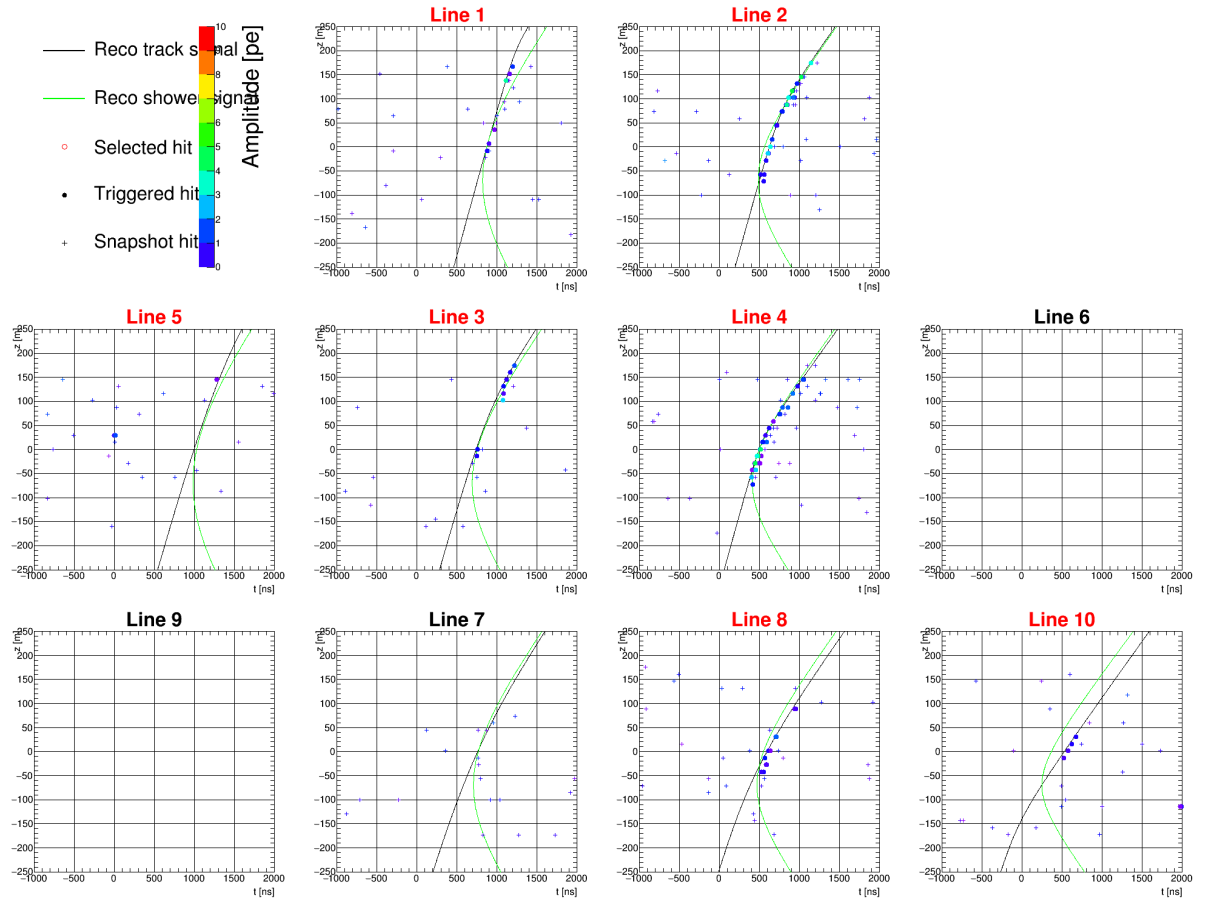
Event	8		
Runnumber	47679	Counter	77946
Event ID	12186	triggers	3D_SCAN, T3, GC, TQ
BDTGauss1	0.43	FisherG2alt	0.63
Aafit $\theta$	2.38	Dusj $\theta$	2.55
Aafit $\phi$	3.82	Dusj $\phi$	2.555.08
Aafit $\lambda$	-5.49	Dusj VLLH	0.89
longitude	162.5	latitude	34.4
Aafit $\beta$	0.01	BB bright $\chi^2$	3.34
BB track $\chi^2$	14.99	$E_{ANN}$ [GeV]	0.73
$E_{ANN}$ [GeV]	0.73	$E_{Dusj}$ [GeV]	0.55
$E_{dEdx}$ [GeV]	4.66	$A_{Dusj}$	658.43
$E_R$ [GeV]	5.24		
$N_{Aafit}$	98	$N_{Dusj}$	102
in analysis	shower	selection	1



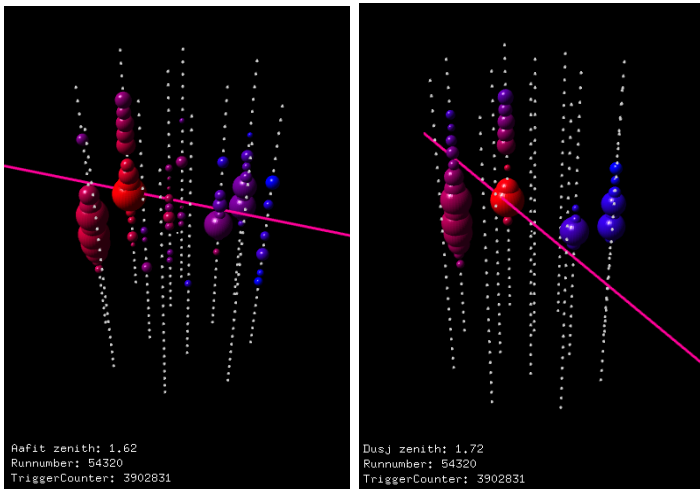
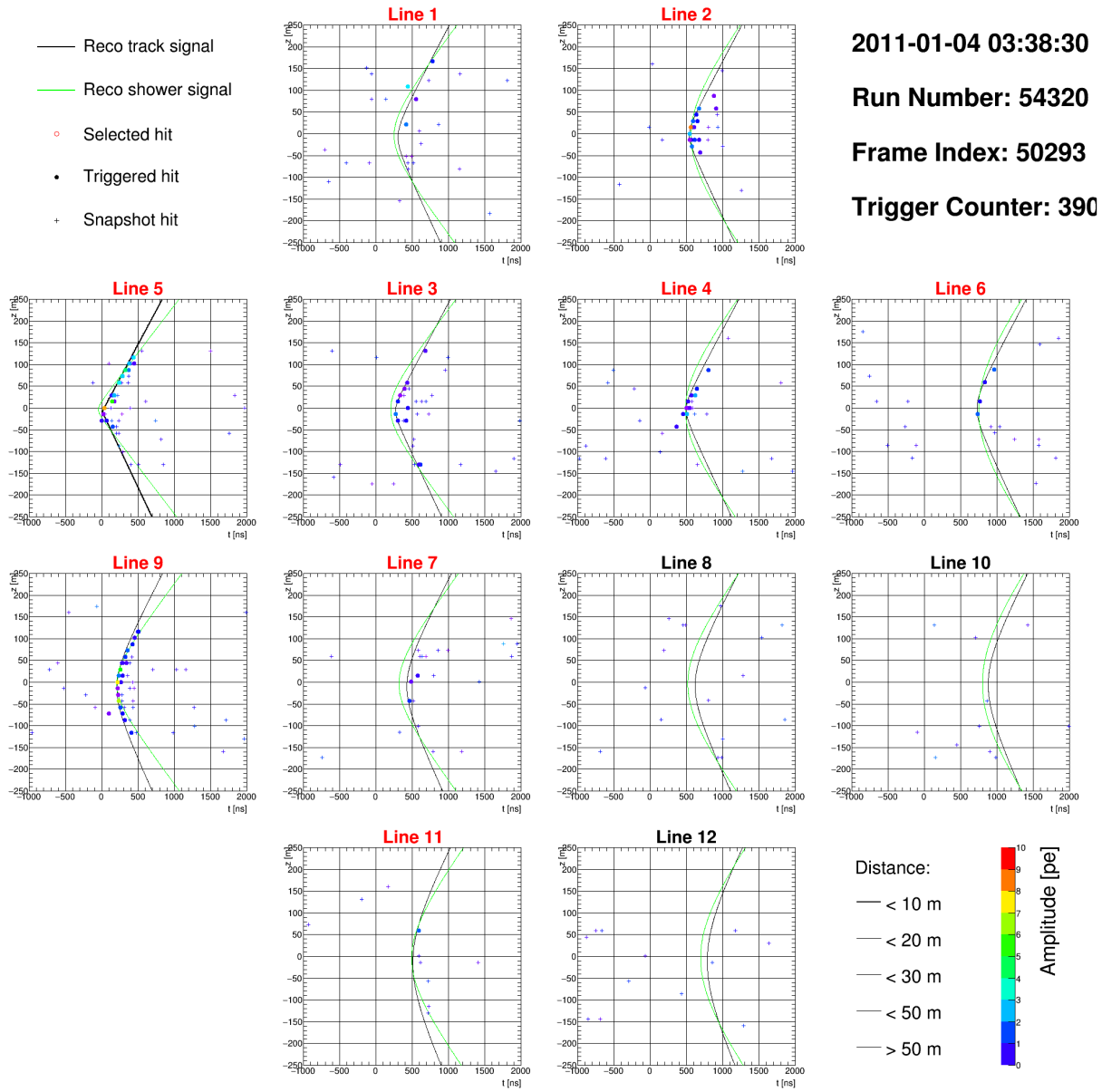
Event		9	
Runnumber	49425	Counter	104853
Event ID	32175	triggers	3D_SCAN, T3
BDTGauss1	0.35	FisherG2alt	0.66
Aafit $\theta$	1.93	Dusj $\theta$	1.75
Aafit $\phi$	3.23	Dusj $\phi$	1.752.49
Aafit $\lambda$	-5.25	Dusj VLLH	0.89
longitude	210.7	latitude	40.8
Aafit $\beta$	0.01		
BB track $\chi^2$	8.58	BB bright $\chi^2$	3.04
$E_{ANN}$ [GeV]	0.72	$E_{Dusj}$ [GeV]	0.61
$E_{dEdx}$ [GeV]	5.1	$A_{Dusj}$	657.98
$E_R$ [GeV]	5.54		
$N_{Aafit}$	115	$N_{Dusj}$	132
in analysis	shower	selection	2



Event		10	
Runnumber	51140	Counter	156280
Event ID	49565	triggers	3D_SCAN, T3, GC
BDTGauss1	0.35	FisherG2alt	0.61
Aafit $\theta$	2.23	Dusj $\theta$	1.96
Aafit $\phi$	4.89	Dusj $\phi$	1.964.91
Aafit $\lambda$	-5.86	Dusj VLLH	0.9
longitude	122.8	latitude	37.5
Aafit $\beta$	0.01		
BB track $\chi^2$	56.0	BB bright $\chi^2$	2.2
$E_{ANN}$ [GeV]	0.61	$E_{Dusj}$ [GeV]	0.56
$E_{dEdx}$ [GeV]	4.66	$A_{Dusj}$	1120.03
$E_R$ [GeV]	5.28		
$N_{Aafit}$	154	$N_{Dusj}$	199
in analysis	-	selection	1



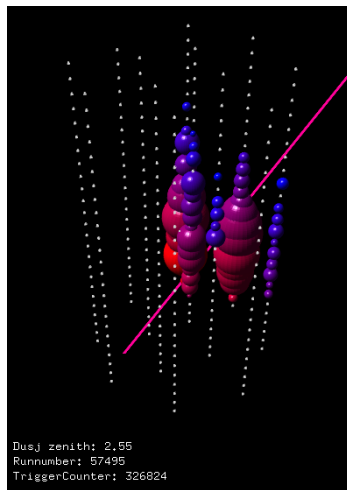
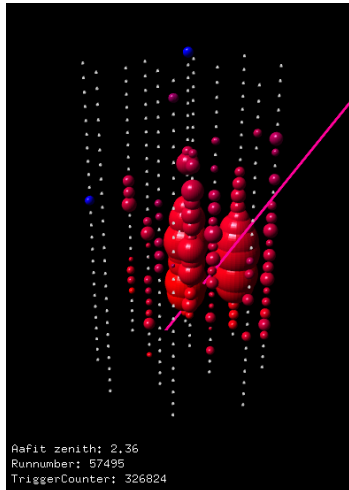
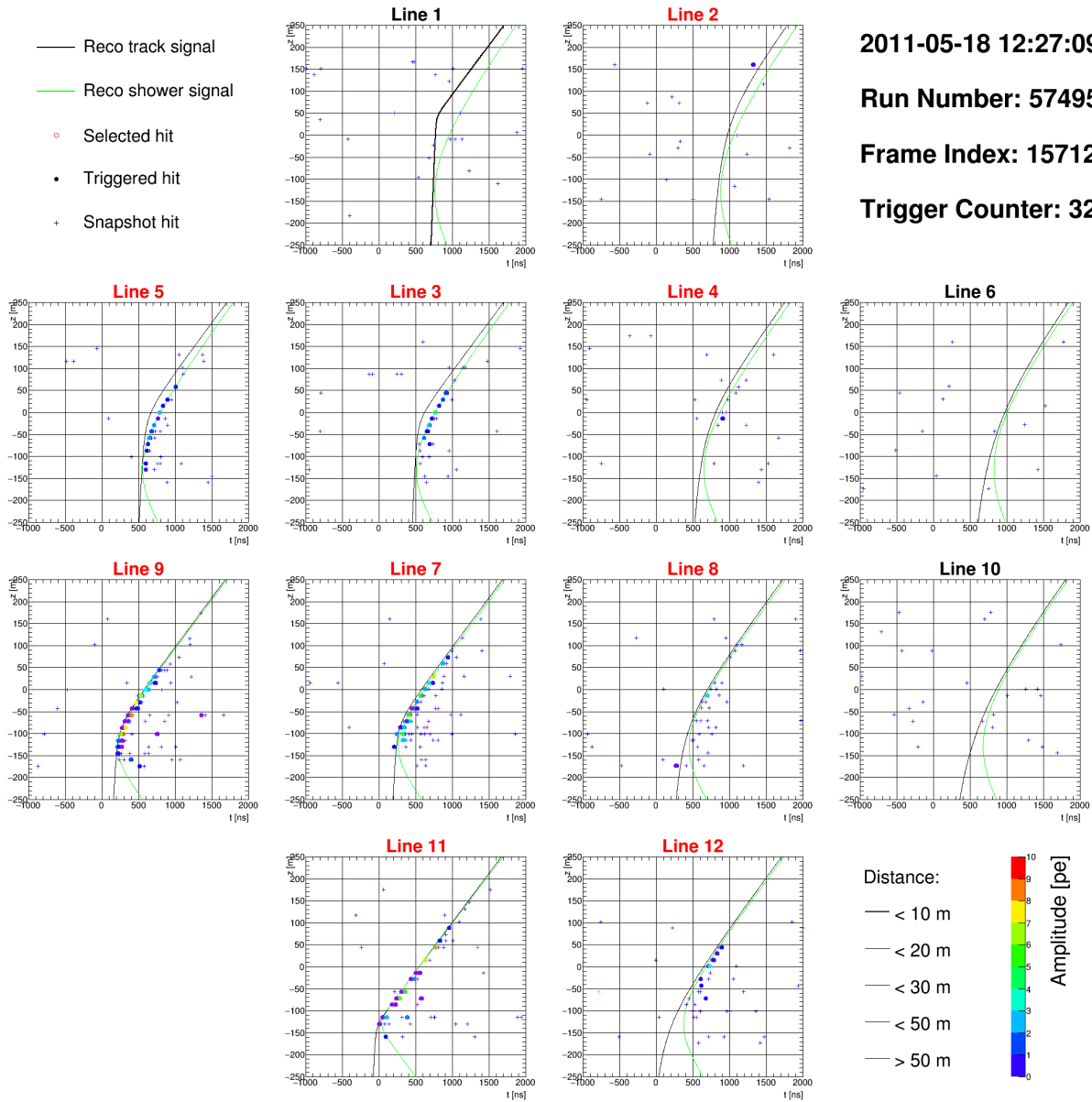
Event		11	
Runnumber	52092	Counter	491305
Event ID	45664	triggers	3D_SCAN, T3, GC
BDTGauss1	0.43	FisherG2alt	0.54
Aafit $\theta$	2.68	Dusj $\theta$	2.03
Aafit $\phi$	5.11	Dusj $\phi$	2.034.52
Aafit $\lambda$	-4.9	Dusj VLLH	0.92
longitude	151.3	latitude	33.3
Aafit $\beta$	0.0		
BB track $\chi^2$	3.85	BB bright $\chi^2$	8.58
$E_{ANN}[\text{GeV}]$	0.7	$E_{Dusj}[\text{GeV}]$	0.67
$E_{dEdx}[\text{GeV}]$	3.84	$A_{Dusj}$	177.26
$E_R[\text{GeV}]$	4.34		
$N_{Aafit}$	123	$N_{Dusj}$	68
in analysis	PS	selection	1



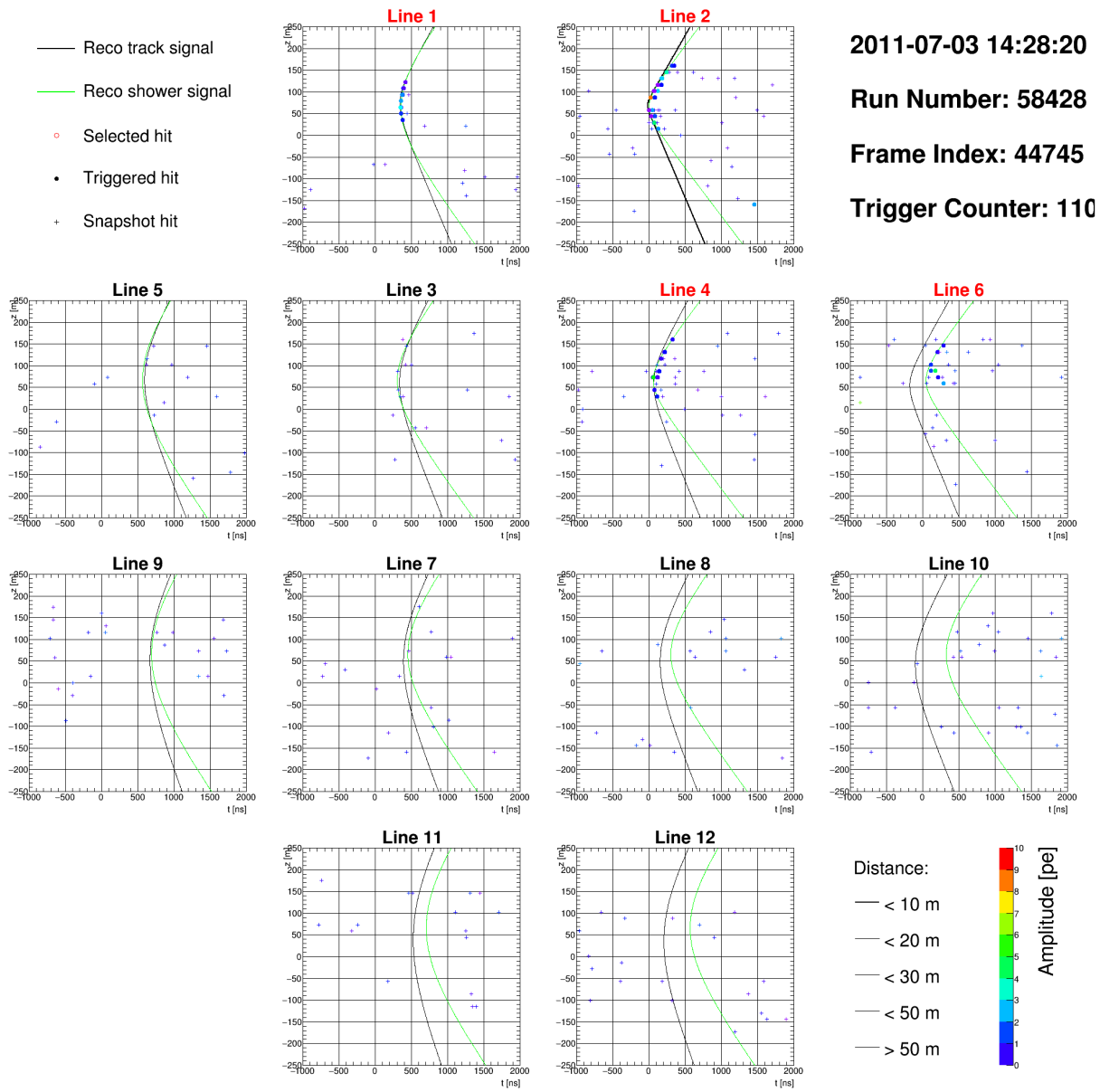
Event		12	
Runnumber	54320	Counter	3902831
Event ID	50293	triggers	3D_SCAN, T3, GC, T2, TQ
BDTGauss1	0.35	FisherG2alt	0.54
Aafit $\theta$	1.62	Dusj $\theta$	1.72
Aafit $\phi$	2.79	Dusj $\phi$	1.722.31
Aafit $\lambda$	-4.46	Dusj VLLH	0.95
longitude	356.6	latitude	33.2
Aafit $\beta$	0.0		
BB track $\chi^2$	3.65	BB bright $\chi^2$	10.62
$E_{ANN}$ [GeV]	0.69	$E_{Dusj}$ [GeV]	0.61
$E_{dEdx}$ [GeV]	4.6	$A_{Dusj}$	261.84
$E_R$ [GeV]	4.55		
$N_{Aafit}$	111	$N_{Dusj}$	80
in analysis	PS	selection	1

- Reco track signal
- Reco shower signal
- Selected hit
- Triggered hit
- + Snapshot hit

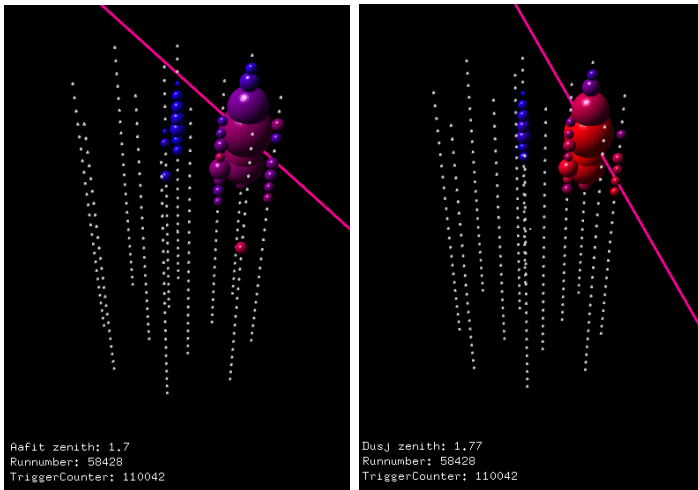
2011-05-18 12:27:09  
 Run Number: 57495  
 Frame Index: 15712  
 Trigger Counter: 326



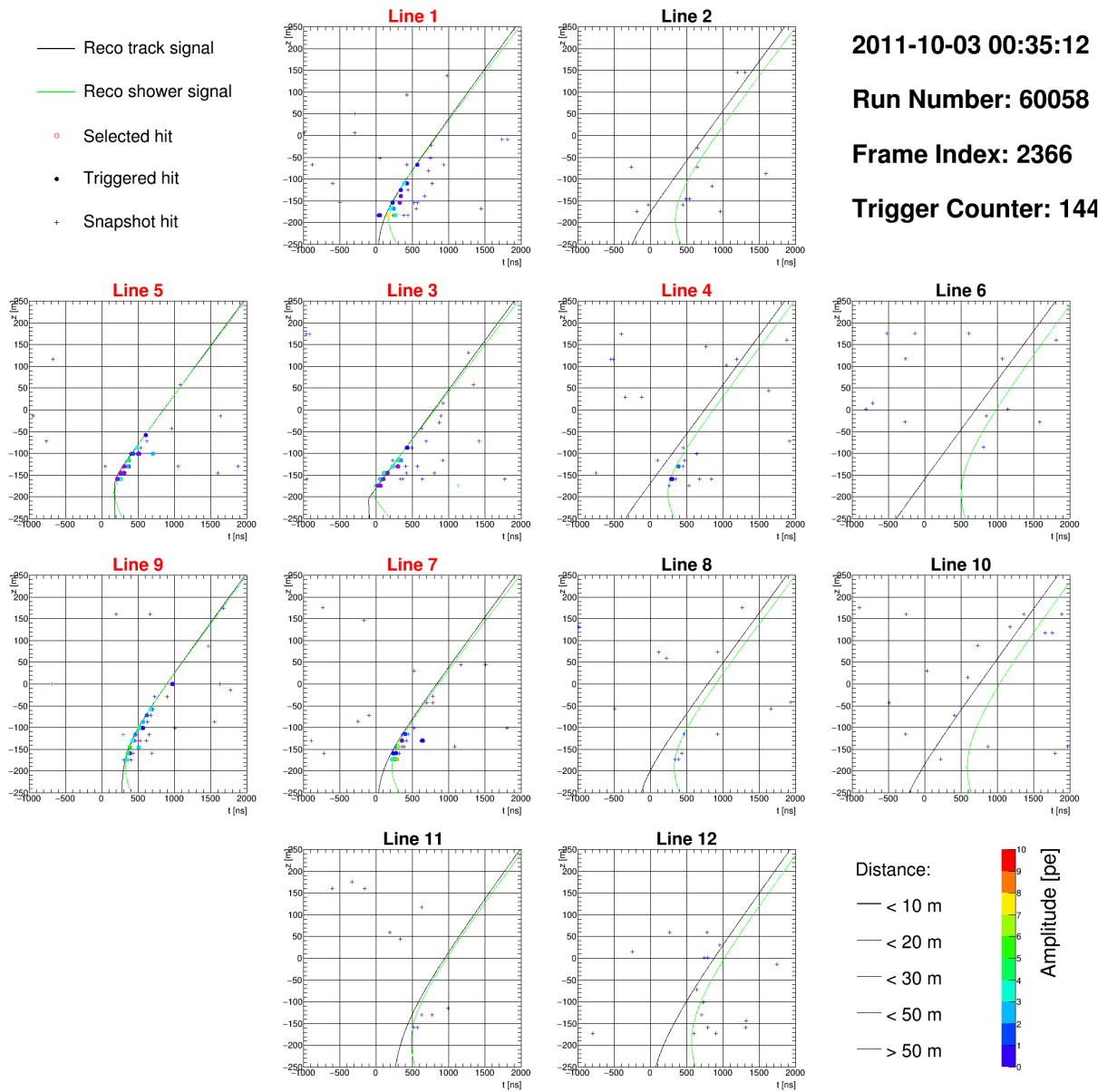
Event		13	
Runnumber	57495	Counter	326824
Event ID	15712	triggers	3D_SCAN, T3
BDTGauss1	0.38	FisherG2alt	0.58
Aafit $\theta$	2.36	Dusj $\theta$	2.55
Aafit $\phi$	4.19	Dusj $\phi$	2.555.58
Aafit $\lambda$	-5.68	Dusj VLLH	0.91
longitude	144.7	latitude	34.5
Aafit $\beta$	0.01		
BB track $\chi^2$	31.58	BB bright $\chi^2$	11.19
$E_{ANN}$ [GeV]	0.66	$E_{Dusj}$ [GeV]	0.61
$E_{dEdx}$ [GeV]	4.72	$A_{Dusj}$	1204.6
$E_R$ [GeV]	5.29		
$N_{Aafit}$	199	$N_{Dusj}$	178
in analysis	-	selection	1



2011-07-03 14:28:20  
 Run Number: 58428  
 Frame Index: 44745  
 Trigger Counter: 110



Event		14	
Runnumber	58428	Counter	110042
Event ID	44745	triggers	3D_SCAN, T3
BDTGauss1	0.39	FisherG2alt	0.54
Aafit $\theta$	1.7	Dusj $\theta$	1.77
Aafit $\phi$	5.3	Dusj $\phi$	1.774.92
Aafit $\lambda$	-5.53	Dusj VLLH	0.91
longitude	128.6	latitude	-19.6
Aafit $\beta$	0.01		
BB track $\chi^2$	19.86	BB bright $\chi^2$	11.86
$E_{ANN}$ [GeV]	0.69	$E_{Dusj}$ [GeV]	0.51
$E_{dEdx}$ [GeV]	5.15	$A_{Dusj}$	307.92
$E_R$ [GeV]	4.7		
$N_{Aafit}$	67	$N_{Dusj}$	65
in analysis	-	selection	1

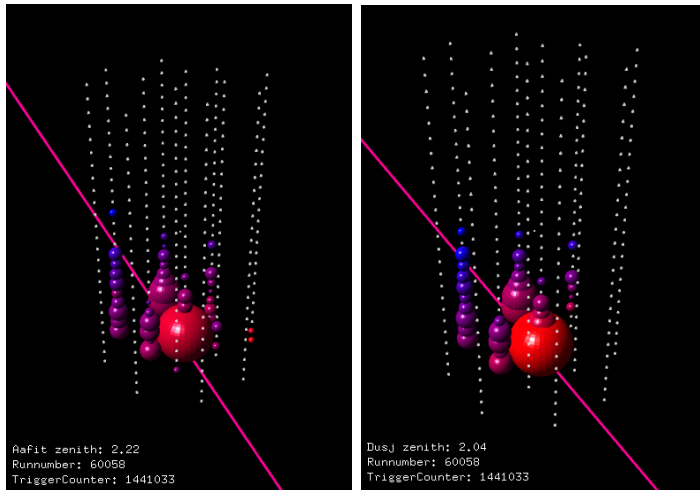


2011-10-03 00:35:12

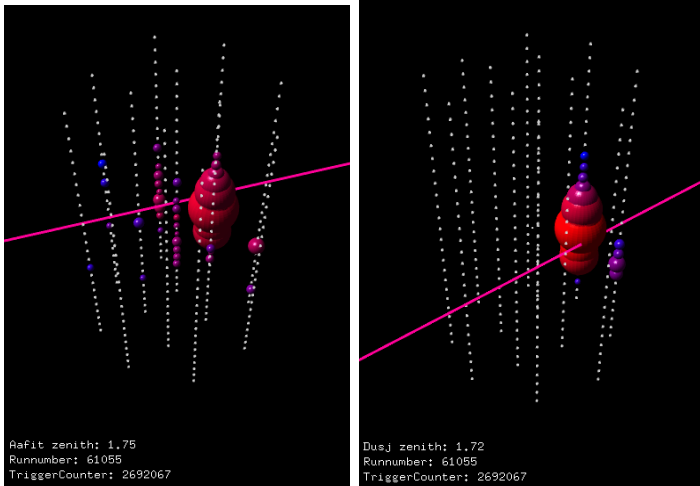
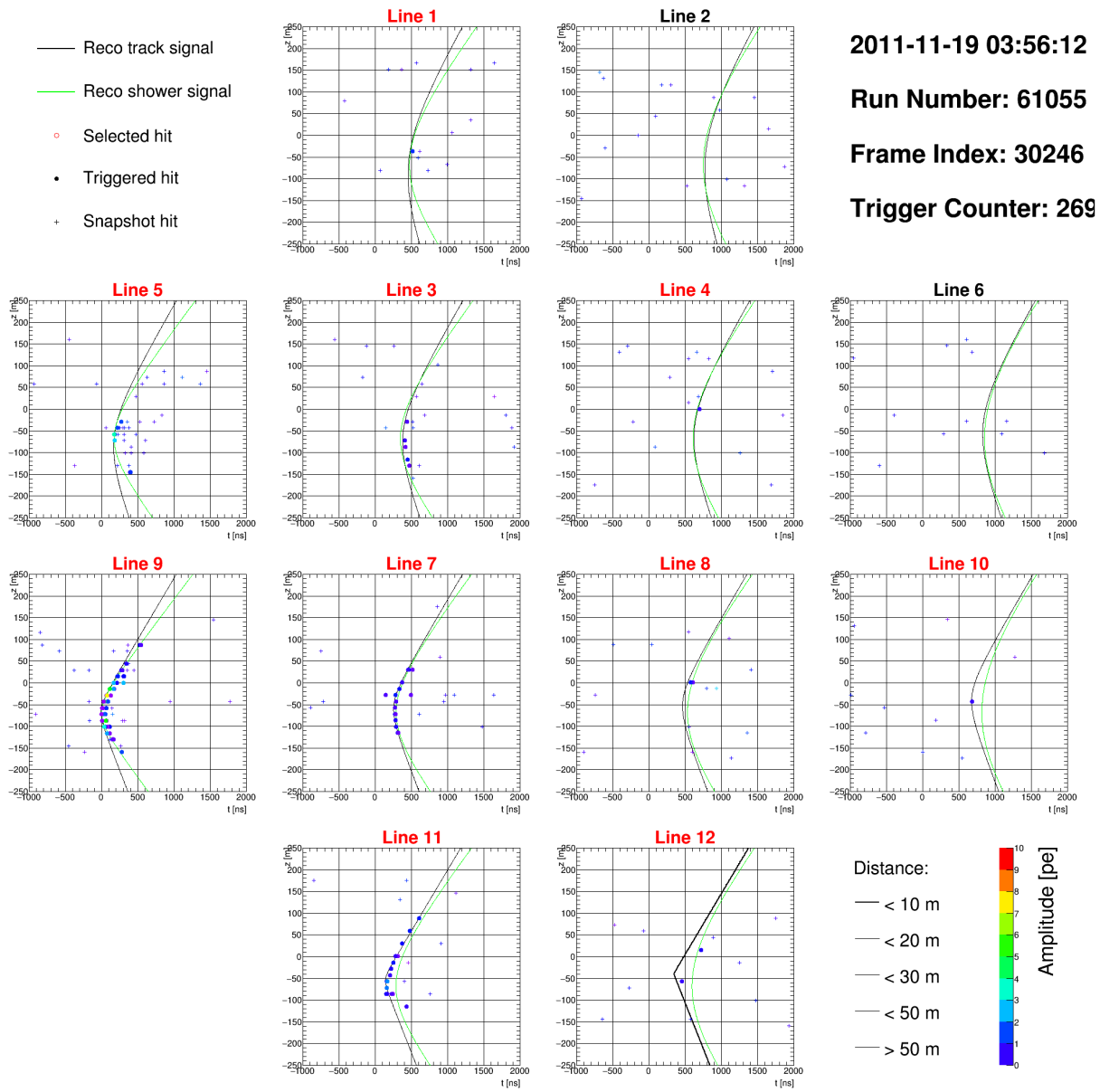
Run Number: 60058

Frame Index: 2366

Trigger Counter: 144



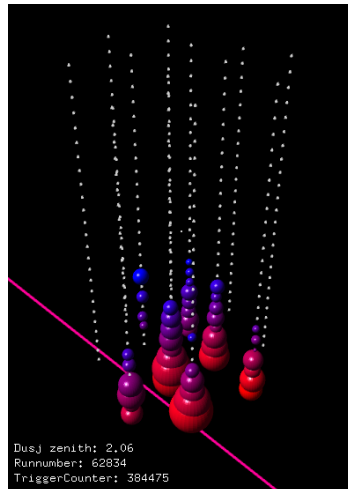
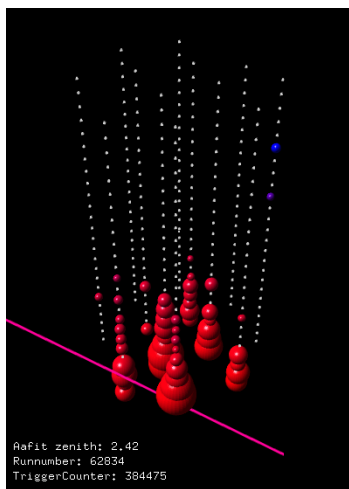
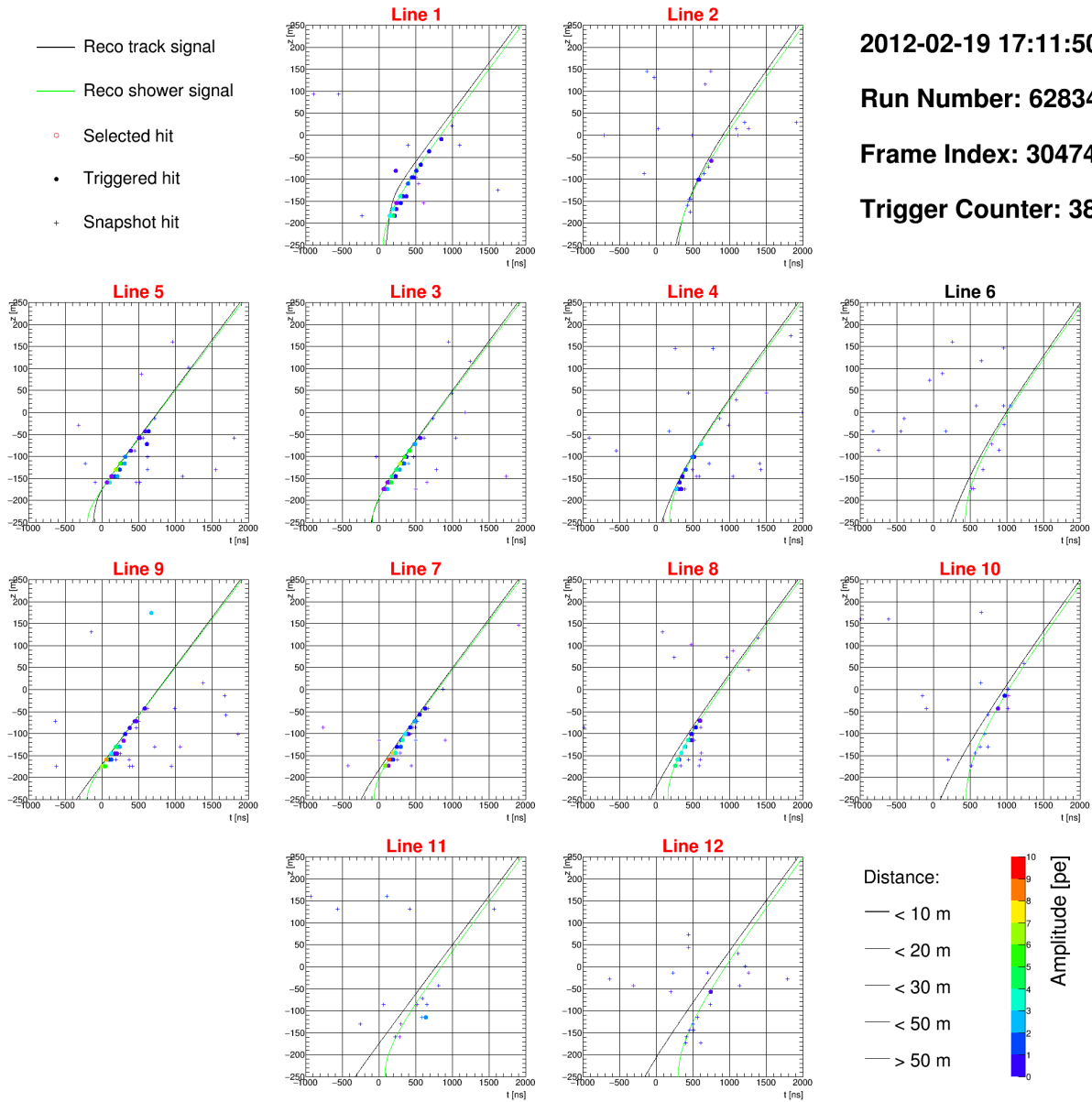
Event		15	
Runnumber	60058	Counter	1441033
Event ID	2366	triggers	3D_SCAN, T3, GC
BDTGauss1	0.42	FisherG2alt	0.62
Aafit $\theta$	2.22	Dusj $\theta$	2.04
Aafit $\phi$	5.91	Dusj $\phi$	2.045.95
Aafit $\lambda$	-5.5	Dusj VLLH	0.93
longitude	84.3	latitude	-9.9
Aafit $\beta$	0.01		
BB track $\chi^2$	4.91	BB bright $\chi^2$	3.35
$E_{ANN}$ [GeV]	0.73	$E_{Dusj}$ [GeV]	0.53
$E_{dEdx}$ [GeV]	5.16	$A_{Dusj}$	502.72
$E_R$ [GeV]	5.35		
$N_{Aafit}$	89	$N_{Dusj}$	96
in analysis	-	selection	2



Event		16	
Runnumber	61055	Counter	2692067
Event ID	30246	triggers	3D_SCAN, T3, GC, T2, TQ
BDTGauss1	0.4	FisherG2alt	0.53
Aafit $\theta$	1.75	Dusj $\theta$	1.72
Aafit $\phi$	2.46	Dusj $\phi$	1.722.98
Aafit $\lambda$	-5.35	Dusj VLLH	0.91
longitude	275.1	latitude	39.8
Aafit $\beta$	0.01	BB track $\chi^2$	8.13
$E_{ANN}$ [GeV]	0.61	$E_{Dusj}$ [GeV]	0.5
$E_{dEdx}$ [GeV]	4.73	$A_{Dusj}$	373.6
$E_R$ [GeV]	4.89		
$N_{Aafit}$	76	$N_{Dusj}$	56
in analysis	-	selection	1

- Reco track signal
- Reco shower signal
- Selected hit
- Triggered hit
- + Snapshot hit

2012-02-19 17:11:50  
 Run Number: 62834  
 Frame Index: 30474  
 Trigger Counter: 384



Event		17	
Runnumber	62834	Counter	384475
Event ID	30474	triggers	3D_SCAN, T3, GC, TQ
BDTGauss1	0.45	FisherG2alt	0.7
Aafit $\theta$	2.42	Dusj $\theta$	2.06
Aafit $\phi$	4.16	Dusj $\phi$	2.063.21
Aafit $\lambda$	-5.16	Dusj VLLH	0.88
longitude	146.5	latitude	23.9
Aafit $\beta$	0.03		
BB track $\chi^2$	8.5	BB bright $\chi^2$	3.06
$E_{ANN}$ [GeV]	0.72	$E_{Dusj}$ [GeV]	0.62
$E_{dEdx}$ [GeV]	5.35	$A_{Dusj}$	537.34
$E_R$ [GeV]	5.39		
$N_{Aafit}$	113	$N_{Dusj}$	138
in analysis	shower	selection	2



# List of Figures

1.1	Primary cosmic ray spectrum . . . . .	8
1.2	Schematic of the second order and first order Fermi mechanisms. . . . .	9
1.3	Hillas plot, showing the dependence on particles at an acceleration site on the magnetic field strength correlated to the size of the site. . . . .	11
1.4	Model of an Active Galactic Nucleus. . . . .	12
1.5	Neutrino cross section and overview over neutrino sources and experiments. . .	15
1.6	Pre-trial p-value sky map of the Northern hemisphere scan in equatorial coordinates. . . . .	16
1.7	Results of different <i>IceCube</i> analyses measuring the astrophysical flux parameters $\Phi_{astro}$ and $\gamma_{astro}$ . . . . .	18
1.8	<i>IceCube</i> spectrum unfolded for an unbroken power-law model. . . . .	19
2.1	Feynman graphs of neutrino $\nu_l$ , $l = e, \mu, \tau$ interaction through $W^\pm$ or $Z^0$ exchange with quarks of a hadron $N$ . . . . .	21
2.2	Neutrino cross-section for NC and CC interactions in the $e$ and $\mu$ channel . . .	22
2.3	Path length of neutrino interaction products in water . . . . .	23
2.4	Average energy loss by muons passing through hydrogen, iron and uranium through radiative processes and ionization. . . . .	24
2.5	Schematic view of the detection principle and schematic view of the detector layout. . . . .	26
2.6	Schematic view of an Optical Module (OM) and a single storey of 3 OMs. . . .	27
2.7	Estimates of prompt atmospheric neutrino fluxes compared to conventional atmospheric neutrino flux estimates for $\nu_e$ and $\nu_\mu$ . . . . .	29
2.8	Production of atmospheric neutrinos and muon in the atmosphere, and absorption of atmospheric muons after passage through water. . . . .	30
2.9	PMT mean rate, salinity, temperature and sea current measured at at the instrumentation line in 2010. . . . .	32
2.10	Average OM efficiency for detection line 1 over nine years of data taking. . . .	34
3.1	Schematic view of the simulation chain . . . . .	38
3.2	Scattering parameters of the 'partic' model, with water scattering and absorption parameters and fraction of scattering due to sea water . . . . .	41
3.3	Logarithmic angular efficiency and quantum efficiency of the optical modules as simulated in KM3. . . . .	42

---

4.1	zt-graphs of hits on four detection lines. . . . .	47
4.2	Overview over the work flow for the Dusz cascade reconstruction. . . . .	48
4.3	Number of Cherenkov photons from the primary particle and radiative processes along an exemplary muon track. . . . .	50
5.1	Comparison of least detectable signal, average upper limit and $f(x) = 2\sqrt{n}$ . . .	55
5.2	Schematic displaying the options for the combination of track and shower analyses. . . . .	56
6.1	Schematic of various multivariate methods. . . . .	61
6.2	Overview over multivariate methods and the pattern recognition cycle. . . . .	64
6.3	Selection criteria for parameter candidates. . . . .	66
6.4	Input parameter evaluation. . . . .	68
6.5	ROC curves for various methods in first test training. . . . .	70
6.6	$N_{\text{events}}$ and $\mathcal{S}$ of various methods at different cut values. . . . .	71
6.7	Angular distribution of events in simulation and reconstructed by Aafit before cuts for 40 runs. . . . .	73
6.8	Correlation between two different BDT setups for muon events from the test sample. . . . .	76
6.9	Output parameter of BDTGauss1 method on 1490d lifetime. . . . .	77
6.10	Simulated event energy and number of hits from the Aafit selection as exemplary energy estimate. . . . .	78
6.11	Signal efficiency $\epsilon_{0.1\%}$ comparison of final TMVA methods for atmospheric neutrino suppression . . . . .	79
6.12	Fisher discriminant output for 1490 days lifetime. . . . .	80
6.13	Correlation of two well-performing Fisher discriminants. . . . .	81
7.1	Schematic overview over the event selection, parameter transformation and multivariate tool application . . . . .	88
7.2	Data processing schematic. . . . .	90
7.3	Accumulated data taking livetime in days over runnumber. . . . .	92
7.4	Distribution of cosmic tau neutrinos $\nu_\tau$ for two classifiers. . . . .	93
7.5	Distribution of atmospheric muon events in the two classifier types, with multiplicity $m$ above and below 200. . . . .	94
7.6	Distribution of number of atmospheric muon events and $2d$ Gaussian fit to the distribution for the BDT and Fisher discriminant. . . . .	95
8.1	Schematic overview over the model rejection and discovery optimization scanning. . . . .	98
8.2	Result of the cut optimization procedure for classifier selection. . . . .	99
8.3	Model rejection factor and discovery potential (for $3\sigma$ at 50%) for various parameter cut configurations. . . . .	101
8.4	Extrapolated muon number and error for different fit intervals. . . . .	103
8.5	Comparison between measurement and simulation in the test sample for the atmospheric muon suppression parameter after primary cuts. . . . .	105
8.6	Comparison between measurement and simulation in the test sample the atmospheric neutrino suppression parameter. . . . .	106

---

8.7	Events from run 38355, classified as <i>sparkling</i> for the atmospheric muon classifier, compared to expectations from simulation. . . . .	107
9.1	Agreement between data and simulation for all events from data selection 1 and 2 for the BDT method and the Fisher discriminant. . . . .	110
9.2	Classifier parameters of the final events, compared to the expected distribution of atmospheric shower- and track-like neutrino events. . . . .	112
9.3	Shower vertex positions as reconstructed by the BBFit Bright Point fit and the Dusj reconstruction for the 12 events of selection 1. . . . .	113
9.4	Reconstruction parameters for the selected events from run selections 1 and 2 compared to the expectation of track- and shower-like atmospheric neutrino events. . . . .	114
9.5	Galactic latitude and longitude of the final events as reconstructed by the Aafit track reconstruction. . . . .	115
9.6	Event 12 as shown in a 3D animation using the Aafit and Dusj hit selection and reconstruction. . . . .	116
9.7	Event 17 as shown in a 3D animation using the Aafit and Dusj hit selection and reconstruction. . . . .	117
9.8	Flux limits for the last track and cascade analyses in ANTARES, the <i>IceCube</i> result and limits and sensitivity and upper limits of this analysis. . . . .	119
9.9	Integrated energy distribution for the events found in 913 days. . . . .	120
10.1	Comparison of the parameter distribution for both multivariate parameters for all measured events after application of the TMVA classifiers. . . . .	124
10.2	Comparison of the parameter distribution of atmospheric neutrinos for the atmospheric muon and atmospheric neutrino classifier. . . . .	125
10.3	Water models tested for the <i>ANTARES</i> site and measurement of the absorption length from atmospheric muons. . . . .	126
A.1	Best model rejection factor and discovery potential for each classifier combination. . . . .	142



# List of Tables

5.1	Event numbers and model rejection factor of the toy analyses. . . . .	57
6.1	Comparison of properties of the different TMVA methods. . . . .	62
6.2	List of parameter candidates for the analysis. . . . .	69
6.3	Scanning results for atmospheric muon suppression. . . . .	74
6.4	Input parameters, parameters transformations and TMVA classifiers for atmospheric muon suppression and cosmic neutrino selection. . . . .	83
7.1	Number of runs and lifetime for measurements and simulation sets. . . . .	90
8.1	Methods list and simulation details for the classifier scanning. . . . .	100
8.2	Method and simulation details for the parameter cut scanning. . . . .	102
8.3	Signal and background expectation including error estimates for 1757.5 days of <i>ANTARES</i> lifetime, and sensitivity towards the test fluxes. . . . .	104
9.1	Event number expectations from simulation and measurement after different cut stages for all selection 1 (selection 2) runs. . . . .	111
9.2	Reconstruction parameters of the events found in the full data sample. . . . .	112
9.3	Signal and background expectation including error estimates for 913 days of <i>ANTARES</i> lifetime. . . . .	118
A.1	TMVA scanning results for atmospheric neutrino suppression. . . . .	139
A.2	TMVA scanning results for atmospheric neutrino suppression using Fisher discriminant. . . . .	139



# Bibliography



# Danksagung

Dass diese Arbeit passiert ist und ihren Abschluss gefunden hat, ist vielen Leuten zu verdanken. Uli Katz, weil er den offenen Raum für die Arbeit gegeben hat, Thomas Eberl, weil er sie mit kreativen und zielführenden Vorschlägen begleitet hat und vielen Kollegen aus der ANTARES-Kollaboration, weil sie den Rahmen für die Analyse geschaffen haben und sie kritisch und konstruktiv reflektiert haben. Am ECAP wurde dabei die Arbeit durch das kollegiale Miteinander in der ANTARES-Gruppe geprägt, besonders in unserem gemütlichen Büro und dadurch, dass man für jedes Anliegen immer überall ein offenes Ohr gefunden hat. Dafür besonderen Dank! Und letztendlich gebührt der wichtigste Dank meinen Eltern, die nicht nur von klein auf Physik zu einem Teil meines Lebens machten, sondern mir ohne viele Fragen und Bedingungen ermöglichten, das zu tun, was ich wollte, und mich immer unterstützen.